TECHNISCHE UNIVERSITÄT MÜNCHEN

Lehrstuhl für Experimentalphysik IV und
Forschungs-Neutronenquelle Heinz Maier-Leibnitz (FRM II)

The Pico- to Nanosecond Dynamics of Phospholipid Molecules

Vinzenz Erik Sebastian Busch

Vollständiger Abdruck der von der Fakultät für Physik der Technischen Universität München zur Erlangung des akademischen Grades eines

Doktors der Naturwissenschaften (Dr. rer. nat.)

genehmigten Dissertation.

Vorsitzender:	Univ.-Prof. Dr. Martin Zacharias
Prüfer der Dissertation:	
	1. Univ.-Prof. Dr. Winfried Petry
	2. Univ.-Prof. Dr. Andreas Bausch
	3. Univ.-Prof. Dr. Tobias Unruh (Friedrich-Alexander-Universität Erlangen-Nürnberg)

Die Dissertation wurde am 04. 01. 2012 bei der Technischen Universität München eingereicht und durch die Fakultät für Physik am 30. 04. 2012 angenommen.

Physik-Department Technische Universität München

Lehrstuhl für Experimentalphysik IV and
Forschungs-Neutronenquelle Heinz Maier-Leibnitz (FRM II)

Dissertation

The Pico- to Nanosecond Dynamics of Phospholipid Molecules

Sebastian Busch

2012

Vollständiger Abdruck der von der Fakultät für Physik der Technischen Universität München zur Erlangung des akademischen Grades eines

Doktors der Naturwissenschaften (Dr. rer. nat.)

genehmigten Dissertation.

Vorsitzender:		Univ.-Prof. Dr. Martin Zacharias
Prüfer der Dissertation:		
	1.	Univ.-Prof. Dr. Winfried Petry
	2.	Univ.-Prof. Dr. Andreas Bausch
	3.	Univ.-Prof. Dr. Tobias Unruh (Friedrich-Alexander-Universität Erlangen-Nürnberg)

Die Dissertation wurde am 04. 01. 2012 bei der Technischen Universität München eingereicht und durch die Fakultät für Physik am 30. 04. 2012 angenommen.

Contents

Zusammenfassung / Summary v

I. Dissertation 1

1. Introduction 3
1.1. Phospholipids in Nature and Application 4
1.2. Some Concepts of Glassy Dynamics 8
1.3. Dynamics of Phospholipids 12

2. Theoretical Principles 17
2.1. Molecular Structure and Dynamics are Described by Correlation Functions 17
2.2. Measuring the Correlation Functions with Neutron Scattering 24

3. Materials and Methods 29
3.1. Preparation and Characteristics of the Phospholipid Samples 29
3.2. Description of the Neutron time-of-flight Spectrometer TOFTOF 35
3.3. Choice of Measurement Parameters 39

4. Data Reduction and Analysis 47
4.1. Extracting the Scattering Function from the Scattered Intensities 47
4.2. Finding the Mechanism of Diffusion with a Fit 50
4.3. Model-free Determination of the Mobility 57

5. Results and Discussion 61
5.1. Methodical Enhancements 61
5.2. Molecular Dynamics in Pure Phospholipid Multibilayers 64
5.3. Multibilayers of DMPC with Additives 70
5.4. Single Bilayers and Monolayers 71

6. Outlook 73
6.1. Methodical Enhancements 73
6.2. Molecular Dynamics in Pure Phospholipid Multibilayers 77
6.3. Multibilayers of DMPC with Additives 79
6.4. Single Bilayers and Monolayers 79

7. Conclusion 83

II. Publications 85

A. List of Publications and Presentations 87
- A.1. Refereed Publications . . . 87
- A.2. Non-refereed Publications . . . 90
- A.3. Talks at International Conferences . . . 90
- A.4. Participation in Seminars and Workshops . . . 91
- A.5. Posters at International Conferences . . . 92

B. Molecular Mechanism of Long-Range Diffusion in Phospholipid Membranes Studied by Quasielastic Neutron Scattering 95

C. Dynamical Transition of Protein-Hydration Water 117

D. The Slow Short-Time Motions of Phospholipid Molecules With a Focus on the Influence of Multiple Scattering and Fitting Artefacts 123

E. The Influence of Additives on the Nanoscopic Dynamics of the Phospholipid Dimyristoylphosphatidylcholine 137

F. The Picosecond Dynamics of the Phospholipid Dimyristoylphosphatidylcholine in Mono- and Bilayers 149

G. FABADA: a Fitting Algorithm for Bayesian Analysis of DAta 163

H. Fitting in a Complex χ^2 Landscape Using an Optimized Hypersurface Sampling 173

III. Additional Information 181

I. Details of the Data Reduction 183
- I.1. Data Reduction Software . . . 183
- I.2. Data Reduction Procedure . . . 188
- I.3. Effective Scattering Cross Section . . . 192

Bibliography 195

Acknowledgements 223

Zusammenfassung / Summary

Zusammenfassung

Die Bewegungen des Phospholipids Dimyristoylphosphatidylcholin wurden mit quasielastischer Neutronenstreuung auf einer Zeitskala im Piko- bis Nanosekundenbereich untersucht. Bis vor Kurzem war man der Meinung, dass die Moleküle bei diesen kurzen Zeiten sich nur kleinräumig in einem Käfig, der von ihren Nachbarn gebildet wird, bewegen können. Ab und zu könnten die Moleküle aus diesem Käfig springen, wenn sich durch thermische Fluktuationen eine Leerstelle darin auftäte. Molekulardynamiksimulationen haben allerdings kürzlich ein anderes Bild gezeichnet: Die Moleküle springen nicht aus ihrem Käfig, sondern bewegen sich vielmehr zusammen mit ihm in flussartigen Strömungen.

Es war nun möglich, die quasielastischen Neutronenstreuungsdaten mit diesem Modell auszuwerten. Die quantitative Übereinstimmung der extrahierten Flussgeschwindigkeiten mit denen der Simulationen ist ein experimenteller Hinweis, dass die bisherige Vorstellung von Sprüngen der Moleküle von Käfig zu Käfig nicht richtig sein kann.

Im Vergleich mit anderen dichten Flüssigkeiten wird klar, dass diese kollektiven Verschiebungen keine Besonderheit der Phospholipide sind sondern ein allgemeines Phänomen, das schon in einer Vielzahl von Systemen beobachtet wurde und dort «dynamische Heterogenitäten» genannt wird, weil es eine räumliche Trennung von schnellen und langsamen Molekülen gibt.

In Natur und Anwendung kommen in den allermeisten Fällen keine reinen Phospholipidsysteme vor, sondern Mischungen mit anderen Molekülen. Während in der Natur Cholesterol eine der wichtigsten Komponenten ist, sind in der pharmazeutischen Anwendung Kostabilisatoren wie Natriumglycocholat von Bedeutung. Diese Kostabilisatoren werden gemeinsam mit dem Phospholipid als Emulgatoren in Nahrungsmitteln und Medikamenten eingesetzt, um eine Entmischung der öligen und wässrigen Komponenten zu verhindern.

Wegen dieser Relevanz von Mischsystemen wurde auch der Einfluss einiger repräsentativer Zusätze auf die Phospholipiddynamik untersucht. Der von makroskopischen Messungen bekannte verlangsamende Effekt von Cholesterol ist zwar auf einer Zeitskala von 55 Pikosekunden noch nicht sehr ausgeprägt, hat aber nach 900 Pikosekunden schon fast sein volles Ausmaß erreicht, das aus makroskopischen Messungen wohlbekannt ist. Interpretiert man dieses Ergebnis im Rahmen der erwähnten Flussbewegungen, wird nicht die Flussgeschwindigkeit, die bei kurzen Zeitskalen die Bewegung dominiert, durch die Cholesterolmoleküle abgebremst, sondern vielmehr wird die Länge verringert, die ein Phospholipidmolekül in solch einer Bewegung zurücklegt, bevor es die Richtung wechselt.

Im Gegensatz dazu ist die Beweglichkeit der Phospholipide in den pharmazeutisch relevanten Systemen deutlich erhöht. In den Fällen, in denen das Phospholipid eine ölige Phase stabilisiert, kann die Phospholipiddichte abgesenkt werden, was die erhöhte Dynamik zur Folge hat. Ein zuvor vermuteter Zusammenhang zwischen der Molekülbeweglichkeit und der Stabilität der Proben kann indes ausgeschlossen werden.

Summary

The motions of the phospholipid dimyristoylphosphatidylcholine were studied on a pico- to nanosecond time scale with quasielastic neutron scattering. Until a short while ago, the opinion prevailed that the molecules can only perform small-scale motions in a cage formed by their neighbours at these short times. Now and then, the molecules could jump out of these cages when a vacancy happened to form in it. However, Molecular Dynamics simulations have recently drawn another picture: the molecules do not escape from their cage but rather move together with it in flow-like structures.

It was now possible to evaluate the quasielastic neutron scattering data with this model. The quantitative agreement of the extracted flow velocities with the ones observed in the simulation is experimental evidence that the hitherto existing picture of molecules jumping from cage to cage cannot be correct.

The comparison with other dense liquids shows that these collective displacements are not a peculiar property of the phospholipids but a universal phenomenon that has previously been observed in many systems where it was termed «dynamical heterogeneities» because fast and slow molecules are spatially separated.

In nature and application, mixtures with other molecules are more frequent than pure phospholipid systems. While cholesterol is one of th most important components in nature, costabilizers like sodium glycocholate are important in pharmaceutical application. These costabilizers are used in combination with phospholipids as emulsifier in nutritional and pharmaceutical products to prevent demixing of oily and watery components.

Because of the relevance of mixed systems, the influence of some representatibe additives was studied, as well. The slowing down effect of cholesterol known from macroscopic measurements is not very pronounced on a time scale of 55 picoseconds but already on a time scale of 900 picoseconds, it has nearly reached the value that is well known from macroscopic measurements. Interpreting this result in the frame of the mentioned flow-like motions, cholesterol does not decrease the flow velocity which dominates the result on the short time scale but rather the length that a molecule covers in of the flow events before changing direction.

In contrast, the mobility of the phospholipids is in the pharmaceutically relevant systems drastically enhanced. In the cases where the phospholipid stabilizes an oily phase, its density can be decreased which results in an enhanced dynamics. A previously conjectured link between the molecular mobility and the stability of the samples can be excluded.

Part I.

Dissertation

Chapter 1.

Introduction

Understanding the motions of phospholipid molecules on a molecular scale is very important for both, basic biological questions and applied problems in pharmaceutical and food industry. In this thesis, these motions are probed with quasielastic neutron scattering on a pico- to nanosecond time scale. During these times, the molecules cover distances in the same order of magnitude as the intermolecular distances. We probe therefore the initial steps of the diffusion.

It was a lucky coincidence that the new neutron time-of-flight spectrometer TOFTOF at the high-flux continuous neutron source Forschungs-Neutronenquelle Heinz Maier-Leibnitz (FRM II) went into routine operation shortly before this thesis was started. The variability and low background of this instrument make it one of the best of its kind worldwide. It was this unique advantage that made it possible to advance our knowledge of the phospholipid dynamics: the unprecedented quality of the data allowed to support collective, flow-like motions as a novel view of the dynamics in phospholipid systems.

With the new generation of neutron scattering instruments, the data is not the limiting factor for the data evaluation any more. It is necessary to enhance the further steps of the extraction of physical information. This is reflected in this thesis: after a concise description of the technique and spectrometer as well as the sample characteristics, a focus will be on improved and new approaches to data reduction and evaluation.

The results are presented in full detail in several publications which originated during the course of this thesis and can be found in the appendices [B–H]. For an in-depth presentation and discussion of the results, the reader is referred to these publications. It is shown there that the molecular motions of phospholipids resemble flow-like motions [B]. Although the corresponding data evaluation was partially influenced by fitting artifacts which were discovered independently [C], it could be assured that this main result is independent from several experimental difficulties [D]. Knowing the dynamics of the pure phospholipid, it was possible to turn to the effects of additives [E] and finally to the situation in pharmaceutically relevant systems [F]. Among the technical innovations that laid the ground for these studies, the arguably most important one was the development of a fit program [G] that is based on a novel algorithm to sample the parameter space [H].

The remainder of this thesis presents a coherent literature review, background information, a more detailed description of the sample preparation and measurements, and a discussion of the different publications in a unified context. The importance of phospholipid molecules in biological and pharmaceutical systems is presented in chapter 1,

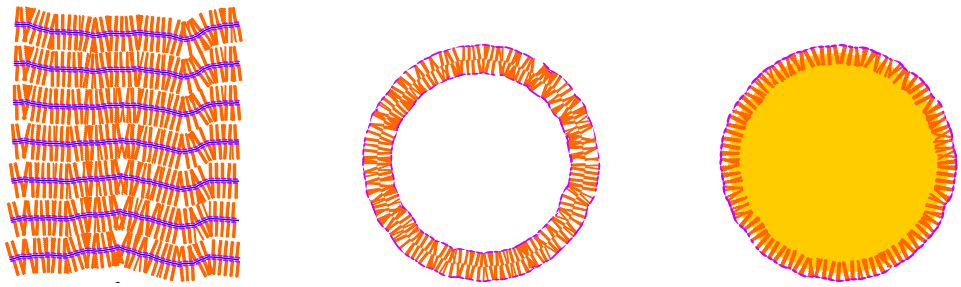

Figure 1.1.: Two-dimensional cuts through typical samples used in this thesis. The head groups of the phospholipid molecules are drawn in violet, and their tail groups in orange. Left: Multibilayers in the lamellar phase, the layers of water are shown in blue. Middle: Single bilayer in a vesicle, the water in and around the vesicle is omitted from the drawing. Right: Monolayer in an emulsion, the oil phase in the droplet is shown in yellow, the water around the droplet is omitted from the drawing.

followed by an introduction to some concepts that are used to describe the dynamics in glass forming systems and an overview how some of these concepts have been successfully used to describe the dynamics in phospholipid membranes. Chapter 2 gives a concise summary of the theory that is used to describe the molecular motions and shows how quasielastic neutron scattering makes it possible to measure them. Having treated the theory, practical aspects of sample preparation and neutron scattering measurements are described in chapter 3. The data obtained in the measurements were treated and evaluated as shown in chapter 4 which led to the results presented in chapter 5 where the dynamics of the phospholipid DMPC is described in detail. Finally, chapter 6 gives impulses in which directions the research presented in this thesis could be continued. In the appendices [B–H], the aforementioned publications are included, appendix [I] gives more details on the treatment of the data.

1.1. Phospholipids in Nature and Application

General Properties of Phospholipids. Phospholipid molecules are amphiphilic, consisting of an hydrophilic *head* group and two lipophilic *tail* groups [8–10]. They form lyotropic liquid crystals with water or oil. The most relevant lyotropic phase in the current context is the lamellar phase where tail groups and head groups, respectively, face each other. As sketched in figure 1.1, these stacks of many bilayers are separated by layers of water between the head groups. They will be called *multibilayers* throughout this thesis. At very large water contents, these stacks disassemble into hollow spheres of *single bilayers*, so-called vesicles which are also sketched in figure 1.1. If the system contains besides the phospholipid and water also an oil phase, a *monolayer* of the phospholipid molecules can act as a stabilizer around oil droplets (cf. figure 1.1).

Within a given lyotropic phase (e. g. the lamellar phase), there are several phases at different temperatures with different arrangements of the molecules within the lamellae.

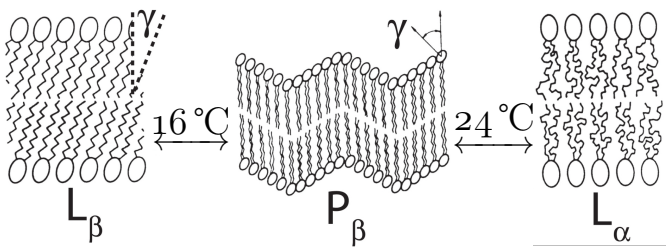

Figure 1.2.: The three phases within the lyotropic lamellar phase of the phospholipid molecules drawn after Sackmann and Merkel [10]: gel phase L_β, ripple phase P_β, and fluid phase L_α. The given temperatures are valid for the here-used DMPC.

The three phases which are discussed in this thesis are sketched in figure 1.2, a more detailed phase diagram is given in section 3.1. The head groups occupy a larger area in the membrane plane than the tails, causing very large lateral pressures within the membrane [11]. In order to achieve optimal packing for both parts of the molecule, the molecules are tilted with respect to the surface normal by an angle γ in the two low temperature phases as shown in figure 1.2 [10]. In the *gel phase* L_β, the membrane surface is smooth and the tails are tilted, being oriented parallel to each other, forming a crystalline like lattice. In the *ripple phase* P_β, the tails are all perpendicular to the average membrane plane but the surface is forms zig-zag like ripples. At high temperatures, the phospholipids are in the *fluid phase* L_α where the tail groups are called to be melted. This is the biologically relevant phase and the one which has a significant amount of lateral diffusion of the phospholipids, about two orders of magnitude more than the low-temperature phases [12].

The class of phospholipid molecules contains several types, differing in the type of head group and the backbone that links it to the tail groups. The current study uses only phosphatidylcholine which contains a diglyceride backbone and after the linking phosphate group a choline head group. The phosphatidylcholines in turn can carry a variety of tail groups. In this thesis, only dimyristoylphosphatidylcholine (DMPC) was used. As can be seen in figure 1.3, the two tail groups are in this case saturated fatty acids, namely myristic acid.

Phospholipids in biology. The paramount importance of phospholipid bilayers for every living being became apparent after the discovery of Gorter and Grendel that they are the key component of cell membranes [13]. Due to this fundamental function, they are actually the most abundant type of organic molecules by number in a human [14]: Given the huge number of cells in our body, the total area of phospholipid membranes in one person amounts to amazing 5 km², about three to four times the area of the inner city of Munich [15].

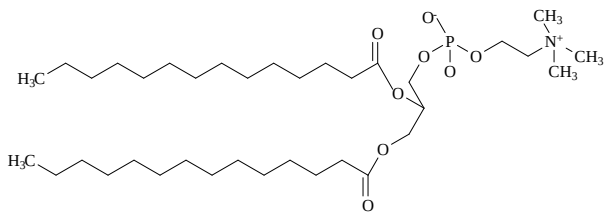

Figure 1.3.: Structural formula of the phospholipid dimyristoylphosphatidylcholine (DMPC). The tail groups contain a fully saturated C_{14} hydrocarbon chain, the head group is zwitterionic.

In most cases, the phospholipid molecules do not exhibit biological functionality themselves but they constitute the barriers of the cell that make it possible to maintain gradients of molecule concentrations. Further, they host membrane proteins [16] which are responsible for a wide variety of functionalities, from molecular transport over messaging to propulsion. These membrane proteins are so densely packed that there are often only a few phospholipid molecules between two of them, not only separating them but also transmitting interactions between them [17, 18]. For these proteins, it is of essential importance to be mobile within the membrane and to be able to change conformation [19]. The membrane proteins even diffuse as dynamic complexes together with the phospholipid molecules [20]. One example for the influence of the mobility on the protein functionality is an enhanced sensitivity of receptors on the cell surface as compared to a static setup [21].

Another important component of the cell membrane is cholesterol. It has a rigid sterol backbone and is mainly located in the lipophilic core of the membrane, its molecular structure is shown later in chapter 3. The probably main biological function is the reduction of the fluidity and permeability of the membrane [22]. In certain mixing ratios, cholesterol is also known to induce a micro phase separation between cholesterol rich and cholesterol poor areas. It is speculated that this mechanism induces the formation of so-called *rafts* in the membrane [23]. With a size of as small as 20 nm [24], they would provide a platform for membrane proteins which profit from a clustering with other proteins in the same raft.

Another possibility of the cell to influence the mobility of the proteins that should be mentioned but will not be discussed in this thesis is the interaction of the cytoskeleton with the membrane [25, 26].

Phospholipids in industry. Phospholipids are not only omnipresent in biology but have also an important place in pharmaceutical and nutritional applications. This is also the area where they receive most public attention. However, this attention usually boils down to the question «What is soy lecithin and why is it in my chocolate?»[1]

This application is a rather basic one that simply prevents the segregation of the lipophilic from the hydrophilic parts. In the last years there was also a lot of development of more complex applications such as *functional food* [27]. In this case, emulsifiers like phospholipids are used for example to increase the bioavailability of lipophilic nutrients by forming emulsions [28].

The same is important for peroral (i. e. through the mouth) drug delivery of lipophilic components and other molecules that are not adsorbed when taken without an appropriate drug delivery system [29–31]. Phospholipids are here one of the many possible choices [32–34] for this task which is of increasing concern: the number of pharmaceutically relevant molecules that are not water soluble – and therefore basically not applicable – is increasing as can be seen in figure 1.4.

Another approach for the delivery of sensitive drugs is to circumvent the digestive tract and choose a parenteral administration. Liposomes, i. e. phospholipid vesicles,

[1] http://www.highonhealth.org/what-is-soy-lecithin-and-why-is-it-in-my-chocolate/

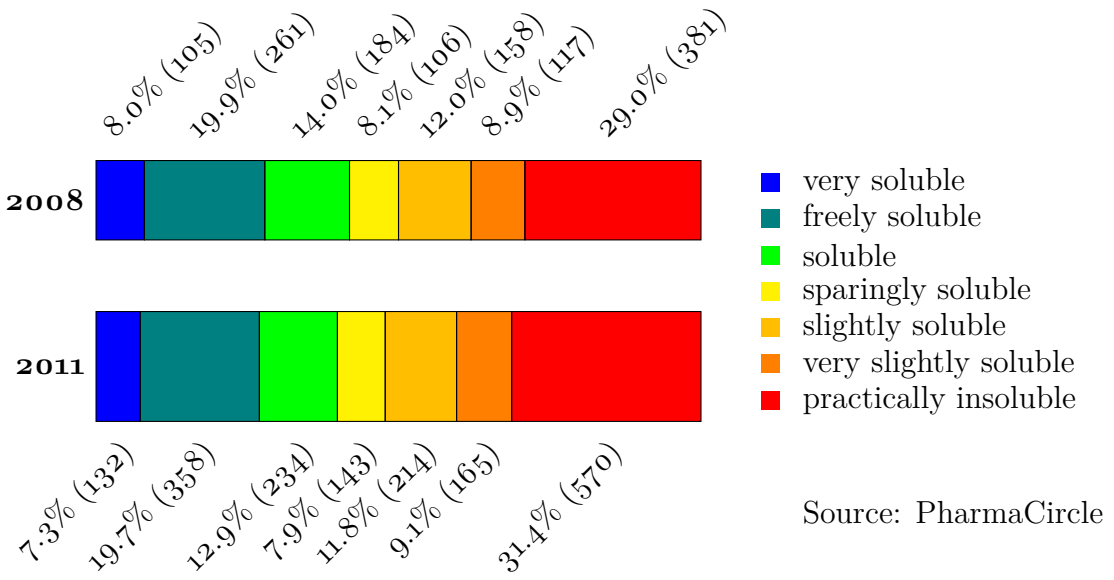

Figure 1.4.: Number of pharmaceutically relevant molecules (from research phase to marketed) in water solubility categories of the United States Pharmacopeia. Although the number of discovered molecules increased in each category during the past three years, only the «very slightly soluble» and «practically insoluble» molecules had also a percentile increase.

can for example be used as carrier for hemoglobin [35], anti-inflammatory drugs [36], or chemotherapeutica for cancer therapy [37]. When combined with fibrin scaffolds, they are also promising candidates for gene delivery systems [38]. For lipophilic drugs, nanoemulsions and nanosuspensions are an option. In these cases, the drug is incorporated into a lipophilic matrix and stabilized with a monolayer of amphiphilic molecules, for example phospholipids [39, 40].

These drug delivery systems consisting of a lipid core covered with a phospholipid monolayer shell are still matter of active research because they have serious problems: On the one hand, if the lipid core is liquid, the contained drug is released too quickly. On the other hand, if a solid lipid is chosen in the nanoparticle, it forms often a single crystal without the drug molecules which are then located at the rim of the particle and are also released too quickly [41–43].

Due to these problems, alternative drug delivery systems are needed. Polymers are one option for the dispersed phase [44, 45] which can even offer a response to external stimuli and are therefore a step in the direction of targeted drug delivery [46, 47]. Also mesoporous silica nanoparticles, possibly coated with phospholipids [48], can be used for a temperature controlled drug release [49].

The adequacy of phospholipids as stabilizing agent is therefore somewhat independent of the choice of the dispersed phase. The stabilizer layer plays a key role for the properties of the drug delivery system: It determines the long-term stability against

chemical degradation [50], the bioavailability [51, 52], and can be used to control the release rate of the drug [53].

These properties can be influenced by adding co-surfactants to the phospholipid. For example, a mixture of phospholipid and bile salt has been shown to be more potent than each of them alone [54] and is even capable of keeping a dispersion of a lipid phase stable while the lipid crystallizes [55, 56]. Such a phase transition of the dispersed phase is an especially challenging task for the stabilizer because it is accompanied by a drastic change of the shape of the particles from droplet-like to disk-like. The stabilizer has to cover the freshly created surfaces before the particles aggregate. The co-surfactants that can cover these surfaces quickly enough were therefore termed *fast*.

That the mobility of the phospholipid molecules plays an essential role in the stabilizing properties can also be inferred from the fact that the stabilization properties change at the main phase transition of the phospholipids [57, 58]: One of the main changes at the main phase transition seen from the outside is the mobility of the phospholipid molecules. It has also been suggested that the distribution of vesicles in the blood stream is influenced by the phase of the phospholipid molecules [59].

Concluding, phospholipids and their dynamics in particular are a worthwhile subject matter. As will be discussed later, this dynamics can be described using the concepts developed for glassy systems. Therefore, an overview of these concepts is given in the following.

1.2. Some Concepts of Glassy Dynamics

On first sight, there seems to be little connection between glasses (disordered materials that lack the periodicity of crystals but behave mechanically like solids [60]) and phospholipids which have a distinct first order phase transition between a fluid and a crystalline state. However, the basic concepts of glass physics have been shown to explain features observed in many soft materials with strongly interacting particles [61]. Biopolymer networks [62] and phospholipid membranes [63] are only some examples.

As a liquid is cooled, it eventually passes its melting temperature T_m where most substances crystallize. It is however possible to avoid crystallization, for example by external measures like confinement, the absence of any crystallization nuclei, or simply by sufficiently high cooling rates. In these cases, the substance becomes a *supercooled liquid* in which the molecular motions slow down as the temperature is decreased. Arbitrary definitions call the substance finally to be in a *glassy state* when the viscosity reaches 10^{13} Poise or the relaxation time 100 seconds. The corresponding temperature is quoted as the glass transition temperature T_g which usually occurs around $\frac{2}{3}\,T_\mathrm{m}$ [60, 64].

Whereas a liquid can change configurations very quickly, the glassy system is basically trapped in one conformation on the experimental time scale due to the long relaxation time. Looking at the energy landscape in the configuration space of the system, this confinement usually means that the system cannot relax to the thermodynamic equilibrium any more on the experimental time scale [60]. This experimental time scale can be much shorter than the 100 seconds quoted before. For example the neutron scattering experiments used

in this thesis have observation times between about one picosecond and one nanosecond. If the relaxation time of a system is one or two orders of magnitude above these values, it appears already frozen in the neutron scattering experiment. This microscopic manifestation of the glass transition can happen at temperatures far above T_g [C].

There are strong parallels between the dynamics of different glass-forming substances, above as well as below T_g. This dynamics is often termed *glassy dynamics* and will be presented in the following. The discussion in this thesis will stick to phenomenological descriptions of the systems and touch the theoretical frameworks that aim to explain the observations only as far as necessary. The main aim of this thesis was to determine how the phospholipid molecules move in membranes with and without additives, in multibilayers and single bilayers, in vesicles and emulsions. As it could be shown that recent concepts from glass physics can help to describe these motions, closer links to the theories of glass physics should be established in future works. A worthwhile starting point for this description could be the probably best known theory of motions in glass-forming systems, the *mode-coupling theory* [65]. It was indeed already used to describe the motions of phospholipid molecules [63]. Although it has been shown that there are systems where the theory fails [66], it has received renewed attention as it was embedded in the bigger framework of the *random first-order transition theory* [67] and was extended so that it could also describe the dynamical heterogeneities which will be presented in the following [68, 69].

Glassy dynamics seen from the liquid side. There is no evidence for a qualitative change of the dynamics anywhere near T_m [65, 70]. The dynamics in supercooled melts show, however, some peculiarities that are not seen in the «normal» behaviour of liquids at high temperatures. Of these, the ones which are important in the current context are: (i) the correlation functions of the system become stretched over a wider time range which can be interpreted as an increasing distribution of the relaxation times and (ii) the average relaxation time of so-called *fragile* glass forming systems varies more strongly with temperature than the Arrhenius dependence predicts.

The main reason for these differences between the dynamics at high and at low temperature is that two-body correlations determine the dynamics at high temperatures whereas many-body correlations become important at the high densities near the glass transition [71]. In other words, every particle experiences a cage of its neighbours as depicted in figure 1.5 [65].

Following the motions of a particle over time, several regimes can be observed: At very short times, the particle does not experience any interaction with its neighbours. It moves in a free flight with a velocity according to a velocity distribution determined by the thermal energy [72]. This motion will *not* be covered in this thesis because it is not relevant for biological and pharmaceutical systems. Because these motions are on a femtosecond time scale, they are not observed by QENS.

Looking on a long time scale, it becomes clear that this initial motion can persist only until the particle interacts with its neighbours which constitute a cage for the particle. For a true long-range motion, the particle has to escape from this cage of

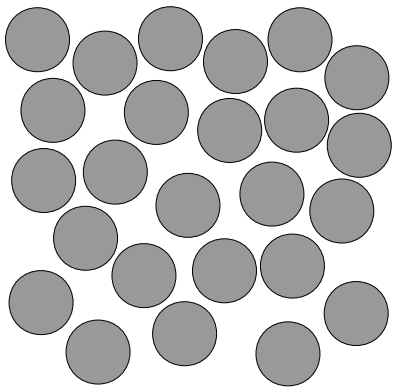

Figure 1.5.: A dense two-dimensional packing of discs. It is clear that a long-range motion of any particle depends on the motions of the surrounding particles, the so-called *cage of neighbours*. The main difference between alternative visions of the dynamics is the behaviour of these neighbours: while the free volume theory acts on the assumption that the central particle escapes from the cage through an opening, other approaches are based on collective rearrangements of the central particle together with its neighbours.

neighbours at some point [73]. While the motion of the particles can be described by relatively simple formulae at *very much* longer time scales, intricate phenomena arise at this intermediate time scale where the cage of neighbours governs the motions [74, 75]. In the case of the phospholipid molecules, this intermediate time scale is on the order of pico- to nanoseconds and therefore perfectly accessible with QENS.

The picture of Cohen and Turnbull, the *free volume theory* [76–78], explains the slowing down of the dynamics upon cooling with this escape step: as the temperature is lowered, the density increases and free volume decreases – it is less likely that the neighbours open up a void that is big enough for the central particle to hop in and escape from the cage. The model has often been criticized being unable to explain several measured quantities [79] and it was recently shown by comparing isothermal and isobaric density changes that the free volume cannot be the only parameter determining the dynamics [80, 81].

An alternative model was developed by Adam and Gibbs, explaining the same phenomenon with an increasing cooperativity [82]. As the sample is cooled down, more and more particles move collectively together in transient clusters, so-called *cooperatively rearranging regions*. Also this approach has problems [83] but it proved in the last years to be a very stimulating picture.

In recent years, *dynamical heterogeneities*, a clustering of velocities in a sample that yields a separation of regions with large dynamics from ones with slow dynamics as shown in figure 1.6, were observed in a variety of dense systems, moving passively [84–87] as well as actively [88–91]. The dynamical heterogeneities, mostly studied very close to the glass transition, were also observed far above this temperature [92, 93]. They were even seen in the liquid phase of systems that cannot be supercooled because they crystallize [94, 95]. These dynamical heterogeneities were identified as the source of the non-Gaussian part of the correlation functions [85, 94, 96] that are well-known to be observed for dense liquids [74, 75].

At long times, these heterogeneities will average out: the fast particles will become slow, the slow particles will become fast; a particle will participate first in a cluster moving in some direction and later in another cluster moving in another direction. These are the steps of a random walk so that a homogeneous isotropic long-range diffusive motion is restored on long time scales. Increasing the temperature will shift the transition

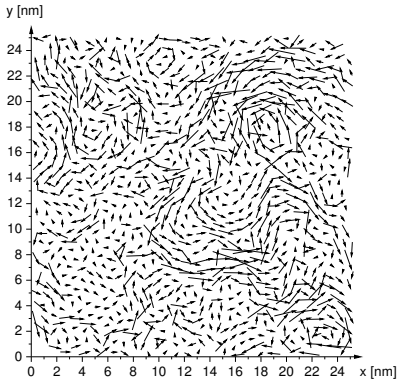

Figure 1.6.: An example of dynamical heterogeneities [E]: The arrows show the displacement of the particles in a fixed time interval. It can be seen that different particles have different velocities and that regions with fast particles are spatially separated from regions with slow particles. A jump-like escape of a particle of its cage of neighbours is not observed, the central particle rather performs a flow-like motion together with its cage. Over longer times, the velocities of the particles change and the picture is homogeneous.

from the heterogeneous to the homogeneous regime to shorter times [97].

Although the identification of dynamical heterogeneities with cooperatively rearranging regions is tempting, the relation between the two is not clarified to date [98]. It is a matter of active debate if there are any structural signatures that could be connected to the dynamical heterogeneities. Recently, *medium-range crystalline ordering*, temporarily ordered domains attracted attention [99–101]. The change in local order was shown to be completely independent of the local free volume but might indeed be the structural cause of dynamical heterogeneities [102, 103]. These ordered regions have a finite life time and occur also in systems that do not crystallize, in contrast to crystal nuclei. However, the medium-range crystalline ordered domains are speculated to be precursors of crystal nuclei, providing an environment in which the nuclei can form [100].

In any case, a growing length scale of the correlations of the dynamics could explain the temperature dependence of the correlation times [60]: *Strong* glass formers which show an Arrhenius temperature dependence are assumed to break and form bonds between neighbouring atoms at all temperatures. The activation energy is therefore independent of the temperature. *Fragile* glass formers which show a super-Arrhenius temperature dependence are assumed to break and form interactions between growing clusters of particles. In this case, a decrease of the temperature causes an increase of the number of bonds that has to be broken and formed for a rearrangement. The activation energy increases therefore with decreasing temperature and the correlation times increase faster than with an Arrhenius temperature dependence.

It was shown that the interactions between the particles influence the temperature dependence of the relaxation times – the softer the interactions, the larger the fragility [104]. There were also studies which found a fragile-to-strong transition of water [105] that was then related to underlying thermodynamical effects. This connection is currently under scrutiny [C] and [106–113] and there is even an ongoing discussion whether one can observe a transition from a fragile to a strong behaviour at all or if the observed effects are not merely fit artifacts [C, D].

Glassy dynamics seen from the solid side. In disordered solids, the low-frequency (*soft*) modes are enhanced over the expectations from the Debye theory valid in normal crystals and show correlations of the velocities of the particles over large distances [114–

116]. The disorder of these systems can be manifested either in the structure or in the interactions of the system which means that even samples with a crystalline structure can exhibit these excess modes [117, 118].

It was found that these soft modes are connected to irreversible reorganizations of the particles [119] whereas neither free volume [120] nor potential energy [121] are. The energy of these surplus modes is correlated with the packing density: as the packing is loosened, the surplus modes are shifted to even lower frequency and become quasilocalized [122].

Depicting the situation, the particles in the disordered solid do not exhibit a long-range mobility when looking on a long time scale. However, when looking only for a short time, one can see that the particles are displaced driven by the soft modes. As these are localized, no regular patterns become apparent but the particles are displaced in some regions more than in others. Apart from the effect that the particles will be pulled back to their original place by the restoring forces, this picture resembles very much the dynamical heterogeneities.

Although it is not yet clear *how* these two effects are linked, there is increasing consensus *that* they are [95, 96, 123–126]. It has also become clear that these modes vary continuously, even through the solidification – which can be a crystallization [95, 127]. This might be connected to the increasing occurrence of the medium-range crystalline ordering that was observed in the liquid state and can be seen as precursors of freezing in simple two dimensional liquids [128].

In summary, the main control parameter that makes a system glassy is the tight packing, i. e. the stereotactic hindrance. As the phospholipids are very tightly packed in the region of the head groups [11], they can be expected to follow the same principles. As will be recapitulated in the following, this close relationship has been used very successfully in the past [129] to describe phospholipid dynamics. It will be proposed in this thesis that the new concepts which have been developed since then in glass physics need to find their way into the description of the phospholipids today.

1.3. Dynamics of Phospholipids

One can distinguish three main contributions to the molecular motions of the phospholipid molecules: the motions of the head groups, the ones of the tail groups, and the motion of the whole molecule as indicated in figure 1.7. The molecules can also change from one leaflet to the other but this process has time constants in the minute regime and is therefore so slow that it will be neglected in the following. The localized motions of the head and the tail groups will be treated less intensively than the long-range motion of the whole molecule because the long-range motion is expected to have more impact on the biologically and pharmaceutically relevant properties of the phospholipid molecules.

The free volume theory for phospholipid systems. The long-range motion of phospholipid molecules is since a long time subject matter of intense research with different techniques that cover different time and length scales: From fluorescence recovery after

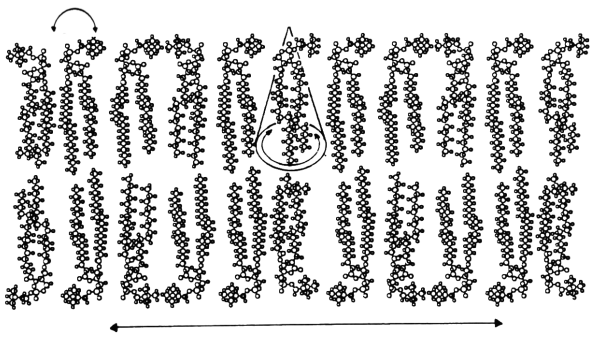

Figure 1.7.: Possible motions in a phospholipid membrane sketched after Cevc [9]. Intramolecularly, one can distinguish small-scale, rapid motions of the head groups from slower and larger motions of the tail groups. Above the main phase transition, the molecules have also a long-range mobility within the membrane.

photobleaching (FRAP) [130, 131] on a time scale of about 10 seconds over nuclear magnetic resonance (NMR) [132] or single molecule tracking [133] on a time scale of about 100 milliseconds and over fluorescence correlation spectroscopy [134, 135] on a time scale of about 10 milliseconds to neutron scattering studies [136, 137] on time scales in the pico- to nanosecond regime. Neutron scattering has not only the advantage to probe the time scale on which the phospholipids explore their immediate neighbourhood but also allows to follow these motions without introducing a marker into the system that might distort the dynamics.

In order to explain the results of diffusion measurements of hydrophobic probe molecules in phospholipid membranes, Galla et al. [129] had the seminal idea to use the free volume theory of Cohen and Turnbull that had been developed for glassy systems [76]. The appeal of this description lies in the simple description of the measurements with basically only one main parameter: the free volume.

This idea was therefore after its formulation in 1979 the predominant theory for roughly 30 years, only slightly refined to take the viscosities of the surrounding solvent into account [138, 139]. Its biggest success was probably the description of seemingly contradicting results obtained by different measurement techniques: the diffusion coefficients determined by quasielastic neutron scattering (QENS) [136, 140] were about two orders of magnitude higher than the ones determined with the macroscopic techniques.

This could be effortlessly explained in the frame of the free volume theory: Because QENS measures on a picosecond time scale, it is sensitive to the rattling of the phospholipid molecules in the cage of their neighbours. This motion does not directly contribute to the long-range motion. Only from time to time, a void opens up in the surrounding cage and the molecule can perform a jump out of the cage which was assumed to be the fundamental step of the long-range diffusion [141].

Collective motions call for a new description. Only a few years ago, molecular dynamics (MD) simulations became capable of describing the molecular dynamics well enough and on sufficiently long time scales that it could contribute to the quest of the diffusion mechanism of phospholipids. The concept of the free volume was questioned as it became clear that the membrane is not adequately described as a two dimensional liquid of hard disks and, in fact, the free volume is ill defined in the membrane [142–144]. It was concluded that the fits of the theory to the data had a high quality but the

extracted parameter values did not have a clear relationship with the quantities they were supposed to represent [145].

Additionally to those fundamental points of critique, there were more and more hints from simulation [146–148] and experiment [137, 149] that the motions of the phospholipid molecules were correlated over nanometer distances – an observation that the free volume theory cannot account for. In some of these MD simulations, also structural order was observed in transiently ordered domains [147] which resemble the medium-range crystalline ordering that had been observed in glassy systems.

A break-through was achieved when Falck et al. [150] demonstrated in an MD simulation that those molecules in their simulation that moved the largest distances in a given time range take the cage of neighbours with them rather than escaping from it. The key idea in this simulation was to connect the position of the phospholipids at the beginning and the end of a given time interval with vectors so that a two-dimensional flow pattern became visible. Before, only the mean-square displacement had been evaluated. This observable is dominated by the motions of the tails at short times [151] which obfuscate the flow motions.

With quasielastic neutron scattering, it is possible to observe motions on the pico- to nanosecond time scale on which these flow-like motions prevail. Further, it is possible to construct models of the molecular motions that distinguish between the localized motions of the tails and the long-range component of the whole molecule. It was therefore obvious to ask [B]

Can this novel view of flow-like motions of the phospholipids on a nanosecond time scale be supported by experimental data?

The visualization of these transiently formed clusters of molecules is remarkably similar to the one of dynamical heterogeneities shown in figure 1.6. The next question was thus [D–F]

Is it possible to interpret these motions in the picture of dynamical heterogeneities?

To answer these questions, different models of the motion of the phospholipid molecules had to be evaluated against the data. In order to distinguish which of the models can describe the data best, a focus of this thesis were data evaluation methods [C, D, G, H].

From pure DMPC to more complex systems. Independent from the exact mechanism of the molecular motions and accordingly more unambiguously determinable is the impact of environmental changes on the phospholipid mobility.

One parameter that has previously been extensively studied and is therefore kept constant in the present contribution is the hydration of the phospholipids. Decreasing

the hydration of the phospholipids gives certainly interesting insights but drives the system of pure DMPC even further away from systems that can be used in a biological or pharmaceutical application. All measurements for this thesis are therefore performed in the biologically relevant fully hydrated state. Nevertheless, the most relevant results of hydration-dependent studies are summarized in the following paragraph.

It is known from QENS measurements that a decrease of the hydration lowers the molecular mobility [152, 153]. Also the direct comparability of QENS measurements with MD simulations was demonstrated [154] which revealed that the dynamics of the head groups varies continuously over the main phase transition. The head group was also studied with dielectric spectroscopy [155]. With rising hydration, the temperature dependence became increasingly Arrhenius-like, i. e. *strong* – similar to colloidal suspensions where the interactions are softened [104]. Also these results were interpreted in terms of slow cooperative motions, involving several lipid molecules.

Instead of going into the direction of this somewhat artificial state, in this work an attempt is made to understand the change of dynamics when going from the pure DMPC multibilayers to systems which are closer to biologically and pharmaceutically relevant systems. A first step into this direction is the use of additives because neither in biological nor in pharmaceutical systems contain *only* DMPC. Cholesterol was chosen as a representative of the additives that are important in biology. It is of major relevance in cell membranes and has therefore also been previously studied. In some of those studies, it was found that the collectivity of the phospholipid motions is influenced by cholesterol [146, 156]. As a substance that is used in pharmaceutical applications, sodium glycocholate was studied. It is an important co-surfactant for drug delivery systems [55, 56], but had not previously been studied with QENS. Consequently, it was studied on the pico- to nanosecond time scale accessible with QENS [E]

How is the mobility of the phospholipids altered by additives?

From mixed DMPC– sodium glycocholate samples, the next step towards drug delivery systems is the change from bilayers to monolayers. This is not a trivial change: monolayers can behave very differently from bilayers, for example does the long-range mobility not show any abrupt change when lowering the temperature [157] whereas bilayers of DMPC undergo a phase transition where the long-range mobility changes by at least an order of magnitude. These monolayers are studied on an oil-water interface which entails that the phospholipid density can actively be changed. An increase of the mobility with increasing area per molecule was observed on the macroscopic scale [158]. However, up to date measurements of the mobility in phospholipid monolayers on a molecular scale are still scare. QENS measurements were hence also performed to clarify [F]

How does the mobility of the phospholipids in monolayers differ from the one in bilayers?

Due to the small fractions of as little as 1% of phospholipid in the sample, these measurements are challenging for both, the measurements and the data evaluation procedures. It is only owed to the very low experimental background of the neutron scattering spectrometer TOFTOF that it was possible to evaluate the contribution of the DMPC. In addition, a focus of this thesis were the data reduction procedures [D, F].

In the next chapter, the theoretical tools to describe molecular motions will be introduced and it will be shown how these quantities can in principle be measured with neutron scattering. The following chapters will present the practical aspects of these measurements as well as their results.

Chapter 2.

Theoretical Principles

A very concise summary of the most important formulae for the description of the molecular structure and dynamics will be given, followed by an equally short description of how these are linked to the quantities measured by neutron scattering. For a more in-depth treatment, the reader is referred to the extensive literature, e. g. [75, 159–164].

2.1. Molecular Structure and Dynamics are Described by Correlation Functions

The definitions of the correlation functions. Introduced by van Hove [165], correlation functions became soon the common way to describe molecular motions. As will be discussed later, one of their big advantages is that they can be accessed by scattering methods. In the following, it will be used that the systems do not exhibit quantum effects, that the various particles are statistically equivalent, and that the system is ergodic.

The *pair correlation function* $G_{\text{pair}}(\boldsymbol{r}, t)$ is then defined as

$$G_{\text{pair}}(\boldsymbol{r}, t) = \sum_{j=1}^{N} \langle \delta \left[\boldsymbol{r} - (\boldsymbol{R}_j(t_0 + t) - \boldsymbol{R}_k(t_0)) \right] \rangle \tag{2.1}$$

with the number of particles N and the position $\boldsymbol{R}_l(t)$ of particle l at time t. The angular brackets $\langle\ \rangle$ denote an ensemble average over all particles k and origins of time t_0. As the system is ergodic, this is equivalent to average over all possible initial states of the system weighed with their probability. When multiplied with $\mathrm{d}\boldsymbol{r}$, it gives the probability to find a particle at time t in the volume $\mathrm{d}\boldsymbol{r}$ at position $\boldsymbol{r}$ if *some* particle was at time $t = 0$ in the volume $\mathrm{d}\boldsymbol{r}$ at position $\boldsymbol{r} = \boldsymbol{0}$.

This information is a rather complicated one as it gives access to correlations between particles – in space and time. From the pair correlation function, only the structural correlations encoded in $G_{\text{pair}}(\boldsymbol{r}, t = 0)$ will be used in this thesis, the dynamical properties of the pair correlations. The dynamics will rather be extracted from the *self correlation function* or *auto correlation function* $G_{\text{self}}(\boldsymbol{r}, t)$ which does not carry any information about the structural arrangement of different particles with respect to each other. It is defined as

$$G_{\text{self}}(\boldsymbol{r}, t) = \langle \delta \left[\boldsymbol{r} - (\boldsymbol{R}_k(t_0 + t) - \boldsymbol{R}_k(t_0)) \right] \rangle \tag{2.2}$$

where the ensemble average can be calculated in an ergodic system over all particles k and the origins of time t_0. $G_{\text{self}}\,\mathrm{d}\boldsymbol{r}$ gives the probability to find a particle at time t in the volume $\mathrm{d}\boldsymbol{r}$ at position $\boldsymbol{r}$ if *this* particle was at time $t = 0$ in the volume $\mathrm{d}\boldsymbol{r}$ at position $\boldsymbol{r} = \boldsymbol{0}$.

It is interesting to note that $G(\boldsymbol{r}, t)$ treats time and space differently: it has the unit (volume)$^{-1}$ but not (time)$^{-1}$. This can be understood from the interpretation as a probability density: A given particle has to be at *some* point in space at *every* instant, therefore the integral over the whole space at any randomly chosen time must be unity. However, the particle will not necessarily visit *every* point in space at *some* instant, the integral over all times at a randomly chosen point in space can therefore have any non-negative value.

Using Fourier transforms, it is possible to express the same information in different representations. The three important ones are:

1. The *correlation function* $G(\boldsymbol{r}, t)$ with the dimension (volume)$^{-1}$ – because $G(\boldsymbol{r}, t)\,\mathrm{d}\boldsymbol{r}$ is a dimensionless probability, discussed above.

2. The *intermediate scattering function* $I(\boldsymbol{Q}, t)$ is the Fourier transform of $G(\boldsymbol{r}, t)$ with respect to $\boldsymbol{r}$. The part corresponding to the self correlation, the self intermediate scattering function, can be written as

$$I_{\text{self}}(\boldsymbol{Q}, t) = \langle \exp\left[\mathrm{i}\boldsymbol{Q} \cdot (\boldsymbol{R}_k(t_0 + t) - \boldsymbol{R}_k(t_0))\right]\rangle \tag{2.3}$$

   which is dimensionless. The imaginary part of this function averages to zero as long as the atomic displacements do not show a preferential direction.

3. The *scattering function* $S(\boldsymbol{Q}, \omega)$ is the Fourier transform of $I(\boldsymbol{Q}, t)$ with respect to the time t and has the dimension $[\omega]^{-1}$ where $[\omega]$ denotes the unit of ω. In this thesis, ω will be measured in units of energy. Also this function is real due to the time reversal invariance of the dynamics in the studied samples.

Returning for a second to the structural information $G_{\text{pair}}(\boldsymbol{r}, t = 0)$, it is now clear that this quantity transforms to $I_{\text{pair}}(\boldsymbol{Q}, t = 0)$ and correspondingly to the *static structure factor* $S_{\text{pair}}(\boldsymbol{Q}) = \int_{-\infty}^{\infty} \mathrm{d}\omega\, S_{\text{pair}}(\boldsymbol{Q}, \omega)$. The self correlation function does not carry structural information and is therefore unity, $G_{\text{self}}(\boldsymbol{r}, t = 0) = 1$, which gives $I_{\text{self}}(\boldsymbol{Q}, t = 0) = 1$ and $\int_{-\infty}^{\infty} \mathrm{d}\omega\, S_{\text{self}}(\boldsymbol{Q}, \omega) = 1$.

None of the samples studied in this thesis has any preferential orientation throughout the whole sample volume, i. e. they are all so-called powder samples. Because the recorded scattering signal is an average over all orientations, the absolute values r and Q will be used instead of the vectors $\boldsymbol{r}$ and $\boldsymbol{Q}$.

In section 2.2, it will be shown that the scattering functions discussed above can be measured by neutron scattering. In order to evaluate the neutron scattering data, the scattering functions of models for molecular motions will be compared to the data. In the following, four different models for molecular motions will be presented together with their corresponding scattering functions: localized periodic and aperiodic motions as well as long-range diffusive and flow motions.

Localized periodic motions. In perfect crystals, vibrations of the molecules or atoms around their average lattice site can be described by phonons. Roughly speaking, incoherent scattering is caused by single nuclei and every phonon will eventually pass over every nucleus. Therefore, all phonons are visible at all measured Q and $S_{\text{inelastic}}(Q,\omega)$ measures the density of states. A sound derivation of this fact can be found in neutron scattering text books [160, 163]. At small energy transfers, only the acoustic phonons are visible. If $Q \ll \pi/a$ where a is the lattice spacing of the crystal, the phonon density of states is in first approximation proportional to ω^2 which results into an energy-independent contribution to the scattering function [159, 166, 167].

With rising Q, an increasing amount of neutrons is scattered with the creation or annihilation of a phonon, given by the *Debye-Waller factor* which describes the distribution of neutron intensity between elastic and inelastic scattering,

$$S(Q,\omega) = \exp\left[-\frac{1}{3}Q^2\langle u^2\rangle\right] \cdot \delta(\omega) + S_{\text{inelastic}}(Q,\omega) \ , \tag{2.4}$$

where $\boldsymbol{u}$ is the displacement vector of the nuclei from their equilibrium position. This formula holds strictly for a cubic crystal where $\langle u_x^2\rangle = \langle u_y^2\rangle = \langle u_z^2\rangle = \frac{1}{3}\langle u^2\rangle$ but it is still approximately correct in other cases [160].

In the case of incoherent scattering, $\int_{-\infty}^{\infty} \mathrm{d}\omega\, S(Q,\omega) = 1$ holds for all Q as stated before. It follows that

$$\int_{-\infty}^{\infty} \mathrm{d}\omega\, S_{\text{inelastic}}(Q,\omega) = 1 - \exp\left[-\frac{1}{3}Q^2\langle u^2\rangle\right] \ . \tag{2.5}$$

Developing the exponential in equation 2.5 into its Taylor series, it can be seen that the lattice vibrations contribute a signal to the inelastic scattering that is roughly constant in ω and has an intensity that increases proportional to Q^2.

Localized aperiodic motions. For a confined or localized motion, the probability to find a particle at the origin develops in the following manner: at time zero, it starts at unity and decays from this value because the particle can explore its cage. The shape of this decay depends on the properties of the motion of the particle in the cage. At long times, the probability to find the particle at the origin does not decay to zero because of the confinement. Fourier transformation of such a correlation function results in a sum of two components: a δ-function in energy space which corresponds to the non-vanishing probability at long times and a broadened component which is the Fourier transform of the initial decay [168]. This combination of a δ and a broadened component is common to all confined motions.

Using an exponential decay as a simple model for the initially decreasing probability to find the particle, one arrives at the scattering function

$$S(Q,\omega) = A_0(Q) \cdot \delta(\omega) + (1 - A_0(Q)) \cdot \frac{1}{\pi}\frac{\Gamma}{\omega^2 + \Gamma^2} \ . \tag{2.6}$$

$A_0(Q)$ is called *Elastic Incoherent Structure Factor* (EISF). Its Q-dependence is determined by the geometry of the motion (two sites jump, diffusion inside a hollow sphere, ...) and the amplitude of the motions [159, 168].

A special case for a confined motion is a particle diffusing in a harmonic potential, a so-called *Brownian oscillator*. Despite the simplicity and physical relevance of this model, it is not often used by the neutron scattering community.

Its equation of motion can be set up as [169]

$$\frac{\mathrm{d}^2 x}{\mathrm{d}t^2} + \beta \cdot \frac{\mathrm{d}x}{\mathrm{d}t} = -\omega^2 \cdot x + F(t) \tag{2.7}$$

where x is the displacement of the particle from the minimum of the potential at time t, β is the friction coefficient, ω the eigenfrequency of the particle in the potential, and $F(t)$ a randomly fluctuating force.

For $t \gg 1/\beta$, the mean-square displacement can be calculated to

$$\langle x^2 \rangle = \epsilon^2 \cdot (1 - \exp[-\Gamma t]) \xrightarrow{t \to \infty} \epsilon^2 \tag{2.8}$$

with

$$\epsilon^2 = \frac{k_\mathrm{B} T}{m\omega^2} \qquad \text{and} \qquad \Gamma = \frac{2\omega^2}{\beta} \ . \tag{2.9}$$

Using the so-called *Gaussian approximation*, this mean-square displacement can be translated into the intermediate scattering function [170–173]

$$\begin{aligned} I(Q,t) &= \exp\left[-Q^2 \cdot \langle x^2 \rangle\right] \\ &= \exp\left[-Q^2 \cdot \epsilon^2 \cdot (1 - \exp[-\Gamma t])\right] \ . \end{aligned} \tag{2.10}$$

This expression can be Fourier transformed into the scattering function when expanding one of the exponential functions into its Taylor series,

$$\begin{aligned} I(Q,t) &= \exp\left[-Q^2\epsilon^2\right] \cdot \exp\left[Q^2\epsilon^2 \exp[-\Gamma t]\right] \\ &= \exp\left[-Q^2\epsilon^2\right] \cdot \sum_{n=0}^{\infty} \frac{\left(Q^2\epsilon^2 \exp[-\Gamma t]\right)^n}{n!} \\ &= \exp\left[-Q^2\epsilon^2\right] \cdot \sum_{n=0}^{\infty} \frac{Q^{2n}\epsilon^{2n}}{n!} \cdot \exp[-n \cdot \Gamma t] \ , \end{aligned} \tag{2.11}$$

which becomes after Fourier transform

$$S(Q,\omega) = \exp\left[-Q^2\epsilon^2\right] \cdot \sum_{n=0}^{\infty} \frac{Q^{2n}\epsilon^{2n}}{n!} \cdot \frac{1}{\pi} \frac{n \cdot \Gamma}{(n \cdot \Gamma)^2 + \omega^2} \tag{2.12}$$

where the $n = 0$ term has to be understood as a δ function in energy. This term gives the elastic incoherent structure factor

$$A_0(Q) = \exp\left[-Q^2\epsilon^2\right] \ . \tag{2.13}$$

Long-range diffusive motions. Diffusion results from a random walk of the particles. It is especially important for processes in the «micron world» [174] but random walk motions can be found on vastly different time and length scales: on the nanoscopic scale for molecular motions, the microscopic scale for the so-called Brownian motion of suspended colloids [175, 176], or the metre scale for the motion of falling snow flakes – this last example will be discussed in an instant. The correlation function is in all cases derived as [75]

$$\text{Space-time correlation function} \qquad G(r,t) = (4\pi Dt)^{-\frac{3}{2}} \exp\left[-\frac{r^2}{4Dt}\right] \tag{2.14}$$

with its Fourier transforms

$$\text{Intermediate scattering function} \qquad I(Q,t) = \exp\left[-DQ^2 t\right] \quad \text{and} \tag{2.15}$$

$$\text{Scattering function} \qquad S(Q,\omega) = \frac{1}{\pi}\frac{DQ^2}{\omega^2 + DQ^2}\,. \tag{2.16}$$

As mentioned above, these formulae can also describe the random walk of snow flakes. They fall in the gravitational field of the earth in z direction, turbulences in the air make them move randomly in the (x, y)-plane. The time-evolution of the position of a snowflake in this plane is resolved by its fall. The Gaussian space-time auto-correlation function 2.14 gives the probability of a snow flake to move a certain distance in the (x, y)-plane after some time t or equivalently after some height loss. The height h of a snow pile under a roof with a point-like hole would have a Gaussian shape. Having not a hole but a semi-infinite plane (an intact roof with an end) gives the integral over all Gaussians with their starting points (centres) from $-\infty$ to 0 (the eaves, cf. figure 2.1). This yields for the height of the snow pile h in the direction x

$$h(x) = \int_{-\infty}^{0} \mathrm{d}x'(4\pi Dt)^{-\frac{1}{2}} \exp\left[-\frac{(x-x')^2}{4Dt}\right] = \frac{1}{2}\left(1 - \operatorname{erf}\left[\frac{x}{\sqrt{4Dt}}\right]\right) \tag{2.17}$$

where D is the diffusion coefficient of the snow flakes and t the time it took the snow flakes to fall from the height of the roof onto the balustrade. It can be seen in figure 2.1 that this functional dependence can reproduce the shape of the snow pile very well.

Going back to the formulae describing the random walk, it can be seen that the full width at half maximum (FWHM) of the Lorentzian scattering function 2.16 is $2\Gamma = 2DQ^2$ with the diffusion coefficient D. It is important to note that the model of Fickean Diffusion does not only comprise the Lorentzian form of the scattering function but necessarily also this quadratic Q-dependence of the line width.

A simple quadratic dependence of the line width on Q is hardly ever observed. Some common cases and their explanations are:

- The line width is too small at intermediate values of Q where structure factor maxima result in a large amount of coherent scattering. This is normally assigned to the so-called de Gennes narrowing [177, 178].

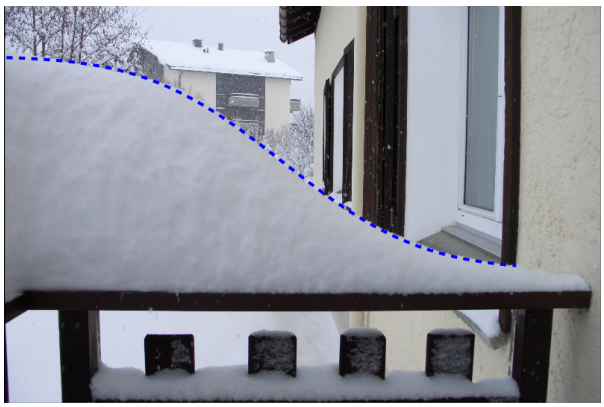

Figure 2.1.: Photograph of fresh snow piling on a balustrade. The roof of the house shields the right part – if snow was falling like rain, the wetness would have a step-like distribution. Due to the random walk of the snow flakes during their fall, the step function is smeared out. Also shown is a fit of equation 2.17, demonstrating that this description agrees very well with the observation.

- The line width is too large at small Q. This is often interpreted as sign of multiple scattering in the sample [179]. It could however be shown in the frame of this thesis that this is not a necessary consequence of multiple scattering [D].
- The line width is too small at large Q. This is often interpreted as a stop-and-go motion [180]. It was however found for the spectra evaluated in this thesis that such a behaviour is also observed when a wrong model is used to fit the data [B].

Long-range flow motions. A type of motion that we are more used to in daily life are flow motions, for example in a river. The particles do not change direction all the time as in the random walk but keep going in the same direction with a constant velocity until it is reflected by an obstacle. The velocity vector has three independent components that give the total velocity according to $v_x^2 + v_y^2 + v_z^2 = \boldsymbol{v}^2$. Assuming that each of the three components has a Gaussian probability distribution around the most probable speed v_0, the probability density function (PDF) for the speed

$$\mathrm{PDF}(\boldsymbol{v}) = \left(\frac{1}{\sqrt{\pi v_0^2}}\right)^3 \exp\left[-\frac{\boldsymbol{v}^2}{v_0^2}\right] \tag{2.18}$$

results [181]. This is the well-known Maxwell-Boltzmann distribution that is for instance found for the velocity distribution of the particles of an ideal gas. In this case of the ideal gas, the most probable speed is $v_0 = \sqrt{2k_\mathrm{B}T/m}$ where m is the mass of the particles, k_B the Boltzmann constant, and T the temperature.

In the phospholipid samples, the molecules are not expected to move completely independent from each other like in an ideal gas but rather collectively. These collective flow motions are confined to the plane of the membrane. However, also in these samples molecules move in all directions of space because the many membranes in the sample are randomly oriented with respect to each other. Even if the molecules are all moving in the same directions in a small volume of the sample, they will move in any other direction in some other part of the sample. The fact that the directions are spatially separated in this case and not in the ideal gas does not change the ensemble averaged correlation and scattering functions which are given in the following.

The probability to find a particle which moved the distance $r = \sqrt{x^2 + y^2 + z^2}$ from the origin during the time t after some arbitrarily chosen origin of time can be calculated. One obtains the space-time correlation function

$$\begin{aligned} G(r,t) &= \int \mathrm{d}^3 v \ \mathrm{PDF}(\boldsymbol{v}) \cdot \delta(\boldsymbol{r} - t\boldsymbol{v}) \\ &= \int \mathrm{d}^3 v \ \left(\frac{1}{\sqrt{\pi v_0^2}}\right)^3 \exp\left[-\frac{\boldsymbol{v}^2}{v_0^2}\right] \left(\frac{1}{t}\right)^3 \delta\left(\frac{1}{t}\boldsymbol{r} - \boldsymbol{v}\right) \\ &= \left(\frac{1}{\sqrt{\pi v_0^2 t^2}}\right)^3 \cdot \int \mathrm{d}x\,\mathrm{d}y\,\mathrm{d}z \ \exp\left[-\frac{v_x^2}{v_0^2}\right] \exp\left[-\frac{v_y^2}{v_0^2}\right] \exp\left[-\frac{v_z^2}{v_0^2}\right] \\ &\qquad\qquad \cdot \delta(x/t - v_x) \cdot \delta(y/t - v_y) \cdot \delta(z/t - v_z) \\ &= (\pi v_0^2 t^2)^{-\frac{3}{2}} \exp\left[-\left(\frac{r}{v_0 t}\right)^2\right] \end{aligned} \tag{2.19}$$

with its Fourier transforms

$$\text{Intermediate scattering function} \quad I(Q,t) = \exp\left[-\frac{1}{2}(Qv_0 t)^2\right] \quad \text{and} \tag{2.20}$$

$$\text{Scattering function} \quad S(Q,\omega) = \frac{1}{Qv_0\sqrt{2\pi}} \exp\left[-\frac{1}{2}\left(\frac{\omega}{Qv_0}\right)^2\right] . \tag{2.21}$$

Combining different motions. It is very useful to see the complicated trajectory of the particles in the sample as a superposition of trajectories that can be described by mathematical models. In the case of the auto correlation functions, this superposition is easily performed:

If *one* particle participates in several independent motions (a, b, ...) the different correlation and scattering functions are composed as

$$G_{\text{one}}(r,t) = G_a(r,t) \cdot G_b(r,t) \cdot \ \cdots \tag{2.22}$$

$$I_{\text{one}}(Q,t) = I_a(Q,t) \cdot I_b(Q,t) \cdot \ \cdots \tag{2.23}$$

$$S_{\text{one}}(Q,\omega) = S_a(Q,\omega) \otimes S_b(Q,\omega) \otimes \ \cdots \tag{2.24}$$

where $\otimes$ denotes a convolution in ω space.

If *several* groups of particles in the observed system (1, 2, ...) perform their motions simultaneously and independently, the correlation and scattering functions are added, weighed with the fraction c_1, c_2, etc. with which they contribute to the scattering signal. How this fraction is determined in practice is discussed in section 4.1.

$$G_{\text{many}}(r,t) = c_1 \cdot G_1(r,t) + c_2 \cdot G_2(r,t) + \ \cdots \tag{2.25}$$

$$I_{\text{many}}(Q,t) = c_1 \cdot I_1(Q,t) + c_2 \cdot I_2(Q,t) + \ \cdots \tag{2.26}$$

$$S_{\text{many}}(Q,\omega) = c_1 \cdot S_1(Q,\omega) + c_2 \cdot S_2(Q,\omega) + \ \cdots \ . \tag{2.27}$$

Of course, each of the G_1, G_2, etc. can be a compound G_{one}, G_{two} etc. as defined above.

In the special case where only a fraction f of the scatterers participates in a confined motion and the other, $(1-f)$, does not, the scattering function becomes, denoting the Lorentzian with L,

$$\begin{aligned} S(Q,\omega) &= f \cdot [A_0 \cdot \delta + (1-A_0) \cdot L] + (1-f) \cdot \delta \\ &= (1 - f + fA_0) \cdot \delta + (f - fA_0) \cdot L \\ &= B_0 \cdot \delta + (1-B_0) \cdot L \qquad \text{with} \quad B_0 = 1 - f + f \cdot A_0 \ . \end{aligned} \tag{2.28}$$

2.2. Measuring the Correlation Functions with Neutron Scattering

There are different methods to measure the correlation functions which operate on very different time and length scales. Optical microscopy measurements are currently limited to sizes above 100 nm [182, 183]. With pulsed field gradient nuclear magnetic resonance, the length scale is very comparable [184]. In contrast to those, neutron and x-ray scattering operate on an Ångström to nanometre scale and have proven to be very useful for the study of phospholipid membranes [185]. X-ray scattering is very a very powerful tool for structural studies. As far as the dynamics is concerned, one can either access the sub-picosecond time scale with inelastic x-ray scattering [186, 187] or the millisecond range with coherent x-ray photon correlation spectroscopy [188]. Neutron scattering gives also access to the dynamics of the samples on a pico- to nanosecond time scale. This is the same time scale that can nowadays be covered with MD simulations. Because of this overlap, MD simulations and scattering methods can be used complementary to validate complex physical models.

Scattering cross sections. It will be outlined in the following how the measured neutron scattering signal is connected to the correlation functions treated previously. The neutrons are assumed to have an exactly known initial energy E_i and a common wave vector $\boldsymbol{k}_i$, i. e. a monoenergetic and collimated beam. Counting the neutrons which are scattered into a solid angle element $\mathrm{d}\Omega$ around a final wave vector $\boldsymbol{k}_f$ and with a final energy between E_f and $E_f + \mathrm{d}E_f$ amounts to measuring

$$\left(\frac{\mathrm{d}^2\sigma}{\mathrm{d}\Omega\,\mathrm{d}E_f}\right)\mathrm{d}\Omega\,\mathrm{d}E_f \tag{2.29}$$

which is the number of scattered neutrons in a certain time divided by the number of incident neutrons during the same time. The quantity $\mathrm{d}^2\sigma/(\mathrm{d}\Omega\,\mathrm{d}E_f)$ is called the *double differential cross section.*

A qualitative understanding of the reasons behind the redistribution of the neutron intensity into different final energies and directions of the wave vector can be obtained easily: Structures in the sample with sizes on the same order of magnitude as the wavelength of the incident neutrons cause a change of the direction of the neutron,

reminding of diffraction of light at a slit. Motions in the sample can be created or annihilated by the neutrons which correspondingly lose or gain energy from the sample.

If these motions are not of interest, the energy dependence of the neutron signal can be integrated out, resulting in the *differential cross section*

$$\frac{\mathrm{d}\sigma}{\mathrm{d}\Omega} = \int \mathrm{d}E_f \, \frac{\mathrm{d}^2\sigma}{\mathrm{d}\Omega \, \mathrm{d}E_f} \, . \tag{2.30}$$

This quantity has the advantage that it is relatively easy to measure by detecting the scattered neutrons without an analysis of their final energy. However, it will become clear in the following that this is not the static structure factor $S(Q)$ mentioned above.

It is further interesting to notice that the integral of the differential cross section over the whole solid angle is not any special quantity and does not have to be preserved: In particular, this is not the bound scattering cross section that is a tabulated property of the nuclei [189]. As a consequence, the absolute number of neutrons which are scattered by a sample increases with increasing temperature of the sample. The reason for this behaviour will be discussed below. The only conserved quantity is the differential cross section in the limit of forward scattering for which one obtains

$$\lim_{\boldsymbol{k}_f \to \boldsymbol{k}_i} \left(\frac{\mathrm{d}\sigma}{\mathrm{d}\Omega} \right) = \frac{\sigma_b}{4\pi} \tag{2.31}$$

where σ_b is the bound scattering cross section of the nucleus.

From scattering cross sections to correlation functions. The double differential cross section can be calculated from properties of the system, assuming that each neutron was scattered only once. It is essentially the transition rate of the neutrons to go from their initial to the final state. This transition is caused by the interaction with the sample which is seen as a time-dependent perturbation, related to the time-dependent position of the point-like nuclei. As the molecules used in the present study do not have significant magnetic moments, only nuclear scattering is considered.

The incident neutron beam is not spin polarized and the polarization of the neutrons is also not analysed after the scattering event. Using that the systems can be described without quantum effects and with the approximation that the spin, isotope, and element of the scattering nuclei are completely uncorrelated with their positions, one obtains for the double differential cross section

$$\frac{\mathrm{d}^2\sigma}{\mathrm{d}\Omega \mathrm{d}E_f} = \frac{1}{\hbar} \frac{\mathrm{d}^2\sigma}{\mathrm{d}\Omega \mathrm{d}\omega} = \frac{1}{\hbar} \frac{1}{2\pi} \frac{k_f}{k_i} \sum_{j,k} \overline{b_j b_k} \int_{-\infty}^{\infty} \mathrm{d}t \; e^{-i\omega t} \left\langle \exp\left[i\boldsymbol{Q} \cdot \left(\boldsymbol{R}_j(t_0 + t) - \boldsymbol{R}_k(t_0) \right) \right] \right\rangle \, . \tag{2.32}$$

In this equation, k_i and k_f are the moduli of the wave vectors of the neutron before and after the scattering event, respectively, and $\boldsymbol{Q} = \boldsymbol{k}_f - \boldsymbol{k}_i$. The scattering length of

nucleus l is b_l, the bar over the scattering lengths denotes an average over all possible nuclear spin orientations and isotope types, and the angular brackets $\langle\ \rangle$ are an ensemble average over all t_0 for the presented ergodic systems.

The average of the product of the scattering lengths is decomposed into the average value of *all* scattering lengths and a variation thereof, called *coherent* and *incoherent* scattering lengths, respectively. This can be visualized by a lattice of scatterers, all with the same scattering length. They will scatter the neutron beam *as a whole*, collective properties will be important and there will be a pattern in Q-space due to the pattern in real space. This is the coherent scattering. In contrast, a large cloud of nuclei which are randomly distributed and non of them close to each other will scatter incoherently: there results no pattern in Q-space as no interference of the scattered neutron waves is possible. The nuclei scatter neutrons as if they were alone.

This reformulation allows to extract the scattering lengths from the sum and split the total double differential cross section into a sum of a coherent and an incoherent part. A comparison of equation 2.32 and equation 2.3 shows that the two summands contain the Fourier transform of the pair (coherent) and self (incoherent) scattering function:

$$\frac{\mathrm{d}^2\sigma}{\mathrm{d}\Omega\mathrm{d}\omega} = \frac{k_f}{k_i}\frac{N}{4\pi}\Big(\sigma_{\mathrm{inc}}S_{\mathrm{self}}(Q,\omega) + \sigma_{\mathrm{coh}}S_{\mathrm{pair}}(Q,\omega)\Big) \tag{2.33}$$

where N is the number of scattering nuclei.

This function shows again that the double integral of the double differential cross section is not a conserved quantity: Taking again the example of increasing the temperature of the sample, the $S_{\mathrm{self}}(Q,\omega)$ will increasingly cause an energy gain of the neutrons (large k_f). As the integral of $S_{\mathrm{self}}(Q,\omega)$ over all energies is a constant [160], this means that the number of neutrons scattered with a smaller k_f decreases. This simple redistribution in $S(Q,\omega)$ is weighed with a factor k_f to get the double differential cross section – which therefore increases with increasing temperature.

So far, the energy change of the neutron was denoted by $\hbar\omega = E_f - E_i$. As is a sloppy habit in neutron scattering, the $\hbar$ is often suppressed in this thesis, resulting in a quantity called ω which is an energy.

That, at least, is the theory. As mentioned above, quite some assumptions are used which will hardly ever be met in any experiment. The three most important of these are:

- It was assumed that the incident neutrons had all the same energy E_i and wave vector k_i, i. e. a collimated, monoenergetic beam. In reality, both quantities are distributed. As the superposition principle holds, the final neutron distributions are a convolution of the initial neutron distribution and the response of the sample. Its influence is discussed in section 3.2 and the corresponding publication [D].

- The recorded signal was assumed to be determined only by a single scattering event in the sample. However, also the geometry and scattering properties of the sample influences the measured neutron signal: The extension of the sample can introduce additional time-of-flight differences, the neutron can be absorbed or scattered a

second time on its way through the sample. Effects caused by the geometry of the sample and the absorption of neutrons in the sample are discussed in section 3.3, multiple scattering is discussed in the corresponding publication [D].

- The scattering cross sections of the nuclei were assumed to be uncorrelated with the positions of the nuclei in the sample. Although this is clearly not the case for a biomolecule which is functional only because the atoms *are* always on the same spots, it is a quite good approximation because by far the largest contribution to the scattered intensity is due to the incoherent scattering of hydrogen – which is due to the spin alignments between neutron and proton and is therefore really not correlated with the position in the molecule.

The details on how the measurements were performed and how these experimental deviations from the theory are visible in the measurements is presented in the following chapter. In the next but one, it will be shown how the data evaluation took these effects into account.

Chapter 3.

Materials and Methods

The preparation of the samples and some of their basic properties are described in this chapter, followed by a description of the neutron spectrometer TOFTOF where the measurements of the systems were performed. Finally, a few examples are given how the obtained spectra are influenced by the set-up of the instrument and how the corresponding settings were chosen for the measurements presented in this thesis.

3.1. Preparation and Characteristics of the Phospholipid Samples

The dynamics of the phospholipid was first studied in multibilayers of only DMPC and D_2O [B, D]. The advantage of this system is that it has only two components and a large signal-to-background ratio which makes it possible to study the motions in detail. Some background information about the hydration water, which is also an interesting subject matter on its own right [C], is given in this section, followed by the description of the preparation of the multibilayers. It is followed by the description of multibilayers of DMPC mixed with additives [E] and the one of single bilayers of pure DMPC [F] which lead to the preparation of monolayers of DMPC mixed with additives on both, emulsions and suspensions [F]. This stepwise increase of the complexity of the systems will make it possible to distinguish the influences of different factors on the phospholipid dynamics.

Hydration water. All systems discussed in this thesis contain hydration water. While it is the main topic of one study [C], it is a nuisance contribution in the case of the phospholipid samples [B, D–F] and will not be evaluated in these cases.

Briefly following the course of the hydration of DMPC, one water molecule per phospholipid molecule corresponds to a mass fraction c_w of roughly 2.5% [8] (cf. figure 3.1). A single layer of water on the phospholipids is reached at 5-6 mol H_2O / mol DMPC [190], corresponding to 0.13 g H_2O / g DMPC or a c_w of about 12%.

This hydration range is interesting for studies of water because the first layer of water adsorbed on surfaces usually does not freeze, making measurements of the water dynamics at low temperatures in the amorphous state possible [105, 155]. However, the interactions between the water molecules and the substrate influence the dynamics of the molecules.

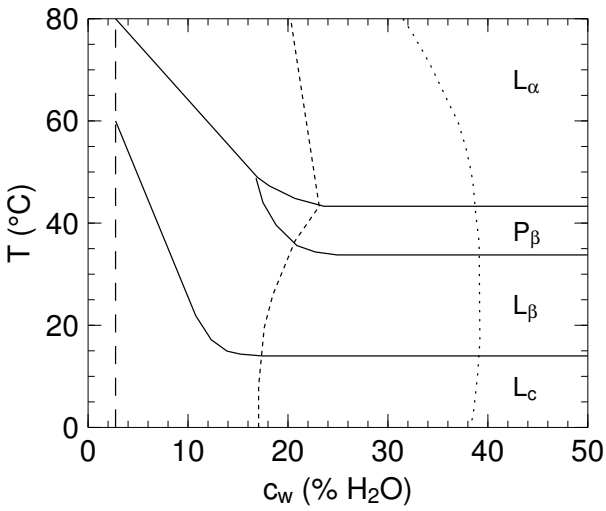

Figure 3.1.: Phase diagram of diacyl-phosphatidylcholines in water [8, 9], the temperature axis refers to DPPC. The main phase transition of DMPC is 8 °C below the one of DPPC, namely at 24 °C. The continuous lines show phase boundaries between the crystalline L_c, gel L_β, ripple P_β, and fluid L_α phase. The broken lines show special hydration values: The long dashed line corresponds to one water molecule per phospholipid molecule, the short dashed line shows the maximal water uptake from the vapour phase, and the dotted line the maximal water uptake from the liquid phase. The crystalline phase L_c is formed only when the sample is stored over several days at 4 °C [9] and is not covered in the measurements presented here.

It is therefore questionable if the hydration water is a suitable model system for bulk water [C].

For the study of phospholipids in the fully hydrated state, the hydration was increased to much higher values. Full hydration is reached at a c_w of about 40% (cf. figure 3.1), therefore many previous studies had aimed to reach exactly this value. However, neutron diffraction on these samples showed long-standing inconsistencies. It was finally found that already very small temperature gradients between the wall of the sample container and the sample are sufficient to decrease the relative humidity from the supposed 100%, resulting in a lower hydration of the sample [191].

As a decrease in hydration was found to influence the dynamics [153], it is necessary to ensure the full hydration of the sample. Therefore, all phospholipid samples were produced with surplus D_2O. The resulting mixture is not homogeneous – areas with fully hydrated phospholipid alternate with bubbles of D_2O. As will be discussed in section 4.1, this does not pose a problem for the data analysis because the corresponding signal of D_2O can be subtracted when the composition of the sample is known.

However, this subtraction necessarily assumes that the reference measurement of a bulk D_2O sample yields the same spectrum as the D_2O in the mixture. The before mentioned interaction between the water and the biomolecules was also observed in water layers adsorbed on phospholipids together with a reduced mobility [192]. These effects

are pronounced in weakly hydrated membranes [193] but hardly visible in fully hydrated membranes because it was shown that only the dynamics of the first layer of water was observably affected on a picosecond time scale [190, 194]. Therefore, the vast majority of the D_2O in the fully hydrated samples can be expected in good approximation to have bulk-like properties and a subtraction of its contribution is thus well justified.

Multibilayers of pure DMPC. The phospholipid DMPC was obtained as dry powder from Lipoid GmbH, Ludwigshafen, Germany, and used as received. The common start of many preparation procedures described in the literature to dissolve the phospholipid in chloroform was purposefully avoided in order to exclude the possibility of any residual chloroform in the samples. The omission of this step did not impede the hydration because the phospholipid was obtained as a very fine powder.

Another difference to the commonly used preparation procedures for neutron scattering measurements [137, 153, 156, 195–200] was the omission of a solid support of the membranes. This brings the disadvantage that the phospholipid layers cannot be aligned with respect to the scattering vector and the measured signal is therefore always a powder average. However, the big advantage is that any distortion of the dynamics by the solid support can be excluded and no misleading signal from the supporting material can possibly be observed.

It is known that a solid support interacts with the phospholipids [201] which sets limits to the similarity between supported lipid bilayers and biologically relevant systems [202]. In fact, some of the measurements presented here [B] have been compared with similar ones which were performed on samples with a solid support [203] where a different dynamical behaviour was observed. It can be speculated that this difference is caused by the interaction with the solid support.

The only step for the preparation of the multibilayers is to hydrate the dry phospholipid powder. To avoid a rapid uncontrolled formation of phospholipid vesicles and nanotubes and other non liquid crystalline phases [204, 205], the first part of the hydration was performed via the vapour phase: A small jar containing the phospholipid was placed in a bigger bottle which could be sealed and contained about 5 ml of D_2O. This assembly was placed in a constant temperature environment at 40 °C (above the main phase transition of the phospholipid, see below) for 24 hours or more. Under these conditions, the phospholipid hydration from the vapour phase reaches about 20% as depicted from the phase diagram displayed in figure 3.1. In a second step, liquid D_2O was added with a pipette up to an amount of at least 50 mass % and the mixture was stirred gently.

Multibilayers of DMPC and additives. The sample preparation was very similar to the one of the pure DMPC multibilayers, the only difference was that one of the additives myristic acid, farnesol, cholesterol, or sodium glycocholate was mixed with the phospholipid powder before the hydration. The compositions of the samples are listed in detail in the corresponding publication [E].

These additives can change the phase transition temperatures and induce even new phases. For example, when adding cholesterol, there is a micro phase separation into

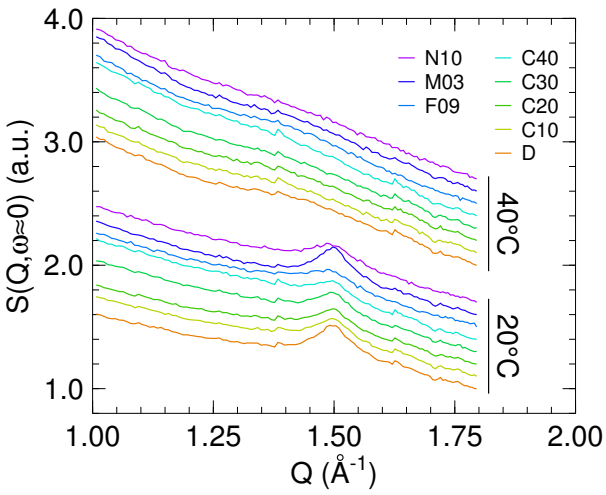

Figure 3.2.: The acyl chain correlation peak of DMPC in multibilayers at 1.5 Å^{-1} shown at two temperatures – below and above the main phase transition – pure (D) and with several additives: sodium glycocholate (N), myristic acid (M), farnesol (F), and cholesterol (C). The numbers indicate the amount of additive in relation to the phospholipid in mol% [E].

a cholesterol-rich and a cholesterol-poor phase [131]. However, on the time- and length scales covered in the presented measurements, the structure and dynamics changed only gradually. This is covered in detail in the corresponding publication [E] and can also be seen exemplarily in figure 3.2. In this figure, the pronounced structure factor maximum in the diffraction patterns at 1.5 Å^{-1} is shown which is caused by the regular arrangement of the acyl chains [156, 206]. It can be seen that the feature is much more pronounced at low temperatures below the main phase transition but not heavily influenced by the additives.

Single bilayers in vesicles. Single bilayers were studied without any solid support in vesicles which are unilamellar hollow spheres with a diameter of about 130 nm that contain the phospholipid only in the outer shell with 5 nm thickness. This diameter was chosen to be in the same order of magnitude as in drug delivery systems. For those, the particles must have a diameter between 10 and 200 nm [44]: smaller particles are filtered out by the kidney and larger particles are sequestrated by the spleen and liver, also the uptake by cells depends on the size. Compared to a cell, these vesicles are therefore rather small as can be seen in figure 3.3. The small size of the vesicles results in an increased curvature of the phospholipid bilayer.

For vesicles with a diameter of about 100 nm, the main phase transition is slightly broadened but still at the same temperature as found for multibilayer samples. Signifi-

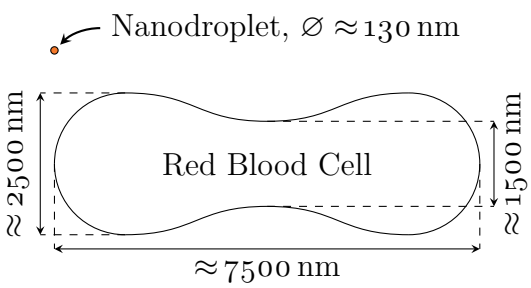

Figure 3.3.: Comparison of the cross-section of a vesicle or nanodroplet and a red blood cell. It can readily be seen that the curvature of the surface is much stronger in the case of the vesicles or nanodroplets as compared to the one of the cell.

cantly smaller vesicles exhibit a very broad transition that is shifted to lower temperatures by several degrees [207].

Most of the vesicle samples consists of the aqueous phase: for vesicles with a diameter of 130 nm, the mass fraction of DMPC in the sample is limited to only approx. 12% at close-packing (volume fraction $\phi = \pi/3/\sqrt{2} \approx 0.740$) or approx. 10% at the maximally random jammed state ($\phi \approx 0.64$) [208].

The vesicles were produced using two techniques: sonication and extrusion. With sonication, the vesicles are produced using ultrasound waves while with extrusion, the mixture of phospholipids and D_2O is pressed through a plastic membrane that contains holes of a well-defined diameter. While the former can produce smaller vesicles, the latter is more gentle to the molecules, the resulting vesicles exhibit less polydispersity, multilamellar vesicles, and chemical degeneration of the phospholipids.

Sonication was performed with a Bandelin Sonopuls UW 2070 ultrasound generator with a tip diameter of 3 mm (MS73), Bandelin electronic, Berlin, Germany. The device uses a frequency of 20 kHz with an output power of up to 70 W. The preparation procedures can be found in table 3.1.

For the extrusion, a commercially available extrusion device [210] was heated together with the syringes and the suspension of the swollen DMPC to 40 °C. The suspension was passed 21 times through a membrane with 100 nm pore size, keeping the equipment all the time close to 40 °C, i. e. above the main phase transition of the phospholipid.

Monolayers in emulsions. Phospholipid monolayers in emulsions were prepared using sonication. Attempts to produce emulsions also by extrusion have not been successful. Extrusion would have offered an opportunity to treat the stabilizer molecules with less stress and potentially also obtain a less polydisperse size distribution of the emulsion droplets.

The monolayers consisted either of pure DMPC or mixed with sodium glycocholate (abbreviated as NaGC or SGC). The sonication procedures can be found in table 3.1, the exact compositions of the samples are listed in the corresponding publication [F].

As in the case of the vesicles, the amount of phospholipid in these samples is very limited. The maximally achievable mass fraction of about 10% obtained there reduces in the case of the emulsions even to half of this value, i. e. 5%, because vesicles contain bilayers and emulsions only monolayers.

Monolayers in suspensions. Phospholipid monolayers in suspensions were prepared using high-pressure homogenization. In these suspensions, the aqueous phase was D_2O and the stabilizer DMPC and NaGC. As dispersed phases, either protonated tripalmitin or perdeuterated tetracosane were used. The suspensions were produced from mixtures of the following compositions:

- 8.46% protonated tripalmitin, 2.13% DMPC, 0.34% NaGC, 89.07% D_2O
- 10.30% perdeuterated tetracosane, 1.19% DMPC, 0.12% NaGC, 88.39% D_2O[1]

[1]Prepared by Martin Schmiele, Friedrich-Alexander-Universität Erlangen-Nürnberg

name	time (min)	cycle	power (%)	∅ (nm)	PDI
vS	2 × 5	3	10		
	2 × 5	3	20	430	0.31
	4 × 5	3	20	131	0.28
eD23N00	5 × 1	1	10		
	1 × 10	3	10	180	0.18
	1 × 5	3	10	154	0.19
	1 × 5	3	10	144	0.21
	1 × 5	3	10	132	0.21
eD13N00	10 × 1	1	10	300	
	10 × 1	1	10		
	1 × 10	1	10		
	1 × 10	3	10	175	
	1 × 10	3	20	136	0.13
eD11N02	2 × 5	3	10		
	2 × 5	3	20	218	0.17
	4 × 5	3	20	174	0.15
	4 × 5	3	20	134	0.14
eD11N01	5 × 1	3	10	220	0.16
	5 × 1	3	10	200	0.12
	1 × 5	1	20	180	0.19
	1 × 5	3	20	168	0.15
	2 × 5	3	20	124	0.14
eD09N02	1 × 10	3	10	179	0.13
	2 × 5	3	20	154	0.14
	2 × 5	3	20	133	0.13

Table 3.1.: Production procedures of the samples that were produced by sonication. The naming follows the same convention as in the corresponding publication [F]: v denotes vesicles, e emulsions. S stands for sonicated, Dxx and Nxx are the mass fractions xx (in ‰) of DMPC and NaGC, respectively. «cycle» indicates how many tenths of each second are spent in the active interval, no ultrasound radiation is produced during the remainder of each second. The z-averaged diameter of the particles ∅ and the polydispersity index PDI are obtained from a cumulant analysis of photocorrelation spectroscopy (PCS) data [209].

- 3.11% perdeuterated tetracosane, 0.92% DMPC, 0.10% NaGC, 95.87% D_2O[1]

Predispersions of these mixtures were prepared 20 °C above the melting temperature of the lipid dispersed phase using high-speed stirring with an IKA UltraTurrax and subsequent high-pressure homogenization using an APV-2000 (APV Deutschland GmbH, Unna, Germany) thermostatted at the same temperature for 2 min at approx. 1.2 kbar. The size of the recrystallized particles was determined by dynamic light scattering (photon correlation spectroscopy, PCS).

It should be noted that the production of the suspensions involves minor uncontrolled losses of material, e. g. evaporation of D_2O, residual material at the UltraTurrax or inside the high-pressure homogenizer. The final composition of the samples will therefore slightly deviate from the original sample weights given here.

3.2. Description of the Neutron time-of-flight Spectrometer TOFTOF

The neutron time-of-flight spectrometer TOFTOF at the Forschungs-Neutronenquelle Heinz Maier-Leibnitz (FRM II) [211, 212] is sketched in figure 3.4. It measures the energy of the neutrons before and after the sample by determining their velocity via their time-of-flight (tof). This takes place in both the primary part of the spectrometer where the neutron beam is prepared by tof monochromatization (TOF-) and in the secondary part where tof is used to measure the energy transfer from or to the sample (-TOF). Hence the name of the instrument: TOFTOF.

The primary spectrometer. The white continuous beam of neutrons from the cold source of the FRM II gets chopped into short bunches of polyenergetic neutrons by a first pair of choppers (see figures 3.4 and 3.5). After a certain distance, this bunch will have broadened due to the different energies and therefore velocities of the neutrons. Then, another chopper pair at the end of the primary spectrometer, (numbers 6 & 7) transmits only a fraction of this bunch. As it took the neutrons in this fraction approximately the same time to travel the distance between the two chopper pairs, they have about the same velocity. The ones that are too fast or too slow are absorbed in the boron coating of the chopper.

To ensure that only neutrons with the wanted velocity can pass the chopper system, two more *higher order choppers* (numbers 3 & 4) are positioned in between. They suppress the transmission of neutrons which have higher order wavelengths.

Chopper 5, the *frame overlap chopper*, completes the setup. It rotates at a fraction of the speed of the others and opens therefore only for every nth pulse, where n is called the *frame overlap ratio*. This prolongs the time that neutrons have after the scattering event to get detected before the fastest neutrons of a new pulse arrive. The maximal neutron energy loss that can be measured before the next pulse reaches the sample will be calculated in section 3.3.

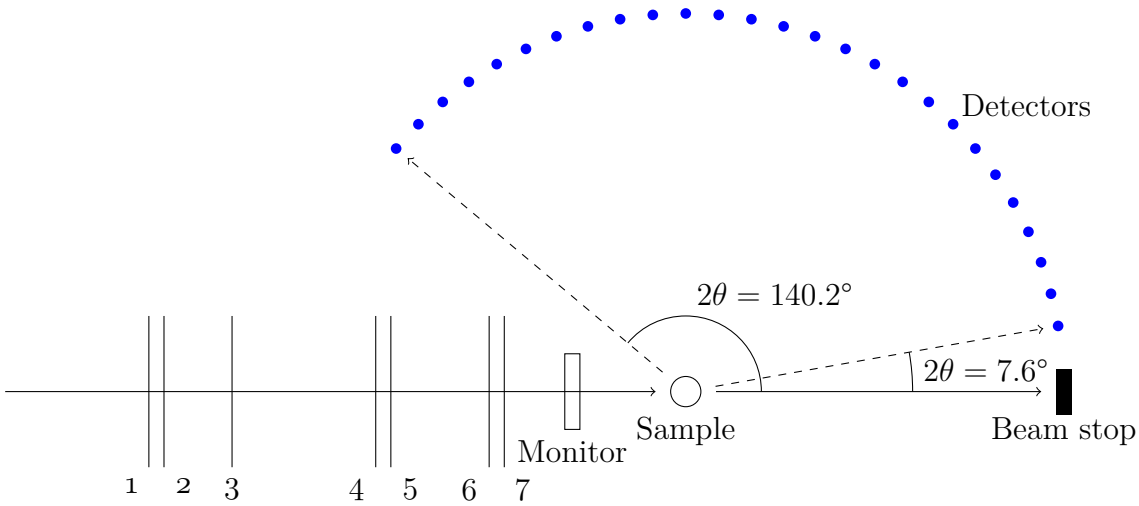

Figure 3.4.: Schematic drawing of TOFTOF. Following the neutron guide, first are choppers 1 & 2 which work together with 6 & 7 as velocity selector. Choppers 3 & 4 remove higher orders, 5 is the frame overlap chopper. The time needed for the neutrons to get from the sample to the detectors encodes their energy. The detectors on the other side of the beam stop are not shown, also the visible ones are only representative for the densely-packed array. One detector covers an angular range of about 0.5°.

The primary spectrometer can be used in many configurations, in some of which it is the main source of uncertainties for the determination of the energy and direction of the neutrons. The energy resolution is given by the precision with which the energy of the transmitted neutrons is determined and can therefore be improved by increasing the chopper rotation speed or by using neutrons with a lower incident energy. The divergence of the neutron beam is given by the neutron guide system and the wavelength of the neutrons, it can be influenced by choosing a smaller neutron wavelength. Both, the energy and momentum transfer resolution, can be calculated and are a function of energy and momentum transfer, respectively. They will be presented in the following.

The energy resolution of the time-of-flight spectrometer decreases with increasing energy transfer. It can be calculated, the published formulae differ from each other [211–214]. The formula used for the conception of the spectrometer [213] is used in this thesis because it reproduces the measurement quite well. This formula is slightly differently formulated in another discussion of the instrumental resolution [214]. Only one characterisation of the spectrometer [211, 212] contains an error in the definition of the opening time of the first chopper pair t_p and the opening time of the last chopper pair t_m. The correct definitions are

$$t_p = \frac{a_p}{360 \cdot \nu_c \cdot 2} \tag{3.1}$$

$$t_m = \frac{a_m}{360 \cdot \nu_c \cdot 2}\ , \tag{3.2}$$

where the quantities are defined as in table 1 of the corresponding publication [211]: a_p

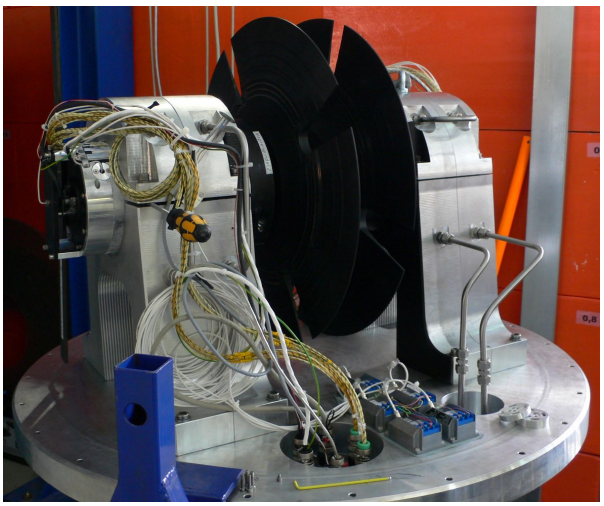

Figure 3.5.: A chopper pair of TOFTOF (the pair 1 & 2) upside-down during maintenance. The discs are made of carbon fibres and coated with boron. The slits in the chopper discs are visible. Due to the high rotation speed of the discs, they are operated in an evacuated environment.

and a_m are the opening angle of the first and the last chopper pair, respectively, and ν_c is the rotation speed of the choppers measured in rounds per second. The factor 2 in the formula is due to the opening time reduction caused by the counter rotating chopper pair. It can be speculated that a wrong reduction of this factor led to the formula given in the aforementioned publication [211, 212]. The resulting energy transfer dependent instrumental energy resolution is shown in figure 3.6 for the set-ups used in this thesis.

The momentum transfer resolution ΔQ is mainly given by the divergence determined by the last part of the neutron guide which has $m = 3.6$ where m is defined as the ratio of the critical angle of total reflection of the neutron guide compared to an hypothetical neutron guide coated with natural nickel. It roughly means that the neutron guide reflects neutrons with an incident angle (measured in degrees) of up to $m \cdot \lambda$ where λ is the wavelength of the neutrons measured in nanometres. The obtained results, shown in figure 3.6, are in good agreement with Monte Carlo simulations of the instrument [213]. This part of the resolution is hardly affected by the wavelength of the neutrons which can be seen from the calculation

$$\Delta Q = Q_{\max} - Q_{\min} = \frac{4\pi}{\lambda} \sin\left(\frac{2\theta + m \cdot \lambda}{2} \frac{\pi}{180}\right) - \frac{4\pi}{\lambda} \sin\left(\frac{2\theta - m \cdot \lambda}{2} \frac{\pi}{180}\right)$$
$$\approx \frac{4\pi^2}{180\lambda} \cdot \left(\frac{2\theta + m \cdot \lambda}{2} - \frac{2\theta - m \cdot \lambda}{2}\right) = \frac{\pi^2}{45} \cdot m \quad (3.3)$$

which is – in this approximation – completely independent of the wavelength.

For the evaluation of the measurements, the limited resolution in Q is neglected. This can be justified because the energy-dependence of the incoherent scattering is evaluated, not the Q dependence of the coherent scattering. This necessitates that the limited resolution of the energy transfer between neutron and sample must be considered. For this purpose, the resolution is measured using a sample that does not show any quasielastic broadening. This can be either the sample at low temperatures or some other solid substance. In the present studies, most of the samples show strong coherent peaks of the formed D_2O ice. Therefore, the second option was used and a vanadium sample was

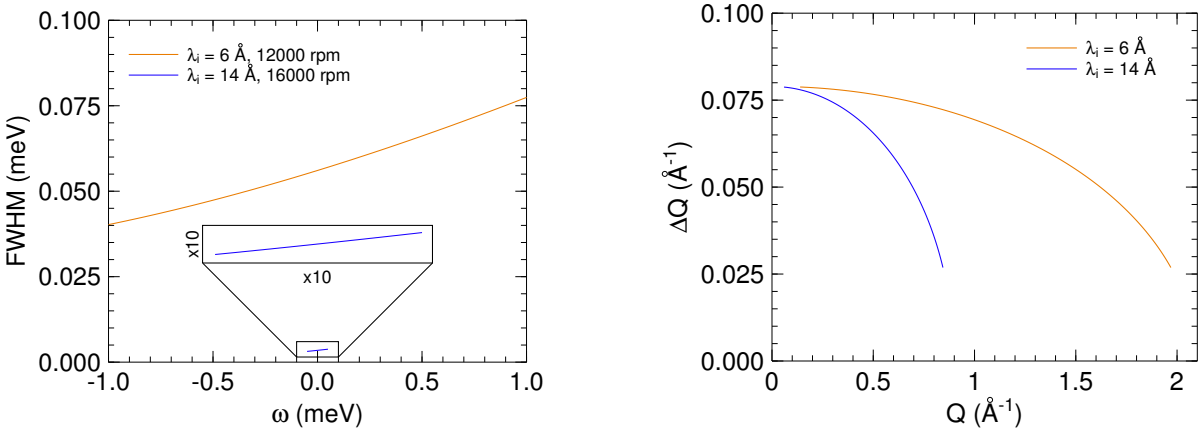

Figure 3.6.: The uncertainty of the determination of energy transfer (left) and momentum transfer (right), shown as a function of the energy transfer and momentum transfer, respectively. The two setups shown are the ones used in this thesis: chopper rotation speed 12000 rpm with incident neutron wavelength of 6 Å as well as 16000 rpm with 14 Å. The uncertainty of the energy transfer determination is shown as the full width at half maximum (FWHM) of the quasi-Gaussian resolution. For better visibility, the high-resolution setup is shown also after magnification of both, energy transfer and FWHM, by a factor 10.

employed for the determination of the resolution.

The secondary spectrometer. The detectors at TOFTOF make use of a nuclear reaction of the neutrons with ^{3}He nuclei to register them. When the neutron is captured by such a nucleus, the compound decays first to an excited state of ^{4}He which has spin zero. This intermediate step causes the extreme sensitivity of the ^{3}He nuclei to the relative spin orientation of the neutron with respect to its own nuclear spin which makes for example spin filters possible. The intermediate state decays into an unbound state of a proton and a tritium which scatter apart and produce a detectable current pulse.

The neutron detection events are binned into time-of-flight channels. The number of channels in a frame can be chosen by the user, it defaults to 1024. Due to a CPU speed of 20 MHz, the width of one channel is always a multiple of 50 ns. As the frame length can be chosen completely arbitrarily by the user (see section 3.3), it follows that it happens

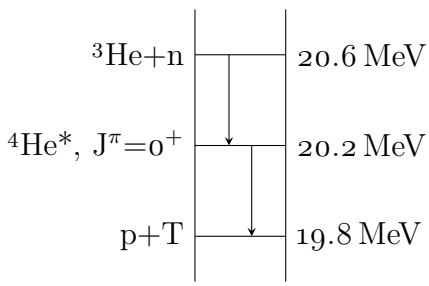

Figure 3.7.: The part of the energy level diagram of ^{4}He which is relevant for the detection of the neutrons (n) [215–217]. The difficulty for neutron detection is the charge neutrality of the neutron. Therefore, the nuclear reaction with ^{3}He is used to generate charged particles (proton, p, and tritium, T) which are then detected.

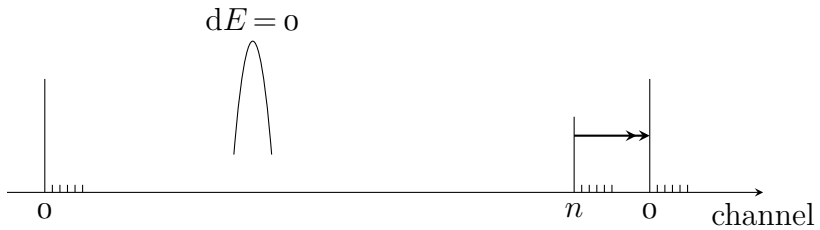

Figure 3.8.: Time-of-flight channel structure of the experiment. A frame starts with time channel 0 when the neutrons are at the sample position. After some time, the elastically scattered neutrons arrive. The next neutron pulse arrives at the sample during the filling of channel n. Because the spectrometer advances immediately to the next frame, the time spent in channel n might be shorter than in the other channels. The intensity peak of elastically scattered neutrons is sketched and labelled with $\mathrm{d}E = 0$.

quite regularly that a new frame starts while not all of the 1024 channels are filled yet. In fact, the new frame will normally start not even after completely filling a channel but at an arbitrary time in between, cf. figure 3.8.

3.3. Choice of Measurement Parameters

Several parameters of the measurements can be adjusted at TOFTOF. In the following, the influence of some of them are described in detail: the dynamic range of momentum and energy transfers accessible to the neutrons, the observation time during which the neutrons can follow the motions of the molecules in the sample, as well as the distribution of the available time between several measurements, the amount and geometry of the sample.

Neutron wavelength and frame length determine the dynamic range. The theoretically accessible window in Q-ω-space is determined by the wavelength of the incoming neutrons. Neutrons can be scattered with scattering angles 2θ between 0° and 180°.

TOFTOF adds two restrictions to that: first, it does not measure the neutrons which are scattered with 2θ below 7.4° or above 140.4° and second, it does not wait an infinite amount of time after a neutron pulse. The latter means that neutrons which have a very low velocity after the interaction with the sample are counted in the next frame as energy gain neutrons.

The ratio of neutron pulses let through by the frame overlap chopper has to be determined by trading off the accessible energy loss range versus flux. Knowing the time between pulses, determined by chopper speed and ratio, it is possible to calculate the minimal speed of a neutron before the fastest neutrons of the next pulse arrive at the detectors. As a worst case scenario, the fastest neutrons are assumed to have an infinite velocity after the sample. This conservative estimate makes sure that no neutron of this

pulse that went through the sample can arrive at the detectors before time zero.

Typical operating conditions were a chopper rotation speed of 12000 rpm, $\lambda = 6$ Å, and ratio 4. The initial energy of the neutrons E_i was therefore

$$E_i = \frac{p^2}{2m} = \frac{(h/\lambda)^2}{2m_n} \approx \frac{81.81}{(\lambda[\text{Å}])^2} \underset{\text{here}}{\approx} 2.27\,\text{meV} \tag{3.4}$$

The largest accessible neutron energy loss in the frame is calculated via the minimal energy that neutrons may have after the scattering process E_f and still arrive at the detectors before the next pulse. This in turn is determined by the time between two pulses which amounts (with two slits per chopper disc and ratio 4) to

$$12000\,\text{rpm} \cdot 2\frac{\text{pulses}}{\text{round}} \cdot \frac{1}{60}\frac{\text{minute}}{\text{second}}/4 = 100\frac{\text{pulses}}{\text{second}} \Rightarrow 0.01\frac{\text{second}}{\text{pulse}}\ . \tag{3.5}$$

The neutrons have at most 0.01 second to travel the 4 m from the sample to the detectors before the next pulse arrives. This corresponds to a final energy after the interaction of

$$E_f = \frac{1}{2}m_n v^2 = \frac{1}{2}m_n \left(\frac{4\,\text{m}}{t\ [\text{second}]}\right)^2 \underset{\text{here}}{\approx} 0.84\,\text{meV} \tag{3.6}$$

The energy a neutron can transfer to the sample while still being detected before the next pulse is consequently

$$E_{\text{max}} = E_f - E_i \underset{\text{here}}{\approx} -1.43\,\text{meV}\ . \tag{3.7}$$

This is also visible in figure 3.9: there is a sharp cut-off on the neutron energy loss side. This cut-off can be shifted by increasing the frame overlap ratio or by shuffling channels from the beginning of the frame to its end. This procedure relies on the fact that only few neutrons gained very large amounts of energy.

The measurements presented in this thesis were performed either with the afore mentioned 12000 rpm, $\lambda = 6$ Å, ratio 4 resulting in 55 µeV instrumental energy resolution or with 16000 rpm, $\lambda = 14$ Å, ratio 8 for an instrumental energy resolution of 4 µeV.

The uncertainty of the energy determination causes an effective observation time. The instrumental energy resolution is mainly determined by the precision with which the primary part of the spectrometer selects monoenergetic neutrons. Two parameters can be used to change this resolution: the chopper speed and the selected wavelength of the incoming neutrons. As described by Heisenberg's uncertainty principle, a more precise selection of the incident neutron energy yields longer neutron wave trains. The wave of one neutron will therefore run longer over the sample, will be influenced by the motions of the nuclei during a longer *observation time*.

The observation times that can be realized at TOFTOF are roughly in the range of 1 ps to 1 ns [218]. These values correspond to the times at which the spectrometer detects a decay of the correlation function of a static scatterer (the vanadium standard) to

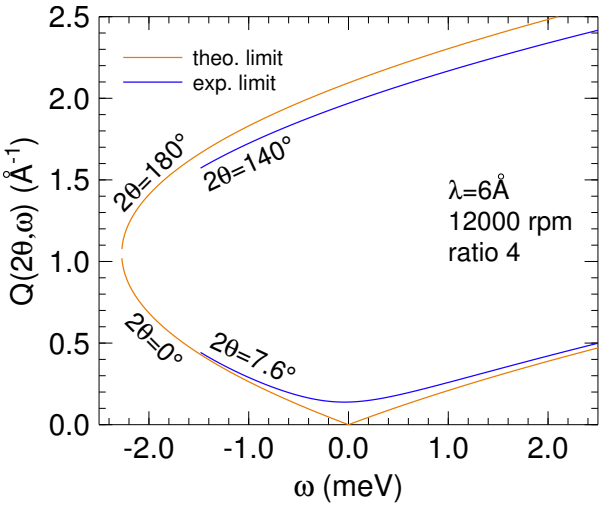

Figure 3.9.: The dynamical range that can be reached with neutron scattering at the typical incident neutron wavelength of 6 Å is compared with the one that can actually be accessed at TOFTOF with the conditions given in the figure. The parts missing at small and large Q are due to the incomplete coverage of 2θ values with detectors, the one missing at large neutron energy loss (here on the left) is caused by the neutron pulse repetition rate. It can be changed by shifting neutrons from the end of the frame with the danger of mixing neutron energy gain and loss.

0.1. Experience has shown that the correlation functions of samples could be evaluated without problems up to this value. In the measurements presented in this thesis, the two employed instrumental energy resolutions of 55 µeV and 4 µeV correspond to observation times of about 60 picoseconds and 900 picoseconds, respectively.

Measurements at different observation times can give very different results. When using the models introduced in section 2.1 to evaluate the data, it is important to keep in mind that this description is only valid on the given time scale.

One macroscopic example where a model is valid only for a given amount of time is water flowing in a river. If one looks at the motion only for a fraction of a second, the water seems to flow in a certain direction. It is however clear that the direction of the flow changes completely if one follows the water over several days and many loops of the river. The model of a flow in a constant direction is therefore valid at short time scales but does not describe the system on long time scales.

Another macroscopic example demonstrates that the distinction between localized and long-range motions in section 2.1 is also only valid on the specified time scale: A closed bottle is half-filled with water and shaken up and down. On a time scale of a fraction of a second, the water is flowing through the bottle – already on a second scale it becomes clear that it is actually only moving back and forth.

Adequate distribution of the measurement time can decrease the resulting error bar. Given the limited time available for a series of measurements, it is necessary to budget the time spent for a specific measurement. There are several opinions on how to distribute the time between the samples, the most common option is to spend the same time on every measurement. It will be shown in the following that this rule can be optimized for the samples measured for this thesis.

In the present case, there is typically a sample measurement and a background measurement, for example pure D_2O. If the sample contains a D_2O volume fraction ϕ and scatters with a rate R_s neutrons per second while the D_2O background scatters with

a rate R_b, the quantity that has to be evaluated is

$$R = R_\mathrm{s} - \phi R_\mathrm{b} \ . \tag{3.8}$$

The aim of distributing the beam time is to minimize the relative error $\Delta R/R$.

The total time t is spent for t_s on the sample and for t_b on the background measurement with $t_\mathrm{s} + t_\mathrm{b} = t$. The respective counts are N_s in the sample and N_b in the background measurement. Assuming a reasonably large number of counts, Gaussian statistics can be used and the statistical error bars of the rates are $\Delta R_\mathrm{s} = \Delta N_\mathrm{s}/t_\mathrm{s} = \sqrt{N_\mathrm{s}}/t_\mathrm{s}$ and $\Delta R_\mathrm{b} = \Delta N_\mathrm{b}/t_\mathrm{b} = \sqrt{N_\mathrm{b}}/t_\mathrm{b}$. When calculating equation 3.8, these add up quadratically:

$$\Delta R^2 = \Delta R_\mathrm{s}^2 + \phi^2 \cdot \Delta R_\mathrm{b}^2 = N_\mathrm{s}/t_\mathrm{s}^2 + \phi^2 \cdot N_\mathrm{b}/t_\mathrm{b}^2 \ . \tag{3.9}$$

For the determination of the time distribution at which the total relative error becomes minimal, the derivative of $(\Delta R/R)^2$ with respect to t_s has to be zero. Assuming that $R_\mathrm{s} - \phi R_\mathrm{b} \neq 0$, i. e. assuming that the sample scatters *some* intensity in addition to the background, this leads to

$$t_\mathrm{s} = \frac{1}{\phi}\sqrt{\frac{R_\mathrm{s}}{R_\mathrm{b}}}t_\mathrm{b} \quad . \tag{3.10}$$

As an example, in a typical sample that consists of 50% protonated DMPC with 50% D_2O, the time of the D_2O background measurement can be less than a fourth of the one of the sample according to this calculation.

The rule oversimplifies the problem because the spectra of the sample and the background have a different energy- and Q-dependence so that the ratio between the signals is a function of these variables and not a single number. This can be considered by calculating the time ratio of the measurements using those points in the evaluated part of the spectra where the signals of the sample and the background are the closest to each other. For the measurements presented in this thesis, this happens at large energy transfers.

The measurement time of the vanadium standard has to be adjusted to the purpose of the measurement. If it is used only for the calibration of the detector intensities, a relatively short measurement is sufficient. However, if it is used to determine the instrumental resolution of the spectrometer and is numerically convolved with the theoretical function fitted to the data, its error bars can be the limiting factor for the precision of the fit results. This problem is discussed in more detail in section 4.2. Special care was taken in the presented data sets to obtain a high quality of this measurement.

The amount of sample can be optimized. Due to the weak interaction with the sample, most neutrons fly straight through the sample and are absorbed in the beam stop. Some neutrons are absorbed by the sample, others are scattered. The amount of sample is normally chosen with three opposing requirements in mind: If there is too little sample in the beam, very few neutrons will be scattered and the resulting bad statistics of the data will impede a detailed analysis. If there is too much sample, neutrons will are more likely to be absorbed within the sample which brings about that the number of

scattered neutrons is not proportional to the amount of sample and makes the background subtraction more challenging. Also in the case of too much sample, neutrons might undergo more than one scattering event. As the theory that is used to evaluate the data assumes that the momentum- and energy-transfer which a neutron experiences is caused by only one scattering event, an occurrence of multiple scattering will impede a detailed analysis, as well.

A common rule of thumb is therefore to use samples with transmission values of about 90% and all the samples studied in this thesis had transmission values in this order of magnitude. The absorption of neutrons in the samples was in most cases found to be of minor importance but will be discussed in the frame of the choice of the sample geometry again. Regarding multiple scattering, it was possible to show in the frame of this thesis [D] that the long-range motional component can be reliably extracted even from samples with a much lower transmission.

Different sample geometries have different advantages. In the present case, the samples were contained either in hollow cylindrical or flat aluminium sample containers. The flat sample containers were oriented with their surface normal towards a scattering angle of 135° in the direction of the detectors.

One difference between the two is that the hollow cylindrical sample containers have the advantage that the absorption of neutrons in the sample depends hardly on the scattering angle [219, 220]. In the case of flat sample containers, neutrons which are scattered into the direction of the plane of the sample have to cover a large distance within the sample. On this way, they are very likely to get scattered again or be absorbed – hardly any of them arrives in a detector in this direction. This effect can clearly be seen in figure 3.10.

From this point of view, hollow cylindrical sample holders such as the one shown in figure 3.11 are clearly favourable and were used for all measurements with an instrumental resolution of 55 µeV in this thesis. It will, however, become clear in the following that they are not suitable for high-resolution measurements at TOFTOF for which the flat sample containers were used, accepting their shadowing effects.

This is due to the other difference between flat and hollow cylindrical sample holders: the distribution of the flight paths. Seen from large scattering angles of about 135°, the distance between the sample in flat sample holder and the detectors is always the same. In contrast, the neutrons can be scattered by the back wall of the hollow cylinder or transverse the hollow cylinder, get scattered by the front wall, and transverse the hollow cylinder again. On a time-of-flight instrument, the energy transfer between the neutron and the sample is calculated from the time the neutrons need from the last chopper via the sample to the detectors. However, this time-of-flight does not only depend on the velocity of the neutrons but also on the length of their flight path. Therefore, such a distribution of flight paths appears as a distribution of energy transfers.

This effect can be nicely seen in figure 3.12 where a hollow cylindrical sample shows two peaks – corresponding to scattering from the front wall and from the back wall. This effect is hardly visible at small scattering angles, i. e. small Q, because the neutrons have

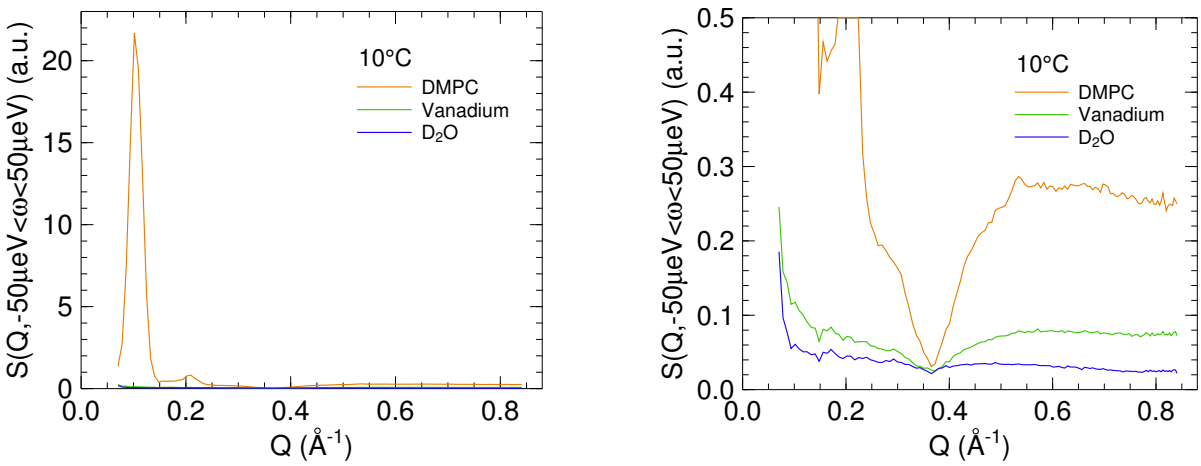

Figure 3.10.: Diffraction patterns of the sample at 10 °C (orange), vanadium (green), and D_2O at 10 °C (blue). The two graphs show the same data on different y scales. The measurement set-up was the one for 4 µeV measurements. The coherent scattering of the sample can be seen at low Q, the dip shortly before $Q = 0.4$ Å^{-1} is caused by the shadowing of the sample container towards scattering angles of 45°. The slowly decreasing intensity at the highest values of Q is because the neutrons which are scattered from regions far away from the beam centre are not transmitted by the radial collimator.

to travel through the sample either before or after the scattering event. In contrast, it is strongly visible at large scattering angles, i. e. large Q, where one neutron does not have to travel through the sample at all while the other has to do so two times.

In principle, it would be possible to account for this effect with a measurement of the instrumental resolution – as it is done for example for the geometrical inaccuracies of the detectors. However, if vanadium has to be used for this measurement, the high absorption cross section of vanadium makes this impossible: As can be seen in figure 3.12, the double peak is not symmetric. The component on the neutron energy loss side has a lower intensity than the other one. This is the peak caused by neutrons which had to travel for a longer time, i. e. the one of the back wall. Neutrons scattered here have to pass two times through the front wall where they can be absorbed. As the intensity loss depends on the absorption properties of the sample, they will be different for the sample and vanadium. The unsymmetrical measurement is therefore not a suitable representation of the instrumental resolution.

The high-resolution measurements presented in this thesis are therefore performed with flat sample holders which are oriented with their surface normal towards a scattering angle of 135° in the direction of the detectors. In this configuration, the neutrons which are emitted into the direction of large scattering angles have all very similar lengths to travel, making a high energy resolution with a symmetric resolution function of the spectrometer possible. The drawback of this configuration is that the long path of the neutrons through the sample towards a scattering angle of 45° causes a shadowing in

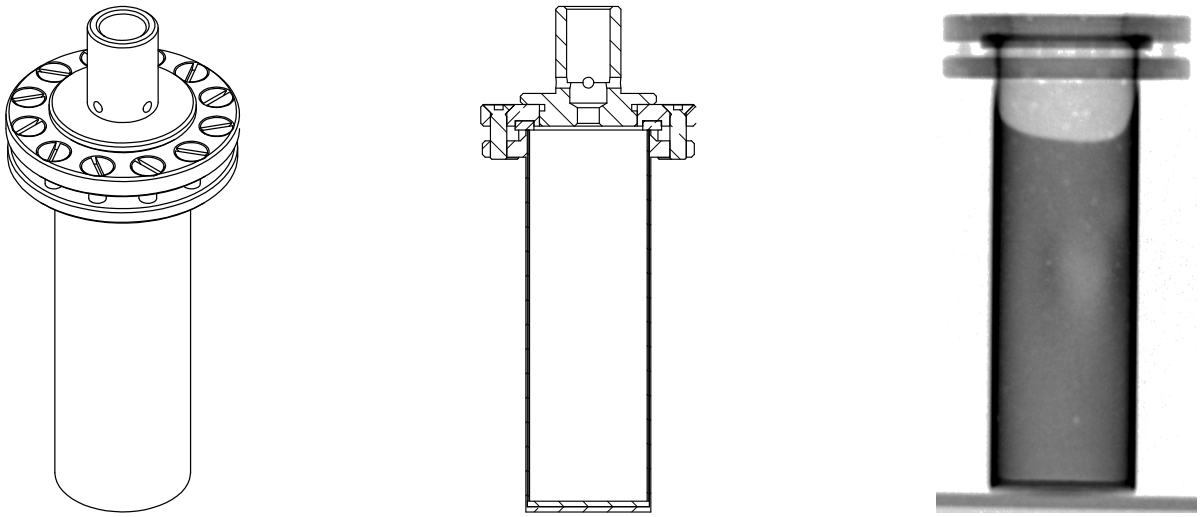

Figure 3.11.: The type of sample cells that were used for the measurement in hollow cylindrical sample containers in this thesis. Left: Three-dimensional technical drawing of the hollow cylindrical sample cells (drawn by Ph. Jüttner, FRM II). Middle: Two-dimensional cut through the sample holder; the sample is only in a thin layer at the outside of the container (drawn by Ph. Jüttner, FRM II). Right: A neutron radiography (kindly provided by Johannes Brunner from ANTARES at the FRM II) of a hollow cylindrical sample container filled with H_2O. The support on which the container was measured is also visible at the bottom. On the top, the two thick aluminium plates which contain the screws are visible along with the Teflon seal. In the middle, a bulging is visible which makes the amount of sample in the beam not proportional to the amount of sample in the sample cell because only the middle part of the sample cell is normally hit by the neutron beam.

Figure 3.12.: Measurement of the vanadium hollow cylindrical standard at TOFTOF with an incoming neutron wavelength of 10 Å, chopper rotation speed 16000 rpm, and frame overlap ratio 8, resulting in an instrumental resolution of about 10 µeV. At large scattering angles, a double peak becomes visible which is caused by scattering of neutrons on the front and back wall of the sample container. The peaks are not of equal height because of neutron adsorption in the front wall.

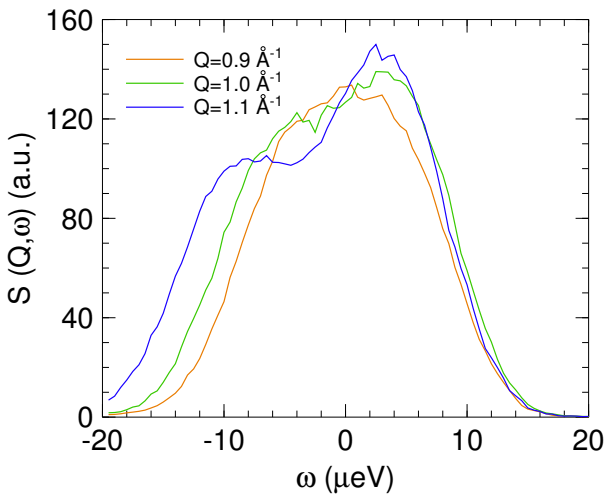

this direction as can be seen in figure 3.10.

A completely different problem is also visible in the radiography of a filled sample container shown in figure 3.11: The sample is not uniformly distributed over the whole can but bulging can occur. Additionally to the uncertainties of the layer thickness due to bulging, there is also the uncertainty of the manufacturing process. Given a sample layer thickness of 0.1 mm and a typical precision of the manufacturing process of 1/100 mm, there is an intrinsic variation of about 10% between sample containers. Also the walls of the containers have varying thicknesses within the same precision. This becomes problematic because the neutron beam does not cover the whole sample container in the vertical direction but only a part in the middle of the container with about three quarters of its height: the uncertainties of the thicknesses of sample layer and container in this area cause directly proportional uncertainties of their contributions to the scattered signal. It will be discussed in section 4.1 how the subtraction of background contributions can absorb these uncertainties and a proposal will be presented in section 6.1 how they could be avoided by using a different design of the sample containers.

Chapter 4.

Data Reduction and Analysis

The measured systems consist of mixtures of several components. Of these components, only the phospholipid is of interest in this thesis. Therefore, the contributions of the other substances to the scattering signal have to be subtracted. Given that the fraction of phospholipid in the samples can be as low as 1%, this is a delicate task and will be described in this chapter.

Also two approaches to evaluate the information that is contained in the spectra will be discussed in detail:

The first one is to create a model of the molecular motions. It is required that this model agrees with previously known facts, e. g. the molecular structure, and with the data measured in the course of this thesis. While the previous knowledge has to be taken into account for creating the model, the compatibility with the data has to be determined from a fit. If this is given, the parameters of the best fit of the model can be extracted – which obviously depend on the choice of the model.

The second, model-free, approach to extract information from the data aims in the opposite direction: By extracting only very few quantities from the data without fitting any model, only a small fraction of the information contained in the spectra is evaluated. The resulting quantities do not have a similarly well-defined meaning as the parameters used in a model. However, they can be extracted very reliably and comparisons between series of similar systems give access to the evaluation of the dynamics upon the change of a control parameter.

Both approaches have been used in the present work: The fit of a model was used to determine the mechanism of the diffusion of the phospholipid molecules. As the results of the fit depend also on the fit procedure, special attention was paid to the fitting process itself. Independently of these results, the evaluation of the structure and dynamics was followed when varying temperature, lateral pressure, and composition by a model-free approach.

4.1. Extracting the Scattering Function from the Scattered Intensities

General data treatment. The scattering functions can be calculated from the measured data in several steps which are given in detail in appendix [I] and are summarized in the

following. Depending on the specifics of the sample compositions and the requirements of the data evaluation, not all of these steps have been performed in each of the presented studies. The concrete data reduction steps are given in the respective publications [B–F].

Generally, the data were converted to be a function of neutron energy transfer, the energy-dependent detector efficiency was corrected, and the detector sensitivity was normalized using the scattering of a vanadium standard. The obtained scattering function $S(2\theta, \omega)$ was corrected for absorption effects.

These absorption effects can be explained with a simple hypothetical example: if the emulsions consisted of a normally-scattering oil phase dispersed in an imaginary water phase that would absorb all neutrons, the signal of the mixture (no scattered neutron) is not equal to the sum of the two single signals (no neutrons from the pure water phase and some neutrons from the pure dispersed phase). This phenomenon is well-known in scattering techniques and is usually corrected with the algorithm of Paalman and Pings [221]. It takes the scattering and absorption cross section of the respective samples and returns scattering angle and energy transfer dependent correction factors that can be used to scale the measurements.

Finally, the data were grouped into spectra at constant Q, resulting in the scattering functions $S(Q, \omega)$ of the whole system in the beam. From this quantity, the contribution of the phospholipid molecules has to be extracted by subtracting the background contributions. Before the methods for the background subtraction for the different samples are discussed in detail, it should be mentioned that the obtained $S_{\text{measured}}(Q, \omega)$ is not exactly equal to the $S(Q, \omega)$ defined in chapter 2: Whereas the theoretical definition is symmetrical with respect to neutron energy loss and energy gain, the occupation of excited states in the real system is governed by the Boltzmann-factor. This causes that it is less likely that the sample transfers energy to the neutron than that the neutron transfers energy to the sample which results in

$$S_{\text{measured}}(Q, -\omega) = \exp\left(\frac{\hbar\omega}{k_{\text{B}}T}\right) \cdot S_{\text{measured}}(Q, \omega) \tag{4.1}$$

where $\omega > 0$ denotes a neutron energy gain scattering event. This is known as the *principle of detailed balance*. It was found for the data presented in this thesis that a correction for this factor did not give better results. The detailed balance was therefore not corrected. This can be justified because the detailed balance factor is approximately constant at the high temperatures of the samples and the low evaluated energy transfers. Furthermore, the signals of some samples were weak so that contributions which do not follow the principle of detailed balance (e. g. the instrumental background) could have had a distorting effect when multiplied with the correction factor.

Background subtraction from the data of multibilayer samples using the respective volume fractions. In the case of the multibilayer samples [B, D, E], the background contributions are at least one order of magnitude below the signal of the phospholipid. In these cases, it was found sufficient to subtract the spectra of the aluminium can and the D_2O weighed with their respective volume fractions. The volume fractions have to

be used because the measurement is always done on the same volume in the beam, not the same mass.

Background subtraction from the data of vesicles and emulsions using the diffraction patterns. For the samples of single bilayers and monolayers [F], there is much less phospholipid in the sample and it was found in these cases that this procedure is not accurate enough to ensure that the background contributions are much smaller than the one of the phospholipid. Reasons for this inaccuracy can be the uncertainties regarding sample composition and volume that have been discussed in sections 3.1 and 3.3, respectively. Also the employed absorption correction is not accurate because it does considers neutrons after a second scattering process as absorbed. In the present samples where a second scattering process is much more probable than absorption, a thorough treatment of multiple scattering effects would be necessary which is not available.

An alternative approach is to use features in the data themselves to determine the contributions of the different components to the total scattering signal [222]. The diffraction patterns of the vesicles and emulsions show very clearly the peaks contributed by the DMPC at 1.5 $Å^{-1}$, the D_2O at 2.0 $Å^{-1}$, and of the perdeuterated hexadecane (dHD) at 1.4 $Å^{-1}$. It was therefore possible to use the diffraction patterns in order to determine how much of the D_2O and dHD signals had to be subtracted in order to remove the corresponding peaks from the diffraction pattern [F].

This method is based on the assumption that the scattering patterns are added without regarding interference effects. This is true in the high Q regime above about 1 $Å^{-1}$ where typical distances below 1 nanometre are probed but it clearly fails at low Q where the layering of DMPC and water molecules and eventually also the droplets as a whole contribute to the coherent scattering signal as becomes visible in the large coherent structure factor maxima at Q values of about 0.1 and 0.2 $Å^{-1}$ (cf. for example figure 3.10).

In order to use this procedure to produce more than only qualitatively correct results, also a target scattering pattern has to exist which is used to fit the coefficients of the subtraction. In the current cases, the scattering pattern of fully hydrated DMPC was used after pro-rata subtraction of the D_2O signal as described before.

Background subtraction from the data of the suspensions currently not possible. For this procedure to work, it is also necessary that the scattering patterns and therefore the structure of the substances must be the same in the bulk and in the emulsion. Although this cannot be assumed for the hexadecane and water molecules close to the phospholipid molecules, most of them are far enough away from the interface to exhibit bulk properties as discussed in section 3.1. However, this requirement turns out to be the main problem for the treatment of the suspension sample data because the scattering patterns of the employed solid fat phases, protonated tripalmitin and perdeuterated tetracosane, are different in the bulk and the nanoparticular state as can be seen in figure 4.1. Therefore, it is not possible to subtract the signal of the bulk material from the one of the nanoparticle system. For this reason, the spectra of the suspension samples were not evaluated in this thesis.

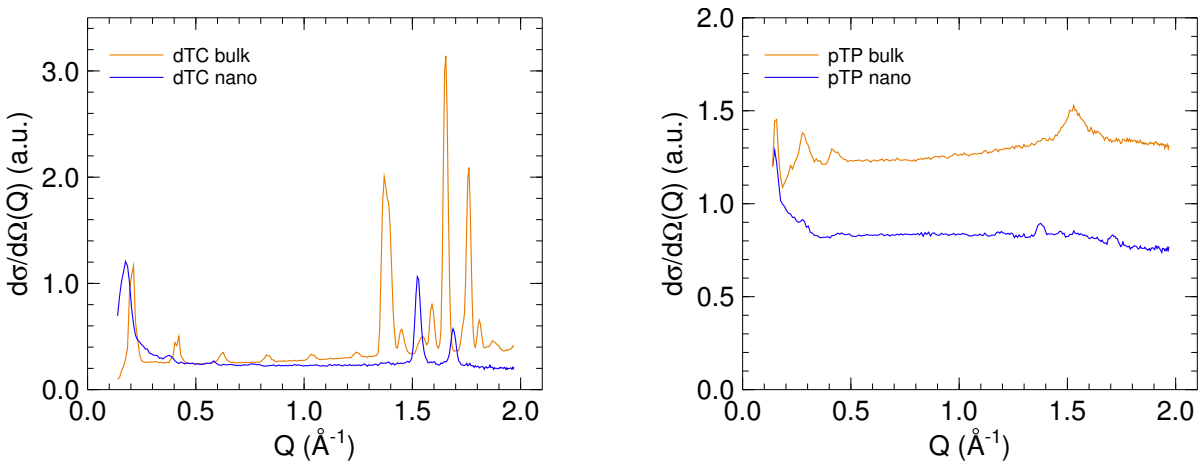

Figure 4.1.: Diffraction patterns of perdeuterated tetracosane (dTC, left) and protonated tripalmitin (pTP, right) as bulk samples (orange) and in nanoparticles (blue). It is obvious that the diffraction patterns of the bulk samples are different from the ones of the nanoparticles.

4.2. Finding the Mechanism of Diffusion with a Fit

Assumptions of fits. It is important to remember that the parameter values with their error bars that are extracted from a fit of a model to the data *are necessarily based on the assumptions*

- the data are correct
- the data error bars are correct
- the model is correct
- the difference between the model and the data can be expressed by a cost function such as χ^2
- the fit algorithm finds the absolute minimum of this cost function for the determination of the parameter values
- the fit algorithm determines the shape of the minimum of the cost function correctly for the determination of the parameter value error bars.

If any of these requirements is not met, the obtained results might not have anything to do with the description of the system or have a completely different value in reality. This uncertainty is *not* expressed in the error bars of the parameters which are defined only on grounds of the above assumptions [G, H].

In the following, each of these requirements will be discussed critically. Also the differences between the Levenberg-Marquardt (LM) algorithm and a Monte Carlo (MC) approach to perform the fit [G, H] will be discussed. Both of these algorithms aim to

find the minimum of the cost function. In the applications presented in this thesis, the quantity

$$\chi^2 = \sum_{i=1}^{N} \left(\frac{f_n - d_n}{\Delta d_n} \right)^2 \tag{4.2}$$

was used as cost function. In this equation, the distance between N data points d_n and the function values of the model f_n are added quadratically, weighed with the error bars of the data points Δd_n. This is a very common cost function which assumes that only the data have error bars – and only in the direction of the dependent variable. The validity of these will be discussed later.

Both, the LM and the MC algorithm, work on one solution candidate in parameter space in this thesis. Further developments like genetic or swarm algorithms which move a whole population of solution candidates simultaneously [223] were not used. These algorithms can provide advantages when searching for optimal values in very rugged cost function hypersurfaces but are not promising be superior to the versions working with only one solution candidate in the cases presented here.

The construction of the model makes assumptions about the data points. When a model function is created, several things are necessarily assumed: For example what the data actually measure or the energy transfer range in which the model is valid. That the data are not simply representing the scattering function of the substance under study can for example be due to multiple scattering [D] or an insufficient background treatment (cf. section 4.1).

In cases where the spectra of samples at low temperatures were evaluated in a large energy range (data *not* covered in this thesis), it was also observed that the correction of the detailed balance factor as described in section 4.1 has hardly any influence on the line shape and is basically invisible when looking only at the FWHM of the data. However, if the data are evaluated with a fit of the sum of a broad and a narrow Lorentzian, the small change in the wings of the data results in a different best fit of the broad Lorentzian which in turn can change the width of the narrow Lorentzian completely.

The choice of the fit range can influence the fitted results in surprising places: again first shifting some broad component of the fit, the results for the narrow component can be distorted, as well. For this reason, care was taken to use consistent fitting ranges for the fits presented this thesis and to mention them in the corresponding publications [B, D] to ensure reproducibility.

The error bars of the data have to be correct. In most cases, the samples scatter strongly enough to legitimate Gaussian error bars [G]. The error propagation through the data processing procedures is mostly straightforward – only during the re-binning into slices of constant Q differences between different computer programs are observed as discussed in appendix [I].

Using a least squares algorithm to maximize the likelihood that the fit represents the data implies that measurement errors occur only in the dependent variable [224]. Also in the evaluations presented in this thesis are the error bars in the direction of the energy

transfer ω and of the momentum transfer Q not taken into account. A way to consider these error bars of the independent variables Δx_i is to translate them into an error bar in the direction of the dependent variable Δy with the so-called *effective variance technique* [224–227],

$$\Delta y = \sqrt{\Delta d^2 + \sum_i \left(\frac{\partial f}{\partial x_i} \Delta x_i \right)^2} \,, \tag{4.3}$$

where Δd is the error bar of the measured point in the direction of the dependent variable and f is the fit function. Although it is known that the correct treatment of these errors is more intricate than this simple redefinition of the error bar, this formula is a good estimate of the result [228]. In the presented measurements, the additional contributions to the error bar were kept as small as possible: In the direction of the energy transfer ω, the spectra are sampled in very narrow intervals so that the corresponding Δx_ω is small. In the direction of the momentum transfer Q, the fit function does not exhibit big changes, i. e. $\partial f / \partial x_Q$ is small. These circumstances made it possible to use the statistical error bar of the data points Δd as a measure of the overall error and to use the standard fitting algorithms.

The «error bars of the model» have to be correct. Using a χ^2 minimization algorithm for the determination of the best fit to the data assumes that the fit function does not carry any statistical error bars. While this is certainly true for the model itself which is a mathematical function, it does not hold any more for the fit function after the numerical convolution of the theoretical scattering function with a vanadium measurement to account for the instrumental resolution: This step introduces the error bars of the vanadium measurement to the calculated curve. To the best knowledge of the author, these error bars are never regarded when fitting quasielastic neutron scattering data. In the following, a procedure is proposed which would allow to take the error bars of the model function into account. For the data evaluation used in this thesis, the standard approach was used which neglects these error bars. It is therefore also demonstrated that the error bars of the vanadium measurements used in this thesis are small enough to justify this approximation.

The probability that a data point d_n measured on some x scale with a Gaussian probability distribution function with standard deviation (error bar) Δd_n is correctly described by a value of a theoretical function f_n that has no error bar, i. e. that is a δ function, is given by [G, H]

$$\mathbb{P}(d_n \mid f_n) = \int_{-\infty}^{\infty} \mathrm{d}x \; \delta(x - f_n) \cdot \frac{1}{\Delta d_n \sqrt{2\pi}} \exp\left[-\frac{1}{2} \left(\frac{x - d_n}{\Delta d_n} \right)^2 \right] = \frac{1}{\Delta d_n \sqrt{2\pi}} \exp\left[-\frac{1}{2} \left(\frac{f_n - d_n}{\Delta d_n} \right)^2 \right] \,. \tag{4.4}$$

In the case that N data points should be described by the theory, one can extract the

quantity

$$\chi^2 = \sum_{n=1}^{N} \left(\frac{f_n - d_n}{\Delta d_n} \right)^2 \tag{4.5}$$

which is minimized during a fit.

However, the value of the fit function is in the presented cases not the theoretical one but its convolution with the vanadium measurement and it therefore has an error bar, as well. The numerical convolution of the theoretical function and the vanadium measurement is performed according to

$$g_n = (f \otimes v)_n = \sum_{m=1}^{N} f_m \cdot v_{n-m} \tag{4.6}$$

where N is the total number of measured points and f_n and v_n are the values of the theoretical function (without error) and of the vanadium measurement (with error bar Δv_n), respectively [D]. Using Gaussian error propagation, this results in a Gaussian probability density function for the point g_n with a standard deviation (error bar) of

$$\Delta g_n = \Delta(f \otimes v)_n = \sqrt{\sum_{m=1}^{N} (f_m \cdot \Delta v_{n-m})^2} \ . \tag{4.7}$$

The χ^2 is now somewhat half-heartedly redefined, taking into account that the fit values of the function changed but neglecting that also the error bars changed (from no error bar to some error bar) as

$$\chi^2 = \sum_{n=1}^{N} \left(\frac{g_n - d_n}{\Delta d_n} \right)^2 \ . \tag{4.8}$$

This definition is implemented in the standard data evaluation programs and was also used throughout this thesis.

A possibility to include the error bars of the fit function follows from the probability definition as in equation 4.4, exchanging the δ function of the theoretical value with the Gaussian distribution of the value of the fit function. Assuming that the data and the fit function have the same sign (usually they are both positive), one arrives at

$$\mathbb{P}(d_n \mid f_n) = \int_{-\infty}^{\infty} \mathrm{d}x \ \frac{1}{\Delta g_n \sqrt{2\pi}} \exp\left[-\frac{1}{2} \left(\frac{x - g_n}{\Delta g_n} \right)^2 \right] \cdot \frac{1}{\Delta d_n \sqrt{2\pi}} \exp\left[-\frac{1}{2} \left(\frac{x - d_n}{\Delta d_n} \right)^2 \right] = \frac{1}{(\Delta g_n^2 + \Delta d_n^2)\sqrt{2\pi}} \exp\left[-\frac{1}{2} \frac{(g_n - d_n)^2}{\Delta g_n^2 + \Delta d_n^2} \right] \ . \tag{4.9}$$

The cost function that the fit has to minimize is therefore

$$\chi^2 = \sum_{n=1}^{N} \left(\frac{(g_n - d_n)^2}{\Delta g_n^2 + \Delta d_n^2} \right) \ . \tag{4.10}$$

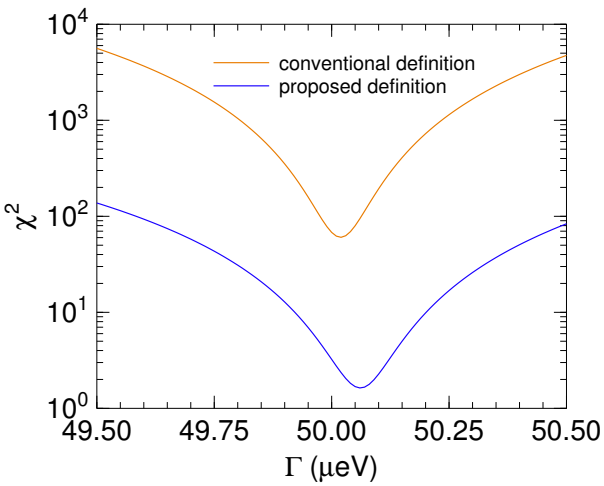

Figure 4.2.: Comparison of the χ^2 landscape in the direction of the line width Γ when fitting a single Lorentzian with fixed amplitude and centre position to toy data. It can be seen that the value of Γ where χ^2 reaches its minimal value varies by less than 1‰.

In order to demonstrate the difference between the two different definitions of χ^2 given in equations 4.8 and 4.10, a toy example was constructed by convolving one Lorentzian with a vanadium measurement and adding random noise as a «data set». The amplitude of the Lorentzian was chosen such that the signal-to-noise ratio was the same as in the case of the real measurements, the half width at half maximum was set to $\Gamma = 50\,\mu\text{eV}$. In a next step, the two χ^2 were calculated for the convolution of a Lorentzian with varying line width and the vanadium measurement. The result, shown in figure 4.2, shows that the best fit, i. e. the minimal χ^2 is achieved at very similar values of Γ. It can be concluded that the good statistical quality of the vanadium measurements makes the conventional approach to calculate χ^2 a valid approximation.

Is the model correct? This somewhat ill-posed question can be either expressed by saying «all models are wrong but some are useful» [229] or «models are never wrong, they are just more or less appropriate» [230].

Regardless of the formulation, a model has to reproduce the scattering function at every value of Q and the Q-dependence of its parameters has to follow the theoretical prediction (linear, quadratic, ...). In some cases, it is completely obvious that one model fits the data better than another [F] but generally it is not straight-forward to decide if the fit reproduces the data – due to the error bars of the data (and the fit, as discussed above).

It is therefore necessary to define a quality criterion that makes it possible to judge the quality of the fit – and to compare different fit functions. χ^2, the sum of the squared distances between the data and the fitted function as shown in equation 4.5, is minimized during the fitting process. A smaller χ^2 designates a closer agreement between data and fit. It is however obvious that this quantity cannot be a valid base for comparison of two models with a different number of parameters.

In the spirit of Ockham's razor, this is avoided by either taking the *reduced* χ^2, χ^2 divided by the numbers of degrees of freedom (which equals number of data points minus the number of parameters) in the Levenberg-Marquardt (LM) approach – or by the explicit sampling of the χ^2 hypersurface in the Monte Carlo (MC) approach, as will

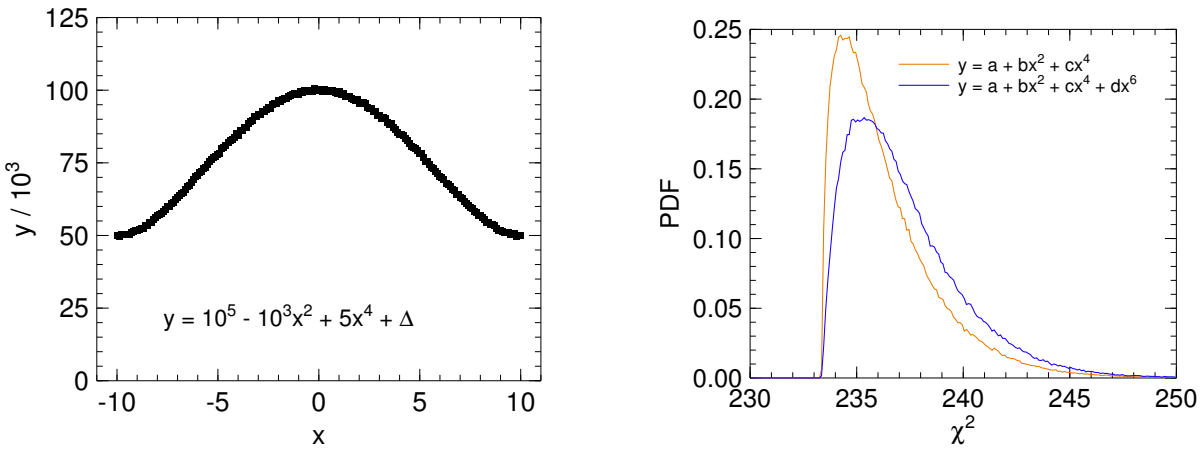

Figure 4.3.: An example for model selection. Left: A polynomial with powers of x 0, 2, and 4, evaluated at 201 points. Gaussian distributed noise (centered around zero) was added, the width of the Gaussian was given by $\sqrt{y}$ as in a counting experiment. Right: The comparison of two possible fit functions: the first with powers of x 0, 2, and 4; the second with 0, 2, 4, and 6. The minimal χ^2 of the model with more parameters is somewhat lower but the maximum and the mean of the probability density function (PDF) is clearly at higher χ^2, showing that the additional parameter is not supported by the data.

be discussed in detail later. Introducing a new parameter into a model will necessarily decrease the minimum χ^2 – but only if it also decreases the *mean* χ^2 or the one with the maximum probability, this parameter is considered to be justified by the data.

An example of such a model selection is shown in figure 4.3, using a simple polynomial. Synthetic data were produced by evaluating the polynomial, adding a Gaussian distributed noise as if the data were obtained in a counting measurement, and setting the data error bars accordingly. This approach was also used for the comparison of different models for the long-range motion of phospholipid molecules [B].

Does the cost function χ^2 represent the model accurately? One difficulty can arise from fitting the histogram $S(Q,\omega)$ with a function as it is normally done. As the data are binned into intervals of Q and ω, it can happen that very narrow components of the fit function disappear between two data points. This is for example the case for a δ function in energy – if it is not positioned at the same place as a data point, it is invisible in the cost function. The normal solution for this problem is to distribute the δ function on the two neighbouring channels.

Errors can also occur when convolving the theoretical model with the instrumental resolution before fitting it to the data [C, D]. One problem is the shortcoming of the vanadium measurement to represent the instrumental resolution. The measurement does not capture the dependence of the resolution on the energy transfer and there is experimental background in the measurement, partially caused by phonons in the vanadium, which is not part of the instrumental resolution. While these points were found

to have only little impact on the evaluation of the data presented in this thesis, there is also a very intricate effect which is caused by the discrete sampling of the theoretical function at the points where the instrumental resolution is determined. As this effect has a visible effect on the data evaluation, it is introduced in the following.

The numerical convolution of the fit function with the vanadium measurement according to equation 4.6 brings about that the fit function is only evaluated at the sampling points of the vanadium measurement. This is unproblematic as long as the value of the function at this point is representative for the whole bin. If the curvature of the fit function is very large, this requirement is no longer fulfilled. A rule of thumb for Lorentzian fit functions was found in the frame of this thesis [D]: the convolution produces erroneous results if the model function has a FWHM below the distance between two points. This was discovered when evaluating very slow motions of protein hydration water [C] which had previously been found to exhibit a line width that narrows drastically with decreasing temperature at high temperatures and then apparently changes to a nearly temperature independent width at low temperatures [105].

Does the fit algorithm find the absolute minimum of the χ^2 hypersurface? Finding the absolute minimum of the χ^2 hypersurface corresponds to finding the optimal parameter values [G, H]. An analogue physical system would be a melt of a somewhat complicated substance that is cooled. The absolute minimum of the energy hypersurface corresponds to the single crystalline state, many local minima around correspond for example to amorphous or polycrystalline structures.

The LM algorithm will only find the bottom of the χ^2 valley in which it was initialized because its steps can lead only downhill in the χ^2 hypersurface. This means that the fitted solution can be very far off the best fit if the initialization values are poorly chosen. The physical analogue is to quench the melt to zero temperature – often, the system will get stuck in an amorphous state and not form a single crystal. This problem is mostly circumvented by human guidance of the LM fit by choosing suitable parameter values or by using a more advanced algorithm.

Of these, MC algorithms provide an elegant solution: They explore the parameter space and can also go uphill in the χ^2 hypersurface. Therefore, they can easily include the possibility to jump from one valley to the next, eventually ending up in the global minimum, even if initialized far away. The physical analogue here is to cool the melt slowly to facilitate crystallisation.

Does the fit algorithm determine the shape of the minimum of the χ^2 hypersurface correctly? The second drawback of LM algorithms is on first sight a smaller one but turns out to be the relevant in the present case: they assume that the parameters are not correlated and the χ^2 depends quadratically on all parameters near the best fit. This assumed quadratic dependence corresponds to a Gaussian probability distribution of the parameter around its best fit value. While this does not influence the parameter values of the best fit, it gives wrong – usually too small – parameter error bars [G, H].

Error bars given by LM algorithms are the standard deviation σ of the assumed

Gaussian distribution of the fitted around the true value. Due to the direct sampling of the parameter space in the MC approach, the results are rather given as explicit probability distribution functions (PDF). From these, it is then possible to extract an error bar which also reflects correlations between the parameters, for example by taking the interval of the PDF which encloses 68% of its area which would be the normal definition in the case of a Gaussian PDF. These error bars can also be asymmetric, in contrast to the ones obtained with LM.

4.3. Model-free Determination of the Mobility

The motions of the molecules cause a re-distribution of the scattered intensity of neutrons with respect to the energy transfer: Whereas a static sample scatters neutrons only elastically, periodic motions decrease the elastically scattered intensity in favour of rising inelastic bands and aperiodic motions cause a broadening of the elastic line.

Simply looking at these features and comparing them between different samples or different temperatures can give valuable information. This has been successfully done by measuring the full width at half maximum (FWHM): a smaller FWHM corresponds to a smaller mobility of the molecules. This type of data evaluation does not allow the validation of a special molecular model of the molecular motions but gives a reliable characteristic of the spectrum, corresponding to the general *mobility* of the molecules.

Even if the amount of sample is too small to allow the exact determination of the line shape, it is often still possible to extract the FWHM. Therefore, this method was used to evaluate the dynamics of the monolayers on emulsion droplets which could be measured only with poor statistics because of the small fraction of the signal intensity that is caused by the phospholipid molecules.

Evaluating the Q-dependence of the scattered intensity. When the scattered neutron intensity is low, either due to the neutron flux or the amount of sample, so-called *elastic scans* are often used [231–233]. In these, the line shape in energy direction is not resolved but only those neutrons are counted that are scattered within an energy transfer that cannot be distinguished from zero within the instrumental resolution. It is then possible to compare the Q-dependence of this intensity as a function of the temperature or between different samples. Without any model for the motions, it can be stated that a stronger Q-dependence corresponds to a bigger mobility of the scatterers on the observation time scale. It is also possible to introduce a model for the motions and extract the mean-square displacement of the scatterers.

This procedure was extended and an explicit detection of the time evolution was introduced by combining measurements with different energy resolutions, corresponding to different observation times [234].

The point measured at zero energy transfer contains always contributions from neutrons which have been scattered with energy transfers within the instrumental resolution. It is therefore also possible to work with a fixed resolution and integrate the scattering signal afterwards over varying energy transfers. Due to the Gaussian shape of the resolution

function, this integration could be called an «error function transform» which is very similar to the normal cosine transform used in Fourier transforms. The error function and the cosine are in fact very similar to each other, up to only a few percent in the relevant range.

It was however concluded that this method to evaluate the molecular mobility is not suited for the samples used in this thesis. The first reason is that although they share the problem of a low amount of the substance of interest in the beam with other studies [234–236], these previous samples were pure substances and were therefore evaluated without any major background subtraction. In contrast, for the composite samples used in this thesis, subtraction is of major importance. It is clear that a method which relies solely on the intensity in a single point is especially sensitive to uncertainties in the background subtraction.

The second reason applies also to the multibilayer samples where the background subtraction is less important: The phospholipid samples studied here do not always have the same structure. Not only the phase transitions but also the additives change the molecular arrangements. As the coherent scattering is sensitive to changes in the structure of the molecules, this can result in intensity shifts (cf. section 3.1). Such an effect would wrongly be attributed to changes of molecular motions.

Evaluating the ω-dependence of the scattered intensity. The line shape of the scattering function carries much more information about the motion of the scatterers than only its highest point. A model-free characterization of the line shape can be attempted by two approaches: The first one is to calculate the Fourier transform of the sample spectra and the instrumental resolution, eliminating resolution effects by dividing the Fourier transform of the data by the one of the instrumental resolution, and evaluating the resulting intermediate scattering function. While this is the method of choice for the direct comparison of molecular dynamics simulations and experiments [154], it did not show any practical advantage in the present data evaluation.

Therefore, the second approach was employed: extracting the full width at half maximum (FWHM) of the sample and the vanadium measurement, subtracting the width of the instrumental resolution from the one of the sample data, and using the remaining broadening as a measure of the dynamics in the sample.

Background contributions which have a sharp peak at zero energy transfer can distort the FWHM as shown in figure 4.4 because they decrease the value of the maximum but not of the points at half height. These contributions can be caused by solid substances. In contrast, a flat background of the same height disturbs the signal much less. In the case of multibilayer samples, vesicles, and emulsions, the FWHM is therefore only possibly distorted by an incorrect subtraction of the empty can as it is the only solid component in the system. The other components of the samples, liquid hexadecane and D_2O, are much less problematic because their spectra are broad lines with respect to the energy transfer. Due to the variances in the sample composition discussed in section 3.1, the contributions of hexadecane and D_2O are less well known than the one of the aluminium can. It is therefore advantageous that these uncertainties do not influence the result very

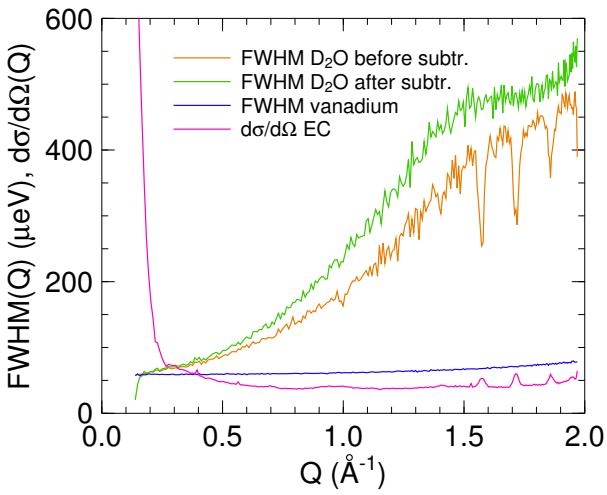

Figure 4.4.: The FWHM of a measurement of D_2O before and after the subtraction of the scattering function of the empty aluminum hollow cylinder (EC), together with the FWHM of the measurement of the vanadium standard for the determination of the instrumental resolution. Also shown is the intensity scattered by the EC. It can be seen that the three (forbidden) Bragg peaks of the aluminium, albeit small, leave a characteristic trace in the FWHM.

much.

The interesting quantity is the FWHM of the scattering function $S(Q, \omega)$ of the sample. However, this is always measured convolved with the instrumental resolution which can be measured separately using a vanadium standard. Unfortunately, a direct deconvolution of the data to access the scattering function is not applicable with standard methods because the level of noise becomes very high after the deconvolution. This might change in the future with more advanced deconvolution techniques [237].

Therefore, the following procedure was applied: The FWHM of the vanadium measurement and the FWHM of the sample measurement were extracted. In order to see how much the sample signal broadens the measured line on top of the instrumental resolution, the FWHM of the vanadium measurement was subtracted from the one of the sample measurement.

In order to check if this procedure can measure the width of the broadening, a toy example was evaluated: A Gaussian with width σ was convolved with Lorentzians with half widths at half maximum Γ between $10^{-1}\sigma$ and $10^{1}\sigma$. It can be seen in figure 4.5 that the result of the subtraction method is nearly proportional to the true value of Γ and does never deviate more than a factor 2. The real spectra that were evaluated with this method have full widths at half maximum of 2σ or less [E, F]. It can be concluded that the observed widths are about a factor 2 smaller than the real values and that there is a small distortion because this effect gets weaker as Γ increases.

These systematic errors introduced by the evaluation method were eliminated by normalizing the extracted widths to the one of a standard, the width of pure DMPC, which was obtained with the same method. These data points were then averaged over all values of Q which resulted in a quantity that was termed the *relative mobility*.

Limits of the model-free approach. As noted before, the approach to extract the FWHM works more reliably than to fit a model with several components to the data. However, it fails if the spectra contain sharp peaks in the energy direction, caused by solid substances in the beam, as is also visible in figure 4.4. This is the case for the suspensions because the dispersed fatty phase is solid. The contribution of this solid

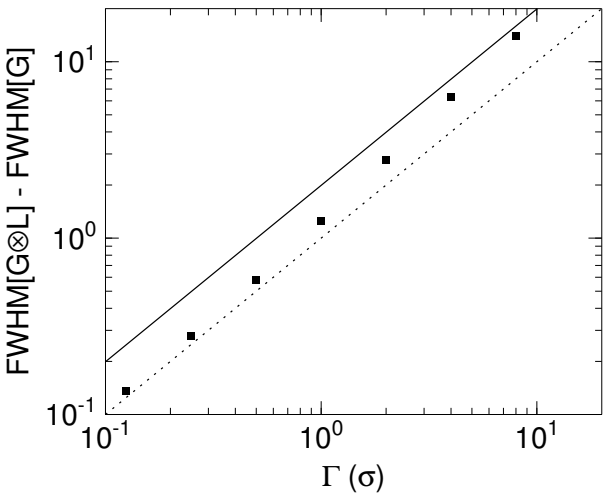

Figure 4.5.: A Gaussian with a standard deviation of σ was convolved with a Lorentzian with different half widths at half maximum Γ. The FWHM of the resulting profile was determined and the FWHM of the Gaussian was subtracted. Also shown are a solid line for the case that the result of the subtraction is equal to Γ and a dotted line if the result is equal to $\Gamma/2$.

substance is practically impossible to determine and can not be subtracted reliably as described in section 4.1. Therefore, the dynamics of the phospholipid in the suspension samples cannot be evaluated with this method.

The thought behind the model-free evaluation of the data is partially that it should be possible to characterize the mobility of the particles without knowing their exact mechanism of motion, e. g. without knowing if the particles are performing flow-like motions or diffusion. However, it is not possible to link the FWHM $\Delta\omega$ with a simple quantity like the mean-square displacement independent of the type of motion of the particle because the distance a particle covers during $t = 1/\Delta\omega$ depends on that type of motion: A particle diffusing with diffusion coefficient D would escape from a sphere with radius r

$$\Delta\omega = 2D \cdot Q^2 = \frac{6D}{r^2} \qquad \Rightarrow \qquad \sqrt{r^2} = \frac{\sqrt{3}}{Q} \tag{4.11}$$

whereas a particle flowing with velocity v would escape from a sphere with radius r

$$\Delta\omega = 2v\sqrt{2\ln 2} \cdot Q \qquad \Rightarrow \qquad r = tv = \frac{v}{\Delta\omega} = \frac{1}{2\sqrt{2\ln 2} \cdot Q} \quad . \tag{4.12}$$

The corresponding formulae that determine the two FWHM are given in section 4.2.

This brings about that a change of the mechanism of the motion (for example from a flow motion to a diffusive motion) can be misinterpreted by this simple method as a change of mobility, even if the particles would take the same time before and after to escape from a sphere with the same radius.

In the following chapter, the results that were obtained with these data evaluation procedures are presented and discussed. The chapter after that one will then propose how the data evaluation techniques could be further improved in the future.

Chapter 5.

Results and Discussion

After describing some methodical studies and enhancements that lay the base for the data evaluation in this thesis, the dynamics of the phospholipid molecules studied with quasielastic neutron scattering will be presented in this chapter in several stages: first, the motions in pure DMPC systems are evaluated in detail so that an in-depth model of the motions can be obtained. Then the influences of several additives are studied, among them the biologically important cholesterol and sodium glycocholate which is used in pharmaceutically relevant systems. Knowing the influence of the additives on bilayers of DMPC, the last step is to compare this behaviour to the one in monolayers of the stabilizer situated on an emulsion droplet.

Following the change in mobility from the pure DMPC over the mixed state with additives to the emulsion systems is possible in a model-free data evaluation without any assumptions. These results are therefore valid independently from the intricate analysis of the motions of the pure phospholipid.

5.1. Methodical Enhancements

The study of the phospholipid motions over the full pico- to nanosecond regime presented in this thesis is challenging for both, the instrument and the data evaluation. In the following, four methodical points are presented where contributions to the state of the art could be made.

High-resolution measurements are possible with time-of-flight spectroscopy. In order to study the long-range motion of phospholipid molecules on a nanosecond time scale, the energy resolution of the neutron scattering spectrometer has to be on the order of few µeV. It was possible to push the length of the observation times at TOFTOF up to the territory of other high-resolution neutron spectroscopy methods, especially backscattering spectroscopy. In the frame of this thesis, the probably best-resolved measurement on a neutron time-of-flight spectrometer has been performed, with an instrumental resolution of only 2 µeV (FWHM) as shown in figure 5.1. The instrumental settings were an incident neutron wavelength of 18 Å, chopper rotation speed 16000 rpm, and frame overlap ratio 10. The measurement time was 20 hours; the data evaluation was performed with the program Frida 1.

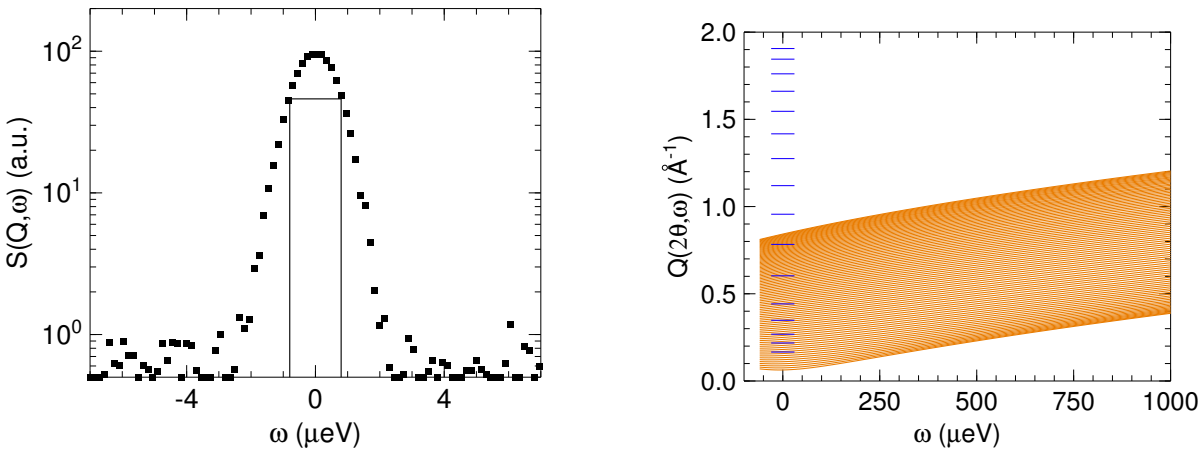

Figure 5.1.: The first measurement with an instrumental resolution of only 2 µeV at TOFTOF. Left: The spectrum of a vanadium sample at $Q = 0.1\,\text{Å}^{-1}$ with the FWHM shown in the figure. The signal-to-background ratio is about 100:1. Right: the corresponding dynamical range of TOFTOF (orange), compared to the one of the backscattering spectrometer SPHERES at the FRM II (blue).

With this measurement, it has been demonstrated that the long-existing gap of about one order of magnitude between the energy resolution of backscattering and time-of-flight spectroscopy is now closed. The two techniques feature complementary advantages: The backscattering spectrometer can measure to higher Q. However, at Q below approx. $0.6\,\text{Å}^{-1}$ where the resolution of the backscattering spectrometer is reduced, the time-of-flight instrument can extend the dynamical range to much higher energy transfers. This range of small Q is especially interesting for the study of long-range motions because small values of Q correspond to large distances in real space.

Measurements used in this thesis were routinely performed with a slightly relaxed energy resolution of 4 µeV in order to obtain shorter measurement times. It should also be noted that the instrumental settings used for the 2 µeV measurements were not within the specifications of the spectrometer. Further validation of this high-resolution mode is therefore needed in order to exclude the possibility that an error in the data analysis program accidentally produces the expected result.

The width of the time-of-flight bins must be adjusted to the expected line broadening. While the instrumental resolution gives the width of an elastic line, e. g. 4 µeV, the choice of the length of the time bins determines the distance between the points at which this line is sampled. It is clear that this sampling must be finer than the resolution to resolve this line – a common rule of thumb is to have around 10 points over the elastic line.

If the sample is static, the measured signal has the width of the instrumental resolution. If there are motions in the sample, the measured signal is the convolution of the instrumental resolution with the line shape of the sample, i. e. it is broader than the resolution. As the physical information is contained only in the additional broadening

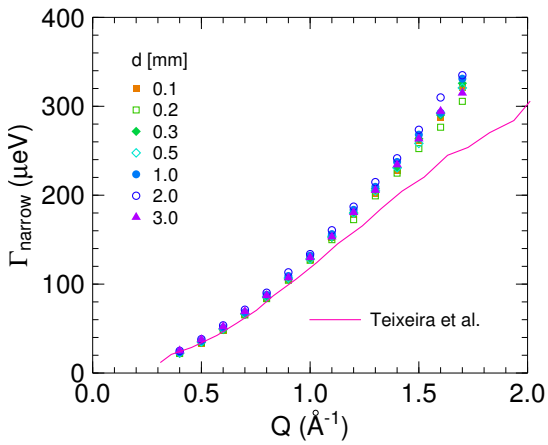

Figure 5.2.: The width of the narrow of two Lorentzians fitted to spectra of H_2O with different thicknesses as indicated in the figure [D], compared to the width of the narrowest of four Lorentzian lines taken from the literature [238] – all at 20 °C.

originating from the sample, the fit function is also convolved with the instrumental resolution before the result is fitted to the data as discussed in section 4.2.

For this convolution, the instrumental resolution has to be determined. This is normally done by the measurement of a static sample – either the sample at low temperature or vanadium. The theoretical fit function can then be either convolved with this measurement directly or with an analytic approximation of it. In the fits presented in this thesis, the theoretical functions were numerically convolved with the vanadium measurement itself.

It was demonstrated in the frame of this thesis [C, D] that the numerical convolution makes it necessary to adjust the choice of the bin width not to measured data or the instrumental resolution but to the theoretical fit function. If the distance between two points is not smaller than about half the width of the narrowest component of the theoretical fit function, this width is systematically distorted towards too large values.

Multiple scattering does not necessarily distort the line width of quasielastic neutron scattering spectra. For the measurements of pure DMPC in multibilayers, a very detailed line shape analysis was performed. In order to evaluate how multiple scattering of the neutrons can distort the spectra, a dedicated measurement of H_2O, a very strong scatterer, was performed. By varying the thickness of the sample, the amount of multiple scattering could be changed and its influence on the results of the data evaluation could be determined. As is shown in the corresponding publication [D], multiple scattering has hardly any influence on the evaluation of the long-range motion. This fact is also visible in figure 5.2 where the line width of the long-range motional component is plotted versus momentum transfer Q for different thicknesses of H_2O. It can be seen that all points basically superimpose on each other.

Another observation can be made in figure 5.2 by comparing the data points measured for this thesis with data from the literature [238]: In their evaluation, the authors used a model of the scattering function with one Lorentzian component more than in the present case [D]. The extracted widths show a weaker Q dependence than the data presented here which follow a Q^2 behaviour rather well [D]. It is not surprising that different models of the scattering function lead to different parameter values but it is interesting that a less detailed model of the scattering function tends to have a width that is closer to a Q^2

dependence. This trend can also be seen in previous measurements of the phospholipid dynamics: When the data quality did not allow a detailed line shape analysis [140], the line width was found to be proportional to Q^2. As different components could be identified in the scattering function, a more intricate model did not show this Q^2 behaviour any more [152].

Monte Carlo fitting techniques can give additional information. The assessment which of two models is a better representation of the data was an important factor for the determination of the mechanism of diffusion in phospholipid multibilayers [B]. Although it is also possible to get a measure for the quality of the fit from the «normal» Levenberg-Marquardt algorithm via the reduced χ^2, this procedure gives only correct results if the minimum of the χ^2 hypersurface is parabolic in all parameter directions and the parameters are not correlated. The Monte Carlo approach [G, H] used in the presented data evaluation [B] does not rely on any assumption because it samples the χ^2 hypersurface explicitly.

Furthermore, the results are not given as parameters with symmetric error bars (a consequence of Levenberg-Marquardt's assumption of a parabolic shape of the χ^2 hypersurface minimum) but as probability distribution functions. It is therefore also possible to see for example if the data determine only an upper limit to the line width.

The advantages of this approach in the current context were therefore the possibility of a model comparison without making any assumptions on the χ^2 hypersurface as well as determining the upper and lower limits of the parameter error bars explicitly.

5.2. Molecular Dynamics in Pure Phospholipid Multibilayers

The question «*how* does the phospholipid molecules move in the membrane?» became relevant again after MD simulations observed flow-like motions of transient clusters of molecules [150]. As the time scale of these simulations was on the same order of magnitude as the observation time of neutron scattering measurements, this observation should also give a ground that makes it possible to explain the neutron spectra consistently.

Whereas a simulation makes it easy to extract very special quantities, e. g. only the motion of the centres of mass, neutron spectra carry the averaged information of all scattering nuclei. In order to extract the long-range motion of the whole molecule, it is necessary to make a model that includes both, this long-range motion and restricted motions of the different parts of the molecule that are mobile but cannot move arbitrarily far away from the other parts.

It was attempted to describe the restricted motions of the phospholipid molecules by the models given in chapter 2.1 and all possible combinations thereof: Brownian oscillators with varying radii for the motions of the protons in the head and tail groups together with a background caused by vibrational modes with low energy. Although not statistically relevant, the fits including the vibrational background exhibited throughout

systematic deviations from the data and were in that regard inferior to the ones using only Brownian oscillators. In all cases, the extracted parameters for the mean-square displacement of the Brownian oscillator and for the level of vibrational background increased at low values of Q.

One could argue that a strict Q^2 dependence of the vibrational background can only be expected in perfect cubic crystals. The surplus contributions at low Q observed in the presented measurements caused by an increased amount of long wavelength vibrational modes which is a well-known feature in disordered systems. However, the deviations in the description of the restricted diffusive motions cannot be explained as appealingly.

This suggested that both effects are actually not physically motivated but rather an artefact. In a dedicated study, it could be shown that multiple scattering is indeed a plausible cause since it redistributes the intensity from the quasi-elastic region to a broad background, in first approximation independently of Q [D].

The corresponding decrease of elastically scattered intensity decreases the elastic incoherent structure factor (EISF) which directly translates into an increased mean-square displacement of the Brownian oscillator, cf. equation 2.13. The intensity of the signal caused by multiple scattering is roughly independent of Q but all influences of the sample on the spectra vanish as $Q \to 0$. Therefore, the influence of multiple scattering is mainly visible at small Q.

Therefore, the decrease of the EISF caused by the multiple scattering had to be accounted for. Using the fact that it is hardly dependent on Q, this can be achieved by introducing an overall scaling factor. However, this additional parameter is correlated with the parameters of the models.

For this reason, the confined motions were evaluated with the approximation that their scattering function is a sum of a δ function and only one Lorentzian, an approximation which was shown previously to be a very good description [239]. A more detailed evaluation requires the correction of multiple scattering effects.

The confined motions could now be described with two components: The head groups are assumed to perform a fast small motion in the very dense neighbourhood of the other head groups while the tail groups perform a slower and more extended motion in the hydrophobic core of the membrane [B].

In the following, the change of motions will be traced from very high temperatures downwards, also crossing the phase transitions.

Simple diffusive behaviour at high temperatures. At temperatures of up to 80 °C, i. e. far above the main phase transition, the spectra with an observation time of 55 ps can be described very well assuming that the head and tail groups perform their restricted motions while they diffuse with the whole molecule along the membrane [F]. This behaviour is expected and known from many liquids, e. g. alkanes [239].

As the temperature is lowered, the evolution of the dynamics can be followed via measures extracted indirectly via the fit of a model or directly from the data. Both methods show that the dynamics slows down as the temperature is lowered, exhibiting the expected Arrhenius behaviour [F]. The same behaviour has been previously observed

with the same technique in other liquids [239, 240] as well as with other techniques in the same system [131, 132, 143–145].

However, there are also differences to the macroscopic measurements [131, 132]: neutron scattering shows a lower activation energy of the long-range motion and a larger velocity. This was observed already before [136] and is due to probing vastly different time- and length scales. It had been explained with the free volume theory [129, 131] which assumes that the phospholipid molecules rattle in a cage of their neighbouring molecules from which they hop out from time to time. While QENS detects the fast rattling motion, the hopping events are the basic steps of the long-range diffusion which is then measured with macroscopic techniques.

The invalidity of these assumptions was shown by MD simulations [142–145, 150] which could be supported with the QENS measurements presented here. It should be noted that these neutron scattering measurements alone would be a weak base to formulate the new view of phospholipid motions that is presented in the following – however, they are in perfect agreement with the observations made in the simulations.

As the temperature is lowered towards the main phase transition, the motions become flow-like. The MD simulations had observed correlated, flow-like motions of the phospholipid molecules [150]. In these «flows», the single molecules do not diffuse independently from each other by a hopping mechanism out of the local cage but rather move together with the neighbours in a certain direction. Regions of flowing and resting molecules were spatially separated.

Exactly the same becomes visible in the neutron scattering data when the temperature is lowered towards the main phase transition (which is at 24 °C): the long-range motion can no longer be explained with the assumption of a simple diffusive motion but rather by flow-like motions [F]. This transition occurs at a certain time (about the persistence time of the flow events) which decreases with increasing temperature of the system. This explains the above mentioned transition of the spectra from diffusive to flow-like at a constant observation time of 55 ps when the temperature was lowered: While the persistence time of the flows was much shorter than the observation time at high temperatures, it increased as the temperature was lowered and the flows became visible in the spectra.

If the velocity of these flow motions is extracted from the measurements [B] and compared with the ones observed in the simulations, an astonishing agreement is found as shown in figure 5.3. This result is clear experimental support for the simulations.

Why was this behaviour not observed before in phospholipid membranes? There are several different answers to this question for the different techniques. From the experimental side, most measurements were performed on a much larger time- and length scale [129, 131, 132, 241] where the single flow events have averaged out: the mean-square displacement is the one of a random walk. Without direct evidence, the elementary steps of this process had been identified as the hopping of the molecules. Replacing this assumption with the novel view of small-scale flow-like events as the elementary step poses no inconsistency.

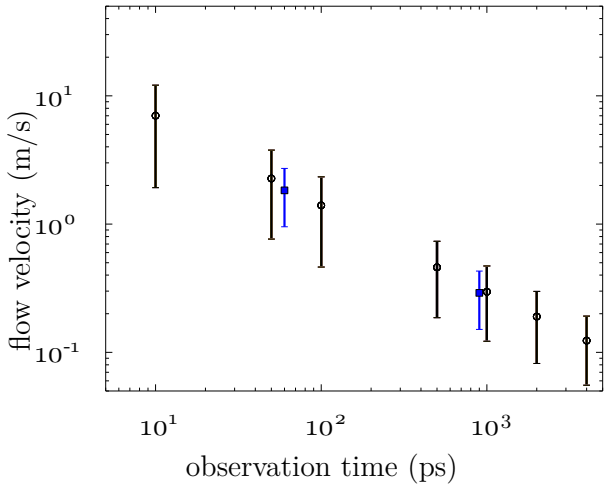

Figure 5.3.: The most probable flow velocity as a function of time. Shown are the results of an MD simulation [150] (black) and the here presented neutron scattering measurements [B] (blue). The error bars of the simulation values denote the velocity distribution in the sample whereas the ones of the measurement show the experimental uncertainty – the width of the corresponding Maxwell-Boltzmann distribution is directly given by the value of the most probable flow velocity.

Previous neutron scattering experiments [136, 140] had already found that the motions on a short time scale are different from the ones observed macroscopically but the data quality two decades ago was not sufficiently good to resolve the details of the long range motion. What appeared as a single Lorentzian in one study or as a combination of a δ function with Lorentzian wings in the other can now be recognized as a broadened function with Lorentzian wings [B]. Also in this case the previous data do not contradict the present interpretation.

One neutron scattering experiment has been set out to check if these flow-like motions are also visible in solid-supported single bilayers [203]. Direct evidence for the motions has not been found in these systems but it was also not possible to perform a consistent data analysis with another model. This is probably due to the very large background contribution of the solid support.

As far as the MD simulations are concerned, most studies concentrated on the mean-square displacement [63, 242] which is however known to be dominated by the restricted motions, especially of the flexible tails of the molecule [151]. Those studies which looked for a correlation of the motions between molecules also found it [137, 148] but the emerging flow patterns became obvious only by the «trick» to show the displacement of the molecules over a certain amount of time which emphasises the long-range motion [150]. This method had been well-known in the analysis of colloidal systems [243, 244] but was not previously used on phospholipid simulations.

It were also colloidal systems in which very similar effects had been observed before [84, 94, 243, 244] which have been termed *dynamical heterogeneities*. These flow-like motions where slow and fast regions are spatially separated in the sample have since then been observed in many systems, including normal liquids above their melting transition [93]. As the density of these systems increases (usually with decreasing temperature), the life times of the dynamical heterogeneities are found to increase.

Considering the phospholipid layer as a quasi two dimensional liquid, it is therefore by no means surprising to find the dynamical heterogeneities also here [E]. The densely packed head groups [11] are the limiting factors that determine the behaviour of the system. Comparing the change of area per molecule in the phospholipid membrane across

the main phase transition to the one of many elements (random close packing) [245], a very similar value is obtained. The density is therefore not exceptionally high which explains why the dynamical heterogeneities can be seen only on the microscopic scale. It is however impressive how close the flow patterns seen in molecular dynamics simulations of phospholipids [150] resemble the ones in two dimensional Lennard-Jones systems [246, 247] which indeed suggests that these flow patterns can be identified with dynamical heterogeneities [E].

As a last question, one can ask why the free volume theory was successful in describing the link between diffusion in phospholipid membranes with the free volume even when its basic assumptions are not met [142–144]. As a side note, concerns about the literal validity of these assumptions have been raised already in some of the pioneering works about the free volume theory applied to phospholipid membranes [131]. It is clear that a less densely packed membrane allows for more motion. Although the free volume is not spatially correlated with the mobility [120], it is needed to allow the collective particle motion [103]. While the precise connection between the amount of free volume and the collective motions is a matter of active research, it seems clear that there is a positive correlation between the two. So the free volume does not connect to the long-range diffusion by facilitating single particle jumps but by facilitating flow-like events. One could imagine that this erroneous assignment is the underlying reason for the discrepancy between the parameters of the free volume theory and the extraction of the quantities that these parameters are supposed to represent from other methods [145].

It is known that true two dimensional systems have a so-called *hexatic* phase between the solid and the liquid phase [248]. The particle trajectories in this hexatic phase remind of dynamical heterogeneities [243]. This poses the question if it has to be considered in the description of the phospholipid membranes, as well. However, dedicated studies found no evidence for a hexatic phase in phospholipid systems [249], in agreement with the observation that this phase appears only in nearly perfectly two dimensional systems [250] for which the phospholipid bilayers do not qualify.

Soft modes preserve limited local mobility below the main phase transition. Upon further lowering of the temperature, a clear first order phase transition is crossed at 24 °C [F] caused by the freezing of the chain groups into a crystalline order. At 16 °C, it is followed by another first order phase transition where the liquid crystalline structure changes [9].

The fast periodic vibrational motions visible in the inelastic part of the spectrum react as expected: The occupation of the relatively slow vibrational modes around 0.5 THz (2 meV) decreases upon solidification and approximately one order of magnitude faster modes (5 THz or 20 meV) are populated as can be seen in figure 5.4.

This part of the spectrum has been studied in detail before on oriented chain-deuterated DMPC [195]. That neither the there-found non-dispersive (optical) mode at about 14 meV nor the dispersive mode around 4 to 5 meV correspond to maxima in χ'' observed here is probably due to the different systems. However, also attempts with the same system as the original study could not reproduce these results due to background contributions to

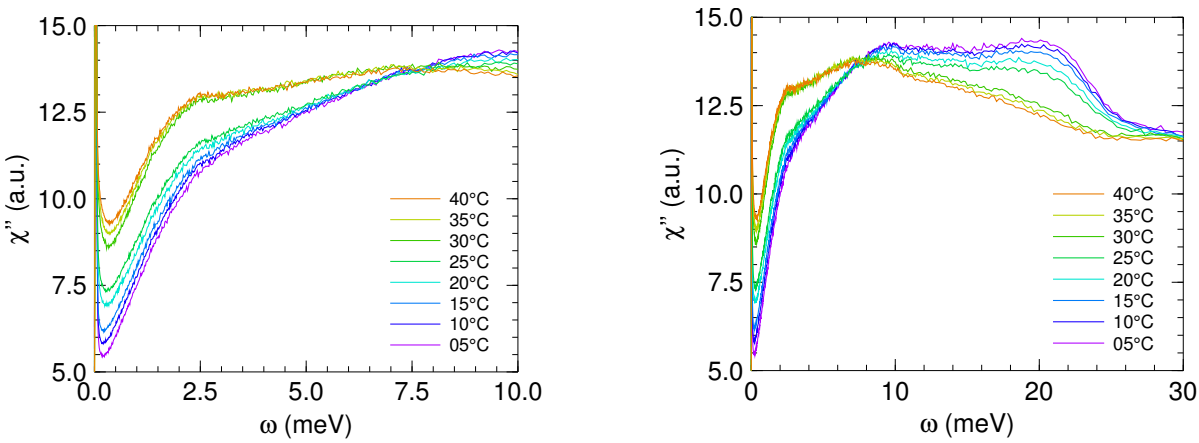

Figure 5.4.: The inelastic spectrum of fully hydrated DMPC. Shown are temperatures between 5 °C and 40 °C in steps of 5 °C. The scattering function was summed over all scattering angles and transformed to the imaginary part of the dynamic susceptibility χ'', dividing by the thermal Boltzmann occupation factor [D]. The main phase transition is clearly visible, in contrast to the pretransition. Upon melting, the membrane softens and the inelastic features move to substantially smaller energies.

the scattering signal that could be assigned to silicon phonons.[1]

Also the very slow aperiodic long-range motion seen with an observation time of 900 ps is influenced by the phase transition as expected: While there is long-range motion in the liquid state above the phase transition, it is frozen below the phase transition [B]. Following the motion of the phospholipids over 900 ps, one realizes that they are bound to their lattice position and cannot move arbitrarily far away from it, in agreement with macroscopic measurements [251].

Only the motion that is seen as the aperiodic long-range motion on the 55 ps time scale shows surprisingly little change when passing through the phase transition. Although there is a decrease of the velocity of the flow-like motions [B], they persist and show no signs of confinement on this time scale [D] – although such a feature was discussed to be visible in the first analysis [B], further investigation showed that it was only a fit artifact [C, D].

Also this feature is well-known from colloidal systems: In the crystalline state, they show very low energetic compressive modes, similar to longitudinal acoustic waves, which resemble the dynamical heterogeneities to a stunning degree on short time scales [116, 118, 243]. It was shown that the colloidal particles move with amplitudes that are about as big as the lattice spacing collectively with their neighbours before the restoring force brings all of them them back to their original positions – the motion of the particles relative to the cage of neighbours is rather small [243]. Given the short observation time of 55 ps and the small corresponding displacements of about an order of magnitude less than the lattice spacing, it is understandable that the confinement of the molecules is not yet visible [D].

[1]Marcus Trapp, Institut Laue-Langevin, private communication

5.3. Multibilayers of DMPC with Additives

After the motions of the pure phospholipid have been characterised, it was possible to study the influence of additives on the dynamics of the phospholipids. This is a first step towards biologically and pharmaceutically relevant systems. The characterization of these systems has purposefully been based on a much simpler and robust model-free data evaluation method than the one of pure DMPC multibilayers. The main reason for taking this approach is to make a subsequent comparison with the monolayer samples possible. The data quality of the phospholipid monolayers is not sufficient for a reliable fit of the model that was used to describe the pure DMPC multibilayers. An additional benefit of this model-free approach is that these results are valid independently of the correctness of the model used for the pure DMPC.

The influence of several additives on the mobility was extracted from the comparison of the FWHM of the samples with the ones of pure DMPC [E]. Of the studied additives, cholesterol, farnesol, myristic acid, and sodium glycocholate, cholesterol had the largest influence, decreasing the dynamics of the phospholipid molecules. The good miscibility of phospholipid and cholesterol made it possible to use much larger amounts of cholesterol than of the other substances, impeding a direct comparison of the influence of the additives at very high concentrations. The relative decrease of the phospholipid mobility was on the nanosecond time scale already about as large as on the millisecond time scale probed with other techniques [132]. The phospholipid molecules do not move very far during the short times observed in the present study, in particular only very few of them had the opportunity to interact with the cholesterol molecules directly.

The decrease of mobility can however be explained seamlessly in the picture of flow-like motions. If one regards the flow events in which the particles participate as the elemental steps of a random walk, one can connect the two by assuming either that the cholesterol decreases the speed of the flow events but leaves the length of such a flow event unchanged or that it decreases the length of a flow event while not changing the speed of the flow motion – or a combination of the two scenarios.

The mean-square displacement $\langle r^2 \rangle$ of a particle performing a random walk as a function of the time t depends on both, the time for a single step δt and the length of the step b as

$$\langle r^2 \rangle(t) \xrightarrow{t \gg \delta t} \frac{t}{\delta t} \cdot b^2 = t \cdot v \cdot b \tag{5.1}$$

where $v = b/\delta t$ is the velocity of the particle during a step. The two scenarios (decreasing v at constant b or constant v with a decreasing b) are therefore in the long time limit equivalent.

They are, however, different on a time scale that is shorter than the length of a flow event δt: If the flow velocity is decreased, the effect is also visible at short times; if the flow length is decreased, the effect should be less visible as the observation time is decreased.

The measurements of mixtures of DMPC with cholesterol show that the influence on the mobility is only a minor effect on the time scale of 55 ps while it is very visible on the 900 ps scale. In fact, the relative decrease of mobility compared to the case of pure DMPC

is on the 900 ps scale already nearly as large as on macroscopic time and length scales [E]. It can be concluded that the influence of cholesterol on the phospholipid dynamics is already nearly fully established on the 900 ps time scale.

In the picture of flow-like motions, this influence consists mainly of decreasing the persistence time of the flow events while not changing the flow velocities very much. This decrease is a smooth function of the cholesterol content, in contrast to early macroscopic measurements [131] but in agreement with subsequent macroscopic measurements [132] and MD simulations [142–144].

Comparing again with the dynamical heterogeneities found in other systems, exactly the opposite behaviour would be expected: an increase of the density results in an increase of the persistence time of the flow motions with a decrease of the flow velocity. That this is not the case here can be understood from the structure of the membrane: while the head group region of the phospholipids is the dense structure that governs the behaviour of the flows in the pure membrane, the cholesterol is mainly incorporated into the tail region of the phospholipids. This brings about that the density in the head group region is only little influenced. It also lets only a very thin part of the cholesterol molecule be present in the head group layer, hereby increasing the polydispersity here. An increase in dispersity was found to decrease the persistence length of dynamical heterogeneities [99] – this connection merits closer investigation in the future.

However, it should be noted that this model-based interpretation is taken from a data evaluation that was model-free on purpose. It should therefore in future works be backed up with a detailed analysis of MD simulations that can be validated with the neutron scattering data.

Of the other additives, sodium glycocholate is the most interesting in the current context because it is also used in drug delivery systems. It was found to slightly increase the dynamics of the phospholipids at a temperature of 20 °C and reversing this effect to a slight decrease at the studied temperatures of 30 °C and 40 °C [E].

5.4. Single Bilayers and Monolayers

The data of single bilayers and monolayers were evaluated with the same model-free approach as the multibilayers of DMPC with additives introduced before.

Vesicles are hollow spheres of single bilayers. The big difference to the multibilayer samples is that they are more or less strongly curved – the curvature has been found to play a role for vesicles with a diameter of less than about 100 nm [252]. The mobility of the molecules increases slightly with increasing curvature [F] which can be attributed to the increasing packing frustration in the bilayer.

The dynamics of the phospholipids in the pharmaceutically relevant systems is not only of importance for the drug release properties but also for the storage stability, e. g. the stability of the emulsion droplets against coagulation. One prominent example is the production of suspensions via melt extrusion: During the production at high temperatures, the fatty phase is liquid and the particle a spherical droplet. At low temperatures, the fat crystallizes and changes its form drastically to a platelet. While

pure DMPC is not capable of keeping the particles from coagulating during this transition, a mixture of DMPC and sodium glycocholate can [55, 56].

The important length and time scale for such a collision of two particles can be estimated on the example of emulsions with a volume fraction of the dispersed phase of typically 10%. With a droplet diameter of 130 nm, the mean surface to surface distance is very close to 100 nm. The droplets diffuse in the water and collide – the time scale between two collisions can be estimated with

$$\langle r^2 \rangle(t) = 6 \frac{k_\mathrm{B} T}{6\pi\eta R} t \tag{5.2}$$

to the order of 1 ms. In this light, measuring the dynamics on a sub-nanosecond scale might seem not directly relevant. In the case of cholesterol, the relative slow-down observed on this short time scale was already very similar to the one on a macroscopic scale which was only slightly more pronounced.

The mobility of the phospholipids on the emulsion droplets was found to be faster than in the multibilayer samples. It increases as the density of the phospholipid molecules decreases [F]. This can be intuitively understood because the molecules can move more freely with less hindering by their neighbours. On this example, it becomes clear that there is no direct correlation between the mobility of the stabilizer and the stability of the emulsion: Samples with little stabilizer are less stable than samples with a large amount of stabilizer – which is also intuitively expected because the coverage of the droplets is better with more stabilizer.

Adding sodium glycocholate results in about the same increase of phospholipid mobility at 20 °C in multibilayers and in the monolayers around emulsion droplets. Having added sodium glycocholate, the density of phospholipid can be further reduced which leads to a further increase of the mobility [F].

Chapter 6.

Outlook

It was possible in this thesis to provide experimental evidence for the flow-like motions of phospholipid molecules that had been observed in MD simulations. Further, the evolution of the mobility on a pico- to nanosecond time scale under the influence of additives and in monolayers around emulsion droplets could be followed.

Both, the results and the tools presented in this thesis lay the ground for tackling further, related challenges. Some of these are sketched in the following.

6.1. Methodical Enhancements

A new generation of sample containers can make the subtraction of background contributions easier. Most of today's sample containers distribute the sample in a thin layer over a relatively large area of a few cm^2. This is owed to two reasons: first, the neutron flux at most instruments is distributed over this area and second, one wants to avoid that the neutrons travel a long time through the sample on their way from a scattering event to a detector which increases the probability to be scattered again or to be absorbed. However, both of these restrictions are currently being lifted: New focussing neutron guides will be able to deliver the neutron flux to a smaller area and new data reduction algorithms will be able to handle multiple scattering effects[1].

The current sample containers have some disadvantages: The thickness of sample and aluminium layers have uncertainties of about 10% in the neutron beam area due to the limited manufacturing precision and bulging of the containers. Because the manufacturing is very complicated, they are reused for different samples. The samples studied in this thesis are water-based and react therefore with the aluminium can. The reaction of the samples with the can causes differences in the scattering of the cans, depending on their history. This contamination of the can and the fact that not the whole can is in the neutron beam impedes a determination of the scattering contributions by the weights of the cans.

Differing amounts of sample in the beam or varying contributions by the container are a big challenge in the present case can be seen easily. The samples discussed here (presented in detail in chapter 3) have the following characteristics: They are heterogeneous mixtures of different substances of which only one is of interest. The part of the sample that is

[1] Joachim Wuttke, JCNS, private communication.

regarded as a nuisance can be as big as a mass fraction of 99 %. These background contributions are also measured as bulk samples and subtracted from the mixture. A very large part of the scattered intensity will therefore be subtracted which can amplify the uncertainties.

Finally, the design of the hollow cylindrical sample containers brings some additional problems: as viscous samples are filled in the outer container and then squeezed into the gap by pushing with the inner container, they are likely to de-mix if more and less viscous parts are present. The fluid part will go first into the gap, followed by the viscous part. Therefore, the sample composition in the beam is actually unknown. When squeezing in the inner container, it can also not be excluded that air bubbles are also trapped which may come out after the sample, replacing parts of it in the neutron beam.

It seems that all these problems could be avoided if one puts the traditional sample containers out of service. Instead, small compact single-use aluminium containers sealed with a cold-welded cover as used in differential scanning calorimetry could contain the sample. These small containers should be completely bathed in the neutron beam so that always the whole sample contributes to the scattering. The weight of the can would give a precise measure of the amount of sample and container in the beam and as every can is used only one time, no contamination effects would have to be expected. Additionally, the small time-of-flight differences in this compact geometry would even improve the resolution of the spectrometer. In contrast to the current containers, air in the sample can would not be a problem because the amount of sample in the beam can be determined by weight if the whole container is in the beam.

Challenges of this approach are that either the neutron flux on the sample is decreased or the divergence increased. However, the Q dependence of the scattering signal is in most analyses of quasielastic neutron scattering data far from being a limiting factor. Also, the compact form makes the correction of multiple scattering and absorption of scattered neutrons mandatory. The corresponding software is in the moment under heavy development so that this should also not be seen as a big hurdle.

The sample environment for moderate temperatures could be trimmed towards faster sample changes. When using the cryostat, the coupling of the stick to the cryostat is always much colder than room temperature. This does not only require care to prevent air from entering into the cryostat but also the sample stick has to be defrosted and dried from the condensed water. Combined with the time that is needed for a decrease of the activation of the aluminium or vanadium, a sample change in the cryostat needs about one hour. Compared to measurement times that can be also as short as one hour, this becomes a limiting time factor at modern neutron scattering instruments.

Flat sample containers introduce the additional problem that the orientation of their surface normal with respect to the incoming neutron beam is important. The current setup does not allow a relative reproducibility of much below 1° and a similar absolute accuracy which might be of minor importance, though.

These problems could be circumvented by an improved sample changing procedure in

which the new sample would be placed in an air lock. After reaching a low pressure, the old sample would be exchanged with the new sample in the cryostat using a manipulator. These measures would speed the sample change up dramatically.

Free data exchange would open the possibility to reanalyze existing data. Currently, data of neutron scattering experiments are hardly accessible to other researchers than the ones who conducted the measurement. This can be an obstacle for checking the results, as became visible during this thesis [C]: Previously presented results [105] were suspected to be an artifact of the data analysis. As the data were not available, a new measurement with another sample had to be performed although it would have probably been sufficient to reevaluate the existing data sets.

Data exchange is currently debated in may fields of science [253]. A few disciplines like astronomy [254] and biology [255, 256] take the lead in this regard. It is obvious that data without the details of the sample preparation are nearly useless in condensed matter physics while this issue is completely negligible in astronomy. Nevertheless, in cases like the one mentioned above where only the data evaluation and not the sample preparation is under scrutiny, free data exchange could prove profitable.

Data reduction software. The software that is currently used for the data reduction at TOFTOF deserves replacement, especially because of the numerous bugs in the program some of which are listed in the appendix [I]. With the presented package *sihl*, there is a functioning alternative which can serve as an immediate replacement until the Scientific Computing group at the FRM II implements a unified data reduction software for the backscattering and time-of-flight spectrometers. Due to its easily extendable object-oriented approach, *sihl* could even be the starting point for this project.

Although the current implementation of data with experimental errors in *chaste* is working, these parts can be replaced with the free and open *uncertainties* package [257] which might be faster. The determination of the time-of-flight of the elastically scattered neutrons will also be performed with a sub-pixel accuracy, using a spline interpolation between the data points. Care will be taken to not take the maximum of the scattered signal in time-of-flight space but in energy space. If sihl was in use on TOFTOF for a longer time, it would be rather straightforward to implement a graphical user interface for it in order to make it more user friendly.

Independently from the data reduction, the data correction for self shielding and multiple scattering in the sample should be tackled. The program that is currently developed for the correction of backscattering spectra[2] could be extended for the time-of-flight spectra. If only the quasielastic region of the spectrum is of interest, this extension should not require much time and effort.

Data analysis procedure. The various advantages of Monte Carlo fit algorithms were discussed in detail. The proposed scaling of the parameter ump lengths [H] which is

[2] Joachim Wuttke, JCNS

implemented in the program FABADA [G] will now be incorporated[3] into the Python package *PyMC* [258]. This will not only make it accessible to a broader user community but also facilitate the comparisons of different parameter jump adaption methods.

The algorithm itself is still based on two parameters that have to be manually adjusted to the problem at hand: The number of steps that are performed before the parameter jumps are adjusted and the cooling schedule of the simulated annealing. A further development of the algorithm would consist of an automated choice of these values.

A simple criterion for the automatic choice of the number of parameter steps could be used as an alternative to previously suggested methods [259]: the χ^2 hypersurface should be sampled until acceptance ratio p_i of the parameter i is defined «well enough» up to an uncertainty s for a meaningful comparison with the target value. Assuming that the acceptance ratio does not change considerably when the jump length is constant, the subsequent tries can be seen as success or failure in n independent experiments each of which has the probability of success p. If the acceptance is for example tuned towards $p = 33\%$ [G], «well enough» would be on the order of $s = 1\%$. Using the standard deviation of the binomial distribution, one arrives at $n = p \cdot (1 - p)/s^2$ which can be evaluated during the Monte Carlo run. With the given example of $p = 33\%$ and $s = 1\%$, this parameter should be varied on the order of 10^4 times before adjusting its jump length. A careful evaluation of the performance of this simple rule compared to the published ones [259] will be performed.

For the adjustment of the cooling schedule, it could be helpful to understand the χ^2 hypersurface as an energy surface and consider the analogy of a cooling liquid. The cooling schedule should then be adjusted such that the system is not trapped in any other than the single crystalline state but can relax to thermal equilibrium. One way to foster this relaxation is to keep the system ergodic so that it can sample all the available states. The ergodicity could be ensured using an idea from swarm methods [223] and take many independent configurations, i. e. parameter combinations which move on the χ^2 hypersurface. It is then possible to check if the time average is equal to the ensemble average which should be the case in an ergodic system. Alternatively, two-time correlation functions could be used to check if the system exhibits aging which would be another indication for non-ergodicity.

Another interesting subject matter is the analogy between the fit and a thermodynamical system itself. The temperature dependence of the relaxation time in glass forming systems is proposed to show an Arrhenius behaviour if the underlying energy surface is simple and a super-Arrhenius behaviour if it contains many local minima. χ^2 hypersurfaces can also be simple or ragged – does the relaxation time of the fitted parameters also show an Arrhenius or super-Arrhenius temperature dependence, respectively?

Once the fit reached the minimum of the χ^2 hypersurface, it essentially performs a random walk in a more or less harmonic potential – confer to the model of the Brownian oscillator used for the localised motions in the phospholipid. Whereas the Levenberg-Marquardt algorithm simply makes the approximation that the potential *is* harmonic, the Monte Carlo algorithm explores it explicitly and experiences all the deviations from a

[3] In collaboration with Jean-François Moulin, Helmholtz Zentrum Geesthacht

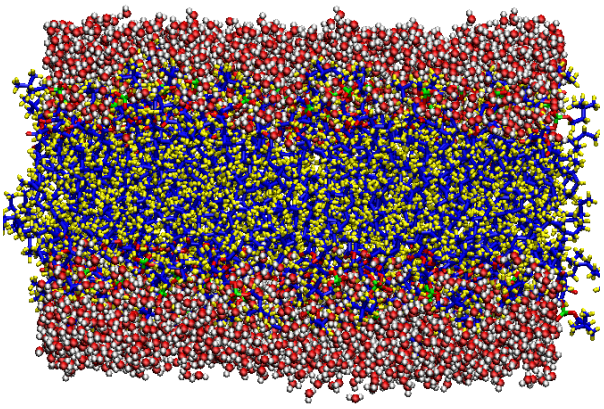

Figure 6.1.: Snapshot of an MD simulation of a fully hydrated DMPC bilayer at 25 °C. The shown simulation consists of 128 phospholipid molecules and 3654 water molecules which were equilibrated for a simulated time of 2 ns. The simulation was performed with the software NAMD2 using the force field CHARMM27, the bound lengths in this all-atom model were considered to be constant. Picture by courtesy of Jordi Martí.

harmonic behaviour that are present. The effect of an anharmonic potential on the mean-square displacement of the particle was discussed on the phenomenon of the so-called dynamical transition of proteins [233]. It would be interesting to see if the error bars of the parameters (corresponding to the mean-square displacements of the parameters) show a similar temperature dependence.

6.2. Molecular Dynamics in Pure Phospholipid Multibilayers

Closer link between measurements and simulations. The potential of the model-based data evaluation is probably exhausted with the model presented, given the quality of the data. More information should be accessible in MD simulations. In the moment, MD simulations from the literature were converted into a sensible model of which the long-range component showed excellent agreement with the one extracted from the neutron scattering data. However, a much more direct comparison would be possible when calculating the intermediate scattering function from the simulation. This could be compared over the full time range with resolution-resolved neutron scattering measurements which has already been proven to work perfectly in the case of n-alkanes.[4]

For this purpose, own MD simulations of a DMPC bilayer have already been started.[5]. A snapshot of this simulation can be seen in figure 6.1. After their validation against simulations from the literature and the QENS data, the properties of the fast and slow regions can be evaluated, checking the local density, short range order, four-point correlation functions, etc.

Coherent neutron scattering measurements could potentially provide further support to the idea of correlated motion of neighbouring molecules because it probes the pair correlation functions. In order to probe the correlations between neighbouring molecules, Q values around $2\pi/8\,\text{Å} \approx 0.8\,\text{Å}^{-1}$ and observation times in the nanosecond range would be needed. Although these values are at the limit of what can be seen at TOFTOF, a

[4]Humphrey Morhenn, Technische Universität München, private communication.

[5]In collaboration with Jordi Martí, Computer Simulation in Condensed Matter Research Group, Universitat Politècnica de Catalunya, Barcelona.

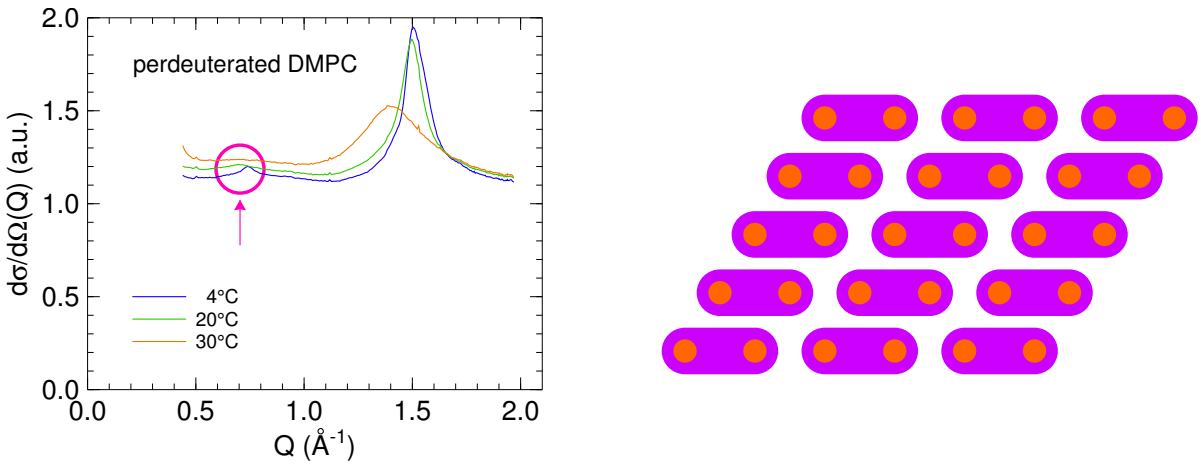

Figure 6.2.: Left: Diffraction pattern of fully hydrated perdeuterated DMPC after subtraction of the water contribution at different temperatures across the phase transitions. In the low temperature measurement, the chain correlation peak at 1.5 Å^{-1} is clearly visible, the small peak highlighted at 0.8 Å^{-1} is caused by the head groups. These peaks broaden significantly and shift to lower values of Q as the temperature is raised. The measurement at 30 °C is performed above the main phase transition – as can be seen from the chain correlation peak. Right: Sketch of the phospholipid molecules, seen from the top [10]. The big head group is shown in violet. The positions of the two chains which are facing away from the observer are shown in orange. It can be seen that the head groups form an orthorhombic lattice with a bigger lattice spacing than the one of the hexagonal lattice of the chains.

separation of coherent and incoherent scattering is here not possible in the moment. Unfortunately, the coherent scattering intensity of perdeuterated DMPC is very small at this position, only about 4% of the incoherent one as shown in figure 6.2. This was also observed in earlier measurements and simulations [206]. It is therefore questionable if an extraction of this signal would be possible even if a neutron spin analysis was installed at TOFTOF that would allow to suppress the incoherent scattering signal. For this reason, most coherent neutron scattering measurements that aim to characterize the correlation of in-plane motions resort to the chain correlations (visible in the peak at 1.5 Å^{-1} in figure 6.2) [137].

Comparison with a quasi-two-dimensional colloidal system Another interesting question is if this behaviour is indeed governed by the phospholipid head groups. This could be tackled by approximating the head groups with ellipsoids – with or without dipole moment – that are confined to two dimensions. From the MD simulation, one could further extract the probability distribution function of the orientation of the ellipsoids out of the plane and use this input parameter in the simplified simulation. If the flow-like motions are indeed caused by the dense packing in the head group area, they should also be visible in this simplified simulation.

6.3. Multibilayers of DMPC with Additives

Further evaluation of the data. The spectra of the mixed systems of phospholipids with additives have so far been evaluated only with the model-free approach [E]. Further information could be extracted either by using a model of the molecular motions or by using the data to validate molecular dynamics simulations. The model used successfully for the evaluation of the data of pure DMPC could be taken as a starting point for the model-based data evaluation.

Molecular dynamics simulations of phospholipids mixed with additives are state of the art. Especially cholesterol has received much attention due to its biological importance [142, 260–262]. Calculating the intermediate scattering function from both, measurements and simulation, would allow to validate the simulations. These simulations would then allow to study the evaluation of the flow patterns upon the addition of cholesterol in detail [E].

Parallels to binary colloidal systems. If the analogy to quasi two dimensional colloidal systems holds, the addition of cholesterol to the DMPC would correspond to add colloidal particles with a smaller size to the system under study. Binary colloidal systems have been used to study glass-forming systems [244, 263, 264] because they do not crystallize in a range of concentrations and ratios of radii. If this effect is related to the suppression of the main phase transition in phospholipids by cholesterol [265] has to be evaluated. From the viewpoint taken in this thesis, this seems rather unlikely because the main phase transition is caused be the tails of the molecules whereas the glassy behaviour is triggered by the densely packed head group area.

Regardless of the influence of cholesterol on the main phase transition of the phospholipids, it would be interesting to study the evaluation of the flow patterns upon the addition of smaller spheres. A decrease of the persistence length of the flow patterns with hardly any influence on the flow speed would be in line with the interpretation of the neutron scattering data [E]. Existing data of polydisperse mixtures seem to be in agreement with this view, exhibiting a decrease of the correlation length of dynamical heterogeneities as the polydispersity increases [99, 266, 267].

6.4. Single Bilayers and Monolayers

Preparation and characteristics of the phospholipid samples. It was found in this thesis that the surface occupancy of the emulsion droplets is an important factor for the mobility of the phospholipid molecules. In order to quantify the results further, the surface occupancy should be characterized in more detail. Three factors are probably of main importance: First, the losses of the different substances during the production. Second, the diameters of the emulsion droplets which are not monodisperse and can therefore have a different total surface. And third, the amount of phospholipid is present either as vesicles or as mixed micelles with sodium glycocholate. The two latter points

will be tackled by structural studies.[6]

More measurements of the dynamics in vesicles and emulsions. So far, the measurements have been performed only at a temperature of 20 °C, below the main phase transition of the phospholipids. This is the phase interesting for the storage of the drug delivery systems – future measurements should study the same systems also at a temperature above the main phase transition which would correspond to the situation where the drug delivery system is used in the human body.

The result is not completely trivial as it was seen in the case of DMPC multibilayers that the addition of sodium glycocholate causes contrary reactions: from an increase of the speed at 20 °C to a slight decrease at 30 °C and 40 °C [E]. However, it is expected that the addition of sodium glycocholate will reduce the density of the phospholipid in the interface by creating micelles. The reduced density will then again result in an increased mobility.

Concerning the mobility of phospholipid monolayers on emulsion droplets, the presented studies [F] were performed at 20 °C, corresponding to storage conditions. Comparing the dynamics with the one at 40 °C, corresponding to body temperature and above the main phase transition of DMPC, is certainly desirable.

Going further, the effects of oil viscosity and interdigitation of the oil molecules into the chain region of the phospholipids can be studied by varying the length of the oil molecules, the length of the phospholipid tails, and the temperature. Measurements on TOFTOF can be complemented with macroscopic measurements of a flat oil-water interface, for example with fluorescence microscopy.

These macroscopic measurements are expected to give better access to the solid fat-water interface because the solid substances do in this case not contribute an interfering signal as they do in the case of the neutron scattering measurements. It is known from such measurements that the phospholipid mobility decreases as the viscosity of the oily phase increases. Does this decrease continue to a complete arrest when the oily phase becomes a solid or are the phospholipids expelled from the crystal and become again more mobile on the surface?

Evaluating the data of the suspensions. It would also be interesting to extend the studies on phospholipid layers on solid lipid nanoparticles: are the phospholipid molecules still mobile if the fatty phase beneath is solid? However, this requires an understanding of the diffraction patterns of the nanoparticles before, cf. section 4.1. Measuring them also at high temperatures where the fatty substance is liquid in the droplets and in bulk allows to determine the amount of this substance in the suspension. If it is then possible to calculate the diffraction pattern of the nanocrystalline phase, a correct subtraction should be feasible.

As it was shown in section 4.1, the bulk substances have strong diffraction peaks at values of Q where the nanocrystalline samples have either only very weak ones or none at all. An idea might therefore be to subtract the spectrum of vanadium instead of the

[6] Martin Schmiele, Friedrich-Alexander-Universität Erlangen-Nürnberg

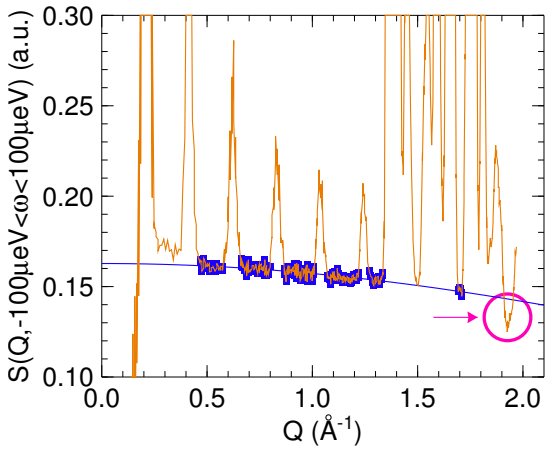

Figure 6.3.: The elastic scattering, integrated in a small region around the elastic line (at this resolution the FWHM is about 60 µeV) of perdeuterated tetracosane (orange). Also shown are the parts of the scattering that seem to contain only incoherent scattering and therefore lose intensity with increasing Q (blue points) according to the Debye-Waller factor which is shown as a fit of a Gaussian to these points (blue line). The region where the total scattering intensity falls below this assumed incoherent level is marked in red. The integration over the given energies was performed at constant scattering angles.

bulk fat. Both have a purely elastic peak, only the scaling of the vanadium needs to be adjusted to the level with which the nanocrystals scatter.

In first approximation, it will be assumed that the crystal is still well-enough defined so that only the incoherent cross section contributes the Q-independent background.[7] Then, the nanocrystalline sample and the bulk fat have to be measured above the melting temperature of the fat which makes it possible to determine the amount of fat in the suspension.

After determining this amount, the ratio between the Q-independent scattering of the fat in the bulk and the level of the vanadium measurement has to be calculated. Also this step is not trivial as shown in figure 6.3. The elastic scattering of perdeuterated tetracosane was divided by the one of vanadium. The measurements have not been corrected for a Lorentz factor because it should be the same for the incoherent scattering of vanadium and tetracosane, respectively. The vibrations in the tetracosane seem to be larger than the ones in the vanadium which leads to the Gaussian decay of the incoherent level with Q. While this can be fitted, the surprising feature is the drop of the scattered intensity below this curve at high Q of about 1.9 Å^{-1} which should not happen if the background is due to incoherent scattering. It should be noted that this dip is at the very end of the measured Q range so further measurements with a shorter neutron wave length are necessary before this feature can be confirmed and explained.

It is only possible to extract the contribution of the phospholipid molecules from the total scattering signal if the amount of phospholipid in the beam is precisely known. In order to enhance the precision of this determination, two factors seem especially worthwhile to improve: The first one is the determination of the fraction of phospholipid that is in the in the interfacial layer and the total surface of this interface. The second one is the certainty that the sample in the beam has the same composition as the one that was prepared which can be ensured by the full immersion of the sample and its container in the neutron beam.

[7] This will be analysed in detail in the dissertation of Martin Schmiele, Lehrstuhl für Kristallographie und Strukturphysik, Friedrich-Alexander-Universität Erlangen-Nürnberg.

In the case of suspensions, the amount of fatty substance in the sample can be determined from the diffraction patterns only if this substance is liquid, in the nanoparticular state as well as in the bulk. If the scattering pattern of the nanoparticles can be calculated, it should be possible to extract the phospholipid dynamics also from the suspension samples. However, this will always be a challenging task because the phospholipid dynamics is not the only narrow component in the spectra any more. For the multibilayer, vesicle, and emulsion samples, the background contributions are automatically separated in the spectra from the signal of the phospholipid which made the data evaluation more robust against small errors in the background subtraction.

Chapter 7.

Conclusion

This thesis aimed to study the molecular motions of phospholipid molecules in different environments. The traditional view that the molecules rattle in a cage of their neighbouring molecules and hop out of this cage from time to time had been challenged by molecular dynamics simulations. These suggested that the phospholipids formed transient clusters that moved in flow-like patterns. As neutron scattering is one of the very few experimental techniques that can probe motions on the pico- to nanosecond time scale that is important for these motions, it was employed to give experimental evidence for one of the opposing views.

It was indeed possible to find experimental support – for the novel view of flow-like motions in the membrane. In the quest for statistically relevant conclusions, the complete data reduction procedure was reimplemented which is now available also for other users of the spectrometer `TOFTOF`. The evaluation of the data was performed with a new program that explicitly samples the parameter space which is compatible with the data. It could be shown with this approach that the model of flow-like motions fits the data.

This occurrence of transient clusters of molecules with similar motions and the spatial separation of fast and slow molecules was found to resemble a feature of glass-forming systems, the so-called dynamical heterogeneities. It was argued that the high density in the head group area is responsible for this similarity. The persistence of these flow-like motions on a picosecond time scale below the main phase transition of the phospholipid was interpreted as localized soft modes, another behaviour known from glass-forming systems.

Interestingly enough, also the old view of cages and hopping motions had been a (very successful) loan from glass physics at the time. Taking into account that this very simple idea has long been replaced with more elaborate concepts in glass physics, it can be suggested that the description of phospholipid membranes does profit from more adaptations of modern viewpoints in glass physics, as the one of dynamical heterogeneities.

Moving away from the systems containing pure DMPC, the influence of a few representative additives on the phospholipid dynamics was studied. Of special interest were cholesterol, a component of cell membranes, and sodium glycocholate which can be used as co-stabilizer of emulsions. Cholesterol decreased the mobility of the phospholipid molecules already on the nanosecond time scale by about the same fraction as on macroscopic time scales. This slowing down was tentatively explained by a reduction of the persistence length of the flow patterns, stimulated by corresponding observations in

colloidal systems.

Sodium glycocholate was not only added to the phospholipid bilayers but this mixture was also used to stabilize emulsion droplets. The distribution of the molecules on the surface of the droplets triggered an increase in the dynamics, probably due to a reduction of their density. This effect was clearly stronger than the influence of sodium glycocholate on the dynamics of the phospholipids. It seems therefore safe to conclude that the influence of sodium glycocholate on the pico- to nanosecond dynamics of the phospholipids is not the key to explain its boosting effect on the stabilizing properties.

A crucial step for the evaluation of the phospholipid mobility in stabilizer layers is the subtraction of the contributions of the other components of the sample which can amount to 99% of the sample mass. It was possible to remove the background contributions in the case of the emulsion samples after the identification of their contributions to the diffraction patterns. It is however exactly this step which impedes currently the evaluation of the suspension samples where the subtraction of the solid phase fails because the nanoparticles do not show the same diffraction pattern as the bulk. This problem will be solvable as soon as the diffraction patterns of the nanoparticles can be computed which is currently attempted.

Studying the dynamics of stabilizing phospholipid monolayers in suspensions is only one of many exciting possibilities for future projects. To name but a few examples,the employed data fitting techniques will be developed further and the comparability of finding the best solution in the parameter space with a crystallizing liquid will be explored. Molecular dynamics simulations and quasielastic neutron scattering measurements of pure DMPC as well as systems with additives will be dovetailed to yield further possibilities to characterise the observed flow patterns. Simultaneously, complementary experiments with quasi two dimensional colloidal systems would allow to analyse if the observed motions and their change upon the addition of co-surfactants are universally valid properties of densely packed systems or rather special properties of these molecules.

The new paradigm of flow-like motions in phospholipid membranes could be fostered with experimental data in this thesis. It is impossible to assess the importance of the presence of dynamical heterogeneities in these systems today. It will most certainly not be such a big leap forward as the introduction of the previous model of hopping motions, but it might prove to be another step towards a better understanding of the dynamical processes in phospholipid membranes.

Part II.

Publications

Appendix A.

List of Publications and Presentations

Listed are the publications and presentations that originated during the course of the thesis. The refereed publications with immediate relevance for the presented work can also be found in full text in the indicated appendices.

A.1. Refereed Publications

1. The Picosecond Dynamics of the Phospholipid Dimyristoylphosphatidylcholine in Mono- and Bilayers.
   Sebastian Busch, Luis Carlos Pardo, Christoph Smuda, and Tobias Unruh.
   Soft Matter, 8:3576, 2012.
   http://dx.doi.org/10.1039/c2sm07380c
   Included in appendix [F].

2. Differences in first neighbor orientation behind the anomalies in the low and high density trans-1,2-dichloroethane liquid
   Muriel Rovira-Esteva, Arul Murugan, Luis Carlos Pardo, **Sebastian Busch**, Josep Lluis Tamarit, Gabriel Julio Cuello, and Francisco Javier Bermejo.
   The Journal of Chemical Physics, 136(12):124514, 2012.
   http://dx.doi.org/10.1063/1.3697849

3. The slow short-time motions of phospholipid molecules with a focus on the influence of multiple scattering and fitting artifacts.
   Sebastian Busch and Tobias Unruh.
   Journal of Physics: Condensed Matter, 23(25):254205, 2011.
   http://dx.doi.org/10.1088/0953-8984/23/25/254205
   Included in appendix [D].

4. The influence of additives on the nanoscopic dynamics of the phospholipid dimyristoylphosphatidylcholine.
   Sebastian Busch and Tobias Unruh.
   Biochimica et Biophysica Acta (BBA) – Biomembranes, 1808(1):199–208, 2011.
   http://dx.doi.org/10.1016/j.bbamem.2010.10.012
   Included in appendix [E].

5. The influence of 2 kbar pressure on the global and internal dynamics of human hemoglobin observed by quasielastic neutron scattering.
   Marie-Sousai Appavou, **Sebastian Busch**, Wolfgang Doster, Ana M. Gaspar, and Tobias Unruh.
   European Biophysics Journal with Biophysics Letters, 40(6):705–714, 2011.
   http://dx.doi.org/10.1007/s00249-011-0678-3

6. FABADA: a Fitting Algorithm for Bayesian Analysis of DAta.
   Luis Carlos Pardo, Muriel Rovira-Esteva, **Sebastian Busch**, María Dolores Ruiz-Martín, and Josep Lluis Tamarit.
   Journal of Physics: Conference Series, 325(1):012006, 2011.
   http://dx.doi.org/10.1088/1742-6596/325/1/012006
   Included in appendix [G].

7. Fitting in a complex χ^2 landscape using an optimized hypersurface sampling.
   Luis Carlos Pardo, Muriel Rovira-Esteva, **Sebastian Busch**, Jean-François Moulin, and Josep Lluis Tamarit.
   Physical Review E, 84(4):046711, 2011.
   http://dx.doi.org/10.1103/PhysRevE.84.046711
   Included in appendix [H].

8. Interplay between intra- and intermolecular structures of 1,1,2,2-tetrachloro-1,2-difluoroethane.
   Muriel Rovira-Esteva, Arul Murugan, Luis Carlos Pardo, **Sebastian Busch**, Josep Lluis Tamarit, Szilvia Pothoczki, Gabriel Julio Cuello, and Francisco Javier Bermejo.
   Physical Review B, 84(6):064202, 2011.
   http://dx.doi.org/10.1103/PhysRevB.84.064202

9. Molecular mechanism of long-range diffusion in phospholipid membranes studied by quasielastic neutron scattering.
   Sebastian Busch, Christoph Smuda, Luis Carlos Pardo, and Tobias Unruh.
   Journal of the American Chemical Society, 132(10):3232, 2010.
   http://dx.doi.org/10.1021/ja907581s
   Included in appendix [B].

10. Dynamical transition of protein-hydration water.
    Wolfgang Doster, **Sebastian Busch**, Ana M. Gaspar, Marie-Sousai Appavou, Joachim Wuttke, and Hugo Scheer.
    Physical Review Letters, 104(9):098101, 2010.
    http://dx.doi.org/10.1103/PhysRevLett.104.098101
    Included in appendix [C].

11. Microscopic structures and dynamics of high- and low-density liquid trans-1,2-dichloroethylene.
    Muriel Rovira-Esteva, Arul Murugan, Luis Carlos Pardo, **Sebastian Busch**,

María Dolores Ruiz-Martín, Marie-Sousai Appavou, Josep Lluis Tamarit, Christoph Smuda, Tobias Unruh, Francisco Javier Bermejo, Gabriel Julio Cuello, and Sylwester J. Rzoska.
Physical Review B, 81(9):092202, 2010.
http://dx.doi.org/10.1103/PhysRevB.81.092202
Physical Review B, 81(9):099908, 2010 (Publisher's note).
http://dx.doi.org/10.1103/PhysRevB.81.099908
Physical Review B, 82(9):099906, 2010 (Erratum).
http://dx.doi.org/10.1103/PhysRevB.82.099906

12. Using polarization analysis to separate the coherent and incoherent scattering from protein samples.
Ana M. Gaspar, **Sebastian Busch**, Marie-Sousai Appavou, Wolfgang Häußler, Robert Georgii, Yixi Su, and Wolfgang Doster.
Biochimica et Biophysica Acta (BBA) – Proteins & Proteomics, 1804(1):76–82, 2009.
http://dx.doi.org/10.1016/j.bbapap.2009.06.024

13. Methyl group dynamics in polycrystalline and liquid ubiquinone Q_0 studied by neutron scattering.
Christoph Smuda, **Sebastian Busch**, René Schellenberg, and Tobias Unruh.
Journal of Physical Chemistry B, 113(4):916–922, 2009.
http://dx.doi.org/10.1021/jp807601g

14. Dynamics in shear flow studied by x-ray photon correlation spectroscopy.
Sebastian Busch, Torben H. Jensen, Yuriy Chushkin, and Andrei Fluerasu.
European Physical Journal E, 26:55–62, 2008.
http://dx.doi.org/10.1140/epje/i2007-10305-2

15. Self-diffusion in molecular liquids: Medium-chain *n*-alkanes and coenzyme Q_{10} studied by quasielastic neutron scattering.
Christoph Smuda, **Sebastian Busch**, Gerd Gemmecker, and Tobias Unruh.
The Journal of Chemical Physics, 129:014513, 2008.
Selected for the Virtual Journal of Biological Physics Research 16(2), 2008.
http://dx.doi.org/10.1063/1.2943673

16. Methyl group dynamics in glassy, polycrystalline, and liquid coenzyme Q_{10} studied by quasielastic neutron scattering.
Christoph Smuda, **Sebastian Busch**, Bernd Wagner, and Tobias Unruh.
The Journal of Chemical Physics, 129:074507, 2008.
Selected for the Virtual Journal of Biological Physics Research 16(5), 2008.
http://dx.doi.org/10.1063/1.2967188

17. Dynamics of well-folded and natively disordered proteins in solution: a time-of-flight neutron scattering study.
Ana M. Gaspar, Marie-Sousai Appavou, **Sebastian Busch**, Tobias Unruh, and

Wolfgang Doster.
European Biophysics Journal with Biophysics Letters, 37:573–582, 2008.
http://dx.doi.org/10.1007/s00249-008-0266-3

18. Diffusive motions in liquid medium-chain n-alkanes as seen by quasielastic time-of-flight neutron spectroscopy.
Tobias Unruh, Christoph Smuda, **Sebastian Busch**, Jürgen Neuhaus, and Winfried Petry.
The Journal of Chemical Physics, 129:121106, 2008.
http://dx.doi.org/10.1063/1.2990026

A.2. Non-refereed Publications

1. QuasiElastic Neutron Scattering at the time-of-flight spectrometer TOFTOF at the FRM II
Christoph Smuda, **Sebastian Busch**, Humphrey Morhenn, and Tobias Unruh
http://www.ph.tum.de/studium/praktika/fopra/versuche/61/Anleitung_TOFTOF.pdf, 2010.

2. sihl: Scattered intensity handling library.
Sebastian Busch.
http://www.thamnos.de/repos/sihl/, 2009–.
Software.

3. Bayesian analysis of QENS data: From parameter determination to model selection.
Luis Carlos Pardo, Muriel Rovira-Esteva, **Sebastian Busch**, María Dolores Ruiz-Martín, Josep Lluis Tamarit, and Tobias Unruh.
http://arxiv.org/abs/0907.3711, 2009.

4. chaste: Collection of tools for handling data with standard errors.
Sebastian Busch.
http://www.thamnos.de/repos/chaste/, 2008–.
Software.

5. FABADA: a Fitting Algorithm for Bayesian Analysis of DAta.
Luis Carlos Pardo, Muriel Rovira-Esteva, and **Sebastian Busch**.
http://gcm.upc.edu/members/luis-carlos/bayesiano, 2008–.
Software.

A.3. Talks at International Conferences

1. «The Pico- to Nanoscond Dynamics in Phospholipid Bi- and Monolayers»
Spring Meeting of the Deutsche Physikalische Gesellschaft
Technische Universität Dresden, Dresden (Germany)
March 2011

2. «Influence of Additives on the Short-Time Dynamics of the Phospholipid DMPC»
   Spring Meeting of the Deutsche Physikalische Gesellschaft
   Universität Regensburg, Regensburg (Germany)
   March 2010

3. «Long-Range Motion of Phospholipids on a Picosecond Timescale as Seen with Quasielastic Neutron Scattering»
   Spring Meeting of the Deutsche Physikalische Gesellschaft
   Technische Universität Dresden, Dresden (Germany)
   March 2009

4. «The Long-Range Motion of the Phospholipid DMPC in Mono- and Bilayers»
   9th International Conference on Quasielastic Neutron Scattering
   Paul Scherrer Institute, Villigen (Switzerland)
   February 2009

5. «The Time-of-Flight Spectrometer TOFTOF at FRM II: Scientific Highlights and Future Prospects»
   JCNS Workshop 2008: Modern Trends in Neutron Scattering Instrumentation
   Bernried (Germany)
   October 2008

6. «Picosecond-Dynamics in DMPC in Mono- and Bilayers Investigated by Quasielastic Neutron Scattering»
   22nd Conference of the European Colloid and Interface Society
   Jagiellonian University, Cracow (Poland)
   September 2008

A.4. Participation in Seminars and Workshops

1. «Getting to grips with the short-time dynamics of cell membrane models»
   Forschungs-Neutronenquelle Heinz Maier-Leibnitz (FRM II)
   Technische Universität München, Burg Rothenfels (Germany)
   May 2011

2. «2nd Backscattering Workshop»
   Jülich Centre for Neutron Science (JCNS)
   Forschungszentrum Jülich GmbH, member of the Helmholtz Association of German Research Centres, Garching bei München (Germany)
   May 2011

3. «2nd Brainstorming meeting ‹New paradigm of how to run a user facility›»
   in the framework of the EU European Spallation Source Preparatory Phase project
   The European Neutron Scattering Association ENSA, Zurich (Switzerland)
   July 2009

4. «Incoherent Quasielastic Neutron Scattering Reveals the Motions of Model Membranes on a Molecular Scale»
   Forschungs-Neutronenquelle Heinz Maier-Leibnitz (FRM II)
   Technische Universität München, Burg Rothenfels (Germany)
   June 2009

5. «1st Brainstorming meeting ‹New paradigm of how to run a user facility›»
   in the framework of the EU European Spallation Source Preparatory Phase project
   The European Neutron Scattering Association ENSA, Zurich (Switzerland)
   February 2009

6. «Phospholipids: Their Role in Nature & Biotechnology, Their Picosecond-Dynamics, and Possible Connections»
   Grup de Caracterització de Materials
   Universitat Polytècnica de Catalunya, Barcelona (Spain)
   October 2008

7. «Phospholipid Dynamics»
   Physik Department E13
   Technische Universität München, Garching bei München (Germany)
   June 2008

A.5. Posters at International Conferences

1. «How glassy are biological membranes?»
   Spring Meeting of the Deutsche Physikalische Gesellschaft
   Technische Universität Dresden, Dresden (Germany)
   March 2011

2. «Panta Rhei – Flow Behaviour in Phospholipid Membranes»
   Spring Meeting of the Deutsche Physikalische Gesellschaft
   Universität Regensburg, Regensburg (Germany)
   March 2010

3. «Fragile–Strong–Crossover in Surface Water?»
   Deutsche Tagung für Forschung mit Synchrotronstrahlung, Neutronen und Ionenstrahlen an Großgeräten
   Freie Universität Berlin, Berlin (Germany)
   February 2010

4. «Phospholipid Dynamics & the Influence of Additives»
   Deutsche Tagung für Forschung mit Synchrotronstrahlung, Neutronen und Ionenstrahlen an Großgeräten
   Freie Universität Berlin, Berlin (Germany)
   February 2010

5. «The Pico- to Nanosecond Dynamics of Phospholipids»
   6th International Discussion Meeting on Relaxations in Complex Systems
   Sapienza – Università di Roma, Rome (Italy)
   September 2009

6. «Dynamics of protein hydration water studied on a nanosecond time scale with neutron backscattering spectroscopy»
   Biomolecular Dynamics and Protein-Water Interactions
   Feldafing (Germany)
   September 2008

7. «Dynamics of Phospholipids used as Stabilizers in Colloidal Dispersions studied by Quasielastic Neutron Scattering»
   Deutsche Neutronenstreutagung
   Technische Universität München, Garching bei München (Germany)
   September 2008

8. «Investigations on the Structure and Dynamics of DMPC-Monolayers used as Stabilizers in Colloidal Dispersions»
   Spring Meeting of the Deutsche Physikalische Gesellschaft
   Technische Universität Berlin, Berlin (Germany)
   February 2008

Appendix B.

Molecular Mechanism of Long-Range Diffusion in Phospholipid Membranes Studied by Quasielastic Neutron Scattering

Sebastian Busch, Christoph Smuda, Luis Carlos Pardo, and Tobias Unruh
Journal of the American Chemical Society, 132(10):3232, 2010
http://dx.doi.org/10.1021/ja907581s

In this publication, the author supervised the work of Sarah Kurmulis with whom he prepared the samples. She helped with the neutron scattering measurements with an instrumental resolution of 55 µeV, he performed the measurements with an instrumental resolution of 4 µeV as well as all of the data reduction and evaluation. The idea to evaluate the data with the flow-model and to show the statistically significant superiority of this model with the Bayesian data evaluation software [G, H] was the author's. He interpreted the results and wrote the publication.

Following a model that was proposed from MD simulations [150], the long-range component of the phospholipid motions can be evaluated as flow-like. This assumption requires a linear increase of the line width σ of the narrow component of a fit to quasielastic neutron scattering data as a function of the momentum transfer Q [268]. Such a behaviour was observed over a large range of Q – deviations at small line widths from this behaviour were shown to be a fit artifact [C, D].

Extracting the flow velocities, a quantitative agreement with the MD simulations is obtained, hereby presenting the first experimental evidence for the correctness of the simulations. The evaluation of the flow-like motions with varying temperature was studied later in more detail [D, F] and it was suggested that they can be identified with dynamical heterogeneities [E].

Reproduced with permission from Journal of the American Chemical Society, 132(10):3232, 2010.
Copyright 2010 American Chemical Society.

J|A|C|S COMMUNICATIONS

Published on Web 02/17/2010

Molecular Mechanism of Long-Range Diffusion in Phospholipid Membranes Studied by Quasielastic Neutron Scattering

Sebastian Busch,† Christoph Smuda,‡ Luis Carlos Pardo,§ and Tobias Unruh*,†

Forschungsneutronenquelle Heinz Maier-Leibnitz (FRM II), Technische Universität München, Garching bei München, Germany, Center for Radiopharmaceutical Science, Eidgenössische Technische Hochschule Zürich, Zürich, Switzerland, and Grup de Caracterització de Materials, Departament de Física i Enginyeria Nuclear, Universitat Politècnica de Catalunya, Barcelona, Spain

Received September 15, 2009; E-mail: tobias.unruh@frm2.tum.de

Phospholipid membranes have been the subject of intense research ever since the discovery of their function as cell membranes in 1925.[1] Not only their natural abundance (every human body contains several square kilometers[2]) but also their widespread application in agricultural, food, and pharmaceutical applications[3] makes them a worthwhile subject matter for structural and dynamical studies.

Whereas the opinions about the structure seem to converge,[4] the discussion about the dynamical properties is in full swing. The fundamental issue is that many processes in cell membranes take place on a scale of a few nanometers, as this is approximately the distance between two proteins,[5] and it turned out in the early 1990s that the dynamics on this scale differs drastically from the macroscopic (micrometer) behavior: Incoherent quasielastic neutron scattering (QENS) experiments[6,7] observed a fast localized motion of the whole molecule on the probed microscopic temporal and spatial scale of up to a few tens of picoseconds and few nanometers whereas macroscopic measurements observed a significantly slower long-range diffusion.[8,9]

This contradiction could be explained by adapting the free volume theory to membranes:[10] The phospholipid molecules are thought to rattle in a cage of neighbors (fast, localized motion) until a free volume of the size of a phospholipid molecule opens up and the molecule can slip into it. This random walk of the molecules from void to void is then observed as the macroscopic slow, long-range diffusive motion. It is clear that "all models are wrong but some are useful",[11] but the remarkable success of this description of macroscopic effects can be misleading, taking its microscopic image too literally. When increased computing power made Molecular Dynamics (MD) simulations of these complex systems feasible, it became more and more obvious that rattling and slipping motions could not be seen on a molecular scale[8,12] although the results were still sometimes interpreted in this frame.[13] Rather, simulation and experiment agreed that the molecular motions are collective in nature[14] and finally, a flow-like behavior as found in quasi-two-dimensional suspensions[15] was observed in MD simulations of phospholipids in the liquid phase.[16]

To resolve this discrepancy, we repeated the neutron scattering studies[6,7] that triggered the implementation of the free volume theory with highly improved instrumentation at the time-of-flight neutron spectrometer TOFTOF[17] at the neutron source FRM II, Munich, Germany. We will show that, in contrast to the former interpretation, QENS does not provide any indication for the picture of phospholipid molecules rattling and escaping from local cages on a molecular scale. Rather, the data agree well with the MD simulations of ballistic, flow-like motions as the means of long-range transport on a nanometer scale in the membranes.

† Technische Universität München, FRM II.
‡ Eidgenössische Technische Hochschule Zürich.
§ Universitat Politècnica de Catalunya.

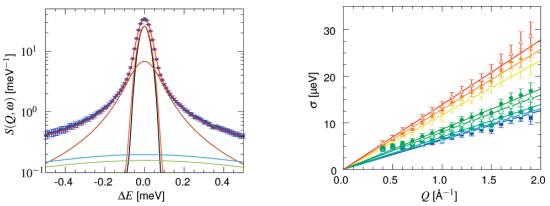

Figure 1. Left: QENS spectrum of DMPC shown exemplarily at 30 °C and $Q = 1.0$ Å^{-1}. The instrumental resolution is displayed as a black line, along with the best fit of eq 1 (red) and its components. Right: the extracted standard deviations σ of the long-range component as a function of Q for temperatures ranging from 5 °C (bottom) to 40 °C (top) in steps of 5 °C. The lines through the origin are fits to the data in the range 0.75 Å^{-1} < Q < 1.45 Å^{-1}. At temperatures below the main phase transition, σ levels off below $Q_c \approx 0.7$ Å^{-1}.

The sample was chosen to be a typical phospholipid, dimyristoylphosphatidylcholine (DMPC), which was hydrated with D_2O to form a liquid crystal of fully hydrated multilayers without solid support. Its dynamics was measured with an observation time of 35 ps, corresponding to an instrumental resolution of 60 μeV (full width at half-maximum).[18] The sample temperature was varied between 5 and 40 °C, probing the dynamics below and in the region of interest above the main phase transition (at 24 °C).

At the spectrometer, neutrons with a well-known energy impinge on the sample and interact with the nuclei. If the sample was static, there would be no energy change $\hbar\omega$ of the neutrons and they would be detected smeared by the instrumental resolution. Aperiodic motions in the sample cause a quasielastic broadened energy spectrum that is measured at different momentum transfers $\hbar Q$ (cf. Figure 1). The shape and width of the broadening are essentially determined by the decay of the autocorrelation function of the hydrogen nuclei.[19] The simplest meaningful function describing the data in the present case was found to consist of a long-range motion of the whole molecule and two localized motions,[20]

$$\begin{aligned} S(Q,\omega) = {} & a(Q)\cdot G(\sigma(Q),\omega) \otimes \\ & [A_{\text{fast}}(Q)\cdot\delta(\omega) + (1 - A_{\text{fast}}(Q))\cdot L(\Gamma_{\text{fast}},\omega)] \otimes \\ & [A_{\text{slow}}(Q)\cdot\delta(\omega) + (1 - A_{\text{slow}}(Q))\cdot L(\Gamma_{\text{slow}},\omega)], \end{aligned} \tag{1}$$

where G denotes a Gaussian and L a Lorentzian with the Q-dependent standard deviation σ and the Q-independent half width at half-maximum Γ, respectively; $\otimes$ designates convolution in energy space. The use of a Gaussian follows from Maxwell–Boltzmann distributed ballistic motions. The function is finally convolved with the instrumental resolution to obtain the experimentally observed scattering function.

For a flow motion, the standard deviation of the Gaussian σ increases linearly with Q, the slope given by the flow velocity. If the

10.1021/ja907581s © 2010 American Chemical Society

molecule is trapped in a cage with a typical dimension r_c, the scattering function splits at Q values below $Q_c \approx (2\pi)/(r_c)$ into a quasielastic part with Q-independent width and an emerging $\delta(\omega)$ component which was however not resolved with these instrumental settings.

It can be seen in Figure 1 that, for temperatures below the main phase transition, $\sigma(Q)$ does level off at small values of Q, indicating that the phospholipid molecules are confined to a length of ~9 Å, approximately the size of the intermolecular distance. The same should hold above the main phase transition, following the picture where the fundamental step of phospholipid long-range diffusion is the escape from the cage: It can be calculated from the macroscopic diffusion coefficient that this event is so rare that 98% of the molecules are still confined during the observation time of 35 ps.[20] However, one can see in Figure 1 that this confinement is breaking down. While we cannot exclude that the leveling off below the phase transition is a limitation of the spectrometer, the absence of confinement above the phase transition is clear. This is a first indication that the molecules are not trapped in a cage of neighbors in the relevant high-temperature phase.

As it is crucial that the observed line broadening is not a fit artifact, a Bayesian data analysis[21] was performed. It could be shown with clear statistical significance that, above the main phase transition, the model incorporating a line broadening is superior to one with only a $\delta(\omega)$ line. This result indicates again that the lateral transport process of phospholipid molecules within a membrane is not governed by decaging events on a picosecond time scale.[20] This finding is in full agreement with recent MD simulations.[16] We conclude therefore that the rattling and escape model cannot describe the dynamical processes on the time scale of some tens of picoseconds.

To check whether it is possible to support the proposed mechanism of flow-like motions of dynamically assembled patches of molecules also on a nanosecond time scale, an experiment probing these times was conducted. In contrast to coherent neutron spin echo spectroscopy, it is not possible with incoherent QENS to check the collectivity of motions directly, but the motions of the single particles can nevertheless be compared to the simulation. As the MD simulations[16] observed a decay of the velocity autocorrelation function in this time regime, one would expect to measure a lower flow velocity than on a time scale of some tens of picoseconds.

The sample was prepared the same way, but the spectrometer was tuned to a much longer observation time of 0.9 ns, corresponding to an instrumental resolution of 4 μeV (full width at half-maximum).[18] The data were analyzed using eq 1, shown in Figure 2. The low temperature measurements (not displayed) have a $\delta(\omega)$ component, indicating confinement[20] which breaks down above the main phase transition. The analysis of the fluid phase at 30 °C allows us to extract the most probable velocity of the Maxwell–Boltzmann distribution of 0.3(nm)/(ns). This value and the decay of the flow velocity compared to the 35 ps measurement are in good agreement with the simulation.[20]

Summarizing, the following picture of phospholipid motion on a pico- to nanosecond time scale emerges: The head and tail of the molecule perform localized diffusive motions visible as two broad components in the scattering function (Figure 1) and a negative part of the velocity autocorrelation function[13,14] at times of a few picoseconds. This is not the footprint of a rattling and escape motion; the whole molecule rather flows with its neighbors as a dynamically assembling patch across the membrane.

This effect should have important consequences for living cells where the distance between proteins is on the here probed nanometer scale.[5] Recently, it could be demonstrated that ballistic motion is the most effective search strategy.[22] This could for example influence G protein coupled signal transduction cascades where two proteins have to come into contact.[23] For such processes, only the microscopic transport mechanism is relevant.

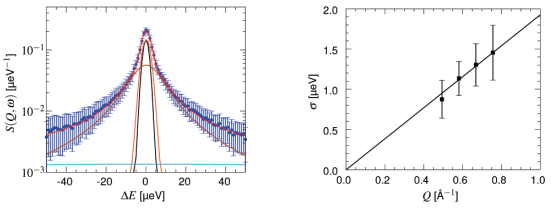

Figure 2. Left: QENS spectrum of DMPC at 30 °C and $Q = 0.76$ Å^{-1}. The instrumental resolution is displayed as a black line, along with the best fit of eq 1 (red) and its three components. Right: the extracted σ as in Figure 1. The line through the origin is a fit to the data points.

Acknowledgment. The authors thank S. Kurmulis for her help during the measurements, Prof. W. Petry for funding, and both him and Prof. E. Sackmann for their readiness for discussions. This work was partly supported by Grants FIS2008-00837 and 2009SGR-1251.

Supporting Information Available: Material characterization, data reduction and analysis details, further comparison with previous work, additional results and complete ref 17. This material is available free of charge via the Internet at http://pubs.acs.org.

References

(1) Gorter, E.; Grendel, F. *J. Exp. Med.* **1925**, *41*, 439.
(2) Alberts, B.; Johnson, A.; Lewis, J.; Raff, M.; Roberts, K.; Walter, P. *Molecular Biolology of the Cell*, 5th ed.; Taylor & Francis Group: 2007.
(3) Taylor, T. M.; Davidson, P. M.; Bruce, B. D.; Weiss, J. *Crit. Rev. Food Sci. Nutr.* **2005**, *45*, 587–605.
(4) Nagle, J. F.; Tristram-Nagle, S. *Biochim. Biophys. Acta (Reviews on Biomembranes)* **2000**, *1469*, 159.
(5) Ramadurai, S.; Holt, A.; Krasnikov, V.; van den Bogaart, G.; Killian, J.; Poolman, B. *J. Am. Chem. Soc.* **2009**, *131*, 12650–6.
(6) Tabony, J.; Perly, B. *Biochimica et Biophysica Acta (Biomembranes)* **1991**, *1063*, 67.
(7) König, S.; Pfeiffer, W.; Bayerl, T. M.; Richter, D.; Sackmann, E. *J. Phys. II France* **1992**, *2*, 1589.
(8) Böckmann, R. A.; Hac, A.; Heimburg, T.; Grubmüller, H. *Biophys. J.* **2003**, *85*, 1647.
(9) Cevc, G., Ed.; *Phospholipids Handbook*; CRC: 1993.
(10) (a) Cohen, M. H.; Turnbull, D. *J. Chem. Phys.* **1959**, *31*, 1164. (b) Galla, H.-J.; Hartmann, W.; Theilen, U.; Sackmann, E. *J. Membr. Biol.* **1979**, *48*, 215. (c) Vaz, W. L. C.; Almeida, P. F. F. *Biophys. J.* **1991**, *60*, 1553–1554.
(11) Box, G. E. P. *J. Am. Stat. Assoc.* **1976**, *71*, 791–799.
(12) (a) Falck, E.; Patra, M.; Karttunen, M.; Hyvönen, M. T.; Vattulainen, I. *Biophys. J.* **2004**, *87*, 1076–91. (b) Almeida, P. F. F.; Vaz, W. L. C.; Thompson, T. E. *Biophys. J.* **2005**, *88*, 4434–8. (c) Falck, E.; Patra, M.; Karttunen, M.; Hyvönen, M. T.; Vattulainen, I. *Biophys. J.* **2005**, *89*, 745–52.
(13) Wohlert, J.; Edholm, O. *J. Chem. Phys.* **2006**, *125*, 204703.
(14) (a) Ayton, G. S.; Voth, G. A. *Biophys. J.* **2004**, *87*, 3299–311. (b) Rheinstädter, M. C.; Das, J.; Flenner, E.; Brüning, B.; Seydel, T.; Kosztin, I. *Phys. Rev. Lett.* **2008**, *101*, 248106.
(15) (a) Perera, D. N.; Harrowell, P. *J. Chem. Phys.* **1999**, *111*, 5441. (b) Diamant, H.; Cui, B.; Lin, B.; Rice, S. A. *J. Phys.: Condens. Matter* **2005**, *17*, S2787.
(16) Falck, E.; Róg, T.; Karttunen, M.; Vattulainen, I. *J. Am. Chem. Soc.* **2008**, *130*, 44–5.
(17) (a) Teixeira, S.; et al. *Chem. Phys.* **2008**, *345*, 133–151. (b) Unruh, T.; Neuhaus, J.; Petry, W. *Nucl. Instrum. Methods Phys. Res., Sect. A* **2007**, *580*, 1414–1422. (c) Unruh, T.; Neuhaus, J.; Petry, W. *Nucl. Instrum. Methods Phys. Res., Sect. A* **2008**, *585*, 201.
(18) Unruh, T.; Šmuda, C.; Busch, S.; Neuhaus, J.; Petry, W. *J. Chem. Phys.* **2008**, *129*, 121106.
(19) (a) Boon, J. P.; Yip, S. *Molecular Hydrodynamics*; McGraw-Hill Inc.: 1980. (b) Bée, M. *Quasielastic Neutron Scattering*; Taylor & Francis: 1988.
(20) See Supporting Information.
(21) Pardo, L. C.; Rovira-Esteva, M.; Busch, S.; Ruiz-Martín, M. D.; Tamarit, J. L.; Unruh, T. http://arxiv.org/abs/0907.3711v3, 2009.
(22) James, A.; Plank, M. J.; Brown, R. *Phys. Rev. E* **2008**, *78*, 051128.
(23) Simon, M. I.; Strathmann, M. P.; Gautam, N. *Science* **1991**, *252*, 802.

JA907581S

Supporting information for: Molecular Mechanism of Long-Range Diffusion in Phospholipid Membranes Studied by Quasielastic Neutron Scattering

Sebastian Busch,[†,‡] Christoph Smuda,[¶] Luis Carlos Pardo,[§] and Tobias Unruh[*,‡,†]

Physik Department E13, Technische Universität München, Garching bei München, Germany, Forschungsneutronenquelle Heinz Maier-Leibnitz (FRM II), Technische Universität München, Garching bei München, Germany, Center for Radiopharmaceutical Science, Eidgenössische Technische Hochschule Zürich, Zürich, Switzerland, and Grup de Caracterització de Materials, Departament de Física i Enginyeria Nuclear, Universitat Politècnica de Catalunya, Barcelona, Spain

E-mail: tobias.unruh@frm2.tum.de

Experimental Details

Dimyristoylphosphatidylcholine (DMPC) was purchased from Lipoid GmbH, Ludwigshafen, Germany, and used as received. The dry phospholipid powder was hydrated with D_2O (99.90%, Euriso-Top, Gif sur Yvette, France) via the vapour phase at 40°C for two days after which the sample was homogeneous and transparent. As the dynamics of the phospholipid is known to depend on the hydration,[1] additional D_2O was added to ensure full hydration during the whole

[*] To whom correspondence should be addressed
[†] Technische Universität München, Physik Department
[‡] Technische Universität München, FRM II
[¶] Eidgenössische Technische Hochschule Zürich
[§] Universitat Politècnica de Catalunya

experiment. The final concentration was adjusted to 50 mass percent. The integrity of DMPC was confirmed by Differential Scanning Calorimetry, cf. Figure 1.

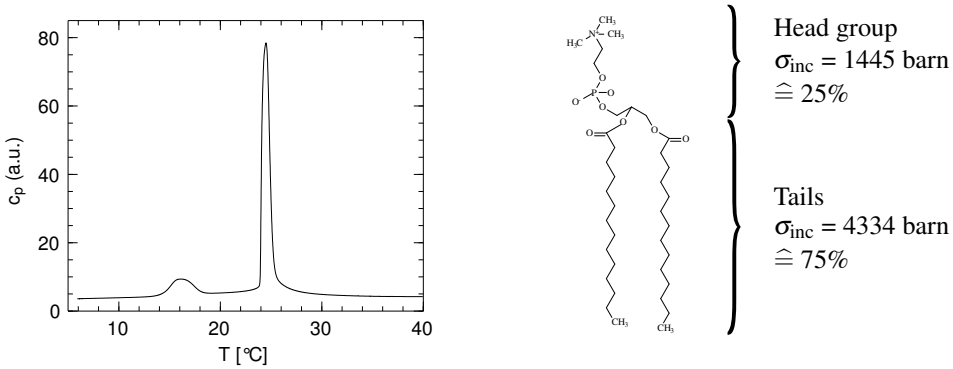

Figure 1: Left: Differential Scanning Calorimetry of a fully hydrated DMPC liquid crystal. The pre- and main phase transition are visible at about 16 and 24 °C, respectively. Right: A DMPC molecule[2] and the corresponding incoherent neutron scattering cross sections[3] of the head and tail group together with the respective fraction compared to the whole molecule.

Two measurement series were performed at the neutron time-of-flight spectrometer TOFTOF[4] at the Forschungsneutronenquelle Heinz Maier-Leibnitz (FRM II), Munich, Germany, to realize two different observation times, 35 ps and 0.9 ns.[5] This was done by changing the instrumental resolution. It is important to note that the instrumental resolution does not correspond to a lower limit of the broadenings which can be determined.

Measuring the momentum and energy transfer between neutron and sample, one obtains the scattering function $S(Q,\omega)$ which is the double Fourier transform of the autocorrelation function.[6,7] Due to the very large incoherent scattering cross section of the protons, they dominate the scattering signal by far. However, as they are sampling the molecule quite uniformly, the motion of the whole molecule becomes visible.

The primary part of the spectrometer uses seven choppers to cut the continuous white beam delivered from the cold source of the reactor into short monochromatic pulses of neutrons. They

interact with the sample and may change momentum and energy. After the sample, the neutrons fly 4 m in the secondary part of the spectrometer until they are detected in one of 600 ^{3}He-filled detector tubes. As the scattering angle of each detector is well-known and the time-of-flight between the sample and the detector is recorded, momentum and energy transfer can be calculated.

The amount of sample was in both cases approx. 1 ml, chosen such that multiple scattering has only a minor effect.

For the 35 ps measurement, the sample was filled in an aluminum hollow cylinder container[8] with a gap thickness of 0.2 mm. A temperature-controlled sample environment was used to stabilize the sample temperature to ± 0.1°C during the measurements. A mean neutron wavelength of $\lambda = 6$ Å, a rotation speed of the choppers of 12000 rpm, and frame overlap ratio 4 were used, leading to an instrumental resolution (FWHM) of about 60 μeV. The temperature was varied from 5 °C to 40 °C in steps of 5 °C. For each temperature, the sample was measured for 8 h and pure D_2O for 4 h. The empty can was measured at the lowest and highest temperature for 4 h each and a Vanadium standard (hollow cylinder with 0.6 mm wall thickness) was measured at 20 °C for 3 h.

For the 0.9 ns measurement, the sample was filled in an aluminum flat slab, its surface normal was oriented to a scattering angle of $2\theta = 135°$. The wavelength was $\lambda = 14$ Å, chopper speed 16000 rpm, and ratio 8, giving a instrumental resolution (FWHM) of about 4 μeV. The temperature was set to 10 °C, 20 °C, and 30 °C, respectively. At each temperature, the sample was measured for 12 h and D_2O for 10 h. The empty can was measured for 10 h at 30 °C and Vanadium powder was measured in the same sample holder for 14 h at 30 °C. The data at scattering angles below $\approx 50°$ were discarded due to self-shielding and coherent small angle scattering of the sample.

The data were treated using the program Frida1[9] and using the Vanadium measurement for three purposes: time-of-flight at zero energy transfer, detector sensitivity normalization, and instrumental resolution.

During the conversion from time-of-flight to energy transfer, the energy-dependent detector efficiency was corrected. At the employed wavelengths, Vanadium scatters the same intensity in every solid angle. The intensity of its elastic line was integrated, corrected for the Debye-Waller

factor, and used for normalization of the detector sensitivities. The instrumental resolution could be determined because the Vanadium atoms do not perform any non-periodic motion and therefore do scatter the neutrons without a quasielastic smearing.

After subtraction of the empty can measurements from both, the sample and the D_2O, an angle- and energy-dependent self-absorption correction[10] was performed before proportional subtraction of the D_2O from the sample signal. It has to be kept in mind that the water adsorbed to the membrane will have other dynamical properties than bulk water which can therefore only serve as an approximate reference. However, as can be seen exemplarily in Figure 2, the scattering signal of D_2O is at least one order of magnitude below the one of DMPC, therefore a slightly incorrect subtraction should not alter the results significantly.

The data were converted from scattering angle 2θ to the absolute value of the scattering vector, Q. The data of the 35 ps measurement were then grouped into bins of constant Q in the range from 0.3 Å^{-1} to 1.9 Å^{-1} in steps of 0.1 Å^{-1}, the data of the 0.9 ns measurement into 4 equidistant bins between 0.49 Å^{-1} and 0.8 Å^{-1}. Some spectra are shown exemplarily in Figure 2. It can be seen that the scattering of D_2O does not give an important contribution to the narrow component due to both, its lower scattering cross section and its much faster dynamics.

We would like to point out that the analysis of the broad component is not essential for the interpretation of the nature of the long-range motion. This is valuable as disturbing effects of multiple scattering or incorrect background subtraction influence this part of the scattering function. Their influence will turn up in the analysis of the internal motions.

The Bayesian analysis, performed with the program FABADA,[11] convolved the theoretical functions numerically with the instrumental resolution. The algorithm was run for 1000000 cycles with an automatic adjustment of the step size every 100000 cycles. The convergence factor was set to 0.66. The fitting ranges were ± 1.0 meV for the 35 ps measurement and ± 50μeV for the 0.9 ns measurement.

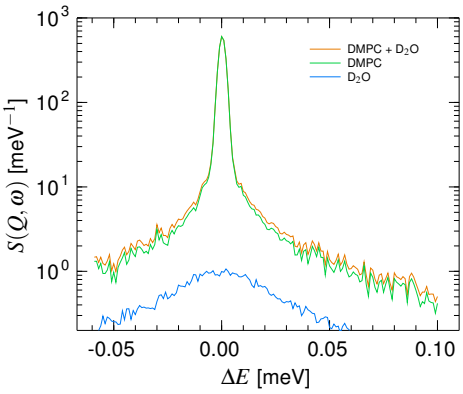

Figure 2: Spectra of the sample (DMPC + D_2O, top), bulk D_2O (bottom), and the pure DMPC (sample after proportional subtraction of the bulk D_2O spectrum, middle) of the 0.9 ns (4 µeV) measurement after conversion to constant Q around $Q = 0.58\text{Å}^{-1}$. It can be seen that the D_2O signal hardly contributes, especially in the region of interest around $\Delta E = 0$.

Proposed Models

It was found that models including one (only long-range) or two (one long-range and one localized) components could not fit the data of the 35 ps measurement. Therefore, four models comprising two localized and one long-range component were compared: Three possibilities for the long-range motion with a quasi model-free approach for the localized motions are discussed: a long-range motion that is so slow that the corresponding line broadening cannot be observed, a diffusive motion, and a flow motion. It will be shown that this comparison favours the last possibility. For this case, a further model with explicit assumptions about the localized motions was fitted showing that the freedom of the generalized approach is necessary to extract information from this complex molecule.

If there is *no* long-range motion visible, the scattering function incorporating two localized

motions (fast and slow) reads

$$S(Q,\omega) = a(Q)\cdot\delta\big(\omega\big)\otimes \\ \big[A_{\text{slow}}(Q)\cdot\delta(\omega) + \big(1-A_{\text{slow}}(Q)\big)\cdot L\big(\Gamma_{\text{slow}},\omega\big)\big]\otimes \\ \big[A_{\text{fast}}(Q)\cdot\delta(\omega) + \big(1-A_{\text{fast}}(Q)\big)\cdot L\big(\Gamma_{\text{fast}},\omega\big)\big] \ . \quad (1)$$

In this and the following equations, $a(Q)$ denotes a prefactor which comprises also the Debye-Waller factor, $A_{\text{slow/fast}}(Q)$ are the elastic incoherent structure factors (EISF) of the respective localized motions that contain information about their geometry and amplitude. The rates of the localized motions are given by the respective half widths at half maximum (HWHM) $\Gamma_{\text{slow/fast}}$ of the Lorentzians L:

$$L(\Gamma,\omega) = \frac{1}{\pi}\cdot\frac{\Gamma}{\Gamma^2+\omega^2} \quad . \quad (2)$$

If a *diffusive* long-range motion is visible, the scattering function changes to

$$S(Q,\omega) = a(Q)\cdot L\big(\Gamma(Q),\omega\big)\otimes \\ \big[A_{\text{slow}}(Q)\cdot\delta(\omega) + \big(1-A_{\text{slow}}(Q)\big)\cdot L\big(\Gamma_{\text{slow}},\omega\big)\big]\otimes \\ \big[A_{\text{fast}}(Q)\cdot\delta(\omega) + \big(1-A_{\text{fast}}(Q)\big)\cdot L\big(\Gamma_{\text{fast}},\omega\big)\big] \quad (3a)$$

where the HWHM of the first component is given by the respective equations

$$\Gamma(Q) = \begin{cases} \hbar\cdot DQ^2 & \text{for continuous diffusion or} \\ \hbar\cdot\frac{DQ^2}{1+DQ^2\tau} & \text{for stop \& go diffusion} \end{cases} \quad (3b)$$

The stop & go motion[12] is taken in the limit where the particle is much longer trapped than diffusing and does not perform oscillatory motions during this period. D denotes here the diffusion coefficient and τ the time between two diffusive events.

Finally, in the case of a *flow* motion, one obtains a Gaussian central component,

$$G(\sigma,\omega) = \frac{1}{\sigma\sqrt{2\pi}} \exp\left[-\frac{\omega^2}{2\sigma^2}\right] \quad , \tag{4}$$

yielding a scattering function of

$$\begin{aligned} S(Q,\omega) = a(Q)\cdot G\big(\sigma(Q),\omega\big)\otimes \\ \big[A_{\text{slow}}(Q)\cdot\delta(\omega) + \big(1-A_{\text{slow}}(Q)\big)\cdot L\big(\Gamma_{\text{slow}},\omega\big)\big]\otimes \\ \big[A_{\text{fast}}(Q)\cdot\delta(\omega) + \big(1-A_{\text{fast}}(Q)\big)\cdot L\big(\Gamma_{\text{fast}},\omega\big)\big] \end{aligned} \tag{5a}$$

where the standard deviation σ of the Gaussian G is determined by

$$\sigma(Q) = \hbar\cdot v_0 Q \tag{5b}$$

when the motions are assumed to be ballistic with a Maxwell-Boltzmann distribution of speeds around the most probable value v_0. This is also the model for the phase of "free flight" the molecules exhibit before the interactions with their environment have built up. However, the two scenarios can be distinguished as during "free flight" , v_0 would be $\sqrt{2k_BT/m}$, whereas in the case of a flow motion, this value has to be much lower. The analogy to a gas requires an isotropic average which is done by using a powder sample where all orientations of the liquid crystal occur statistically throughout the sample.

The standard deviation σ of a Gaussian is connected to its full width at half maximum by

$$\text{FWHM} = 2\cdot\sqrt{2\ln(2)}\cdot\sigma \approx 2.4\cdot\sigma \quad . \tag{6}$$

As it turns out that the fast component is very broad, the data were for comparison also fitted with a model of long-range flow, a Brownian oscillator as the slow localized motion, and low energetic vibrational motions for the fast localized motions. Using a Debye model, it can be

calculated that this contribution is in first order expansion a background proportional to Q^2 and nearly independent of energy at the present temperatures,

$$S(Q,\omega) = a(Q)\cdot G\big(\sigma(Q),\omega\big)\otimes \exp\left[-Q^2\delta^2\right]\cdot\sum_{n=0}^{\infty}\frac{Q^{2n}\delta^{2n}}{n!}\cdot L\big(n\Gamma_{\text{slow}},\omega\big)+ b\cdot Q^2\cdot\frac{\hbar\omega}{\exp\left[\frac{\hbar\omega}{k_BT}\right]-1}\,. \quad (7)$$

The scaling factor b was introduced to account for Q and ω independent factors such as the Debye frequency. The advantage of this model is that it does not need an artificial division of the scatterers into two classes and has less parameters than model (5). It has also some disadvantages: the intensities of the elastic and quasielastic component are linked, it lacks generality, and the assumptions (Debye model &c.) can only be approximately correct.

Identification of the Long-Range Motion

Visibility of the Broadening

First, we determine whether a long-range motion can be seen with QENS before we try to distinguish the type of motion – diffusion or flow. This broadening is not influenced by disturbing effects such as solvent subtraction of multiple scattering.[13]

Macroscopic measurements of the long-range diffusional motion have shown that the diffusion coefficient below the main phase transition is nearly three orders of magnitude below the one above the main phase transition.[14] It is therefore not possible any more to resolve this motion with QENS, as can be seen in Figure 3 for the 0.9 ns measurement. There, it is obvious that the central line is not broadened beyond the instrumental resolution at temperatures below the main phase transition.

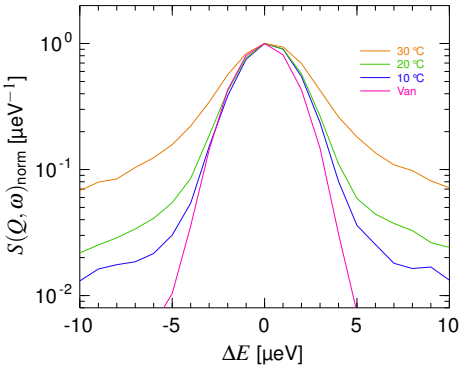

Figure 3: Spectra of Vanadium and DMPC at three temperatures, all at $Q = 0.58\,\text{Å}^{-1}$ and normalized to $S(Q,\omega = 0)$. It can be seen that the measurement at 30 °C has a significant broadening in the central region whereas the other two have the same HWHM as Vanadium, only shifted by a background caused by localized motions.

Check of the Rattling & Jump Model

The rattling & jump model, the primary step of diffusion is thought to be the displacement of a phospholipid molecule into a neighbouring void. Using the molecular area of DMPC[15] and the long-range diffusion coefficient of $8.4 \cdot 10^{-12}\,\frac{\text{m}^2}{\text{s}}$,[14] every molecule should do such a jump only every

$$\frac{0.64\,\text{nm}^2}{4 \cdot 8.4 \cdot 10^{-12}\,\frac{\text{m}^2}{\text{s}}} \approx 20\,\text{ns}\,. \tag{8}$$

This means that during the 35 ps observation time, 98% of the molecules do *not* perform a long-range motion in this model. This should result in a not broadened central line as in equation (1), given that this line is caused by the long-range motion.

As in the case of the 35 ps measurement the instrumental resolution does not allow for a clear separation of central line broadening and a shift induced by internal motions any more, the decision cannot be made by a simple optical inspection as it was possible in Figure 3. Therefore, a Bayesian data analysis was performed. This method has already previously been successfully used to analyze QENS data of phospholipids.[16]

In this method, the sum of squared residuals is essentially understood as an energy. The best

fit to the data with the minimal χ^2 corresponds therefore to the state with lowest energy. A thermodynamic system would however for any non-zero temperature explore also states with higher energies. The Bayesian algorithm does so by generating parameter sets around the best fit with a Monte Carlo method.

The probability that the fit populates a state with a given χ^2 depends on the χ^2 hypersurface and the number of degrees of freedom (i. e. parameters). If a new parameter is introduced, the most probable χ^2 will decrease if and only if the data can support this additional parameter.

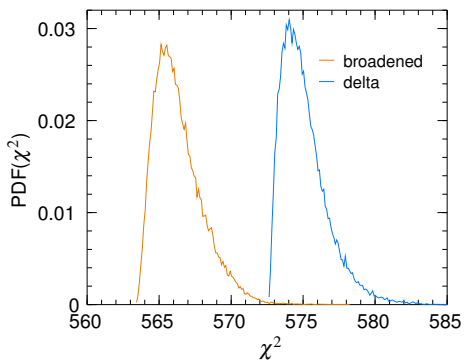

Figure 4: Comparison of the models broadened central line vs. non-broadened central line using a Bayesian data analysis of the data at 25 °C and 1.4 Å^{-1}. It can be seen that the data do favour the model with a broadened central line.

It can be clearly seen in Figure 4 that at a temperature above the main phase transition, the data favour the broadened model (5) over the "rattling & jump" model (1).

Diffusion or Flow

A point not discussed in the main paper is whether this broadening is due to a diffusive or flow motion. In the previous neutron scattering experiments, always a diffusive motion was assumed.[17] As lined out above, the diffusive motion results in a Lorentzian line shape with $\Gamma \propto Q^2$ whereas the flow motion results in a Gaussian line shape with $\sigma \propto Q$. As the fits of a Lorentzian / Gaussian to the data are of the same quality, one can not exclude either possibility.

In the case of the 35 ps measurement, the model of simple diffusion does not fit the half widths at half maximum satisfactorily, cf. Figure 5 (giving a diffusion coefficient of $180 \cdot 10^{-12}\,\frac{\mathrm{m}^2}{\mathrm{s}}$). As normally done with complex liquids, this fit can be improved by assuming a stop & go motion, yielding a diffusion coefficient of $240 \cdot 10^{-12}\,\frac{\mathrm{m}^2}{\mathrm{s}}$ and a stopping time of 10 ps. As calculated above, this cannot be the rattling phase of the rattling & jump model. The diffusion coefficient resulting from either model is about two orders of magnitude above the macroscopic diffusion coefficient.

The introduction of this additional parameter can be naturally avoided when assuming a flow motion with the most likely velocity $v_0 \approx 1.8\,\frac{\mathrm{nm}}{\mathrm{ns}}$ at 30 °C and $v_0 \approx 2.1\,\frac{\mathrm{nm}}{\mathrm{ns}}$ at 40 °C. The good agreement with the MD simulation can be seen in Figure 6.

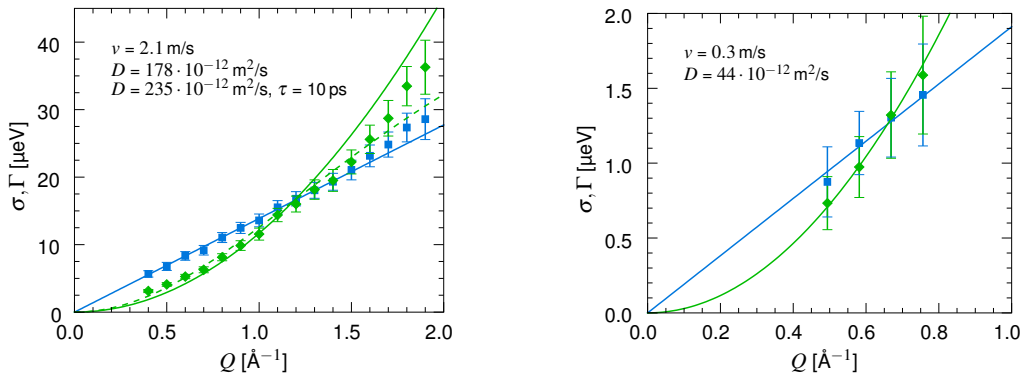

Figure 5: Left: Evaluation of the 35 ps measurement at 40 °C with models (3) and (5). The resulting line widths (standard deviations and half widths at half maximum, respectively) are fitted with the corresponding equations (3b) and (5b). Both diffusion models are plotted: continuous diffusion as drawn-out line and stop & go diffusion as dashed line. Right: Same for the 0.9 ns measurement at 30 °C (the only one measured above the main phase transition). Due to the limited amount of data points, stop & go diffusion was not fitted.

For the 0.9 ns measurement, both, diffusion and flow do fit the line width (standard deviation and half width at half maximum, respectively). However, the diffusion coefficient is $40 \cdot 10^{-12}\,\frac{\mathrm{m}^2}{\mathrm{s}}$, still one order of magnitude above the macroscopic value. In contrast, the velocity of a ballistic motion coincides very nicely with the value obtained by Falck et al. at a simulation time of 1 ns – about $0.3\,\frac{\mathrm{nm}}{\mathrm{ns}}$. This suggests that the reason for the observed faster motion is indeed the flow

motion.

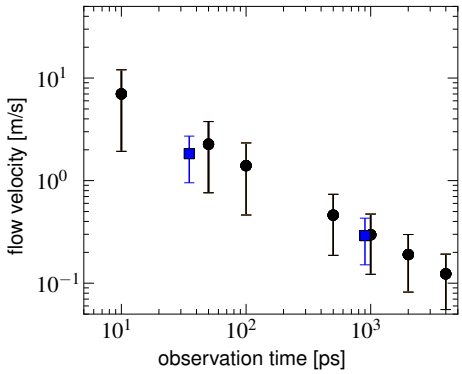

Figure 6: Flow velocity as a function of observation time. Black: results from MD simulation of DPPC roughly 20 K above the main phase transition, taken from Falck et al. [18] Blue: results from the present study of DMPC, also roughly 20 K above the main phase transition (at 30 °C). The error bars indicate the width of the Maxwell-Boltzmann distribution.

It should be noted that the flow velocity is nearly three orders of magnitude below the thermal expectation value $\sqrt{2k_BT/m}$. Therefore, it can be excluded that this is the initial phase of "free flight" every molecule performs before the interactions with the neighbouring molecules have completely built up. This is in agreement with time scales obtained from NMR experiments and MD simulations.[19,20]

Identification of the Internal Motions

This study is not focussed on the internal motions which have been investigated elsewhere in detail (cf. the references in the following). Their interpretation is decoupled from the long-range motion and therefore not essential for the question examined here. However, as they are measured naturally along with the long-range motion on a quasielastic neutron scattering spectrometer, we add a short overview over different models and possible interpretations.

Explicit Model

Fitting model (7) with a vibrational background and a Brownian oscillator to the 35 ps measurement at 30 °C yields at large Q for the Brownian oscillator a δ^2 of 0.25 Å^2. However, this value is not independent of Q but increases at small Q to more than 1 Å. Also the intensity of the vibrational background shows anomalies in this region, not following a Q^2 behaviour any more but levelling off at a plateau. These effects are probably due to the rigidity of the model and multiple scattering effects.[13,21]

Also other explicit models incorporating for example CH_3 group rotation had the same problems at low Q. Therefore, the generalized model was preferred which is flexible enough to be largely unaffected by the disturbing effects. As will be shown, the extracted δ^2 is in agreement with the value extraced here in the high Q limit.

Generalized Approach

In model (5), the localized motions were assumed to have an exponentially decaying intermediate scattering function that levels off at a plateau value, the EISF. The rates of the decays were fitted to 0.11 ps^{-1} for the slow motion and 1.4 ps^{-1} for the fast motion. The corresponding EISF, shown in Figure 7, does not decay to zero at large Q which was accounted for by assuming that not all protons participate in both motions.

The EISF is influenced by both, the spread of the motion and the fraction of participating protons.[22] The introduction a fraction of participating scatterers p results in a definition of the EISF as a function of the EISF that would be observed if all scatterers participated,

$$A_{\text{fraction}} = 1 - p + p \cdot A_{\text{all}} \ . \tag{9}$$

As can be seen in Figure 7, the EISFs drop stronger as the temperature is increased, corresponding to an increased mobility. The values of the fast and the slow motion are very similar for the low temperatures, however the slow motion spreads significantly more than the fast motion

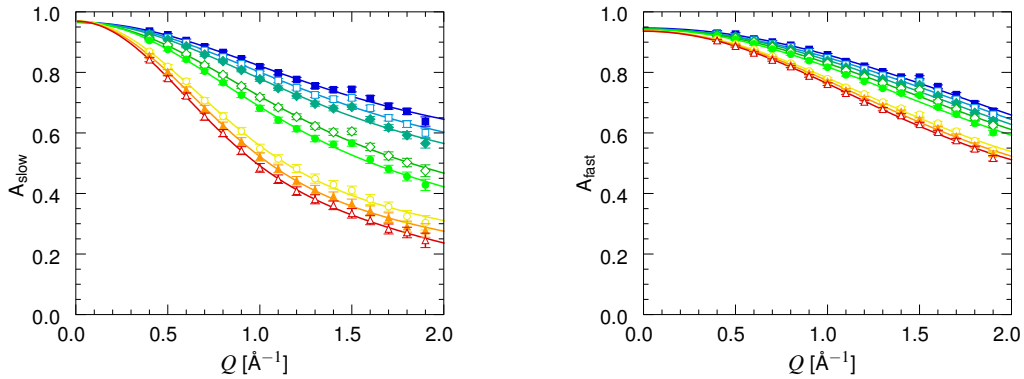

Figure 7: The elastic incoherent structure factor of the slow and fast localized motion, respectively. The drawn-out lines are fits of equations (10) and (11) to the data points. The points at 1.5 Å^{-1} are left out due to anomalies caused by coherent scattering. The size of the fast motion increases notably at the main phase transition, the one of the slow motion at both, the pre and main transition.

when the sample is heated. The main phase transition is effecting both motions, the pretransition only the slow motion.

Arguing that the tails dominate the scattering signal, these motions can be attributed to two modes from the tails. Following Doxastakis et al.,[23] these two modes could be fast torsional vibrations around mean values and conformational jumps between these values as they observed in MD simulations of dry phospholipid.[24]

Another tentative assignment of the two motions would be – justified only by approximate correspondence of the fractions of participating scatterers with the scattering cross sections of head and tail, respectively – a slow, large-scale motion of the tails and a fast, more restricted motion of the head groups. The EISF of the slow component (tentatively assigned to the tails) was in this frame analyzed with the model of particles diffusing inside spheres[24,25] with increasing radii. This assumes that the protons can move in a small restricted volume which gets bigger the further away the proton is located from the backbone. It reads

$$A_{\text{slow}}(Q) = a \cdot \left(p \cdot \frac{1}{N} \cdot \sum_{i=0}^{N} \left(\frac{3 \cdot j_1(Q \cdot R_i)}{Q \cdot R_i} \right)^2 + (1-p) \right) \tag{10a}$$

with

$$R_i = R_{\min} + \frac{i}{N} \cdot (R_{\max} - R_{\min}) \ . \tag{10b}$$

A prefactor a was introduced to account for multiple scattering effects as $A(Q \to 0) \neq 1$, cf. Figure 7.[13] j_1 is the spherical Bessel function of first order. N was set to 13, the number of hydrocarbon units in the tails, but no change was observed when increasing N to e. g. 30. The minimal radius of the spheres increases with temperature from 0.0 to 0.2 Å, the maximal from 2.0 to 3.6 Å. Both phase transitions are visible as increase of the radii, as can already be seen in Figure 7.

For the thorough analysis of the data with the model "diffusion inside a sphere", one would need to employ a more explicit fit function than equation (5). However, as shown above, this does not lead to consistent results due to the introduced inflexibility which is given here essentially by the prefactor a. It is obvious that this effect is strongest at small values of Q which explains the difficulties of the explicit model in this region.

The EISF of the fast motion, which was preliminary assigned to motions of the head group, was analyzed with the model of a Brownian oscillator,[7,26] describing particles that perform diffusive motions in a harmonic potential by

$$A_{\text{fast}}(Q) = a \cdot \left(p \cdot e^{-Q^2 \cdot \delta^2} + (1-p) \right) \ . \tag{11}$$

The resulting mean squared displacement δ^2 rises with temperature from 0.24 to 0.37 Å^2. Note that this agrees well with the large Q limit obtained from the explicit model equation (7) which is a further indication that it is valid to use the generalized approach. The main phase transition is visible as increase of the mean squared displacement.

It seems natural to assign the fast motion to the head group and the slow one to the tails. The head groups are more densely packed and perform fast oscillating diffusive motions between their neighbours. The tails have more space, are more affected by the phase transitions, and can be described by the plausible model of diffusion in spheres with increasing radii. Also the fractions of participating protons agree roughly with the scattering cross sections shown in Figure 1. It should

however be noted that these fractions change with temperature which shows that – as expected – the localized motions of this complex molecule cannot be described by such a simple model.

References

(1) (a) König, S.; Bayerl, T. M.; Coddens, G.; Richter, D.; Sackmann, E. *Biophysical Journal* **1995**, *68*, 1871; (b) Klösgen, B.; Reichle, C.; Kohlsmann, S.; Kramer, K. D. *Biophysical Journal* **1996**, *71*, 3251.

(2) Pearson, R. H.; Pascher, I. *Nature* **1979**, *281*, 499.

(3) Sears, V. F. *Neutron News* **1992**, *3*, 26.

(4) (a) Unruh, T.; Neuhaus, J.; Petry, W. *Nucl. Instrum. Methods Phys. Res., Sect. A* **2007**, *580*, 1414–1422; (b) Unruh, T.; Neuhaus, J.; Petry, W. *Nucl. Instrum. Methods Phys. Res., Sect. A* **2008**, *585*, 201.

(5) Unruh, T.; Smuda, C.; Busch, S.; Neuhaus, J.; Petry, W. *The Journal of Chemical Physics* **2008**, *129*, 121106.

(6) (a) Squires, G. L. *Introduction to the Theory of Thermal Neutron Scattering*; Dover Publications, 1996; (b) Bée, M. *Quasielastic Neutron Scattering*; Taylor & Francis, 1988; (c) Boon, J. P.; Yip, S. *Molecular Hydrodynamics*; McGraw-Hill Inc.,US, 1980.

(7) *Neutron Scattering in Biology: Techniques and Applications (Biological and Medical Physics, Biomedical Engineering)*, 1st ed.; Fitter, J., Gutberlet, T., Katsaras, J., Eds.; Springer, 2006.

(8) (a) Wuttke, J. *Physica B Condensed Matter* **1999**, *266*, 112; (b) Wuttke, J. *Physica B Condensed Matter* **2000**, *292*, 194.

(9) Wuttke, J. *Fast Reliable Interactive Data Analysis*. `http://sourceforge.net/projects/frida/`.

(10) Paalman, H. H.; Pings, C. J. *Journal of Applied Physics* **1962**, *33*, 2635.

(11) (a) Pardo, L. C.; Rovira-Esteva, M.; Busch, S. *Fitting Algorithm for Bayesian Analysis of Data*. `http://gcm.upc.edu/members/luis-carlos/bayesiano`; (b) Pardo, L. C.; Rovira-Esteva, M.; Busch, S.; Ruiz-Martín, M. D.; Tamarit, J. L.; Unruh, T. *http://arxiv.org/abs/0907.3711v3* **2009**; (c) Sivia, D. S.; Skilling, J. *Data Analysis: A Bayesian Tutorial*, 2nd ed.; Oxford University Press, USA, 2006.

(12) Singwi, K. S.; Sjölander, A. *Physical Review* **1960**, *119*, 863.

(13) Busch, S. et al. *in preparation* **2010**.

(14) *Phospholipids Handbook*, 1st ed.; Cevc, G., Ed.; CRC, 1993.

(15) Cevc, G.; Marsh, D. *Phospholipid Bilayers: Physical Principles and Models (Cell Biology : a Series of Monographs, Vol 5)*; John Wiley & Sons, 1987.

(16) Sivia, D. S.; Carlile, C. J.; Howells, W. S.; König, S. *Physica B Condensed Matter* **1992**, *182*, 341.

(17) Tabony, J.; Perly, B. *Biochimica et Biophysica Acta (BBA) - Biomembranes* **1991**, *1063*, 67.

(18) Falck, E.; Róg, T.; Karttunen, M.; Vattulainen, I. *J. Am. Chem. Soc.* **2008**, *130*, 44–5.

(19) Ayton, G. S.; Voth, G. A. *Biophys. J.* **2004**, *87*, 3299–311.

(20) Wohlert, J.; Edholm, O. *The Journal of Chem. Phys.* **2006**, *125*, 204703.

(21) Perez, J.; Zanotti, J.-M.; Durand, D. *Biophysical Journal* **1999**, *77*, 454.

(22) Smuda, C.; Busch, S.; Schellenberg, R.; Unruh, T. *Journal of Physical Chemistry B* **2009**, *113*, 916–922.

(23) Doxastakis, M.; Sum, A. K.; de Pablo, J. J. *The journal of physical chemistry. B* **2005**, *109*, 24173–81.

(24) Doxastakis, M.; García Sakai, V.; Ohtake, S.; Maranas, J. K.; de Pablo, J. J. *Biophys. J.* **2007**, *92*, 147–61.

(25) König, S.; Pfeiffer, W.; Bayerl, T. M.; Richter, D.; Sackmann, E. *Journal de Physique II France* **1992**, *2*, 1589.

(26) (a) Knapp, E. W.; Fischer, S. F.; Parak, F. *The Journal of Physical Chemistry* **1982**, *86*, 5042; (b) Knapp, E. W.; Fischer, S. F.; Parak, F. *The Journal of Chemical Physics* **1983**, *78*, 4701; (c) Parak, F.; Knapp, E. W.; Kucheida, D. *Journal of Molecular Biology* **1982**, *161*, 177.

(27) Teixeira, S.; Ankner, J.; Bellissent-Funel, M.-C.; Bewley, R.; Blakeley, M.; Coates, L.; Dahint, R.; Dalgliesh, R.; Dencher, N.; Dhont, J.; Fischer, P.; Forsyth, V.; Fragneto, G.; Frick, B.; Geue, T.; Gilles, R.; Gutberlet, T.; Haertlein, M.; Hauß, T.; Häußler, W.; Heller, W.; Herwig, K.; Holderer, O.; Jurányi, F.; Kampmann, R.; Knott, R.; Kohlbrecher, J.; Kreuger, S.; Langan, P.; Lechner, R. E.; Lynn, G.; Majkrzak, C.; May, R.; Meilleur, F.; Mo, Y.; Mortensen, K.; Myles, D.; Natali, F.; Neylon, C.; Niimura, N.; Ollivier, J.; Ostermann, A.; Peters, J.; Pieper, J.; Rühm, A.; Schwahn, D.; Shibata, K.; Soper, A.; Straessle, T.; Suzuki, U.; Tanaka, I.; Tehei, M.; Timmins, P.; Torikai, N.; Unruh, T.; Urban, V.; Vavrin, R.; Weiss, K.; Zaccai, G. *Chemical Physics* **2008**, *345*, 133–151.

Appendix C.

Dynamical Transition of Protein-Hydration Water

Wolfgang Doster, **Sebastian Busch**, Ana M. Gaspar, Marie-Sousai Appavou, Joachim Wuttke, and Hugo Scheer
Physical Review Letters, 104(9):098101, 2010
http://dx.doi.org/10.1103/PhysRevLett.104.098101

In this publication, the author participated in the measurements and data evaluation. He performed the fits presented in figure 3 of the publication. He participated actively in the preparation of the manuscript and wrote large parts of its third page, relying on previous versions of Wolfgang Doster and Joachim Wuttke. He also took part in the development of the data evaluation software used in this publication.

The mean correlation times $\langle\tau\rangle$ of protein hydration water had previously been found to exhibit a peculiar shape when shown in an Arrhenius plot [105]: a transition from a fragile, super-Arrhenius temperature dependence at high temperatures and small correlation times to a strong, Arrhenius behaviour at low temperatures and correspondingly long correlation times. As long correlation times correspond to small line widths in the neutron scattering spectra, this means that the levelling off of the data points at long correlation times corresponds to a levelling off at small line widths: a phenomenon that was also observed in the phospholipid samples [B].

It could be shown here that this levelling off can be prevented by using an improved fit routine. With a closer study of the mechanisms that cause this fit artifact, it became clear that the levelling off observed for the phospholipid samples is also not related to a physical effect but merely to the data evaluation procedure [D].

Wolfgang Doster, Sebastian Busch, Ana M. Gaspar, Marie-Sousai Appavou, Joachim Wuttke, and Hugo Scheer, Physical Review Letters, 104(9):098101, 2010.
"Copyright 2010 by the American Physical Society."

PRL **104,** 098101 (2010) PHYSICAL REVIEW LETTERS week ending 5 MARCH 2010

Dynamical Transition of Protein-Hydration Water

W. Doster,* S. Busch, and A. M. Gaspar
Physik Department E 13 and ZWE FRM II, Technische Universität München, 85747 Garching, Germany

M.-S. Appavou and J. Wuttke
Forschungszentrum Jülich, JCNS at FRM II, Lichtenbergstrasse 1, 85747 Garching, Germany

H. Scheer
Botanisches Institut II, Ludwig-Maximilians-Universität München, Menzinger Strasse 67, 80638 München, Germany
(Received 22 July 2009; published 2 March 2010)

Thin layers of water on biomolecular and other nanostructured surfaces can be supercooled to temperatures not accessible with bulk water. Chen *et al.* [Proc. Natl. Acad. Sci. U.S.A. **103**, 9012 (2006)] suggested that anomalies near 220 K observed by quasielastic neutron scattering can be explained by a hidden critical point of bulk water. Based on more sensitive measurements of water on perdeuterated phycocyanin, using the new neutron backscattering spectrometer SPHERES, and an improved data analysis, we present results that show no sign of such a fragile-to-strong transition. The inflection of the elastic intensity at 220 K has a dynamic origin that is compatible with a calorimetric glass transition at 170 K. The temperature dependence of the relaxation times is highly sensitive to data evaluation; it can be brought into perfect agreement with the results of other techniques, without any anomaly.

DOI: 10.1103/PhysRevLett.104.098101 PACS numbers: 64.70.pm, 87.15.H−

In contrast to bulk water, protein-hydration water can be supercooled down to a glass transition at $T_g \simeq 170$ K. Near T_g translational degrees of freedom arrest, which induces discontinuities in the specific heat and the thermal expansion coefficient of the hydration water [1–4]. Because of the dynamic nature of the glass transition, freezing of microscopic degrees of freedom can already be observed far above T_g.

The *protein dynamic transition* is an abrupt onset of atomic displacements on the microscopic length and time scale probed by quasielastic neutron scattering (QENS). First observed 20 years ago in hydrated myoglobin and lysozyme at $T_\Delta \simeq 240$ K [5], it is now known to be a generic property of hydrated proteins, while it is absent in dehydrated systems. It is therefore related to the dynamics of the hydration shell.

In QENS, mean squared dispacements $\langle \delta x^2 \rangle$ are deduced from the elastic scattering intensity $S(q, 0)$. Because of the finite spectrometer resolution (FWHM $2\Delta\omega$), one actually measures $S(q, |\omega| \lesssim \Delta\omega)$. Full spectral measurements show that the anomalous decrease of the central peak is compensated by increasing inelastic wings [5,6]. These effects have been interpreted as precursors of the glass transition. Since QENS probes structural relaxation at $\Delta\omega^{-1} \simeq 100$ ps, while the calorimetric T_g refers to a time scale of 100 s, it is natural that T_Δ is located far above T_g: the protein dynamic transition is the microscopic manifestation of the glass transition in the hydration shell. The time-scale dependence of T_Δ also explains its variation with viscosity [7–9].

Recently, these views have been challenged by the suggestion that there might be a time-scale independent transition. Support came mainly from QENS experiments on the backscattering spectrometer HFBS at NIST. In hydrated lysozyme, DNA and RNA, a kink was found not only in $S(q, |\omega| \lesssim \Delta\omega)$, but also in the α relaxation time $\langle \tau \rangle$ deduced from full spectra $S(q, \omega)$ [10–13]. This change of $\langle \tau \rangle(T)$ from high-T super-Arrhenius to low-T Arrhenius behavior at $T_L \simeq 220$ K has been interpreted as a *fragile-to-strong-transition (FST)* from the high density (HDL) to the less fluid low density phase (LDL) of supercooled water [14]. In this view, a qualitative change in the dynamics occurs when the so-called Widom line is crossed, which extrapolates the phase boundary beyond the conjectured critical point [15,16].

Similar behavior was found for confined water in various nonbiological environments [[17,18] and references therein]; T_L was mostly located between 215 and 228 K. There were, however, two remarkable exceptions: making a substrate hydrophobic lowered T_L by 35 K [19]; using another neutron spectrometer with wider dynamic range lowered T_L by about 10 to 20 K [20]. Critics objected that relaxation times measured by other spectroscopic techniques show no anomaly at T_L [21–23].

In this Letter we will argue that the changing temperature dependence of $\log(\langle \tau \rangle)$ is likely to be an artifact of the data analysis, and that the kink in the elastic intensity also admits a conventional, *dynamic* interpretation. We will refer to the hydration shell of different proteins. If the anomalies observed around T_L were due to an intrinsic property of water, then the choice of the protein should not matter.

To improve the empirical base, we measured the motion of protein-hydration water with enhanced sensitivity, using

 © 2010 The American Physical Society

a new neutron spectrometer and a fully deuterated protein. We chose deuterated C-phycocyanin (D-CPC), a light harvesting, blue copper protein. Deuteration drastically reduces scattering from the protein so that we become more sensitive to weak quasielastic scattering from the hydration water. CPC has been investigated by neutron scattering before [24–28]. The sample was purified from a preparation of Crespi [28,29] with nearly 99% deuteration. The absorbance ratio $A_{620\,\mathrm{nm}}/A_{280\,\mathrm{nm}} \simeq 7.3$ is above the analytic-grade value of 5 [30]. The integrity of the secondary structure was ascertained by CD spectroscopy. The protein was dialyzed against distilled water, freeze dried, and rehydrated to $h = 0.3$ g/g [27], the same degree of hydatrion as in Ref. [10].

QENS was performed on 500 mg of hydrated D-CPC with the new backscattering spectrometer SPHERES at FRM II [31]. It has a resolution (FWHM) of 0.62 μeV (HFBS 0.85 μeV), high flux, and an outstanding signal-to-noise ratio of 1000:1. Scattering wave numbers q range from 0.2 to 1.8 Å^{-1}. We chose about the same energy range ± 10 μeV as customary at HFBS. Spectra at temperatures T between 100 and 300 K were collected for 6 to 12 h. An empty cell measurement was subtracted and spectra were normalized to a vanadium standard. The analysis was performed with the program FRIDA [32].

Figure 1 displays selected spectra in the relevant temperature range. The logarithmic intensity scale emphasizes both the broad, asymmetric wing of the instrumental resolution function, unavoidable in a crystal spectrometer, and the quasielastic scattering. At least two distinct components of the scattering function $S(q, \omega)$ can be observed: (i) An elastic component that has the shape of the instrumental resolution function $R_q(\omega)$. It is mainly due to the coherent structure factor of the protein (as evidenced by strong small-angle scattering for $q \ll 1$ Å^{-1} [27]), as well as to a protein incoherent term mainly due to the exchanged protons (25%). Also immobilized water near charged groups contributes to this component. (ii) A quasielastic component that appears above about 170 K. It is mainly due to motion of adsorbed H_2O molecules.

To start with a model-free data characterization, we examined the T dependence of the integrated inelastic intensity for different ω intervals, preferentially on the $\omega < 0$ side where the resolution wing is weaker. Between 180 and 230 K, the inelastic intensity begins to rise strongly. There is no sharp kink; the temperature of maximum inflection depends on the ω range and on q [Fig. 2(a)]. This is a first indication for a dynamic phenomenon rather than a hidden phase transition: the q and T dependence is compatible with a smooth onset of translational diffusion. The elastic intensity in compensation shows a steplike decrease at 220 K in parallel with data obtained with lysozyme. This suggests a common transi-

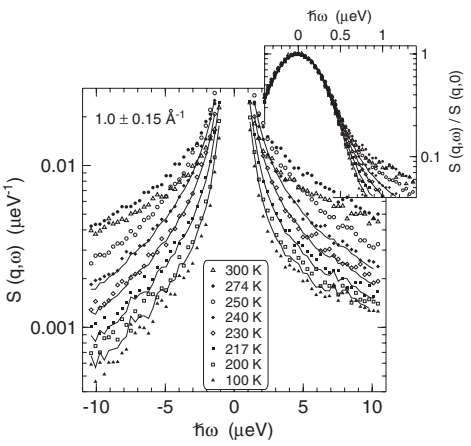

FIG. 1. Neutron scattering spectra of H_2O on D-CPC at $q = 1.0 \pm 0.15$ Å^{-1}. Note the truncated logarithmic scale. Solid lines are fits with (1), convoluted with the instrumental resolution (sample data at 100 K).—Inset: central peak, normalized to the value at $\omega = 0$.

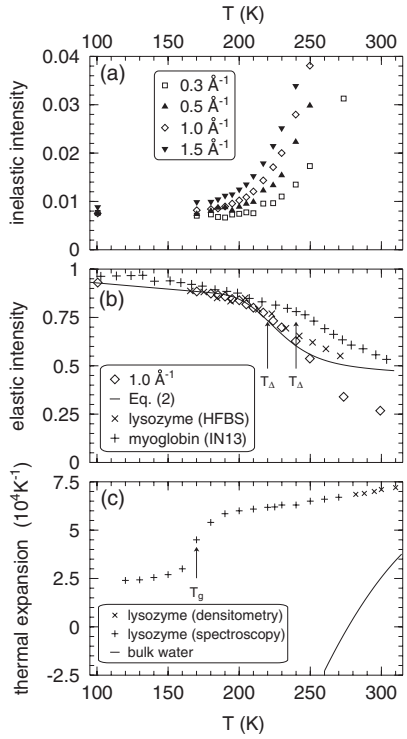

FIG. 2. (a) Scattering intensity integrated over $\hbar\omega < -3$ μeV. (b) Elastic scattering intensity $S(q, 0)$ and result of (2), compared to literature data [5,10]. (c) Thermal expansion coefficient α_P of water in hydrated lysozyme powder (+, spectroscopic measurement [3]), of hydration water in lysozyme solution (×, densitometry, [36]), of bulk water (line).

PRL **104,** 098101 (2010) PHYSICAL REVIEW LETTERS week ending 5 MARCH 2010

tion temperature of both hydrated proteins [Fig. 2(b)]. In the following, we concentrate on $q = 1.0 \pm 0.15$ Å^{-1}.

To analyze the spectra, we use the same model as Chen *et al.* [10], consisting of an elastic line and a Kohlrausch-Williams-Watts function (KWW, Fourier transform of a stretched exponential [33]):

$$S_{\rm th}(q,\omega) = f_q\left\{a_1\delta(\omega) + a_2\int_{-\infty}^{\infty}\frac{dt}{2\pi}e^{i\omega t-(|t|/\tau)^\beta}\right\}. \quad (1)$$

The Debye-Waller factor $f_q = \exp(-\langle\delta x^2\rangle q^2)$ accounts for phonon scattering outside our energy window. The mean squared displacement $\langle\delta x^2\rangle$ is assumed to be linear in T; from 100 and 170 K: $\partial\langle\delta x^2\rangle/\partial T = 7\times10^{-4}$ Å^2/K. β was fixed to 0.5 as in the analysis of Chen *et al.*

Equation (1) can fit the data sets for $T \leq 240$ K, hereby covering the temperature range of the proposed transition. At higher T, the data start to deviate from Eq. (1): additional quasielastic scattering, likely due to relaxational or fast anharmonic motion of the protein, is not included in this bimodal model.

In a first attempt to extract the relaxation times, we have used a standard fitting procedure for the data evaluation. Fitting the quasielastic wings for $T < 240$ K, we are in the regime $\omega\tau \gg 1$, where the KWW function goes in first order with $(\omega\tau)^{-1-\beta}$. In such a power-law regime, the fit parameters amplitude and time-scale τ are degenerate. Therefore, the 240 K data were used to determine the relative contribution of the water $a_2/(a_1 + a_2)$ to 0.42 which was then used as input for the other temperatures.

However, this approach neglects a severe limitation of the standard fitting procedure for narrow lines: When fitting the central peak, the convolution of $S_{\rm th}$ with the experimental resolution $R_q(\omega)$ becomes nontrivial for $T \lesssim 220$ K where the peak in the KWW function becomes so sharp (compared to the experimental energy binning) that the straightforward calculation $S_{\rm th}(q,\omega)\otimes R_q(\omega)$ as a Riemann sum yields a wrong amplitude a_1. Because of the mentioned degeneracy of amplitude and time scale, this results in a distorted $\langle\tau\rangle$. We have therefore repeated the fits with an improved fitting procedure, neglecting the erroneous a_1 and fixing directly a_2 at 0.42.

Figure 3 shows an Arrhenius plot of the mean relaxation time $\langle\tau\rangle = \int dt\exp(-t/\tau)^\beta = \beta^{-1}\Gamma(\beta^{-1})\tau$ resulting from both fitting procedures. As can be seen, the temperature dependence of the relaxation times obtained from the standard fitting procedure resembles the results of Chen *et al.* This trend is however not observed any more in the results of the improved fitting procedure which agree well with the structural (α-)relaxation times of water on other proteins taken from literature (also shown). There is a good agreement with high-T myoglobin data measured by QENS over a wider energy range than covered here [8] and for $T \lesssim 220$ K with both, NMR [34] and dielectric spectroscopy [4] which show a smooth increase without inflection at 220 K. The curvature of $\langle\tau\rangle$ in the Arrhenius

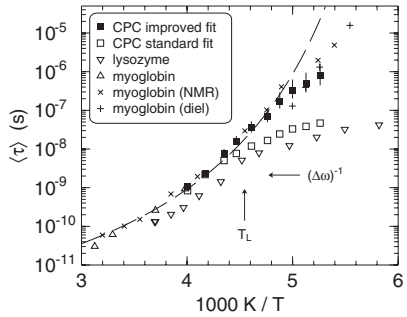

FIG. 3. Average relaxation times $\langle\tau\rangle$ versus reciprocal temperature for hydration water on different proteins: (■): *c*-phycocyanin with improved fitting procedure and (□): with a standard fitting procedure. Error bars were estimated by varying β between 0.45 and 0.55. (▽): lysozyme, QENS [10]. (△): myoglobin, QENS with wide ω range [8]. (×): myoglobin, NMR [34]. (+): myoglobin, dielectric loss [4], vertical arrow: conjectured T_L of the FST, horizontal arrow: instrumental resolution $(\Delta\omega)^{-1}$. Dashed line: Vogel-Fulcher fit to the data above 200 K with fixed $T_g = 170$ K, yielding $\langle\tau\rangle_0 = 6.5\times10^{-13}$ s, $T_H = 745$ K, and $T_0 = 147$ K.

plot indicates fragile behavior according to a Vogel-Fulcher relation, $\langle\tau\rangle = \langle\tau\rangle_0\exp[T_H/(T - T_0)]$.

For low T, our $\langle\tau\rangle$ exceeds the resolution $\Delta\omega^{-1} \simeq 2$ ns by some orders of magnitude. Still, for $|\hbar\omega| \gtrsim 2$ μeV there are clear quasielastic wings that allow to determine τ within the chosen model with fixed parameters a_2 and β. Therefore, this analysis can be used to probe the spectral behavior for the predicted FST discontinuity.

Whereas our first analysis, using the standard fitting procedure, reproduces the results from hydrated lysozyme [10]—the basis for the postulated FST at 220 K—we can rule out any discontinuity at this temperature using the improved fitting procedure. We suspect therefore that also the various results backing the FST are affected by the problems of the standard fitting procedure: In the power-law regime $\omega\tau \gg 1$, fitted $\langle\tau\rangle$ are meaningful only if the amplitude a_2 has been fixed at a physically reasonable value. In the FST reports, the amplitude, if mentioned at all, is just called a *scaling constant* [17]. The fitted $\langle\tau\rangle(T)$ are therefore possibly distorted by an uncontrolled drift of $a_2(T)$. This could explain why the crossover temperature T_L varies with pressure, while the crossover time appears constant [13].

Below approximately 200 K, the relaxation times extracted from our improved technique deviate slightly from the Vogel-Fulcher relation. Being orders of magnitude above the instrumental resolution, a detailed discussion of this effect seems inadequate. If it were real, one could attribute it to the onset of the glass transition which is known to be about 30 K broad [4,35]. The observed process would then no longer be the isotropic α relaxation [34].

In contrast to the kink in $\langle\tau\rangle$, the kink in the observed elastic scattering intensity $S(q, |\omega| \lesssim \Delta\omega)$ is an undisput-

able experimental fact. Figure 2(b) shows that observations at SPHERES (D-CPC) and HFBS (lysozyme [10]) almost coincide below 240 K. The difference at higher T can be explained by our use of deuterated CPC, which reduces the relative contribution of the protein.

The expected elastic scattering is

$$S_{\rm exp}(q,0) = \int d\omega S_{\rm th}(q,\omega) R_q(-\omega) = f_q\left\{a_1 R_q(0) + (1-a_1)\int_0^\infty \frac{dt}{\pi} e^{-(t/\tau)^\beta}\tilde{R}_q(t)\right\} \quad (2)$$

with $\tilde{R}_q(t) = \int d\omega \cos(\omega t) R_q(\omega)$. Indeed, the low-$T$ data are perfectly reproduced by Eq. (2) using the values from the Vogel-Fulcher relation for $\langle\tau\rangle$. This confirms the long established explanation of the protein dynamic transition as a time-scale dependent glass transition: When τ^{-1} exceeds the instrumental resolution $\Delta\omega$, then the central part of the KWW spectrum starts to broaden so that $S(q, |\omega| \lesssim \Delta\omega)$ falls below f_q.

This is further corroborated by elastic scattering ($q = 1.4$ Å^{-1}) from hydrated myoglobin on the thermal neutron backscattering spectrometer IN13 [5]. Its resolution width $2\hbar\Delta\omega = 8$ μeV is an order of magnitude larger than that of HFBS or SPHERES, and the kink in $S(q, |\omega| \lesssim \Delta\omega)$ is observed accordingly at a higher temperature, namely, the often reported $T_\Delta \simeq 240$ K.

Previous QENS experiments were motivated by the hope that hydration layers would provide an opportunity to study water in a deeply supercooled state that is not accessible in the bulk. However, thin hydration layers seem to be qualitatively different from bulk water [21]. This view is also supported by literature data of the thermal expansion coefficient α_P of lysozyme hydration water [Fig. 2(c)]. In concentrated solution, α_P is nearly T independent and much larger than the bulk value [36]. In hydrated powder, α_P is estimated from the O-H stretching frequency of water, which varies with the average H bond length. A striking step is found near 170 K, induced by the softening of the O-H–O hydrogen bond network [3]. No anomaly is observed at $T_L \simeq 220$ K.

All observations agree, however, with a glass transition of the hydration shell and a dynamic onset temperature T_Δ, which varies with the probe frequency [Fig. 2(b)]. The different values of α_P for bulk and hydration water could indicate that the protein acts as a patch-breaker [37], suppressing critical fluctuations present in bulk water.

This work has been supported by Deutsche Forschungsgemeinschaft through SFB 533. We thank the late Henry Crespi for providing D-CPC.

*wdoster@ph.tum.de

[1] W. Doster, BBA Proteins and Proteomics **1804**, 3 (2010).
[2] Y. Miyazaki, T. Matsuo, and H. Suga, J. Phys. Chem. B **104**, 8044 (2000).
[3] F. Demmel, W. Doster, W. Petry, and A. Schulte, Eur. Biophys. J. **26**, 327 (1997).
[4] H. Jansson and J. Swenson, BBA Proteins and Proteomics **1804**, 20 (2010).
[5] W. Doster, S. Cusack, and W. Petry, Nature (London) **337**, 754 (1989).
[6] W. Doster, S. Cusack, and W. Petry, Phys. Rev. Lett. **65**, 1080 (1990).
[7] H. Lichtenegger *et al.*, Biophys. J. **76**, 414 (1999).
[8] W. Doster and M. Settles, BBA Proteins and Proteomics **1749**, 173 (2005).
[9] W. Doster, Eur. Biophys. J. **37**, 591 (2008).
[10] S.-H. Chen *et al.*, Proc. Natl. Acad. Sci. U.S.A. **103**, 9012 (2006).
[11] S.-H. Chen, L. Liu, and Y. Zhang, J. Chem. Phys. **125**, 171103 (2006).
[12] X.-Q. Chu *et al.*, Phys. Rev. E **77**, 011908 (2008).
[13] X.-Q. Chu *et al.*, J. Phys. Chem. B **113**, 5001 (2009).
[14] P. Poole, F. Sciortino, U. Essmann, and H. E. Stanley, Nature (London) **360**, 324 (1992).
[15] K. Ito, C. T. Moynihan, and C. A. Angell, Nature (London) **398**, 492 (1999).
[16] L. Xu *et al.*, Proc. Natl. Acad. Sci. U.S.A. **102**, 16558 (2005).
[17] E. Mamontov *et al.*, Chem. Phys. **352**, 117 (2008).
[18] E. Mamontov *et al.*, Phys. Rev. E **79**, 051504 (2009).
[19] X.-Q. Chu *et al.*, Phys. Rev. E **76**, 021505 (2007).
[20] E. Mamontov *et al.*, J. Phys. Chem. C **112**, 12334 (2008).
[21] J. Swenson, H. Jansson, and R. Bergman, Phys. Rev. Lett. **96**, 247802 (2006).
[22] S. Pawlus, S. Khodadadi, and A. P. Sokolov, Phys. Rev. Lett. **100**, 108103 (2008).
[23] M. Vogel, Phys. Rev. Lett. **101**, 225701 (2008).
[24] H. D. Middendorf and S. J. Randall, Phil. Trans. R. Soc. B **290**, 639 (1980).
[25] M. C. Bellissent-Funel, J. Teixera, K. F. Bradley, and S.-H. Chen, J. Phys. I (France) **2**, 995 (1992).
[26] I. Köper, S. Combet, W. Petry, and M. C. Bellissent-Funel, Eur. Biophys. J. **37**, 739 (2008).
[27] A. Gaspar *et al.*, BBA Proteins and Proteomics **1804**, 76 (2010).
[28] K. Bradley, S.-H. Chen, M. C. Bellissent-Funel, and H. L. Crespi, Biophys. Chem. **53**, 37 (1994).
[29] H. L. Crespi, in *Stable Isotopes in The Life Sciences* (IAEA, Vienna, 1977), p. 111.
[30] G. Patil, S. Chethana, A. S. Sridevi, and K. S. M. S. Raghavarao, J. Chromatogr. A **1127**, 76 (2006).
[31] J. Wuttke *et al.* (to be published), see http://www.jcns.info/jcns_spheres.
[32] J. Wuttke, FRIDA: fast reliable inelastic data analysis (http://www.messen-und-deuten.de/frida).
[33] J. Wuttke, libkww (http://www.messen-und-deuten.de/kww); arXiv:0911.4796v1.
[34] S. A. Lusceac, M. R. Vogel, and C. R. Herbers, BBA Proteins and Proteomics **1804**, 41 (2010).
[35] S. Khodadadi, A. Malkovskiy, A. Kisliuk, and A. P. Sokolov, BBA Proteins and Proteomics **1804**, 15 (2010).
[36] M. Hiebl and R. Maksymiw, Biopolymers **31**, 161 (1991).
[37] H. E. Stanley and J. Teixera, J. Chem. Phys. **73**, 3404 (1980).

Appendix D.

The Slow Short-Time Motions of Phospholipid Molecules With a Focus on the Influence of Multiple Scattering and Fitting Artefacts

Sebastian Busch and Tobias Unruh
Journal of Physics: Condensed Matter, 23(25):254205, 2011
http://dx.doi.org/10.1088/0953-8984/23/25/254205

In this publication, the author conceived the experiments and prepared the samples. The measurements were performed either by himself, together with students in the frame of teaching activities, or by Humphrey Morhenn. He performed the data evaluation and explained the mechanism behind the fit artefacts that he had got to know in the course of another publication [C]. He interpreted the results and wrote the publication.

The line width σ of the narrow component of a fit to quasielastic neutron scattering data, assigned to the long-range component, had previously been found to level off at small widths [B]. In this publication, it was shown that this effect is due to the same fit artifacts discussed elsewhere [C]. Although in this case a normal Levenberg-Marquardt algorithm is used for fitting, the artifact influences the results of a Monte Carlo fit [G, H] the same.

After taking measures to avoid the fit artifacts, is can be seen that the line widths do not level off at small values, on the observation time of about 60 ps, a confinement of the molecules is therefore not visible – neither above nor below the main phase transition of the phospholipid. This was interpreted as the consequence of relatively large lateral displacements caused by sloppy modes which are proposed to be connected to the dynamical heterogeneities that are visible above the main phase transition [E].

Copyright 2011 by the Institute of Physics (IOP).

IOPscience iopscience.iop.org

Home Search Collections Journals About Contact us My IOPscience

The slow short-time motions of phospholipid molecules with a focus on the influence of multiple scattering and fitting artefacts

This article has been downloaded from IOPscience. Please scroll down to see the full text article.

2011 J. Phys.: Condens. Matter 23 254205

(http://iopscience.iop.org/0953-8984/23/25/254205)

View the table of contents for this issue, or go to the journal homepage for more

Download details:
IP Address: 129.187.254.46
The article was downloaded on 09/06/2011 at 12:22

Please note that terms and conditions apply.

IOP Publishing Journal of Physics: Condensed Matter
J. Phys.: Condens. Matter **23** (2011) 254205 (11pp) doi:10.1088/0953-8984/23/25/254205

The slow short-time motions of phospholipid molecules with a focus on the influence of multiple scattering and fitting artefacts

Sebastian Busch[1] **and Tobias Unruh**[1,2]

[1] Physik Department E13 and Forschungs-Neutronenquelle Heinz Maier-Leibnitz (FRM II), Technische Universität München, Lichtenbergstraße 1, 85748 Garching bei München, Germany
[2] Lehrstuhl für Kristallographie und Strukturphysik, Friedrich-Alexander-Universität Erlangen-Nümberg, Staudtstraße 3, 91058 Erlangen, Germany

E-mail: sbusch@ph.tum.de and tobias.unruh@krist.uni-erlangen.de

Received 14 January 2011, in final form 28 February 2011
Published 8 June 2011
Online at stacks.iop.org/JPhysCM/23/254205

Abstract
Quasi-elastic neutron scattering is a powerful tool for the study of non-periodic motions in condensed matter, as a detailed line shape analysis can give information about the geometry and rate of the scatterers' displacements. Unfortunately, there are also a number of artefacts which can masquerade as signatures of motions and can therefore lead to erroneous results. Their influence on the evaluation of the motions of the phospholipid dimyristoylphosphatidylcholine (DMPC) is discussed. On a 60 ps timescale, the long-range motion of the molecules has a flow-like character with similar velocities above and below the main phase transition. It is proposed that the concepts of dynamical heterogeneities and 'floppy modes' developed in glass physics provide a framework for explaining the observed behaviour.

(Some figures in this article are in colour only in the electronic version)

1. Introduction

Recently, a quasi-elastic neutron scattering (QENS) experiment on the fully hydrated phospholipid dimyristoylphosphatidylcholine (DMPC) was published [1]. It corroborated collective flow-like motions as a novel view of the long-range motion of phospholipid molecules that had been put forward on the basis of molecular dynamics simulations [2]. A fit to the data showed that the component which was assigned to the long-range flow-like motion of the molecules levelled off at temperatures below the main phase transition (24 °C) and low values of Q as shown in figure 1. This was discussed as a sign of a confinement of the molecules during the 60 ps observation time in a cage of their neighbours—or an artefact [1, 3, 4].

The macroscopic diffusion of phospholipid molecules is known to decrease by about one order of magnitude when the membrane is cooled below the main phase transition [5]. In contrast, the high-Q part of the broadening caused by the long-range motion shown in figure 1 decreases much less. The confinement length that was extracted from the position of the deviation of the linear behaviour at low Q to about 9 Å coincides quite well with the molecular repeating distance in the membrane. This made a flow-like motion of the single molecules until they hit the cage of the neighbouring molecules seem reasonable.

However, it was already speculated there that this might be an artefact, as the broadening is very small compared to the instrumental resolution. A caging effect should also not only cause a plateau of the quasi-elastic broadening but also simultaneously cause an emerging elastic $\delta(\omega)$ component which was not observed. On a physical level, it is not clear why the flow-like, collective motions of the molecules, together with their caging neighbours above the phase transition, should persist at low temperatures for the single molecules within the cages.

The present contribution aims to clarify the picture of the motions of phospholipid molecules on a 60 ps timescale below the main phase transition. The two likely artefacts that could

 © 2011 IOP Publishing Ltd Printed in the UK & the USA

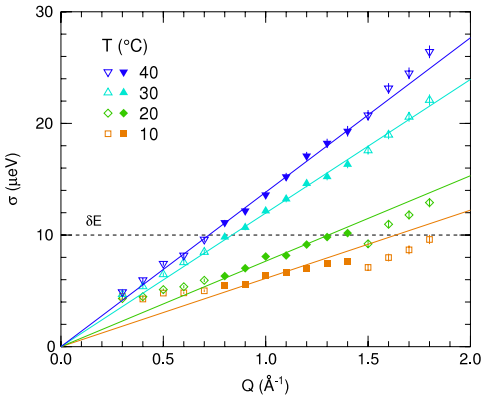

Figure 1. Width of the narrow Gaussian line of a three-component fit to the spectra of the fully hydrated phospholipid dimyristoylphosphatidylcholine (DMPC), very similar to the results published before in [1] where it was speculated that the levelling off of the widths at low temperatures and small Q could either be a signature of confinement of the molecules or an artefact. The distance between two data points in the spectra, $\delta E = 10\ \mu$eV, is indicated in the figure. The energy resolution is about 60 μeV, corresponding to an observation time of about 60 ps. The solid lines are fits to the filled points in the medium-Q region.

simulate the observed plateau of the broadening at low Q are studied: multiple scattering and fitting artefacts.

Only two years after the collection of the first neutron diffraction patterns ever in 1946 [6], multiple scattering was identified as the source of a spurious background contribution [7]. A few years later, efforts to treat multiple scattering (semi-)analytically began [8–11] and later complemented with Monte Carlo simulations [12–19].

However, still by far most quasi-elastic neutron scattering experiments study samples with very high transmission, in order to be able to neglect rather than correct multiple scattering. The transmission needed to justify this neglect is not agreed on in the literature—some authors feel safe with samples with a transmission of 99% [20], most adjust their samples to achieve a transmission of about 90% [21, 22], while others still feel comfortable with samples with a transmission as low as 70% [23].

It is also often unclear what to expect from uncorrected multiple scattering. An artificial broadening due to multiple scattering was, for example, assumed to yield a diffusion coefficient that was higher [24] than the generally accepted value [25, 26]. Others suggested that this broadening results in a Q dependence of the linewidth as shown in figure 1 which is normally interpreted as confined diffusion [4]. Offsets of the linewidth and the elastic incoherent structure factor (EISF) are also often observed [1, 11, 27, 28], some of which were shown to be due to multiple scattering.

Whereas the neutron scattering community is well aware of the problem of multiple scattering, fitting artefacts are widely ignored, which can lead to erroneous results: one crucial step is the numerical convolution of the theoretical fit function with the measured instrumental resolution [29]. The instrumental resolution gets more important as neutron spectroscopy is employed for the study of very slow motions because the line broadening caused by the sample gets small.

It is even sometimes said that the instrumental resolution should be seen as a lower limit for the detectable broadening. However, while this is a valid rule of thumb for localized motions, many measurements of long-range motions which cause a broadening of the whole line are done below this limit: from neutron scattering studies of diffusion in water [30] over proteins [28] to metallic liquids [31] or x-ray scattering studies of glass formers [32].

In the following, a short repetition of the basic assumptions of neutron scattering data evaluation is presented, highlighting the points where multiple scattering and fit artefacts come into play. After giving a description of the systems studied, the effects of multiple scattering and the point density used for the fit are described generally enough to be useful also for other experiments. The consequences for the evaluation of long-range and localized motions are presented and, with this knowledge, a coherent picture for the phospholipid dynamics is proposed.

2. Concepts of QENS data evaluation

The evaluation of QENS data relies vitally on the fact that the recorded number of neutrons as a function of solid angle and energy transfer, the double-differential cross section, can be transformed into the scattering functions $S^{\mathrm{exp}}_{\mathrm{coh,inc}}(\boldsymbol{Q},\omega)$ via [33–35]

$$\left(\frac{\mathrm{d}^2\sigma}{\mathrm{d}\omega\,\mathrm{d}\Omega}\right) = \frac{N\sigma_{\mathrm{coh}}}{4\pi}\frac{k_f}{k_i}S^{\mathrm{exp}}_{\mathrm{coh}}(\boldsymbol{Q},\omega) + \frac{N\sigma_{\mathrm{inc}}}{4\pi}\frac{k_f}{k_i}S^{\mathrm{exp}}_{\mathrm{inc}}(\boldsymbol{Q},\omega). \tag{1}$$

In this relation, it is assumed that a monochromatic beam of neutrons was scattered at most once in the sample and that the scattering lengths of the atoms do not correlate with their positions. It is often further simplified by neglecting the coherent scattering contributions of hydrogen-rich samples and using only the absolute value of the scattering vector, Q, for powder samples.

In order to account for the non-perfect monochromaticity of the incident neutron beam and the finite energy resolution of the spectrometer, the experimentally obtained scattering function $S^{\mathrm{exp}}_{\mathrm{inc}}(Q,\omega)$ is understood as the convolution of the instrumental resolution function $R(Q,\omega)$ with the theoretical scattering function $S^{\mathrm{theo}}_{\mathrm{inc}}(Q,\omega)$:

$$S^{\mathrm{exp}}_{\mathrm{inc}}(Q,\omega) = S^{\mathrm{theo}}_{\mathrm{inc}}(Q,\omega) \otimes R(Q,\omega). \tag{2}$$

For the analysis of QENS data, this convolution is carried out only in the energy direction. As the real resolution of the spectrometer does not strictly follow an analytical function, the integral form of this convolution

$$S^{\mathrm{exp}}_{\mathrm{inc}}(Q,\omega) = \int_{-\infty}^{\infty} S^{\mathrm{theo}}_{\mathrm{inc}}(Q,\omega') \cdot R(Q,\omega-\omega')\,\mathrm{d}\omega' \tag{3}$$

is mostly replaced by the discrete equivalent

$$S^{\mathrm{exp}}_{\mathrm{inc}}(Q,\omega_n) = \sum_{m=1}^{N} S^{\mathrm{theo}}_{\mathrm{inc}}(Q,\omega_m) \cdot R(Q,\omega_n-\omega_m) \cdot \delta\omega \tag{4}$$

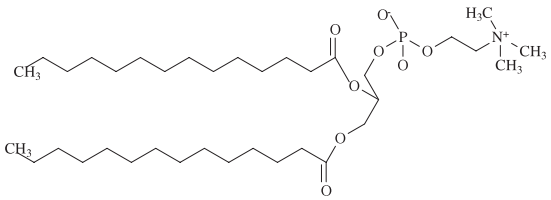

Figure 2. Molecular structure of DMPC.

where N is the total number of points of a spectrum in the energy direction and $\delta\omega$ the width of a bin.

The relevant motions of the scatterers are then assumed to be independent of each other so that the scattering function can be approximated as composed of e.g. translational, rotational, and vibrational contributions [36]:

$$S_{\rm inc}^{\rm theo}(Q,\omega) = S_{\rm inc}^{\rm trans}(Q,\omega) \otimes S_{\rm inc}^{\rm rot}(Q,\omega) \otimes S_{\rm inc}^{\rm vib}(Q,\omega). \quad (5)$$

The amount of physics and approximations contained in these equations is so overwhelming that it seems safe to postulate that by far most neutron scatterers (including the authors) settle for using these approximations after following the calculations a few times.

In this contribution, we discuss the influence of two of these steps: (a) the assumption that all detected neutrons were scattered only once in the sample and (b) the consideration of the limited instrumental resolution by the discrete convolution of the theoretical scattering function with an experimentally obtained instrumental resolution function.

3. Experimental details

3.1. Materials

A vanadium hollow cylinder standard with an outer radius 11.75 mm and wall thickness 0.6 mm was measured at 20 °C. The transmission was calculated by numerical integration of the path length of the neutrons through the scatterer in transmission geometry and assuming an exponential decay of the neutron intensity in the medium [37] to 93%.

For all samples, hollow cylindrical aluminium sample containers [38, 39] with an inner radius of the outer aluminium layer of 11.25 mm and varying radii of the inner aluminium layer were used. The choice of the insert determined the gap size and therefore the sample layer thickness.

The phospholipid dimyristoylphosphatidylcholine (DMPC; see figure 2) was obtained from Lipoid GmbH, Ludwigshafen (Germany), and used as received. It was hydrated at 40 °C via the gas phase with D_2O 99.90% from Euriso-Top, Gif-sur-Yvette (France), for at least 48 h until a clear phase formed. Subsequently, further D_2O was added up to 50 wt% to ensure full hydration during the whole experiment. With a gap size of 0.2 mm, a calculated transmission of 85% was obtained. The measurements were performed at 10, 20, 30, and 40 °C. Also pure D_2O was measured at these temperatures.

Pure H_2O, already used previously for multiple-scattering studies [40, 41], was taken from a Barnstead EASYpure II ultrapure water system with a resistivity of $\rho \geqslant 18.2$ MΩ cm and filled into the sample containers with gap sizes of 0.1, 0.2, 0.3, 0.5, 1.0, 2.0, and 3.0 mm. These samples have calculated transmissions of 85%, 72%, 62%, 46%, 23%, 6.4%, and 2.2%, respectively; the mean free path length of a neutron in H_2O is about 2 mm. The measurements were performed at 20 °C.

3.2. Measurements and data treatment

All experiments were performed at the cold neutron time-of-flight spectrometer TOFTOF [42, 43] at the Forschungs-Neutronenquelle Heinz Maier-Leibnitz (FRM II), Garching bei München, Germany. The spectrometer is equipped with detectors in an angular range from 7.5° to 140°.

An incident neutron wavelength of 6 Å was used, hereby giving for quasi-elastic scattering access to Q values from 0.3 to 1.8 Å^{-1}. The maximal momentum transfer of elastically scattered neutrons at this wavelength is $\hbar \cdot 2.1$ Å^{-1} for backscattered neutrons. An instrumental resolution of about 60 μeV (full width at half-maximum) was reached with a chopper rotation speed of 12 000 rpm which required a frame overlap ratio of 4. The corresponding observation time is about 60 ps [44].

Today's normal way of histogramming the data online during the experiment adds a restriction to the rebinning of the data. The online histogramming was done using 1024 time channels, resulting in a width of about 7.5 μeV of the bins at zero energy transfer. These data points were then rebinned into bins with a constant step in energy of $\delta E = 10$ μeV during data reduction into slices of constant Q. Additionally, the phospholipid was also measured with an online histogramming into 4096 time channels, resulting in a width of about 1.9 μeV at zero energy transfer and a constant step of $\delta E = 2$ μeV after rebinning.

The data were normalized to the scattering of the vanadium standard to correct for different detector efficiencies. An empty can measurement was subtracted from all measurements and the D_2O spectra were subtracted pro-rata from the ones of the phospholipid at the corresponding temperatures. The obtained spectra were not normalized to the amount of sample in the beam or the total scattered intensity.

Diffraction patterns $\mathrm{d}\sigma/\mathrm{d}\Omega(2\theta)$ were obtained by integrating the double-differential cross section over all energies. Spectra were obtained by regrouping the data into slices of constant Q [37]. In energy, the spectra were evaluated in the region of $\Delta E = \hbar\omega$ from -1 to $+1$ meV where positive values for the energy transfer denote an energy gain of the neutron during the scattering process(es).

The fits of the theoretically calculated scattering functions $S_{\rm inc}^{\rm theo}(Q,\omega)$ to the measured ones $S_{\rm inc}^{\rm exp}(Q,\omega)$ were numerically convolved with the instrumental resolution $R(Q,\omega)$ as determined by the measurement of the vanadium hollow cylinder standard.

In order to enhance the visibility of the inelastic part of the spectrum, a representation as the imaginary part of the dynamic susceptibility is also shown; the transformation was performed using

$$\chi''(Q,\omega) = S_{\rm inc}^{\rm exp}(Q,\omega)/n(\omega) \quad (6)$$

where the scattering functions are divided by the Bose occupation factor

$$n(\omega) = 1/(\exp[\hbar\omega/(k_B T)] - 1). \quad (7)$$

Intermediate scattering functions $I_{inc}^{exp}(Q, t)$ were obtained via the cosine Fourier transform of the energy spectra and subsequent division of the sample data by the instrumental resolution as determined by the vanadium measurement. Again, the data were not normalized to $I_{inc}^{exp}(Q, t = 0) = 1$. Instead, an overall scaling factor a was included into the fitting function.

3.3. Fitting models

The data for the phospholipid were fitted with a convolution of a Gaussian for the long-range flow-like motion with two localized diffusive contributions, each of the form

$$S_{inc}^{theo}(Q, \omega) = A_0(Q) \cdot \delta(\omega) + (1 - A_0(Q)) \cdot L(\Gamma_{broad}(Q), \omega) \quad (8)$$

where L denotes a Lorentzian

$$L(\Gamma(Q), \omega) = \frac{\Gamma(Q)/\pi}{\Gamma(Q)^2 + \omega^2}. \quad (9)$$

The different localized contributions were assigned to the motions of the atoms in the head and tail groups [1]. The Gaussian then captures only the long-range motion of the whole molecule. The Gaussian line shape with a linewidth of

$$\sigma(Q) = v \cdot Q \quad (10)$$

results from the assumption of flow motions with Maxwell–Boltzmann distributed flow velocities around the most likely velocity v [1].

The spectra of H_2O were fitted with a common function in quasi-elastic neutron scattering, the sum of two Lorentzians which is motivated [44] by the convolution of a long-range diffusive motion

$$S_{inc}^{theo}(Q, \omega) = L(\Gamma_{narrow}(Q), \omega), \quad (11)$$

with a localized motion (8). With a scaling prefactor a accounting for the scattering power of the sample, this yields

$$\begin{aligned} S_{inc}^{theo}(Q, \omega) &= a \cdot L(\Gamma_{narrow}(Q), \omega) \otimes [A_0(Q) \cdot \delta(\omega) \\ &\quad + (1 - A_0(Q)) \cdot L(\Gamma_{broad}(Q), \omega)] \\ &= a \cdot A_0(Q) \cdot L(\Gamma(Q)_{narrow}, \omega) \\ &\quad + a \cdot (1 - A_0(Q)) \cdot L(\Gamma(Q)_{narrow} + \Gamma(Q)_{broad}, \omega). \end{aligned} \quad (12)$$

A specific model for the localized motion, giving an expression for $A_0(Q)$ as used in previous works [30], was avoided because of the distortion by multiple scattering [1, 17, 36].

For the evaluation of the intermediate scattering function, another fit function will be used which is also very common for the evaluation of QENS data: a stretched exponential,

$$I_{inc}^{theo}(Q, t) = a \exp[-(t/\tau)^{\beta}]. \quad (13)$$

The alternative, a sum of two exponential decays, gives results very similar to the ones obtained from the fit of the scattering function with two Lorentzians, as one would expect [45, 46]. The resulting relaxation time is shown as the mean relaxation time $\langle\tau\rangle = \tau\Gamma(\beta^{-1})\beta^{-1}$ where Γ is the Gamma function, reducing the dependence of τ on β [17, 29].

4. Results

4.1. Multiple scattering

This section is organized as follows. After looking qualitatively at the data and their distortion caused by multiple scattering, the two most common methods for the quantitative evaluation of QENS data will be presented: fits of a sum of Lorentzians to the scattering function $S_{inc}^{exp}(Q, \omega)$ and the fit of a stretched exponential to the intermediate scattering function $I_{inc}^{exp}(Q, t)$.

4.1.1. The angular dependence of the scattered intensity. The algorithm of Paalman and Pings [47] was used to calculate the path lengths of the neutrons through the samples as a function of the scattering angle. Using the average scattering cross section, the probabilities for them to be scattered were determined from this length [37]. Only those neutrons which were scattered exactly once were considered to be detected. To facilitate comparability with the measured data, the resulting differential scattering cross sections were scaled with a factor that was chosen such that the calculated integral scattering cross section in the angular range covered is equal to the measured one for the 0.1 mm sample; see figure 3(a).

The energy-integrated scattering cross section, the diffraction pattern that one would measure at a standard diffraction instrument, is shown in figure 3(b). Several differences from the calculated one are visible. (a) The scattered amount of neutrons is much higher than expected from the calculation because double-scattered neutrons are not actually lost. (b) Increasing the thickness of the water layer generally also increases the scattered intensity. This increase is, however, very small for the thick samples—the 3.0 mm sample scatters hardly more, at small scattering angles even less than for the 2.0 mm sample. (c) The angular variation of the scattered intensity is lower than expected from the calculation.

The elastically scattered intensity determined by integration of an energy range of ± 60 μeV is shown in figure 3(c). It can easily be seen that the amount of elastically scattered neutrons does not scale linearly with the amount of sample—the thickest sample even scatters fewer neutrons elastically than the thinnest at low angles.

4.1.2. Intensity redistribution in (Q, ω)-space. Comparing the scattering function $S_{inc}^{exp}(Q, \omega)$ of the thinnest and the thickest sample in figure 4(a), it becomes clear that the elastic signal of the 3.0 mm measurement depends much less on Q than that of the 0.1 mm measurement, in agreement with figure 3(c). At higher energy transfers, the 3.0 mm sample has up to one order of magnitude more signal than the 0.1 mm measurement. This artificial gain in intensity distorts the dynamical susceptibility even more than the scattering function.

To look closer at the redistribution of the scattered intensity in the quasi-elastic region, the double-differential scattering cross section of the 3.0 mm measurement and that of the 0.1 mm measurement were independently normalized to the same total scattering cross section in the dynamical range. The data for the 3.0 mm measurement were then

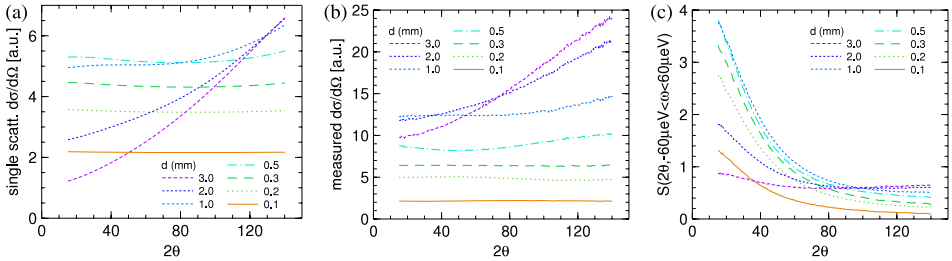

Figure 3. From left to right: (a) calculated angular dependence of the differential cross section of H_2O, caused only by single-scattered neutrons; (b) measured angular dependence of the differential cross section of H_2O; (c) measured angular dependence of the elastic part of the scattering function of H_2O.

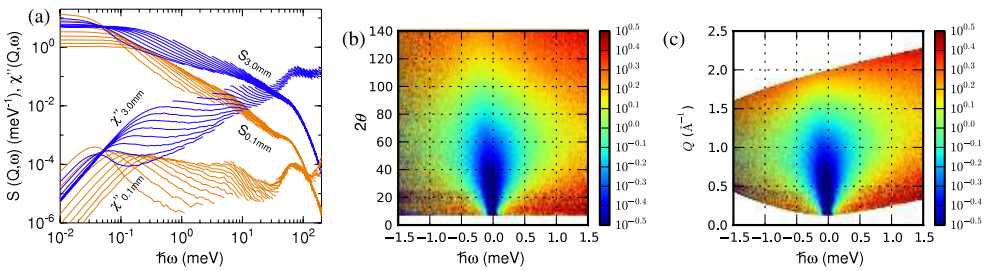

Figure 4. From left to right: (a) the scattering function $S^{\mathrm{exp}}_{\mathrm{inc}}(Q,\omega)$ as well as the imaginary part of the dynamical susceptibility $\chi''(Q,\omega)$ for two H_2O samples (0.1 and 3.0 mm sample layer thickness) and values of Q from 0.4 to 10.0 $\mathrm{Å}^{-1}$ in steps of 0.2 $\mathrm{Å}^{-1}$; due to the dynamical range of the spectrometer, the data at low Q do not reach high energy transfers and vice versa; (b) the ratio of the normalized double-differential cross sections of the 3.0 mm measurement and the 0.1 mm measurement; (c) the same as for (b) but after conversion from scattering angle 2θ to Q.

divided by the ones for the 0.1 mm measurement. The result is shown as a function of energy transfer and scattering angle in figure 4(b) and also as a function of energy transfer and Q in figure 4(c). Values smaller than 10^0 designate areas where multiple scattering caused a loss of intensity, values bigger than 10^0 those where additional, multiply scattered neutrons were detected.

The pattern shows a slight asymmetry with respect to the energy transfer. The lower intensity observed on the neutron energy loss side was attributed to the higher absorption probability for slower neutrons.

At low scattering angles, the signal of the 0.1 mm measurement decreases more rapidly as a function of energy transfer than the signal of the 3.0 mm measurement which is more smeared out; cf figure 4(a). This leads to the high relative intensity at low scattering angles and large energy transfers. With increasing scattering angle, the shapes of the scattering functions become more similar to each other.

4.1.3. Evaluation of the scattering function with two Lorentzians. In the fit with two Lorentzians (12), the properties of the narrow and the broad one, corresponding to long-range and localized motions, respectively, are discussed in the following.

The arguably most important observation in the measurements presented is shown in figures 5(a) and (b): the linewidth of the narrow Lorentzian is largely unaffected by multiple scattering. This means that a reliable determination of the diffusion coefficient is possible even when a massive amount of multiple scattering is present. This will be detailed in the discussion.

The intensity distribution between the two Lorentzians, the EISF, follows quite well for the thin samples; the expected Gaussian-like decrease with Q; see figure 5(c). However, it is already visible in the 0.1 mm measurement that the EISF does not extrapolate to 1 as Q approaches 0. This well-known sign of multiple scattering [36] gets much stronger with increasing sample layer thickness.

The width of the broad Lorentzian is shown in figure 5(d). An overall trend to larger widths with increasing Q is visible, on top of which a thicker sample size increases the width rather independently of Q. As can be seen in figure 5(a), the data are at large energy transfers even flatter than the fit. This means that multiple scattering causes a very broad, background-like contribution.

4.1.4. Evaluation of the intermediate scattering function with a stretched exponential. The intermediate scattering function can be fitted well with a stretched exponential as can be seen in figure 6(a).

The prefactor, displayed in figure 6(b), is basically the value $I^{\mathrm{exp}}_{\mathrm{inc}}(Q,t=0)$, i.e. the zeroth Fourier

J. Phys.: Condens. Matter **23** (2011) 254205 S Busch and T Unruh

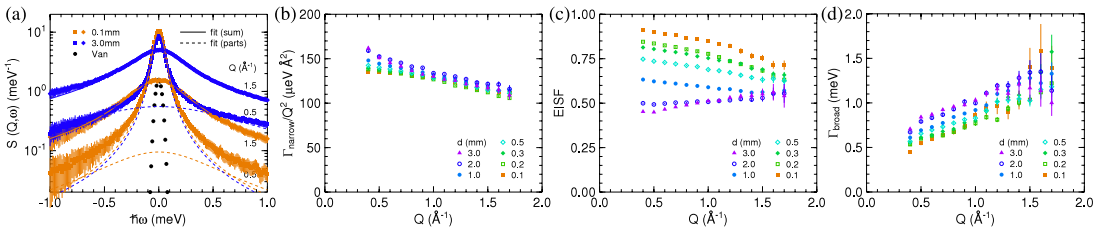

Figure 5. From left to right: (a) scattering function of H_2O, shown at two Q values and two sample layer thicknesses; also shown is a vanadium measurement as a measure of the instrumental resolution and fits of the sum of two Lorentzians to the data (solid lines), and for the two measurements at low Q, also the two components of the fit are shown (dashed lines); (b) the linewidth of the narrower of the two Lorentzians; (c) the elastic incoherent structure factor A_0; (d) the linewidth of the broader of the two Lorentzians.

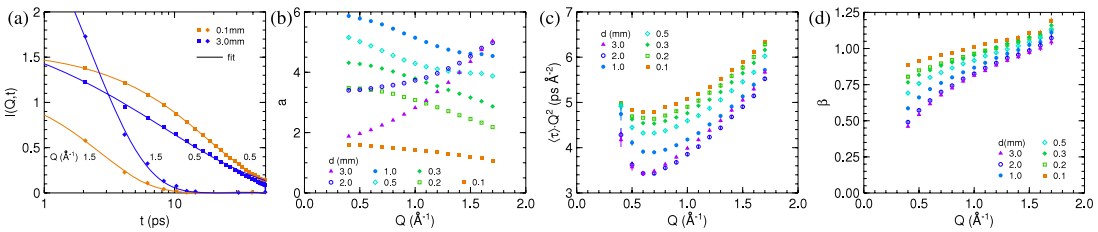

Figure 6. From left to right: (a) intermediate scattering function of H_2O, shown at two Q values and two sample layer thicknesses; also shown is the fit of stretched exponentials to the data (solid lines); (b) the prefactor a; (c) the mean relaxation time multiplied by Q^2; (d) the stretching exponent β.

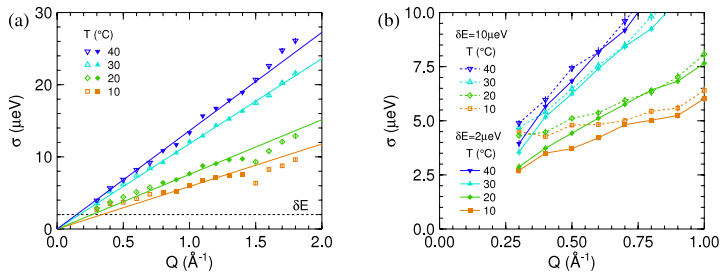

Figure 7. From left to right: (a) width of the narrow Gaussian line of a three-component fit to the spectra of the fully hydrated phospholipid dimyristoylphosphatidylcholine (DMPC); the levelling off of the widths at low temperatures and small Q (cf figure 1) is practically nonexistent, the distance between two data points, $\delta E = 2\ \mu$eV, is indicated in the figure, the energy resolution is about 60 μeV, and the solid lines are fits to the filled points in the medium-Q region; (b) close-up view of the low-Q region of the width of the narrow Gaussian line of a three-component fit to the spectra of DMPC, measured with different point distances; it can be clearly seen that the effect of levelling off at small Q can be nearly completely removed by choosing a higher point density.

component, which is the area under the scattering function, $\int_{-1\ \mathrm{meV}}^{1\ \mathrm{meV}} S_{\mathrm{inc}}^{\mathrm{exp}}(Q,\omega)\,\mathrm{d}\omega$. The limits of the integration are given by the region where the scattering function was evaluated—which in turn is limited by the dynamical range of the experiment.

The mean relaxation time is influenced by multiple scattering, both in its average value and its Q dependence. The strongest effect can be observed in figure 6(c) at intermediate Q (around 0.7 Å^{-1}) where the apparent speed-up is most pronounced, in agreement with Monte Carlo simulations [17].

The stretching factor is more influenced than the mean relaxation time [14]. Stretching increases (β decreases) systematically, most at small values of Q; cf figure 6(d).

4.2. Fitting artefacts

The width of the narrow component of the fit to the phospholipid data with a binning of $\delta E = 10\ \mu$eV is shown in figure 1. The analogous fit to the data with $\delta E = 2\ \mu$eV yields the linewidths in figure 7(a). Also shown in both figures are fits of straight lines to the medium-Q-range data points and the width of the bins.

It can be seen that in the case of the coarse energy binning shown in figure 1, the data points deviate strongly from the linear behaviour at low Q and level off to a value of about $\delta E/2$. With a finer energy binning, figure 7(a), they display a much more linear behaviour.

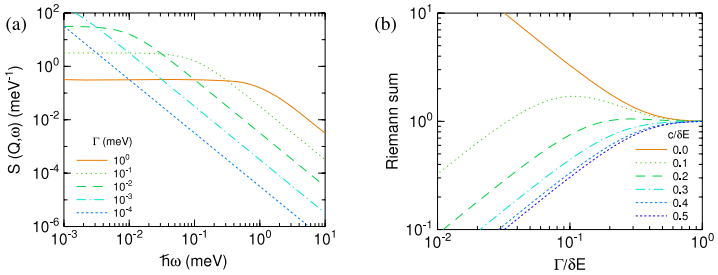

Figure 8. From left to right: (a) Lorentzian curves with different widths plotted double logarithmically; after a plateau, the curves become a power law for $\hbar\omega \gtrsim \Gamma$; (b) the Riemann sum over a Lorentzian as a function of its width Γ, shown for different values of their centres c; both width and centre are given in units of the distance between two points at which the Lorentzians are evaluated, δE; for $\Gamma \lesssim \delta E/2$, the Riemann sum deviates significantly from the correct value of 1, and the direction of the deviation depends on the relative position of the centre of the Lorentzian with respect to the points.

This is shown in detail in figure 7(b) where the fit results for the two energy binnings are compared. The effect is striking: the levelling off which was discussed as being either confinement or a fit artefact [1] is clearly the latter.

5. Discussion

5.1. Evaluation of the long-range motion

Both the geometry and the rate of the long-range motion are surprisingly little affected by multiple scattering. The rate of the diffusion is connected to the overall value of $\Gamma_{\text{narrow}}/Q^2$ or $\langle\tau\rangle \cdot Q^2$, the geometry to the dependence on Q of these quantities.

The evaluation of the scattering function $S(Q, \omega)$ with the sum of two Lorentzians where the narrower one accounts for the long-range motion yields very robust parameters for the narrow component. As can be seen in figure 5(b), only for small Q does an increasing scattering power of the sample correlate with an increase of the linewidth.

Of the large deviation of the measured linewidth from the expected values for low Q shown in figure 1, up to 125%, only a very small part can be attributed to multiple scattering: extrapolating the 72% and 85% transmission measurements to one with 100% transmission, we expect a deviation at small Q of about 3%. This extrapolation is known to be not suitable for the precise evaluation of multiple scattering [40, 41] but it shows that the effects caused by multiple scattering are more than one order of magnitude lower than the observed deviations in figure 1.

In great contrast, the fitting artefacts distort the observed geometry of the long-range motion heavily. It will be shown in the following that a systematically too large line broadening (or too small correlation time) is obtained.

A Lorentzian line is practically indistinguishable from a power law for any $\hbar\omega \gtrsim \Gamma$, namely $(\Gamma/\omega)^2$, as shown in figure 8. This means that for any energy transfer bigger than Γ, the fit can be shifted to bigger values of y either by increasing the always present prefactor a or—completely equivalently—by increasing Γ.

Increasing a or increasing Γ makes a difference only at energy transfers smaller than Γ: increasing a increases the values of y in this range whereas increasing Γ decreases them. It is therefore this range which determines a and Γ.

The discrete convolution of the theoretical fit function $S_{\text{inc}}^{\text{theo}}(Q, \omega)$ with the instrumental resolution $R(Q, \omega)$ is the origin of this problem: whereas R is in the present case very well-behaved, $S_{\text{inc}}^{\text{theo}}$ becomes so sharply peaked as Γ decreases that the evaluated values at the points near zero energy transfer are not representative for the whole bin any more. This is because the curvature in the centre of the Lorentzian is $-2/(\pi\Gamma^3)$ and diverges therefore for $\Gamma \to 0$.

The consequence is that the integral convolution in (3) cannot be substituted by the discrete convolution (4) any more: whereas the integral under the Lorentzian is unity independently of Γ, the Riemann sum deviates very strongly when the linewidth is smaller than about half of the distance between two evaluated points, $\Gamma \lesssim \delta E/2$.

It will be shown in the following that the systematically too large fit value for the linewidth does not depend on the direction of this deviation in the critical cases discussed here ($\Gamma \approx 1\ \mu$eV, $\delta E = 10\ \mu$eV):

(a) If the sum is calculated as too big (the centre of the Lorentzian is close to a measured point), the central points are mistakenly calculated as too high. Only the central point which is evaluated at the centre of the Lorentzian is in the plateau region of the Lorentzian.

(a.1) The fit can increase Γ and thereby lower the central points through both the natural decrease (figure 8(a)) and the better calculation (figure 8(b)). Simultaneously, the function values in the wings of the Lorentzian will increase (figure 8(a)) which will be compensated by a smaller value for the prefactor a, making only a small counter-contribution to lower the central points.

(a.2) The fit could alternatively decrease the prefactor to get the central points down. This leads to a fit curve that is systematically below the data points at large energy transfers—it will be shifted upwards by increasing Γ.

(b) If the sum is calculated as too small (the centre of the Lorentzian is close to the middle in between two measured

points), the central points are mistakenly calculated as too low. The points which are evaluated close to the centre of the Lorentzian are already in the power law wing region of the Lorentzian.

(b.1) The fit can increase Γ and hereby increase the central points through both the natural increase (figure 8(a)) and the better calculation (figure 8(b)). Simultaneously, the function values in the wings of the Lorentzian will increase (figure 8(a)) which will be compensated by a smaller value for the prefactor a which cannot compensate the increase caused by the better calculation though.

(b.2) The fit could alternatively increase the prefactor to get the central points up. This leads to a fit curve that is systematically above the data points at large energy transfers—it would need to be shifted downwards by decreasing Γ. However, this would yield even lower central points (figure 8(b)) and is therefore not an option for the fit.

In conclusion, the fit will always yield a linewidth Γ that is too broad if $\Gamma \lesssim \delta E/2$. In the example of the phospholipid measurements shown in figures 1 and 7, the deviation from a linear behaviour at small Q is decreased from 125% (in figure 1) to about 30% (in figure 7) by choosing a smaller energy step between measured points.

This 30% deviation might very well be due to the background in the resolution measurement, caused by the instrument and phonons in the vanadium. Comparing the fits using a convolution with the instrumental resolution as determined by a vanadium measurement at temperatures between 4 and 300 K as well as Gaussians with flat background, the fitted values differed by this order of magnitude without showing clear trends. This will be studied in more detail and presented in a forthcoming publication.

5.2. Evaluation of the localized motions

The evaluation of the localized motions in the two-component fit of the scattering function is influenced in both rate and geometry. This is because the multiply scattered neutrons obtain relatively large energy transfers, yielding a nearly flat background in the energy direction. With an increasing amount of multiple scattering, this background increases. The broad Lorentzian which accounts for localized motions therefore broadens and gets more intensity.

The geometry is increasingly hard to evaluate from the EISF as it does not approach 1 for small momentum transfers any more. It seems to be the most sensitive indicator for multiple scattering. Including an arbitrary scaling factor in the definition of the EISF as done previously [1] makes an approximate evaluation possible at reasonable transmissions [17].

In the following, we will try to explain the effects of multiple scattering with simple phase space arguments, assuming for the calculation of Q that the neutron does not change its energy in a scattering process and neglecting the geometry of the sample [48]. Knowing that the spectrum of multiply scattered neutrons is essentially a convolution of the double-differential cross section with itself for every scattering process [12], and that double scattering is the most probable multiple-scattering event [49], the Q values of the two scattering events are the interesting quantities. The width of the observed scattering function will then be approximately the sum of those of the two single-scattering processes.

Using Monte Carlo simulations [17], it was determined that the probability distribution of the scattering angles of the single-scattering processes is—independent of the total scattering angle—nearly triangular with a maximum probability of 90°, corresponding to a Q already of $0.71\,Q_{\max}$ (elastic), in this case 1.5 Å^{-1}. A similar assessment has also been used elsewhere [50]. Half of the neutrons will be scattered with a larger Q and result in a very broad line contributed by the multiply scattered neutrons.

The upper limit for the values of Q that can possibly participate in a double-scattering event is given by the wavelength of the neutrons: $Q_{1,2}^{\max} = 4\pi/\lambda$. The lower limit for $Q_{1,2}$ seen from a given Q_{tot} can be deduced from figure 9(a) where the vectorial momentum transfer of the first scattering process is denoted as $\boldsymbol{Q}_1$, that of the second as $\boldsymbol{Q}_2$, and the total (observed) as $\boldsymbol{Q}_{\text{tot}} = \boldsymbol{Q}_1 + \boldsymbol{Q}_2$. This means, for the absolute values, $Q_1 + Q_2 \geqslant Q_{\text{tot}}$. The distribution of possible Q values in the scattering process and therefore of relaxation times is therefore largest at small Q_{tot} (cf figure 6(d)).

The shift with regard to the scattering angle and the cut-off of Q resulting from the choice of the wavelength of the incoming neutrons brings about the change of this wavelength influencing multiple scattering not only for coherently scattering samples [10, 15–17] but also for incoherently scattering samples [17, 49], although to a smaller extent.

To understand the resulting linewidth, one needs the conditional probability for the two scattering events given some Q_{tot}. We have calculated the mean Q_2 after a given Q_1 as follows (cf figure 9(a)): the probability for a certain (Q_1, Q_2) combination is directly proportional to the number of allowed $(\boldsymbol{Q}_1, \boldsymbol{Q}_2)$ combinations, weighted with the corresponding solid angles.

The probability of having an event with a certain $\boldsymbol{Q}_{1,2}$ is inversely proportional to the surface of a sphere with radius $Q_{1,2}$, $1/(4\pi Q_{1,2}^2)$. Multiplying these two probabilities gives the one for reaching a certain $\boldsymbol{Q}_{\text{tot}}$ via a given point of connection of $\boldsymbol{Q}_1$ and $\boldsymbol{Q}_2$. Each of the two scattering events has to be multiplied with the solid angle accessible with a given scattering angle, $\sin(2\theta_{1,2})/\lambda$.

As all connection points which satisfy $Q_{1,2} \leqslant Q_{\max}$ can be used equivalently, this probability has to be multiplied with the circumference l of the circle around $\boldsymbol{Q}_{\text{tot}}$,

$$l = \frac{\pi}{Q_{\text{tot}}} \cdot \text{Re}\{[-(Q_{\text{tot}} - Q_1 - Q_2) \cdot (Q_{\text{tot}} - Q_1 + Q_2)(Q_{\text{tot}} + Q_1 - Q_2) \cdot (Q_{\text{tot}} + Q_1 + Q_2)]^{1/2}\}, \quad (14)$$

where Re denotes the real part of the argument.

The result, symmetrical in Q_1 and Q_2, is displayed in figure 9(b). It can be seen that even if one scattering process already has $Q_1 = Q_{\text{tot}}$, the other scattering process still has a nonzero Q_2. Two limiting behaviours can be observed: on the

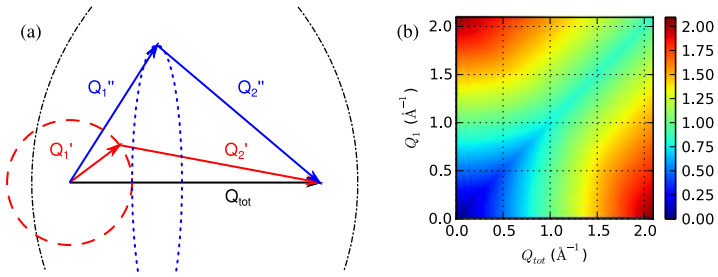

Figure 9. From left to right: (a) two scattering processes, denoted with subscripts 1 and 2, with their respective scattering vectors $\boldsymbol{Q}_1$ and $\boldsymbol{Q}_2$ combine to a total scattering process with $\boldsymbol{Q}_{\text{tot}}$; the black dash–dotted lines denote the external borders in between which a point of connection between the two scattering events must be such that the given $\boldsymbol{Q}_{\text{tot}}$ can be reached with two quasi-elastic scattering processes, the red dashed line is a section of the sphere on which $\boldsymbol{Q}_1'$ may end and the paper plane—note that only points on this sphere which are within the black dash–dotted line can contribute to the scattering process shown—and the blue dotted line shows the projection of the circle (which is perpendicular to the paper plane) on which the point of connection between the two $\boldsymbol{Q}''$ can revolve; (b) mean Q_2 for a given combination of Q_1 and Q_{tot}.

one hand, for Q_1 and $Q_{\text{tot}} \gtrsim 1.0$ Å^{-1}, the mean Q_2 depends basically only on $|Q_{\text{tot}} - Q_1|$ and is never less than about 1.0 Å^{-1}. On the other hand, for Q_1 and $Q_{\text{tot}} \lesssim 1.0$ Å^{-1}, we observe $Q_2 \approx \max(Q_1, Q_{\text{tot}})$. Scattering events where the second scattering process has a very small Q compared to Q_1 and Q_{tot}, i.e. broadening the signal only slightly, are very rare. This causes the distinctness between the signal and the much broader contribution of multiply scattered neutrons.

5.3. Phospholipid motions

It is clear that the long-range motion extracted from a measurement with an observation time of 60 ps is not the macroscopic long-range motion. This manifests for example in a higher velocity [1] and lower influence of additives [51] than observed macroscopically. Although the molecule travelled only a distance of about 1 Å [1] during this short time, the interactions with the neighbours, the cage, are already established. The observed flow-like motion is not the initial phase of free flight before the molecule experiences the presence of the surrounding neighbours. This is evidenced by both the clear existence of localized (caged) motions and the small flow velocity which is nearly three orders of magnitude below the thermal expectation value [1].

As shown in the present contribution, the neutron scattering data show no significant evidence for a restriction of the flow-like long-range motion to a cage within the observation time—above and below the main phase transition.

We explain this with 'floppy modes': the molecules are pushed around by density fluctuations resembling longitudinal acoustic phonons in crystals. Below the phase transition, a restoring force will eventually push them back to the original place. Due to the 'floppiness' of the material, the molecules travel more than the 1 Å during which the experiment follows them before the restoring force gets big enough to restrict their motion. Therefore, this effect does not leave a trace in the data. Above the phase transition, the molecules are transported by many short subsequent uncorrelated flow events.

These low-frequency 'floppy modes' are known from disordered colloidal crystals [52], colloidal glass formers, and supercooled liquids, and signal the onset of macroscopic elasticity [53]. Phospholipid membranes also exhibit elasticity above and below the main phase transition [54] and the observed flow patterns [2] resemble very much dynamical heterogeneities [51], a hallmark of glassy dynamics, which were again suggested to be linked with the 'floppy modes' [55].

The reason that the dynamics of phospholipids resembles dense, supercooled systems so much is probably the very high density in the head group area of the phospholipids [51]. This similarity has proven to be extremely useful already, in the past, when the free volume theory developed for glasses [56] was adapted to membranes [57, 58]. Transposing the newer concepts developed in glass physics, dynamical heterogeneities and 'floppy modes' to phospholipid membranes not only seems relevant but also can explain the observed features effortlessly.

6. Summary and conclusions

The molecular motion of the phospholipid DMPC was studied below and above the main phase transition on a timescale of about 60 ps, taking the influence of multiple scattering and fit artefacts into particular consideration.

Multiple scattering was shown to be only a minor nuisance for the determination of the long-range motion of an incoherent scatterer. As an example, H_2O samples with transmissions between 85% and as low as 2% were studied. The multiply scattered neutrons are lost in the elastic region of the signal and create a background which is a very broad line in energy space. In a multicomponent analysis, they affect therefore only the evaluation of localized motions. This, together with the excellent agreement of the results with Monte Carlo simulations, shows that one could more often dare to use strongly scattering samples for quasi-elastic measurements.

The fit of a theoretical scattering function to measured data after numerical convolution with a measured resolution function can give erroneous results. A delicate combination of correlated fitting parameters and a discretization problem during the convolution with the measured instrumental resolution causes an error in an unexpected place: the

linewidth. Analysing the data with different bin widths should give indications if this problem is present. The lower limit for the bin width is often given by the online histogramming of the neutrons during the experiment—a complete event recording of the detected neutrons, in principle possible, would remove this limitation.

Flow-like motions of the phospholipid molecules bear a striking resemblance to dynamical heterogeneities above the main phase transition and to 'floppy modes' below. The confinement of the molecules below the main phase transition is not visible in the long-range component of the fit due to the short observation time of the experiment. It seems that the description of motions in the phospholipid membrane could profit greatly from transferring the up-to-date concepts used in glass physics.

Acknowledgments

We would like to express our gratitude to Professor W Petry who has extensively supported our work. We enjoyed the lively discussions with him and his special interest in the multiple-scattering effects discussed here. We have very much profited from the earlier work of and many discussions with J Wuttke who first pointed out the importance of the numerical convolution to us. We would like to thank A Stadler for discussions; G Brandl, F Lipfert, B Mihiretie, and A Tischendorf for their participation in the measurements of H_2O; and H Morhenn for performing the phospholipid measurements.

References

[1] Busch S, Smuda C, Pardo L C and Unruh T 2010 Molecular mechanism of long-range diffusion in phospholipid membranes studied by quasielastic neutron scattering *J. Am. Chem. Soc.* **132** 3232
[2] Falck E, Róg T, Karttunen M and Vattulainen I 2008 Lateral diffusion in lipid membranes through collective flows *J. Am. Chem. Soc.* **130** 44–5
[3] Swenson J and Howells W S 2002 Quasielastic neutron scattering of propylene glycol and its 7-mer confined in clay *J. Chem. Phys.* **117** 857
[4] Zorn R 2010 Neutron spectroscopy for confinement studies *Eur. Phys. J. Spec. Top.* **189** 65
[5] Ghosh S, Adhikari A, Mojumdar S S and Bhattacharyya K 2010 A fluorescence correlation spectroscopy study of the diffusion of an organic dye in the gel phase and fluid phase of a single lipid vesicle *J. Phys. Chem.* B **114** 5736–41
[6] Shull C 1995 Early development of neutron scattering *Rev. Mod. Phys.* **67** 753
[7] Wollan E and Shull C 1948 The diffraction of neutrons by crystalline powders *Phys. Rev.* **73** 830
[8] Vineyard G 1954 Multiple scattering of neutrons *Phys. Rev.* **96** 93
[9] Sköld K, Rowe J, Ostrowski G and Randolph P 1972 Coherent- and incoherent-scattering laws of liquid argon *Phys. Rev.* A **6** 1107
[10] Sears V F 1975 Slow-neutron multiple scattering *Adv. Phys.* **24** 1
[11] Zorn R, Frick B and Fetters L J 2002 Quasielastic neutron scattering study of the methyl group dynamics in polyisoprene *J. Chem. Phys.* **116** 845
[12] Copley J R D 1974 Monte Carlo calculation of multiple scattering effects in thermal neutron scattering experiments *Comput. Phys. Commun.* **7** 289
[13] Wuttke J, Kiebel M, Bartsch E, Fujara F, Petry W and Sillescu H 1993 Relaxation and phonons in viscous and glassy orthoterphenyl by neutron scattering *Z. Phys.* B **91** 357
[14] Wuttke J, Chang I, Randl O G, Fujara F and Petry W 1996 Tagged-particle motion in viscous glycerol: diffusion-relaxation crossover *Phys. Rev.* E **54** 5364
[15] Russina M and Mezei F 1999 New procedure for multiple scattering correction *Neutrons and Numerical Methods*; *AIP Conf. Proc.* **479** 47–54
[16] Mezei F and Russina M 1999 Intermediate range order dynamics near the glass transition *J. Phys. Condens. Matter* **11** A341
[17] Wuttke J 2000 Multiple-scattering effects on smooth neutron-scattering spectra *Phys. Rev.* E **62** 6531
[18] Trouw F R, Borodin O, Cook J C, Copley J R D and Smith G D 2003 Quasielastic neutron-scattering study of the local dynamics of poly(ethylene glycol) dimethyl ether in aqueous solution *J. Phys. Chem.* B **107** 10446
[19] Hugouvieux V, Farhi E, Johnson M R and Kob W 2004 Virtual neutron scattering experiments *Physica* B **350** 151
[20] Pieper J, Buchsteiner A, Dencher N A, Lechner R E and Hauss T 2009 Light-induced modulation of protein dynamics during the photocycle of bacteriorhodopsin *Photochem. Photobiol.* **85** 590–7
[21] Stadler A M, Embs J P, Digel I, Artmann G M, Unruh T, Büldt G and Zaccai G 2008 Cytoplasmic water and hydration layer dynamics in human red blood cells *J. Am. Chem. Soc.* **130** 16852–3
[22] Trapp M, Gutberlet T, Jurányi F, Unruh T, Demé B, Tehei M and Peters J 2010 Hydration dependent studies of highly aligned multilayer lipid membranes by neutron scattering *J. Chem. Phys.* **133** 164505
[23] Thompson H, Skipper N T, Wasse J C, Howells W S, Hamilton M and Fernandez-Alonso F 2006 Proton dynamics in lithium–ammonia solutions and expanded metals *J. Chem. Phys.* **124** 024501
[24] Aliotta F, Fontanella M E, Pieruccini M, Salvato G, Trusso S, Vasi C and Lechner R E 2002 Percolative phenomena in lecithin reverse micelles: the role of water *Colloid Polym. Sci.* **280** 193
[25] Spehr T L 2010 Water dynamics in soft confinement *PhD Thesis* Technische Universität Darmstadt
[26] Spehr T L, Frick B, Zamponi M and Stühn B 2011 Dynamics of water confined to reverse AOT micelles *Soft Matter* accepted doi:10.1039/C1SM05204G
[27] Gaspar A M, Appavou M-S, Busch S, Unruh T and Doster W 2008 Dynamics of well-folded and natively disordered proteins in solution: a time-of-flight neutron scattering study *Eur. Biophys. J. Biophys. Lett.* **37** 573–82
[28] Stadler A M, Digel I, Artmann G M, Embs J P, Zaccai G and Büldt G 2008 Hemoglobin dynamics in red blood cells: correlation to body temperature *Biophys. J.* **95** 5449–61
[29] Doster W, Busch S, Gaspar A M, Appavou M-S, Wuttke J and Scheer H 2010 Dynamical transition of protein-hydration water *Phys. Rev. Lett.* **104** 098101
[30] Teixeira J, Bellissent-Funel M-C, Chen S-H and Dianoux A-J 1985 Experimental determination of the nature of diffusive motions of water molecules at low temperatures *Phys. Rev.* A **31** 1913
[31] Meyer A, Wuttke J, Petry W, Randl O G and Schober H R 1998 Slow motion in a metallic liquid *Phys. Rev. Lett.* **80** 4454
[32] Sette F, Krisch M H, Masciovecchio C, Ruocco G and Monaco G 1998 Dynamics of glasses and glass-forming liquids studied by inelastic x-ray scattering *Science* **280** 1550
[33] Van Hove L 1954 Correlations in space and time and Born approximation scattering in systems of interacting particles *Phys. Rev.* **95** 249

[34] Furrer A, Mesot J and Strässle T 2009 *Neutron Scattering in Condensed Matter Physics* (*Series on Neutron Techniques and Applications*) 1st edn (Singapore: World Scientific)
[35] Squires G L 1996 *Introduction to the Theory of Thermal Neutron Scattering* (New York: Dover)
[36] Bée M 1988 *Quasielastic Neutron Scattering* (London: Taylor and Francis)
[37] Wuttke J 1990 *Frida1: Fast Reliable Interactive Data Analysis* Software http://sourceforge.net/projects/frida/
[38] Wuttke J 1999 Improved sample holder for multidetector neutron spectrometers *Physica* B **266** 112
[39] Wuttke J 1999 Self-absorption coefficient for tubular samples—erratum and addendum to Physica B 266 (1999) 112 *Physica* B **266** 194
[40] Slaggie E L 1967 Multiple scattering in slow-neutron double-differential measurements *Nucl. Sci. Eng.* **30** 199–212
[41] Slaggie E L 1969 Multiple scattering in double differential measurements as a function of neutron path length *Nucl. Sci. Eng.* **36** 105–7
[42] Unruh T, Neuhaus J and Petry W 2008 The high-resolution time-of-flight spectrometer TOFTOF *Nucl. Instrum. Methods Phys. Res.* A **585** 1414–22
[43] Unruh T, Neuhaus J and Petry W 2008 The high-resolution time-of-flight spectrometer TOFTOF (vol 580, p 1414, 2007) *Nucl. Instrum. Methods Phys. Res.* A **585** 201
[44] Unruh T, Smuda C, Busch S, Neuhaus J and Petry W 2008 Diffusive motions in liquid medium-chain n-alkanes as seen by quasielastic time-of-flight neutron spectroscopy *J. Chem. Phys.* **129** 121106
[45] Smuda C, Busch S, Gemmecker G and Unruh T 2008 Self-diffusion in molecular liquids: medium-chain n-alkanes and coenzyme Q_{10} studied by quasielastic neutron scattering *J. Chem. Phys.* **129** 014513
[46] Smuda C 2009 Diffusive Bewegungen in molekularen Flüssigkeiten *PhD Thesis* Technische Universität München
[47] Paalman H H and Pings C J 1962 Numerical evaluation of x-ray absorption factors for cylindrical samples and annular sample cells *J. Appl. Phys.* **33** 2635
[48] Busch S 2007 Protein diffusion in concentrated solutions *Master's Thesis* Technische Universität München
[49] Settles M 1996 Die Zeitabhängigkeit und die Geometrie der intramolekularen Dynamik globulärer Proteine bis 100ps aus Neutronenstreudaten *PhD Thesis* Technische Universität München
[50] Cusack S and Doster W 1990 Temperature dependence of the low frequency dynamics of myoglobin. Measurement of the vibrational frequency distribution by inelastic neutron scattering *Biophys. J.* **58** 243
[51] Busch S and Unruh T 2011 The influence of additives on the nanoscopic dynamics of the phospholipid dimyristoylphosphatidylcholine *Biophysica Acta (BBA) - Biomembranes* **1808** 199–208
[52] Kaya D, Green N L, Maloney C E and Islam M F 2010 Normal modes and density of states of disordered colloidal solids *Science* **329** 656–8
[53] Ghosh A, Mari R, Chikkadi V, Schall P, Kurchan J and Bonn D 2010 Density of states of colloidal glasses and supercooled liquids *Soft Matter* **6** 3082
[54] Harland C W, Bradley M J and Parthasarathy R 2010 Phospholipid bilayers are viscoelastic *Proc. Natl. Acad. Sci.* **107** 19146
[55] Donati C, Douglas J, Kob W, Plimpton S, Poole P and Glotzer S C 1998 Stringlike cooperative motion in a supercooled liquid *Phys. Rev. Lett.* **80** 2338
[56] Cohen M H and Turnbull D 1959 Molecular transport in liquids and glasses *J. Chem. Phys.* **31** 1164
[57] Galla H-J, Hartmann W, Theilen U and Sackmann E 1979 On two-dimensional passive random walk in lipid bilayers and fluid pathways in biomembranes *J. Membr. Biol.* **48** 215
[58] Vaz W L C and Almeida P F F 1991 Microscopic versus macroscopic diffusion in one-component fluid phase lipid bilayer-membranes *Biophys. J.* **60** 1553–4

Appendix E.

The Influence of Additives on the Nanoscopic Dynamics of the Phospholipid Dimyristoylphosphatidylcholine

Sebastian Busch and Tobias Unruh
Biochimica et Biophysica Acta (BBA) – Biomembranes, 1808(1):199, 2011
http://dx.doi.org/10.1016/j.bbamem.2010.10.012

In this publication, the author conceived all experiments (the MD simulation was performed by Tobias Unruh). The experiments were performed either by himself or together with students in the frame of teaching activities. He performed the data evaluation, interpreted the results, and wrote the publication.

In contrast to the previous study of the pure phospholipid [B], where a very intricate model was used together with involved fitting procedures [G, H], the mixtures investigated here were evaluated with a model-free approach. This excludes any distortion by fit artifacts [C, D]. It also makes it possible to compare these results directly with the ones obtained from very small amounts of sample where reliable model fitting is not possible [F].

Reprinted from Biochimica et Biophysica Acta (BBA) - Biomembranes, 1808, Sebastian Busch, Tobias Unruh, The influence of additives on the nanoscopic dynamics of the phospholipid dimyristoylphosphatidylcholine, 199-208, Copyright (2011), with permission from Elsevier.

Biochimica et Biophysica Acta 1808 (2011) 199–208

Contents lists available at ScienceDirect

Biochimica et Biophysica Acta

journal homepage: www.elsevier.com/locate/bbamem

The influence of additives on the nanoscopic dynamics of the phospholipid dimyristoylphosphatidylcholine

Sebastian Busch, Tobias Unruh *

Technische Universität München, Forschungsneutronenquelle Heinz Maier-Leibitz (FRM II), Lichtenbergstraße 1, 85748 Garching bei München, Germany
Physik Department E13, James-Franck-Straße 1, 85748 Garching bei München, Germany

ARTICLE INFO

Article history:
Received 21 May 2010
Received in revised form 17 September 2010
Accepted 19 October 2010
Available online 29 October 2010

Keywords:
DMPC
Dynamics
QENS
Myristic acid
Farnesol
Cholesterol
Sodium Glycocholate
Dynamic Heterogeneity

ABSTRACT

The influence of additives on the molecular dynamics of the phospholipid dimyristoylphosphatidylcholine (DMPC) in its fully hydrated liquid crystalline phase was studied. Quasielastic neutron scattering (QENS) was used to detect motions with dimensions of some Ångstroms on two different time scales, namely 60 ps and 900 ps. The effects of myristic acid, farnesol, cholesterol, and sodium glycocholate could consistently be explained on the basis of collective, flow-like motions of the phospholipid molecules. The influence of the additives on these motions was explained by packing effects, corresponding to the reduction of free volume. Cholesterol was found to decrease the mobility of DMPC seen on the 900 ps time scale with increasing cholesterol content. In contrast, all other studied additives have no significant effect on the mobility.
© 2010 Elsevier B.V. All rights reserved.

1. Introduction

The dynamics in phospholipid membranes connects to a variety of topical questions, ranging from the function of cell membranes [1] to the design of food products [2] or drug delivery systems [3,4]. While additives are used to control the mobility accurately in the cell membrane by the organism to ensure proper functioning, they are regarded as a tool to adjust fundamental properties like storage stability and drug release in pharmaceutical technology. Due to this importance, the motions in phospholipid membranes have been studied with a variety of techniques for more than 20 years—with and without additives.

For pure phospholipids, it was found that the dynamics is much faster on a picosecond time scale as observed with quasielastic neutron scattering (QENS) than with more macroscopic techniques as e.g. fluorescence recovery after photobleaching (FRAP). This was explained with the *free volume model* [5] which states that the two techniques observe different processes. It was assumed that the fast motion which is observed by QENS corresponds to the rattling of the molecules in a cage of their neighbors from which they escape from time to time into an opening void due to thermal fluctuations. This hopping process from void to void was then thought to be the fundamental step of the slow long-range motion measured by FRAP.

To date, evidence accumulates that this microscopic picture is not correct [6,7]. The hopping motions which were proposed as transition from the fast short-time dynamics to the slow long-time dynamics were never observed. Instead, it seems that relaxation in the membrane takes place through cooperative processes [8]. The molecules perform flow-like motions together with their neighbors, taking the cage of neighboring molecules with them [6].

These flow-like motions have so far not been detected with macroscopic techniques such as nuclear magnetic resonance (NMR), fluorescence correlation spectroscopy (FCS), or FRAP which means that the motion, i.e. the mean squared displacement (*msd*), of a single molecule becomes diffusion-like on a sub-millisecond time scale. This does not conflict with a decay of the correlation between molecules on a microsecond time scale [9], which only requires that the mean-squared displacement of neighbouring molecules become diffusion-like in a correlated manner. This would for example be the case if a patch of neighboring molecules participates in several flow events in random directions: even if the molecules in the patch itself stay correlated among each other, the trajectory of each molecule becomes diffusive.

The collective relaxations seem to be closely related to dynamic heterogeneities [10–12] observed in simple liquids, colloids, and other systems [13–19]. To demonstrate this similarity, we have performed a state-of-the art molecular dynamics (MD) simulation of a canonical

* Corresponding author.
E-mail addresses: sbusch@ph.tum.de (S. Busch), tobias.unruh@frm2.tum.de (T. Unruh).

0005-2736/$ – see front matter © 2010 Elsevier B.V. All rights reserved.
doi:10.1016/j.bbamem.2010.10.012

(NVT) ensemble of a 2D-Lennard–Jones liquid, following previous studies [20]. The 1024 particles were distributed inside a square 2D-box of 25.237 nm side length and equilibrated for 10^6 time steps, corresponding to 1 ns, followed by a 100 ps production run. The Lennard–Jones potential between two particles i and j located at a distance r_{ij} from each other is given by

$$V_{L-J}\left(r_{ij}\right) = 4\epsilon_{ij}\left[\left(\frac{\sigma_{ij}}{r_{ij}}\right)^{12} - \left(\frac{\sigma_{ij}}{r_{ij}}\right)^{6}\right] \quad (1)$$

The parameter $\sigma_{ij} = 0.7$ nm was chosen inspired by phospholipid molecules [21,22] and $_{ij} = 5.0$ kJ/mol close to the thermal kinetic energy of particles in a two dimensional system to be in the fluid phase. Periodic boundary conditions were applied and a Berendsen temperature coupling with time constant of 50 fs to a temperature bath with 310.14 K was used.

By connecting the positions for each particle at time $t = 1.0$ ns with its position 100 ps later by an arrow, the picture in Fig. 1 was obtained. It can be seen that neighboring particles move often collectively with similar speeds and directions and that different areas move very differently—some patches are nearly static while others move with relatively high velocities. These are the so-called *dynamic heterogeneities*. As mentioned above, this picture strongly resembles similar representations of the simulated dynamics of DPPC molecules in bilayers [6]. The similarity of the displacement patterns observed in 2D Lennard–Jones systems and phospholipid membranes has also been observed recently in other simulations [23].

We suggest that this similarity indicates that the mobility of the molecules on the picosecond time scale is determined mainly by the closely 2D-packed head groups of the phospholipid molecules which were compared to a densely packed 2D liquid already before [22]. In comparison, the tail groups are more loosely packed at temperatures above the main phase transition [24]. From colloids, it is well known that more densely packed systems exhibit slower dynamics [25]. We assume therefore that the dense phospholipid head groups are the limiting factor for the mobility.

Independently from the validity of the microscopic mechanism, free volume is accepted to play an important role in dynamic processes—at least these quantities are positively correlated [24,26–28]. However, we will interpret the results also in the frame of correlated, flow-like motions.

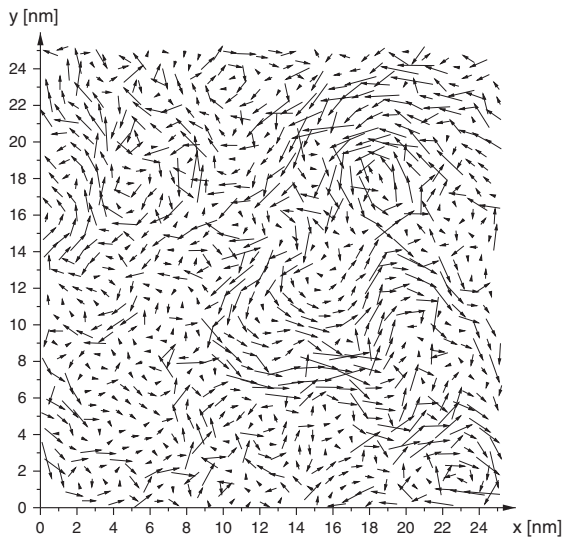

Fig. 1. Visualization of flow-like motions observed in an MD simulation of a simple 2D-Lennard–Jones liquid. The arrows connect the position of the particles with a time difference of 100 ps.

In the present article, we discuss the influence of additives on the mobility of phospholipid molecules (dimyristoylphosphatidylcholine, DMPC) in this frame. We propose that the chain-like molecules myristic acid (MA) and farnesol increase the area covered by the membrane but not the density—and do therefore not change the mobility. Cholesterol increases the density in the chain area and hereby causes a decrease of the mobility. In contrast, the co-emulsifier sodium glycocholate (NaGC, SGC) has basically no influence which can be explained by the larger hydrophilic head group.

2. Materials and methods

2.1. Samples

D_2O (99.90%) was supplied by Euriso-Top, Gif sur Yvette, France. The phospholipid DMPC was purchased from Lipoid GmbH, Ludwigshafen, Germany and used as received. All other substances (myristic acid, cholesterol, farnesol, and sodium glycocholate) were obtained from Sigma Aldrich, Münster, Germany and also used without further purification. The relevant molecular structures are displayed in Fig. 2.

The additives were mixed with the phospholipid in the ratios given in Table 1 with mole fractions x_{additive} of up to 40 mol%. The mixtures were then exposed to a saturated D_2O atmosphere at 40 °C for at least 48 h until a clear sample consisting of randomly-oriented liquid-crystalline domains formed. Finally, additional D_2O was added to ensure full hydration during the whole experiment. All samples were bulk samples to exclude potential disturbing effects of a support.

2.2. Basic properties of the samples

D_2O was used instead of H_2O because it has essentially the same chemical properties but a significantly smaller neutron scattering cross section which facilitates the subtraction of its signal.

DMPC is a typical phospholipid with amphiphilic properties due to its hydrophilic head and hydrophobic tail groups. When adding water (or D_2O), it self-assembles in bilayers and forms liquid crystalline phases. In both, H_2O and D_2O, it has a main phase transition at 24 °C which is attributed to the melting of the chains. The macroscopic diffusion coefficient below the main phase transition has been found to be about one order of magnitude below the one above the main phase transition [29]. Phospholipids like DMPC can be used to stabilize dispersed particles with respect to aggregation and coalescence. In this case, DMPC acts as an interface active substance and stabilizes the particles by forming a molecular monolayer in the interface between the particle and the dispersion medium.

Myristic acid is a water-insoluble chain-like molecule which is the fatty acid contained in DMPC. Previously, it was found that stearic acid generates a slight positive excess volume at low concentrations [30]. Free fatty acids can cause cell death which was attributed to an increased membrane permeability for hydrophilic substances [31]. The phase diagram of the myristic acid–DMPC–water system as a function of the myristic acid mole fraction x_{MA} is known [32]. During the preparation of the samples, it was observed that their viscosity increased significantly with increasing amount of MA.

Farnesol is insoluble in water, too. Due to the double bonds it is stiffer than MA. It can cause apoptosis which, however, seems to be caused by interactions with proteins rather than with the membrane [33]. The phase diagram of the farnesol–DMPC–water mixture as a function of the farnesol content was studied e.g. by NMR [34,35].

Cholesterol, also insoluble in water, is known to increase the membrane bending rigidity [36] and to suppress the phase transitions of the phospholipid [37]. Cells use it to regulate the properties of the cell membrane [38]. It is known that it has a condensing effect on the

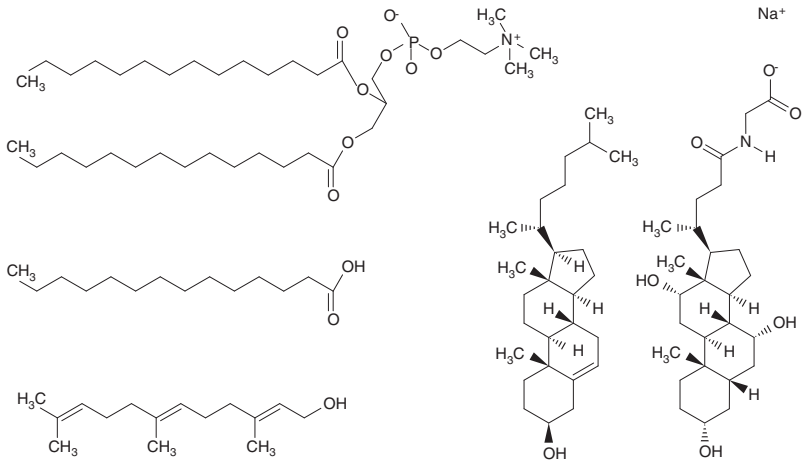

Fig. 2. Structures of molecules discussed in this work. Left: phospholipid DMPC (top), myristic acid (middle), farnesol (bottom); center: cholesterol; right: sodium glycocholate.

membrane, as summarized by Róg et al. [39], which corresponds to the filling-up of voids in the lipophilic core of the membrane [40]. A simultaneous decrease of phospholipid mobility was observed by several groups [24,26,27,41–44] but also an increase of the dynamics has been reported [45,46]. The motions of cholesterol in phospholipid membranes were also previously studied with QENS [47], complementary to the present study of the phospholipid motions. The phase diagram of the cholesterol–DMPC–water system is well studied, for example by differential scanning calorimetry [48] and electron paramagnetic resonance (EPR) [43].

Sodium glycocholate is a water soluble ionic surfactant with a critical micelle concentration of about 8 mM [49,50]. It is used in the digestive system to emulsify fatty substances and hereby enabling absorption [38]. In pharmaceutical technology, it is used to stabilize dispersions which undergo a phase transition of the dispersed phase from liquid (production) to solid (storage). During crystallization, the interface of the particles expands abruptly due to the change of the particle shape from spherical to platelet-like. In dispersions stabilized by phospholipids, it is assumed that the newly formed interface cannot be stabilized fast enough to avoid aggregation. It was found that these instabilities can be prevented when using NaGC as co-stabilizer [51]. The stabilizing property of NaGC is attributed to its high mobility. One question addressed in this contribution is whether this kind of *rapidness* in covering freshly generated interfaces can be observed by QENS. During preparation of the samples, it was observed that samples containing NaGC were more fluid and had a less turbid appearance.

Table 1
Compositions of the samples. The missing quantity up to 100% is D_2O. $^a x_{additive}$, related to amount of phospholipid; ^{b}related to sample mass.

Name	[Additive] /mol%[a]	[Additive] /mass%[b]	[DMPC] /mass%[b]
Additive: none			
D	–	–	50.1
Additive: myristic acid			
M01	1.0	0.12	33.6
M02	1.7	0.20	33.5
M03	2.6	0.30	33.4
Additive: farnesol			
F05	4.7	0.8	49.0
F09	9.1	1.6	49.0
F14	13.5	2.5	49.0
F18	17.8	3.4	48.0
Additive: cholesterol			
C05	5.1	1.5	48.8
C10	10.0	3.0	47.1
C20	19.9	6.2	43.8
C30	30.0	9.8	40.1
C40	40.1	13.8	36.2
Additive: sodium glycocholate			
N05	5.2	1.7	48.5
N10	10.0	3.3	46.8
N14	13.6	3.3	32.7

2.3. Neutron scattering

The focus of this work is the influence of additives on the motion of phospholipid molecules on a pico- to nanosecond time scale as observed with quasielastic neutron scattering. An advantage of neutron scattering with respect to other methods like electron paramagnetic resonance spectroscopy or fluorescence correlation spectroscopy is that marker molecules are not needed [52,53].

The measurements were performed with the neutron time-of-flight spectrometer TOFTOF [54] at the research reactor FRM II (Garching, Germany), equipped with a temperature-controlled sample environment. Neutrons with well-known momentum and energy interact with the sample. The resulting changes in momentum and energy give access to structural and dynamical information, respectively [55,56]. The uncertainty of the determination of the energy transfer between sample and neutron determines the interaction time of the neutron and the nuclei, the observation time. Several factors influence this uncertainty, among them the initial neutron wavelength and the sample geometry. Two measurement series were performed, both giving access to $Q \approx 1$ Å^{-1}, and to time scales of 60 ps and 900 ps, respectively [57].

To realize the 60 ps measurement, the samples were filled into hollow cylindrical aluminum sample containers, minimizing self-shielding effects [58], with a sample layer thickness of 0.2 mm. An incident neutron wavelength of 6 Å, a chopper rotation speed of 12000 rpm, and a chopper ratio of 4 were chosen, leading to an elastic line width of about 60 μeV and an accessible Q range of about 0.4–1.8 Å^{-1}.

For the 900 ps measurement, a flat sample holder was used which was oriented such that its surface normal pointed to a scattering angle of 135° measured towards the location of the detectors, hereby minimizing flight-time uncertainties at the expense of a strong self-shielding around scattering angles of 45°. The corresponding

spectrometer settings were 14 Å, 16000 rpm, and ratio 8, leading to an elastic line width of only 4 μeV and an accessible Q range of about 0.1–0.8 $Å^{-1}$.

The raw data were converted to depend on energy transfer rather than time of flight, determining the time of flight of elastically scattered neutrons from a measurement of vanadium in the same geometry as the respective sample. All scattering intensities were corrected for self absorption effects. The energy-dependent detector efficiency was corrected and the detector sensitivities were calibrated using the elastic scattering of the vanadium standard scatterer, neglecting the smooth dependence of the scattered intensity described by the Debye–Waller factor [59].

Diffraction patterns were obtained by integrating the double differential cross section $d^2\sigma/d\Omega/d\omega$ over an energy range $\hbar\omega$ that covered twice the instrumental resolution, similar to a so-called elastic scan which is often used to evaluate the motions of biomolecules.

For the evaluation of the quasielastic scattering, the double differential cross section was converted to the scattering function $S(2\theta,\omega)$ by multiplication with the ratio of the moduli of initial and final neutron wave vector [55] which was subsequently grouped into slices of constant Q [59]. For the 60 ps measurement, the bins in Q were chosen to have a distance of 0.1 $Å^{-1}$ in the range between 0.4 and 1.8 $Å^{-1}$ and the bins in $\hbar\omega$ ranged from −1.00 to 1.00 meV with a step width of 10 μeV. The 900 ps measurements were grouped in Q from 0.50 to 0.76 $Å^{-1}$ in steps of 0.09 $Å^{-1}$ and in $\hbar\omega$ from −50 to 100 μeV in steps of 1 μeV. At lower values of Q than evaluated here, the self-shielding of the flat sample geometry and the coherent scattering of the sample, cf. Fig. 3, make a reliable calculation of the incoherent scattering signal impossible. A D_2O background measurement was pro rata subtracted. The scattering angle dependent instrumental resolution was determined by the width of the elastic line of a vanadium measurement.

Due to the large incoherent neutron scattering cross section of hydrogen and the masking of the water by deuteration, the scattering signal of D_2O constitutes only about 5% of the total scattering signal and can be subtracted without problems. The evaluated signal is caused by all organic molecules in the sample, dominated by the phospholipid due to its high concentration. Even in the samples with high cholesterol content, at least 70% of the scattering signal is caused by the phospholipid.

2.4. Data analysis

As done previously [7], one can create a mathematical model of the phospholipid molecules which incorporates several kinds of motion (e.g. a long-range translational flow-motion and two kinds of internal molecular reorientations). This model is fitted to the data, allowing to extract the parameter values (e.g. the width of the narrowest component which gives the flow velocity). This approach has the advantage of giving concrete numbers, for example for the flow velocity, but the disadvantage that these values can depend on the choice of model.

As this contribution is not focused on a detailed model of molecular motion or the extraction of absolute parameter values but on the *relative change* of mobility induced by additives, a model-independent data evaluation was performed. Two quantities are suitable for that purpose: the elastically scattered intensity and the full width at half maximum. Often, the *msd* is extracted from the elastically scattered intensity. However, this method is not particularly sensitive to the long-range motion, and can easily be influenced if the background is insufficiently corrected. Therefore, the full width at half maximum (FWHM) was extracted from the scattered intensities as a function of Q. Digitization effects were avoided by a linear interpolation between the two points on either side of the half maximum [59].

To get a measure of the broadening caused by the sample on top of the instrumental resolution $\Delta(Q)$, the FWHM of the vanadium standard was subtracted from the sample FWHM to obtain $\Delta(Q)$. If the signal caused by the sample is Gaussian, $\Delta(Q)$ is indeed its FWHM. For a Lorentzian broadening, $\Delta(Q)$ is in the region of interest about 70% of the FWHM but is in very good approximation proportional to it. It is therefore in both cases a valid measure of the broadening. All results will be shown in this form.

For the samples containing cholesterol, in an additional step we divide the $\Delta(Q)$ obtained from samples with additive by the ones of pure DMPC at the corresponding temperature. As the width is proportional to the mobility of the particles, this gives directly the ratio of mobility of the samples with additive compared to the one of pure DMPC. It was observed that the result depends hardly on Q, as expected. Therefore, an average over all values of Q was taken which we denote with *relative mobility*.

3. Results

3.1. Structural effects

The low-Q region of the diffraction patterns is shown in Fig. 3, obtained from the measurements with an incident neutron wavelength of 14 Å. It can be seen that the resulting diffraction patterns drop slightly with increasing Q. This is not connected to structural properties of the sample but is rather caused by the motional

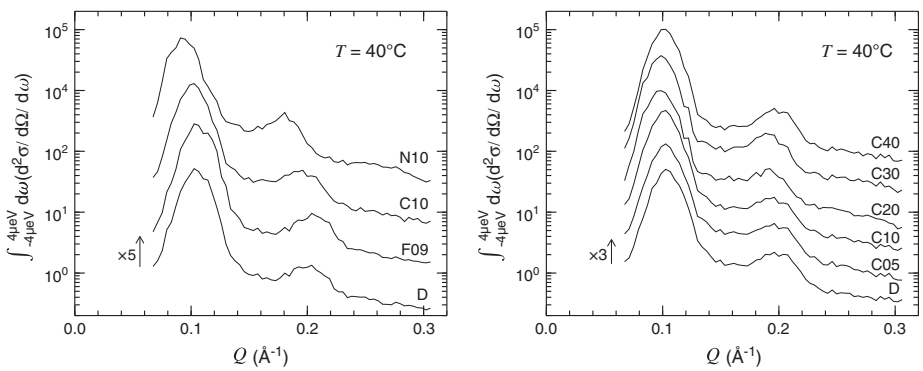

Fig. 3. Diffraction patterns of selected samples, as all samples in this study fully hydrated liquid crystals at 40 °C. All diffraction patterns except the ones of pure DMPC (D) are shifted by the factors indicated in the figure. Left: influence of about 10 mol% of the additives farnesol (F), cholesterol (C), and sodium glycocholate (N) compared to pure DMPC (D). Right: changes upon increasing the cholesterol content from 0 mol% (bottom) up to 40 mol% (top).

broadening of the quasielastic line which makes intensity move out of the integrated energy transfer region. The peaks are caused by the coherent scattering interferences due to the repeating units of the bilayers in the direction of the surface normal.

It can be seen that the overall diffraction pattern and therefore the bilayered structure of the membrane stacks is conserved. The peak position does not shift upon addition of 10 mol% farnesol, meaning that the repeating distance of the bilayers is not affected. A shift to lower values of Q can be observed when adding either 10 mol% of cholesterol or sodium glycocholate, corresponding to an increase of the repeating distance. The trends in the diffraction patterns of cholesterol agree with the ones observed by X-ray scattering [60,61] and MD simulations [62].

There is another correlation peak in the diffraction patterns at higher values of Q caused by the repeating distances of the chains within the membrane plane, becoming visible in the measurements using an incident neutron wavelength of 6 Å (not shown). While it is quite pronounced at 1.5 $Å^{-1}$ at 20 °C, it smears out drastically and moves to about 1.4 $Å^{-1}$ at temperatures above the chain melting transition. The additives do not change the position of this peak which does however not allow conclusions about a possible change of the area per lipid [22]. The peak height decreases with increasing cholesterol content, in agreement with previous studies [63].

3.2. Molecular mobility on a 60 ps time scale

While the diffraction patterns, obtained from integration of the energy-dependent spectra, yield information about the structure of the sample, the energy-dependence itself is connected to the motions of the molecules. Looking at a time scale of about 60 ps, the central line is visibly broadened compared to the one of a vanadium standard (instrumental resolution) of 60 μeV as can be seen in Fig. 4 exemplarily for some samples. The spectra–and therefore the observed motions–of the different samples are quite similar on this time scale.

The full width at half maximum $\Delta(Q)$ as defined above was extracted from the data at different momentum transfers Q. All spectra exhibit a line which is significantly broader than the instrumental resolution. All $\Delta(Q)$ show a small dip at $Q = 1.5$ $Å^{-1}$ at 20 °C which shifts to about 1.4 $Å^{-1}$ at higher temperatures as can be seen in Figs. 5 and 6. This is due to the so-called *de Gennes narrowing* at the structure factor maximum of a disordered phase. Therefore, these dips in $\Delta(Q)$ coincide with the peaks at large Q in the diffraction patterns discussed above.

The addition of myristic acid does not induce changes of this feature. Farnesol makes the dip less pronounced, especially at 20 °C, in contrast to cholesterol which also reduces the dip—except at 20 °C, similar to sodium glycocholate.

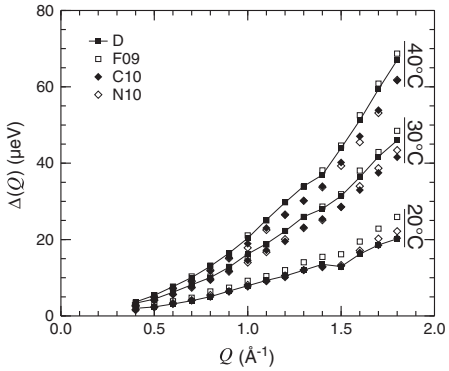

Fig. 5. Broadenings (FWHM) caused by selected samples: pure DMPC (D), farnesol (F), cholesterol (C), and sodium glycocholate (N). The points of pure DMPC are connected by straight lines for better clarity. Seen with an instrumental resolution of 60 μeV, corresponding to an observation time of 60 ps, at 20 °C, 30 °C, and 40 °C.

For a quick overview of the different effect of different substances, $\Delta(Q)$ of pure DMPC and samples with 10 mol% of all the studied additives except MA are compared with each other in Fig. 5. At 20 °C, below the main phase transition, the additives cause either no effect or an increased mobility compared to the pure DMPC. At the higher temperatures, farnesol seems to cause a small increase of the dynamics while cholesterol and NaGC slow the motions down by more or less the same amount.

Looking in more detail at the concentration dependent influence of the different additives one at a time in Fig. 6, it is evident that the addition of myristic acid has no systematic influence on the 60 ps dynamics of DMPC in its fluid phase; there is a trend towards lower mobility which is more pronounced at 20 °C. A systematic increase of the dynamics is observed for the Farnesol doped samples on the time scale of 60 ps, both, below and above the main phase transition. The addition of cholesterol does not change the dynamics at 20 °C at all but shows a clear systematic effect on the dynamics above the main phase transition. This decrease is rather continuous, compatible with NMR measurements [44]. Sodium glycocholate affects the line width similar to cholesterol above the main phase transition. Additionally, it enhances the dynamics at 20 °C slightly but not as much as farnesol.

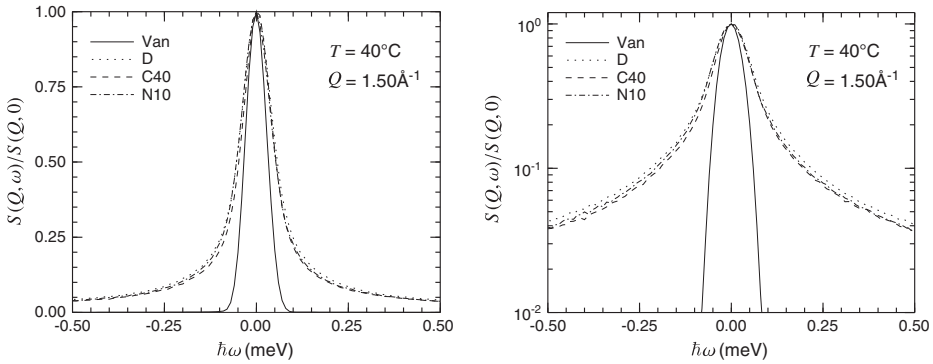

Fig. 4. Plot of selected normalized spectra–pure DMPC (D), 40 mol% cholesterol (C40), and 10 mol% sodium glycocholate (N10)–measured at 40 °C shown together with the instrumental resolution as determined by a vanadium measurement (Van), as seen with an instrumental resolution of 60 μeV, corresponding to an observation time of 60 ps, at a momentum transfer of $Q = 1.5$ $Å^{-1}$. The same spectra are shown on a linear scale (left) and on a logarithmic scale (right).

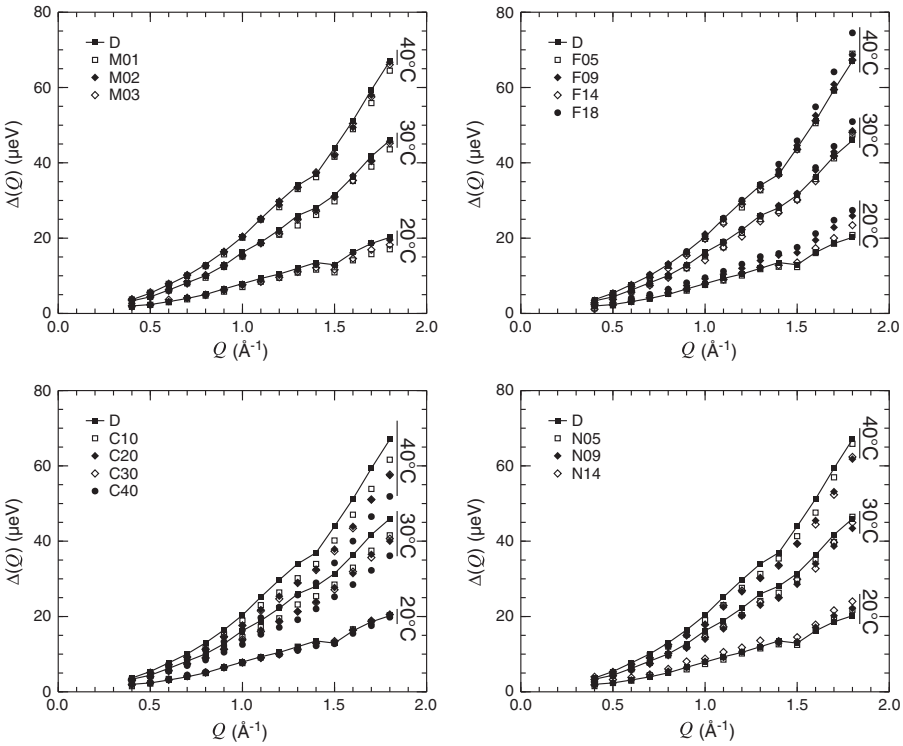

Fig. 6. Broadenings (FWHM) caused by all discussed samples at all discussed temperatures as observed with an instrumental resolution of 60 μeV, corresponding to an observation time of 60 ps. Top left: myristic acid; top right: farnesol; bottom left: cholesterol; bottom right: sodium glycocholate. The points of pure DMPC are connected by straight lines for better clarity.

3.3. Molecular mobility on a 900 ps time scale

On a time scale of 900 ps, the differences between the spectra are more pronounced (cf. Fig. 7). However, it becomes already clear when looking at the spectra that the influence depends very much on the type of additive: NaGC shows hardly any effect whereas cholesterol narrows the line considerably (which is still clearly broader than the instrumental resolution).

This picture is confirmed by the extracted widths $\Delta(Q)$ of the 10 mol% samples compared with the one of pure DMPC in Fig. 8: on a time scale of 900 ps and at a temperature of 40 °C, none of the probed additives causes an increase of the dynamics. Instead, farnesol and NaGC have basically no influence on the speed of the motions. Indeed, the width extracted from the samples with 10 mol% farnesol or sodium glycocholate differ by only 1% from the one of pure DMPC. In contrast, cholesterol causes a slowing down which is much more pronounced than on the 60 ps scale.

The quasielastic broadening of measurements with increasing cholesterol content is displayed in Fig. 9. The dynamics decreases continuously with increasing cholesterol concentration.

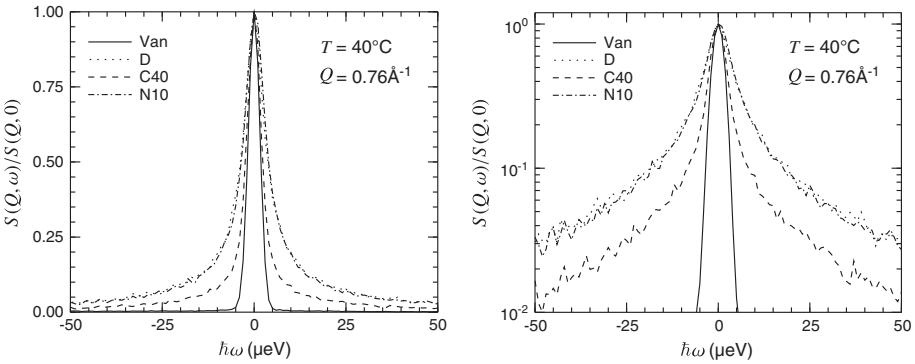

Fig. 7. Plots of selected normalized spectra–pure DMPC (D), 40 mol% cholesterol (C40), and 10 mol% sodium glycocholate (N10)–measured at 40 °C shown together with the instrumental resolution as determined by a vanadium measurement (Van), as seen with an instrumental resolution of 4 μeV, corresponding to an observation time of 900 ps, at a momentum transfer of Q = 0.76 Å^{-1}. The same spectra are shown on a linear scale (left) and on a logarithmic scale (right).

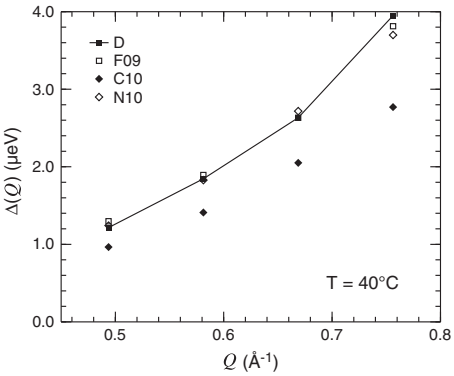

Fig. 8. Broadenings (FWHM) caused by selected samples: pure DMPC (D), farnesol (F), cholesterol (C), and sodium glycocholate (N). The points of pure DMPC are connected by straight lines for better clarity. Seen with an instrumental resolution of 4 μeV, corresponding to an observation time of 900 ps, at 40 °C.

4. Discussion

Different motions dominate the *msd* of atoms and molecules and hereby the signal of a QENS experiment when studying a sample on different time scales [57]: On a short time scale, fast motions–which are mostly reorientations within the molecule–predominate. On longer time scales, these motions can only contribute a constant to the *msd* which is then governed by the slower but non-localized motions of the whole molecule. Within the short times, the molecules explore their immediate vicinity whereas the larger motions have already previously been interpreted in the frame of flow-like motions of transient assembling patches of molecules in the membrane [6,7].

It is not surprising that these flow motions resemble the dynamical heterogeneities observed in 2D Lennard–Jones fluids, colloidal systems or granular media as the head groups form a dense 2D system. As the density in the head region is larger than the one in the tail region [24,64], we speculate that the mobility of the phospholipid molecules in the native membranes will be governed by the interaction of the head groups.

Additives can influence the head and tail region separately by increasing or decreasing the respective density (Fig. 10). If an additive caused a density in-/decrease in the head region, this would translate directly into a de-/increase of the DMPC mobility. For the more loosely

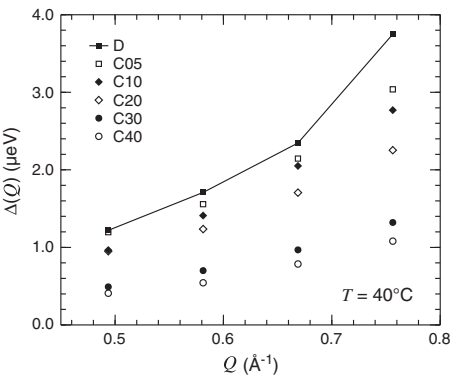

Fig. 9. Broadenings (FWHM) caused by samples with increasing cholesterol content at 40 °C as observed with an instrumental resolution of 4 μeV, corresponding to an observation time of 900 ps. The points of pure DMPC are connected by straight lines for better clarity.

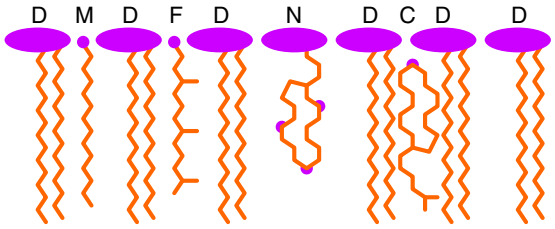

Fig. 10. Sketch of the proposed configuration of the molecules, denoted by D (DMPC), M (myristic acid), F (farnesol), N (NaGC), and C (cholesterol). The hydrophilic parts are schematically displayed as violet bubbles, the hydrophobic chains and steroid as orange sticks.

packed tails, the connection is more intricate: A density decrease would not cause a further increase of the mobility as the head groups are the limiting factor already. Nevertheless, when increasing the density in the tail group region of a membrane by additives, a reduced mobility of DMPC molecules should be observed.

Thus, we suggest to interpret the influence of additives on the dynamics of DMPC in the liquid crystalline phase according to the amount of free volume in the DMPC bilayer created or annihilated by the intercalation of guest molecules and the influence of this free volume on the flow-like motions in the membrane. The results of our measurements, summarized in Table 2 for the different additives, are discussed in this sense below. We would like to stress that we do *not* see this as a support for the free volume theory which relies on further assumptions such as jump-like motions of the molecules.

If only the head region is densely packed, the displacements of the molecules will be caused by the density fluctuations there. If also the tail region is densely packed, the molecules will be influenced also by density fluctuations in this region. Should the fluctuations in the two regions be completely correlated, there will be no influence on the flow-like motions of the molecules. Every decorrelation between the two will decrease the persistence time of a flow event of one molecule. This interpretation also agrees with results from coarse-grained simulations which found a disrupting effect of cholesterol on the collective diffusion of the phospholipid molecules [65]. A reduction of the flow time and correspondingly flow length of a random walk translates directly in a reduction of the resulting diffusion coefficient.

4.1. Myristic acid

Although the effects of myristic acid as an additive did not cause a significant effect on the microscopic scale (cf. Fig. 6), drastic changes of the macroscopic behavior (increasing viscosity) of the phospholipid were observed already for low myristic acid concentrations. It cannot be excluded that stronger effects would be visible if the concentration could be increased to levels comparable to, e.g., cholesterol. But this does not seem not to be very likely because myristic acid is a chain-like molecule and can thus be expected to be oriented mainly parallel to the DMPC chains. The hydrophilic carboxyl group can be expected to stick into the headgroup region of the DMPC layers. Therefore,

Table 2
Summary of the observed effects of several additives on the dynamics of DMPC on time scales of 60 and 900 ps. While ∅ indicates no change of the dynamics, the number of + and − correspond to the degree of increase or decrease of the mobility.

	60 ps			900 ps
	20 °C	30 °C	40 °C	40 °C
MA	−	∅	∅	
Farnesol	++	+	+	∅
Cholesterol	∅	−	−	−
NaGC	+	−	−	∅

myristic acid should not fill up free volume in the tail region of DMPC bilayers and should also not alter their head group packing significantly [30]. This is in agreement with corresponding studies using short chain alcohols as additives where also no effect on the phospholipid dynamics was observed [66].

4.2. Farnesol

The behavior of farnesol inside DMPC bilayers seems to be similar to the one of myristic acid. From NMR measurements, it could not be determined whether the molecules intercalate between the DMPC molecules or are placed in between the two leaflets [35]. The diffraction patterns in Fig. 3 show no influence of Farnesol on peak distance and height of the first two layer repeating peaks. Although we cannot exclude that a change in the bilayer thickness is exactly compensated by an accompanying change in water thickness, we see no evidence for a change of the bilayer thickness upon the addition of farnesol. This indicates that the molecules intercalate between the DMPC molecules. Respecting that the effect on the mobility of DMPC is negligible, we conclude that the molecules align themselves along the phospholipid molecules similar to the case of myristic acid. It is known from NMR measurements [34] that farnesol has a different influence on the surrounding phospholipid molecules compared to cholesterol. While cholesterol causes an increase of the molecular order parameters, farnesol does not. However, farnesol lowers the main phase transition temperature which might explain the unusual increased dynamics at 20 °C: the addition of farnesol probably induces a melting of the phospholipid chains.

4.3. Cholesterol

Cholesterol causes an increasing thickness of the membrane. This was also observed by X-ray diffraction and simulations and reflects the condensation effect [39,60,61]. The incorporation of cholesterol into the phospholipid membrane can be understood in the frame of the umbrella model [67]: The hydrophobic cholesterol molecule resides between the hydrophobic tails of the phospholipids. The hydrophilic heads of the phospholipid shield the tails and cholesterol from the surrounding water. This leads to an increase of the density in the hydrophobic part of the bilayers.

This density increase reduces the free volume in the chain region of the DMPC molecules. In this situation, the mobility of the phospholipid molecules is no more mainly determined by the dynamic inhomogeneities in the densely packed head groups but also by those in the now more closely packed tail groups resulting in a significantly slower molecular transport.

The influence of cholesterol on DMPC as seen with quasielastic neutron scattering in the present study is summarized in Fig. 11: the widths $\Delta(Q)$ are normalized to the widths of pure DMPC at the same temperature and averaged over all Q values, yielding the *relative mobility*. It can immediately be seen that in no case the addition of cholesterol causes an increased dynamics of DMPC.

The motions detected within an observation time of 60 ps are not affected by the addition of cholesterol at temperatures below the main phase transition. At temperatures above the main phase transition, the tails experience the density increase caused by cholesterol. The relative decrease of the linewidth is completely identical at 30 °C and 40 °C for all measured cholesterol concentrations which indicates that the observed motions are not sensitive to the absolute distance from the phase transition temperature as one might expect for local motions.

The mobility decrease of DMPC is enhanced when looking on a time scale of 900 ps where the influence of 5 mol% cholesterol affects the phospholipids more strongly at 30 °C than at 40 °C. The corresponding motions are, therefore, more sensitive to an increase in density if the sample temperature is closer to the main phase

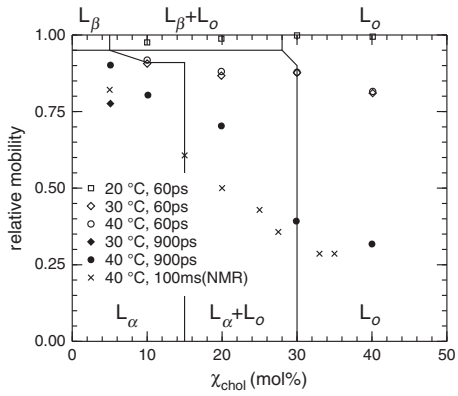

Fig. 11. The relative mobility (mobility normalized to the one of pure DMPC, cf. text) as a function of cholesterol concentration at different temperatures. Open symbols are extracted from measurements with an instrumental resolution of 60 μeV, corresponding to an observation time of 60 ps; closed symbols are extracted from measurements with an instrumental resolution of 4 μeV, corresponding to an observation time of 900 ps. NMR measurements taken from Filippov et al. [44] at 40 °C are also shown. The phase boundaries are drawn after EPR results of Sankaram [43] and are only valid for the displayed measurements. They are only displayed to show the respective phases of the measurements and do not represent a phase diagram.

transition temperature which we see again as a signature of the long-range nature of this motion.

Also other techniques were used to measure the long-range motion of the phospholipid molecules. MD simulations [24] of the phospholipid DPPC at 50 °C, i.e. 8 K above the main phase transition of pure DPPC, show a strong impact of cholesterol on the phospholipid mobility on a 100 ns time scale—stronger than our measurements at 40 °C, even a bit more than the one at 30 °C, i.e. 6 K above the main phase transition of pure DMPC.

Fluorescence correlation spectroscopy of the phospholipid DLPC [42] on a 10 ms time scale at 25 °C, i.e. 27 K above the main phase transition of DLPC, shows an impact of cholesterol on the dynamics which is very comparable to the results obtained on a 100 ms time scale with NMR [44] for DMPC at 40 °C.

The comparison between all these results is not straightforward as different temperatures and even phospholipids were used. Only the NMR measurements were done with exactly same temperature and phospholipid as studied here and show a very good agreement with our results. All these techniques measure on longer time scales than QENS and we would therefore expect them to show a stronger impact on the dynamics—as they do. The NMR data also show a stronger influence of cholesterol on the phospholipid motions the closer the temperature is to the main phase transition.

Much in contrast, two measurements on even larger time (about 10 s) and length scales using FRAP [41,43] observed a smaller impact of cholesterol on the dynamics. The degree varies between the measurements, one [43] even observes no impact up to about 15 mol% cholesterol in the sample. The difference between the FRAP measurements and the values obtained by NMR were discussed in terms of the susceptibility of FRAP to the formation of microdomains in the membrane [44].

4.4. Sodium glycocholate

Sodium glycocholate is a charged molecule. It is known that charged phospholipids induce an increase of the thickness of the water layer between the bilayers but not of the membrane itself [68]. This swelling is the thickness increase observed in the diffraction patterns. At low concentrations, the influence of NaGC on the

dynamics of the phospholipid is similar to the one of cholesterol. However, cholesterol is uncharged, has not such an influence on the structure and can, therefore, be present in membranes in much higher concentrations.

The practical importance of sodium glycocholate is based on its ability to stabilize emulsions even during crystallization of the oily phase. In the case of triglyceride or alkane nanoemulsions, the shape of the stabilized particles changes drastically during crystallization: from a spherical droplet to an elongated crystalline platelet. This is connected to a sudden increase of the surface of the particle. One could imagine that this results in a partial coverage of the particle with stabilizer—the uncovered surfaces are then the origin of aggregation. A redistribution of the stabilizer onto the naked surface could prevent aggregation, happens however so slowly that the aggregation took place before.

As the addition of sodium glycocholate prevents aggregation, it could have had the effect of enhancing the dynamics of the phospholipid, making the redistribution of the stabilizer so fast that aggregation is suppressed.

However, sodium glycocholate does not influence the phospholipid dynamics. It can be excluded that it did not mix with the phospholipid because it is water soluble, caused a decrease of viscosity, made the sample more transparent, and changed the bilayer spacing. As NaGC is hydrophilic, an enhanced partition into the chain region should not be expected. We see two likely structural arrangements: Either the NaGC is intercalated inside the bilayer oriented with the hydrophilic part in the region of the phospholipid head groups and the hydrophobic part in the chain region of the bilayer. Obviously, this leads to hardly any change in the free volume in either region of the membrane. Or–as already previously speculated for sodium cholate in lecithin [69] –a flat placement of the molecules on the bilayer in the head region. This would lead to a density decrease in the tail region which would, as we have argued before, not influence the dynamics.

4.5. Other influences on membrane dynamics

Using NMR, the influence of the antimicrobial peptide gramicidin was found to be comparable to the one of cholesterol on a sub-nanosecond time scale [70]. Also neutron scattering experiments showed a decreased mobility on a time scale of about 150 ps [71]. Our results are in good agreement with the view that the effects caused by gramicidin are directly comparable with the ones caused by cholesterol. However, we would like to point out that the underlying mechanism might be very different as gramicidin is approximatively barrel-like [72] and does therefore not increase the density in the tail region. However, the same study showed that the hydration of the phospholipid molecules in the vicinity of the peptide is decreased. A decreased hydration is in turn known to decrease the dynamics [73] so the decreased hydration might actually influence the dynamics more than the change in density.

In MD simulations, it was observed that proteins in the membrane cause a slowing down of adjacent phospholipid molecules [23]. This effect could be reproduced for a number of different proteins in the membrane and also 2D Lennard–Jones systems which suggests that this effect is partly caused by the obstacles hindering phospholipid motions, and complemented by specific effects due to protein-lipid interactions.

Whereas these interactions of phospholipids with peptides and proteins might be dominated by other effects than density changes, their aforementioned use as stabilizer in suspensions and emulsions could be directly influenced by the density as it might very well be that the amount of phospholipid is lower than what one would need for a full monolayer around the particles. Preliminary results indeed seem to show that the effect of decreasing mobility upon increasing density can hereby be reversed, observing increasing dynamics when artificially decreasing the density by stretching a monolayer [28,74].

5. Conclusion

Summarizing, we studied the effect of several additives on the dynamics of the phospholipid DMPC on time scales of 60 ps and 900 ps. Myristic acid and farnesol, two more linear, chain-like molecules seem to incorporate into the membrane without modification of the mobility. Cholesterol has a pronounced slowing down effect on the dynamics. This effect can be qualitatively understood assuming that the persistence lengths of flow patterns decrease. The flow-like mobility of the molecules is the equivalent to dynamic heterogeneities observed in supercooled liquids, suspensions and granular systems. Sodium glycocholate has–in contrast to its strong macroscopic influences–no effect on the mobility.

Acknowledgments

We would like to thank W. Petry for his enduring interest and support as well as L. C. Pardo, T. Gutberlet, and J. Horbach for many stimulating discussions.

References

[1] D. Axelrod, Lateral motion of membrane proteins and biological function, J. Membr. Biol. 75 (1) (1983) 1, doi:10.1007/bf01870794.
[2] L. Sagalowicz, M.E. Leser, Delivery systems for liquid food products, Curr. Opin. Colloid Interface Sci. 15 (1-2) (2010) 61, doi:10.1016/j.cocis.2009.12.003.
[3] C. Peetla, A. Stine, V. Labhasetwar, Biophysical interactions with model lipid membranes: applications in drug discovery and drug delivery, Mol. Pharm. 6 (5) (2009) 1264–1276, doi:10.1021/mp9000662.
[4] K. Kawano, E. Onose, Y. Hattori, Y. Maitani, Higher liposomal membrane fluidity enhances the in vitro antitumor activity of folate-targeted liposomal mitoxantrone, Mol. Pharm. 6 (1) (2009) 98–104, doi:10.1021/mp800069c.
[5] W.L.C. Vaz, P.F.F. Almeida, Microscopic versus macroscopic diffusion in one-component fluid phase lipid bilayer-membranes, Biophys. J. 60 (6) (1991) 1553–1554, doi:10.1016/S0006-3495(91)82190-7.
[6] E. Falck, T. Róg, M. Karttunen, I. Vattulainen, Lateral diffusion in lipid membranes through collective flows, J. Am. Chem. Soc. 130 (1) (2008) 44–45, doi:10.1021/ja7103558.
[7] S. Busch, C. Smuda, L.C. Pardo, T. Unruh, Molecular mechanism of long-range diffusion in phospholipid membranes studied by quasielastic Neutron Scattering, J. Am. Chem. Soc. 132 (10) (2010) 3232, doi:10.1021/ja907581s.
[8] M.C. Rheinstädter, J. Das, E. Flenner, B. Brüning, T. Seydel, I. Kosztin, Motional coherence in fluid phospholipid membranes, Phys. Rev. Lett. 101 (24) (2008) 248106, doi:10.1103/physrevlett.101.248106.
[9] T. Apajalahti, P.S. Niemelä, P.N. Govindan, M.S. Miettinen, E. Salonen, S.-J. Marrink, I. Vattulainen, Concerted diffusion of lipids in raft-like membranes, Faraday Discuss. 144 (2010) 411, doi:10.1039/b901487j.
[10] W. Kob, C. Donati, S. Plimpton, P. Poole, S.C. Glotzer, Dynamical heterogeneities in a supercooled Lennard–Jones liquid, Phys. Rev. Lett. 79 (15) (1997) 2827, doi:10.1103/physrevlett.79.2827.
[11] C. Donati, J. Douglas, W. Kob, S. Plimpton, P. Poole, S.C. Glotzer, Stringlike cooperative motion in a supercooled liquid, Phys. Rev. Lett. 80 (11) (1998) 2338, doi:10.1103/physrevlett.80.2338.
[12] H.R. Schober, C. Gaukel, C. Oligschleger, Collective jumps in amorphous materials, Defect Diffus. Forum 143-147 (1997) 723, doi:10.4028/www.scientific.net/ddf.143-147.723.
[13] R. Richert, Heterogeneous dynamics in liquids: fluctuations in space and time, J. Phys. Condens. Matter 14 (23) (2002) R703, doi:10.1088/0953-8984/14/23/201.
[14] A. Marcus, J. Schofield, S.A. Rice, Experimental observations of non-Gaussian behavior and stringlike cooperative dynamics in concentrated quasi-two-dimensional colloidal liquids, Phys. Rev. E 60 (5) (1999) 5725, doi:10.1103/physreve.60.5725.
[15] W.K. Kegel, Direct observation of dynamical heterogeneities in colloidal hard-sphere suspensions, Science 287 (5451) (2000) 290, doi:10.1126/science.287.5451.290.
[16] B. Cui, B. Lin, S.A. Rice, Dynamical heterogeneity in a dense quasi-two-dimensional colloidal liquid, J. Chem. Phys. 114 (20) (2001) 9142, doi:10.1063/1.1369129.
[17] R. Zangi, S.A. Rice, Cooperative dynamics in two dimensions, Phys. Rev. Lett. 92 (3) (2004) 035502, doi:10.1103/physrevlett.92.035502.
[18] A.S. Keys, A.R. Abate, S.C. Glotzer, D.J. Durian, Measurement of growing dynamical length scales and prediction of the jamming transition in a granular material, Nat. Phys. 3 (4) (2007) 260, doi:10.1038/nphys572.
[19] R. Matena, M. Dijkstra, A. Patti, Non-Gaussian dynamics in smectic liquid crystals of parallel hard rods, Phys. Rev. E 81 (2) (2010) 021704, doi:10.1103/physreve.81.021704.
[20] M. Hurley, P. Harrowell, Kinetic structure of a two-dimensional liquid, Phys. Rev. E 52 (2) (1995) 1694, doi:10.1103/physreve.52.1694.
[21] S. Tristram-Nagle, Y. Liu, J. Legleiter, J.F. Nagle, Structure of gel phase DMPC determined by X-ray diffraction, Biophys. J. 83 (6) (2002) 3324, doi:10.1016/s0006-3495(02)75333-2.

[22] J.S. Hub, T. Salditt, M.C. Rheinstädter, B.L. de Groot, Short-range order and collective dynamics of DMPC bilayers: a comparison between molecular dynamics simulations, X-ray, and neutron scattering experiments, Biophys. J. 93 (9) (2007) 3156–3168, doi:10.1529/biophysj.107.104885.
[23] P.S. Niemelä, M.S. Miettinen, L. Monticelli, H. Hammaren, P. Bjelkmar, T. Murtola, E. Lindahl, I. Vattulainen, Membrane proteins diffuse as dynamic complexes with lipids, J. Am. Chem. Soc. 132 (22) (2010) 7574, doi:10.1021/ja101481b.
[24] E. Falck, M. Patra, M. Karttunen, M.T. Hyvönen, I. Vattulainen, Lessons of slicing membranes: interplay of packing, free area, and lateral diffusion in phospholipid/cholesterol bilayers, Biophys. J. 87 (2) (2004) 1076–1091, doi:10.1529/biophysj.104.041368.
[25] P.N. Pusey, W. van Megen, Observation of a glass transition in suspensions of spherical colloidal particles, Phys. Rev. Lett. 59 (18) (1987) 2083, doi:10.1103/physrevlett.59.2083.
[26] P.F.F. Almeida, W.L.C. Vaz, T.E. Thompson, Lipid diffusion, free area, and molecular dynamics simulations, Biophys. J. 88 (6) (2005) 4434–4438, doi:10.1529/biophysj.105.059766.
[27] E. Falck, M. Patra, M. Karttunen, M.T. Hyvönen, I. Vattulainen, Response to comment by Almeida et al.: free area theories for lipid bilayers—predictive or not? Biophys. J. 89 (1) (2005) 745–752, doi:10.1529/biophysj.105.065714.
[28] M. Javanainen, L. Monticelli, J.B. de la Serna, I. Vattulainen, Free volume theory applied to lateral diffusion in Langmuir monolayers: atomistic simulations for a protein-free model of lung surfactant, Langmuir 26 (19) (2010) 15436–15444, doi:10.1021/la102454m.
[29] S. Ghosh, A. Adhikari, S. Sen Mojumdar, K. Bhattacharyya, A fluorescence correlation spectroscopy study of the diffusion of an organic dye in the gel phase and fluid phase of a single lipid vesicle, J. Phys. Chem. B 114 (17) (2010) 5736–5741, doi:10.1021/jp911971p.
[30] G. Peters, F. Hansen, M. Møller, P. Westh, Effects of fatty acid inclusion in a DMPC bilayer membrane, J. Phys. Chem. B 113 (1) (2009) 92–102, doi:10.1021/jp806205m.
[31] V. Oberle, Untersuchungen zum Einfluß freier Fettsäuren auf die Eigenschaften biologischer und Modellmembranen, Ph.D. thesis, Martin-Luther-Universität, Halle (Saale), 1999.
[32] R. Koynova, B. Tenchov, G. Rapp, Mixing behavior of saturated short-chain phosphatidylcholines and fatty acids: eutectic points, liquid and solid immiscibility, non-lamellar phases, Chem. Phys. Lipids 88 (1) (1997) 45, doi:10.1016/s0009-3084(97)00043-1.
[33] J. Joo, A. Jetten, Molecular mechanisms involved in farnesol-induced apoptosis, Cancer Lett. 287 (2) (2010) 123–135, doi:10.1016/j.canlet.2009.05.015.
[34] A.C. Rowat, J.H. Davis, Farnesol-DMPC phase behaviour: a (2)H-NMR study, Biochim. Biophys. Acta 1661 (2) (2004) 178–187, doi:10.1016/j.bbamem.2004.01.002.
[35] A.C. Rowat, D. Keller, J.H. Ipsen, Effects of farnesol on the physical properties of DMPC membranes, Biochim. Biophys. Acta 1713 (1) (2005) 29–39, doi:10.1016/j.bbamem.2005.04.014.
[36] G. Orädd, V. Shahedi, G. Lindblom, Effect of sterol structure on the bending rigidity of lipid membranes: a 2H NMR transverse relaxation study, Biochim. Biophys. Acta (BBA) - Biomembr. 1788 (9) (2009) 1762–1771, doi:10.1016/j.bbamem.2009.06.019.
[37] D.A. Mannock, R.N. Lewis, R.N. McElhaney, A calorimetric and spectroscopic comparison of the effects of ergosterol and cholesterol on the thermotropic phase behavior and organization of dipalmitoylphosphatidylcholine bilayer membranes, Biochim. Biophys. Acta 1798 (3) (2010) 376–388, doi:10.1016/j.bbamem.2009.09.002.
[38] J.M. Berg, J.L. Tymoczko, L.Stryer, Biochemie, Spektrum Akademischer Verlag, 5. a. edn., ISBN 9783827413031, 2003.
[39] T. Róg, M. Pasenkiewicz-Gierula, I. Vattulainen, M. Karttunen, Ordering effects of cholesterol and its analogues, Biochim. Biophys. Acta 1788 (1) (2009) 97–121, doi:10.1016/j.bbamem.2008.08.022.
[40] E. Falck, M. Patra, M. Karttunen, M.T. Hyvönen, I. Vattulainen, Impact of cholesterol on voids in phospholipid membranes, J. Chem. Phys. 121 (24) (2004) 12676–12689, doi:10.1063/1.1824033.
[41] J.L. Rubenstein, B.A. Smith, H.M. McConnell, Lateral diffusion in binary mixtures of cholesterol and phosphatidylcholines, Proc. Natl Acad. Sci. USA 76 (1) (1979) 15–18.
[42] J. Korlach, P. Schwille, W.W. Webb, G.W. Feigenson, Characterization of lipid bilayer phases by confocal microscopy and fluorescence correlation spectroscopy, Proc. Natl Acad. Sci. USA 96 (15) (1999) 8461–8466.
[43] P.F.F. Almeida, W.L.C. Vaz, T.E. Thompson, Lateral diffusion in the liquid phases of dimyristoylphosphatidylcholine/cholesterol lipid bilayers: a free volume analysis, Biochemistry 31 (29) (1992) 6739, doi:10.1021/bi00144a013.
[44] A. Filippov, G. Orädd, G. Lindblom, The effect of cholesterol on the lateral diffusion of phospholipids in oriented bilayers, Biophys. J. 84 (5) (2003) 3079, doi:10.1016/s0006-3495(03)70033-2.
[45] A.-L. Kuo, C.G. Wade, Lipid lateral diffusion by pulsed nuclear magnetic resonance, Biochemistry 18 (11) (1979) 2300, doi:10.1021/bi00578a026.
[46] J. Zidar, F. Merzel, M. Hodošček, K. Rebolj, K. Sepčić, P. Maček, D. Janežič, Liquid-ordered phase formation in cholesterol/sphingomyelin bilayers: all-atom molecular dynamics simulations, J. Phys. Chem. B 113 (2009) 15795, doi:10.1021/jp907138h.
[47] C. Gliss, O. Randel, H. Casalta, E. Sackmann, R. Zorn, T.M. Bayerl, Anisotropic motion of cholesterol in oriented DPPC bilayers studied by quasielastic neutron scattering: the liquid-ordered phase, Biophys. J. 77 (1) (1999) 331, doi:10.1016/s0006-3495(99)76893-1.
[48] R. Tampe, A. Von Lukas, H.-J. Galla, Glycophorin-induced cholesterol-phospholipid domains in dimyristoylphosphatidylcholine bilayer vesicles, Biochemistry 30 (20) (1991) 4909, doi:10.1021/bi00234a011.
[49] P. Schurtenberger, N. Mazer, W. Känzig, Micelle to vesicle transition in aqueous solutions of bile salt and lecithin, J. Phys. Chem. 89 (6) (1985) 1042, doi:10.1021/j100252a031.
[50] K. Matsuoka, M. Maeda, Y. Moro, Micelle formation of sodium glyco- and taurocholates and sodium glyco- and taurodeoxycholates and solubilization of cholesterol into their micelles, Colloids Surf., B 32 (2) (2003) 87, doi:10.1016/s0927-7765(03)00148-6.
[51] K. Westesen, B. Siekmann, Investigation of the gel formation of phospholipid-stabilized solid lipid nanoparticles, Int. J. Pharm. 151 (1) (1997) 35, doi:10.1016/s0378-5173(97)04890-4.
[52] S. Teixeira, J. Ankner, M.-C. Bellissent-Funel, R. Bewley, M. Blakeley, L. Coates, R. Dahint, R. Dalgliesh, N. Dencher, J. Dhont, P. Fischer, V. Forsyth, G. Fragneto, B. Frick, T. Geue, R. Gilles, T. Gutberlet, M. Haertlein, T. Hauß, W. Häußler, W. Heller, K. Herwig, O. Holderer, F. Jurányi, R. Kampmann, R. Knott, J. Kohlbrecher, S. Kreuger, P. Langan, R.E. Lechner, G. Lynn, C. Majkrzak, R. May, F. Meilleur, Y. Mo, K. Mortensen, D. Myles, F. Natali, C. Neylon, N. Niimura, J. Ollivier, A. Ostermann, J. Peters, J. Pieper, A. Rühm, D. Schwahn, K. Shibata, A. Soper, T. Strässle, U. Suzuki, I. Tanaka, M. Tehei, P. Timmins, N. Torikai, T. Unruh, V. Urban, R. Vavrin, K. Weiss, G. Zaccai, New sources and instrumentation for neutrons in biology, Chem. Phys. 345 (2–3) (2008) 133–151, doi:10.1016/j.chemphys.2008.02.030.
[53] V. García Sakai, A. Arbe, Quasielastic neutron scattering in soft matter, Curr. Opin. Colloid Interface Sci. 14 (6) (2009) 381, doi:10.1016/j.cocis.2009.04.002.
[54] T. Unruh, J. Neuhaus, W. Petry, The high-resolution time-of-flight spectrometer TOFTOF, Nucl. Instrum. Methods Phys. Res. Sect. A 580 (3) (2007) 1414–1422, doi:10.1016/j.nima.2007.07.015, and 585 (3) (2008) 201, doi:10.1016/j.nima.2007.11.019.
[55] A. Furrer, J. Mesot, T. Strässle, Neutron Scattering in Condensed Matter Physics (Neutron Techniques and Applications) (Series on Neutron Techniques and Applications), 1 ed., World Scientific Publishing Company, ISBN: 9789810248314, 2009.
[56] M. Bée, Quasielastic Neutron Scattering, Taylor & Francis, ISBN: 9780852743713, 1988.
[57] T. Unruh, C. Smuda, S. Busch, J. Neuhaus, W. Petry, Diffusive motions in liquid medium-chain n-alkanes as seen by quasielastic time-of-flight neutron spectroscopy, J. Chem. Phys. 129 (2008) 121106, doi:10.1063/1.2990026.
[58] J. Wuttke, Improved sample holder for multidetector neutron spectrometers, Phys. B Condensed Matter 266 (1-2) (1999) 112, doi:10.1016/s0921-4526(98)01503-8.
[59] J. Wuttke, Frida1: Fast Reliable Interactive Data Analysis, http://sourceforge.net/projects/frida/, URL http://sourceforge.net/projects/frida/, software, 1990–.
[60] W.-C. Hung, M.-T. Lee, F.-Y. Chen, H.W. Huang, The condensing effect of cholesterol in lipid bilayers, Biophys. J. 92 (11) (2007) 3960–3967, doi:10.1529/biophysj.106.099234.
[61] B. Brüning, M.C. Rheinstädter, A. Hiess, B. Weinhausen, T. Reusch, S. Aeffner, T. Salditt, Influence of cholesterol on the collective dynamics of the phospholipid acyl chains in model membranes, Eur. Phys. J. E Soft Matter 31 (4) (2010) 419–428, doi:10.1140/epje/i2010-10574-6.
[62] M. Alwarawrah, J. Dai, J. Huang, A molecular view of the cholesterol condensing effect in DOPC lipid bilayers, J. Phys. Chem. B 114 (22) (2010) 7516–7523, doi:10.1021/jp101415g.
[63] S.W. Hui, N.B. He, Molecular organization in cholesterol-lecithin bilayers by x-ray and electron diffraction measurements, Biochemistry 22 (5) (1983) 1159, doi:10.1021/bi00274a026.
[64] S.J. Marrink, R.M. Sok, H.J.C. Berendsen, Free volume properties of a simulated lipid membrane, J. Chem. Phys. 104 (22) (1996) 9090, doi:10.1063/1.471442.
[65] G.S. Ayton, G.A. Voth, Mesoscopic lateral diffusion in lipid bilayers, Biophys. J. 87 (5) (2004) 3299–3311, doi:10.1529/biophysj.104.047811.
[66] T. Gutberlet, D. Posselt, T. Unruh, Influence of short chain alcohols on local dynamics of DMPC, Experimental Report 935, Forschungsneutronenquelle Heinz Maier-Leibnitz (FRM II), Technische Universität München, Germany, 2008.
[67] J. Huang, A microscopic interaction model of maximum solubility of cholesterol in lipid bilayers, Biophys. J. 76 (4) (1999) 2142, doi:10.1016/s0006-3495(99)77369-8.
[68] R.P. Rand, Interacting phospholipid bilayers: measured forces and induced structural changes, Annu. Rev. Biophys. Bioeng. 10 (1981) 277–314, doi:10.1146/annurev.bb.10.060181.001425.
[69] J. Ulmius, G. Lindblom, H. Wennerstroem, L.B.A. Johansson, K. Fontell, O. Soederman, G. Arvidson, Molecular organization in the liquid-crystalline phases of lecithin-sodium cholate-water systems studied by nuclear magnetic resonance, Biochemistry 21 (7) (1982) 1553, doi:10.1021/bi00536a014.
[70] Z.Y. Peng, V. Simplaceanu, S.R. Dowd, C. Ho, Effects of cholesterol or gramicidin on slow and fast motions of phospholipids in oriented bilayers, Proc. Natl Acad. Sci. USA 86 (22) (1989) 8758–8762.
[71] U. Wanderlingh, G. D'Angelo, V. Conti Nibali, M. Gonzalez, C. Crupi, C. Mondelli, Influence of gramicidin on the dynamics of DMPC studied by incoherent elastic neutron scattering, J. Phys. Condens. Matter 20 (10) (2008) 104214, doi:10.1088/0953-8984/20/10/104214.
[72] J.A. Killian, B. De Kruijff, Importance of hydration for gramicidin-induced hexagonal HII phase formation in dioleoylphosphatidylcholine model membranes, Biochemistry 24 (27) (1985) 7890, doi:10.1021/bi00348a007.
[73] S. König, W. Pfeiffer, T.M. Bayerl, D. Richter, E. Sackmann, Molecular dynamics of lipid bilayers studied by incoherent quasi-elastic neutron scattering, J. Phys. II Fr. 2 (8) (1992) 1589, doi:10.1051/jp2:1992100.
[74] S. Busch, et al., in preparation.

Appendix F.

The Picosecond Dynamics of the Phospholipid Dimyristoylphosphatidylcholine in Mono- and Bilayers

Sebastian Busch, Luis Carlos Pardo, Christoph Smuda, and Tobias Unruh
Soft Matter, 8:3576, 2012
http://dx.doi.org/10.1039/c2sm07380c

In this publication, the author prepared the samples, partially with Tobias Unruh. He performed the measurements, developed the method for the determination of the amount of background to be subtracted, and performed the data reduction and evaluation. He interpreted the results and wrote the publication.

After the detailed study of phospholipid motions in multibilayers of pure DMPC [B, D] and the characterisation of the change of this dynamics under the influence of additives [E], the mixed systems of DMPC and additives are now used in pharmaceutically relevant systems. The data evaluation is model-free as previously [E] because the low amount of sample does not allow a more detailed evaluation. It was found that the mobility of the phospholipid molecules on the emulsion droplets increases with increasing area per molecule.

Reproduced by permission of The Royal Society of Chemistry.

Soft Matter

Dynamic Article Links

Cite this: *Soft Matter*, 2012, **8**, 3576

www.rsc.org/softmatter

PAPER

The picosecond dynamics of the phospholipid dimyristoylphosphatidylcholine in mono- and bilayers†

Sebastian Busch,*[a] Luis Carlos Pardo,[b] Christoph Smuda[c] and Tobias Unruh*[ad]

Received 14th December 2011, Accepted 18th January 2012
DOI: 10.1039/c2sm07380c

The dynamics of the fully hydrated phospholipid dimyristoylphosphatidylcholine (DMPC) were studied on a time scale of about 60 picoseconds with quasielastic neutron scattering. Three types of samples were employed: multibilayers without solid support, single bilayers in vesicles, and monolayers in emulsions of perdeuterated hexadecane. The vesicles and emulsion droplets had diameters of about 130 nanometres; some of the emulsions also contained sodium glycocholate to enhance the stability. It could be shown that the mobility of the phospholipid molecules in the observed time regime increases from multibilayers over single bilayers to monolayers. Additionally, the high quality of the data of the multibilayer samples allows an evaluation of the molecular mechanism of the motions: while the interpretation in the frame of flow-like motions fits well at temperatures shortly above the main phase transition, the model of diffusive motions fits better at high temperatures of up to 80 °C.

1 Introduction

The dynamics of phospholipids is of interest in fields as different as biology – they are the main constituent of cell membranes[1,2] – or pharmaceutical and food technology, where they can function as a bio-compatible stabilizing agent around lipid emulsions or suspensions, facing the dispersed phase with their lipophilic tail groups and the aqueous surrounding with their hydrophilic head group.[3–5]

It was found that the stabilizer layer plays an important role for the stability of the emulsions, not only concerning coagulation but also chemical degradation.[6] The stabilizing capability of phospholipids can be greatly enhanced by adding co-stabilizers such as sodium glycocholate (NaGC)[7,8] which can provide stability even for crystallizing emulsion droplets which undergo a change of shape from droplet-like to platelet-like.[9] It was speculated that the speed with which the freshly created surfaces are covered with the stabilizing agent has a major influence on the stability during this transition. The dynamics of the phospholipid molecules with and without co-stabilizer, in bi- and monolayers promises therefore to be a key component in the understanding of the stabilizing mechanisms.

The evolution of phospholipid dynamics over many length and time scales necessitates the use of different techniques to get a complete picture. More macroscopically, one uses from fluorescence recovery after photobleaching (FRAP) on a 10 s scale,[10,11] through pulsed field gradient nuclear magnetic resonance (PFG-NMR) on a 100 ms scale,[12] to fluorescence correlation spectroscopy (FCS) on a 10 ms scale.[13] Nanoscopically, the dynamics on a scale of fundamental molecule–molecule interactions is accessible with quasielastic neutron scattering (QENS), which was used in this study to see the motions of the phospholipid dimyristoylphosphatidylcholine (DMPC) on a 60 ps time scale.

The vast majority of QENS experiments have been performed on multibilayer stacks which were aligned with the help of a supporting solid substrate.[14–17] Although it has been argued that these systems can behave differently from single bilayers, for example in vesicles,[18] these differences can be expected to be small on small spatial scales. Also, the influence of the solid support was seen to act only on the leaflet in direct contact with the support.[19,20]

In order to facilitate comparisons with vesicles, experiments on non-supported multibilayers have also been performed, *e. g.* refs 21–23. In these, a novel view of the nanoscopic dynamics that had been proposed by molecular dynamics (MD) simulations[24] could be supported: the phospholipid molecules do not move independently from each other but form transient clusters which

[a]*Technische Universität München, Physik Department E13 and Forschungs-Neutronenquelle Heinz Maier-Leibnitz (FRM II), Lichtenbergstr. 1, 85748 Garching bei München, Germany. E-mail: sbusch@ph.tum.de; Fax: +49-89-289-14911; Tel: +49-89-289-14922*
[b]*Universitat Politècnica de Catalunya, Grup de Caracterizació de Materials, Departament de Física i Enginyeria Nuclear, ETSEIB, Diagonal 647, 08028 Barcelona, Catalonia, Spain*
[c]*Eidgenössische Technische Hochschule Zürich, Animal Imaging Center–PET, Center for Radiopharmaceutical Sciences of ETH, PSI and USZ, Wolfgang-Pauli-Str. 10, 8093 Zürich, Switzerland*
[d]*Friedrich-Alexander-Universität Erlangen-Nürnberg, Lehrstuhl für Kristallographie und Strukturphysik, Staudtstr. 3, 91058 Erlangen, Germany. E-mail: Tobias.Unruh@physik.uni-erlangen.de; Fax: +49-9131-85-25182; Tel: +49-9131-85-25189*

† Electronic supplementary information (ESI) available: details of thin layer chromatography as well as differential scanning calorimetry, the calculation of the area per molecule, and the fit functions. See DOI: 10.1039/c2sm07380c

This journal is © The Royal Society of Chemistry 2012

exhibit correlated, flow-like motions. Before, the accepted view of diffusion in phospholipid membranes had been that the molecules rattle in a cage of their neighbours from which they escape only rarely by a jump into a void that had been created in the cage by thermal fluctuations.[25] It became clear in the simulations that this picture is not correct on a nanoscopic level because the molecules do not escape from their cage but rather move together with the cage.

With the extremely high density in the head group region of the phospholipids in mind,[26] it is not surprising that these flow patterns resemble *dynamical heterogeneities* which are well-known from glass physics where they are seen as a universal feature of densely-packed systems.[27–31] Similar effects have even been observed in dense, actively swimming cells.[32–34] It should however be noted that in these more complicated systems, other effects might also play a role, for example an exchange of information between the cells.

Also, unsupported multibilayer stacks are not necessarily good model-systems for cell membranes or stabilizing layers which are a single bilayer and a monolayer, respectively. The behaviour of molecules in monolayers and single bilayers has already been shown to differ from each other,[35] making it impossible for multibilayer data to describe both simultaneously. The differences seem to depend heavily on the details of the system – while some studies saw an increase of dynamics by a factor of 2–3 compared to multibilayers,[36] others observed a decrease by the same factor.[37] This triggered recent endeavours to use QENS for the study of single bilayers on support,[38] single bilayers without support, *i.e.* vesicles,[39] and even monolayers.[40]

In this contribution, we present the evolution of the dynamics that were previously characterized by QENS in DMPC multibilayers[21–23] when changing two control variables: first, the multibilayers are compared with single bilayers in vesicles and monolayers in emulsions – with and without the co-stabilizer NaGC – being more similar to cells and drug delivery systems, respectively. Second, the multibilayers are studied at elevated temperatures (30–80 °C), providing further experimental ground for the treatment of phospholipid motions in the frame of glass-forming systems.

2 Materials and methods

2.1 Samples

The phospholipid dimyristoylphosphatidylcholine (DMPC) was obtained from Lipoid GmbH, Ludwigshafen, Germany; sodium glycocholate (NaGC or SGC) from Sigma Aldrich, Münster, Germany; perdeuterated *n*-hexadecane (dHD, $C_{16}D_{34}$, 98%) from Cambridge Isotope Laboratories, MA, USA; D_2O from Euriso-Top, Gif sur Yvette, France. All substances were used as received. The structural formulae of these molecules except D_2O are displayed in Fig. 1.

The multi-bilayer samples were prepared by hydrating the dry DMPC powder at 40 °C *via* the vapour phase with D_2O for two days until the white powder became homogeneous and clear, indicating that the sample was in the liquid crystalline phase. Further D_2O was added up to at least 50 weight%, *cf.* Table 1, to ensure full hydration of the phospholipid during the whole experiment.

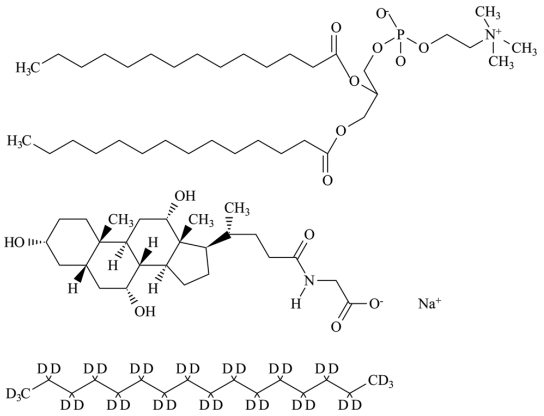

Fig. 1 Molecules used in this study. From top to bottom: dimyristoylphosphatidylcholine (DMPC), sodium glycocholate (NaGC), and perdeuterated hexadecane (dHD, $C_{16}D_{34}$). As the experiments were performed in D_2O, the exchangeable protons of OH and NH groups are replaced by deuterium as well.

Vesicles were produced by mixing the amounts of DMPC and D_2O given in Table 1, leaving it for at least one day at 40 °C. Two procedures were used to form vesicles: sonication and extrusion, see below. The size and polydispersity of the vesicles were checked with photon correlation spectroscopy (PCS).

Sonication was performed with a Bandelin Sonopuls UW 2070 ultrasound generator with a tip diameter of 3 mm (MS73), Bandelin electronic, Berlin, Germany. The device uses a frequency of 20 kHz with an output power of up to 70 W. It was operated with duty cycle 3/10 and 20% of the maximal output power for approx. 30 min.

Extrusion was performed inside a hot-air cabinet thermostatted at 40 °C through a 100 nm pore size membrane in an extrusion device manufactured by Avestin, Mannheim, Germany[41] 21 times.

Hexadecane nanoemulsions[42] were prepared by sonication (as described above) of thoroughly mixed DMPC, NaGC, dHD, and

Table 1 Samples used in this study. The short names used in this manuscript are shown together with the compositions and the particle sizes where applicable. The name is composed of m, v, or e, corresponding to multibilayer, vesicle, or emulsion, respectively, and D, N, E, S for DMPC, NaGC, extruded, and sonicated, respectively. The concentrations of the substances are given in mass%, the missing amount to make 100% is D_2O. The diameter Ø (*z*-average) and polydispersity index PDI are determined with photocorrelation spectroscopy

Name	[DMPC] (%)	[NaGC] (%)	[dHD] (%)	Ø (nm)	PDI
mD	50	—	—	—	—
mN	33	3.3	—	—	—
vE	5.0	—	—	143	0.07
vS	4.8	—	—	131	0.28
eD23N00	2.3	—	7.5	132	0.21
eD13N00	1.3	—	10.1	136	0.13
eD11N02	1.1	0.21	8.8	134	0.14
eD11N01	1.1	0.11	8.8	124	0.14
eD09N02	0.87	0.22	9.1	133	0.13

D_2O in the compositions given in Table 1. DMPC and NaGC act as stabilizers for the droplets of dHD in D_2O. These emulsions are not thermodynamically stable microemulsions but the coalescence of the droplets is only kinetically hindered. The size and polydispersity of the droplets were checked with PCS.

The PCS measurements were performed with a Brookhaven Instruments goniometer and light scattering system BI-200SM, using a Mini L-30 Diode Laser with 30 mW at 637 nm and a scattering angle of 90°. The samples were diluted to obtain count rates of approximately 100 kcps and the scattered intensity was correlated with a TurboCorr correlator. The size and polydispersity of the particles were determined with the BIC BI-9000 Particle Sizing Software.

Although the *z*-averages of the diameter of the samples were similar, the polydispersity differed widely, as can be seen in Table 1. As the big particles essentially determine the *z*-average,[43] this means that there are many small vesicles in those samples which have a large polydispersity. This is primarily the case for sonicated samples, in agreement with a previous publication.[44]

2.2 Neutron scattering measurements

Slow neutrons are scattered by the nuclei in the sample. During this scattering process, motions of the molecules translate into an energy transfer between the neutron and the sample. Aperiodic motions result in a broadening of the elastic line (*quasi*-elastic). The total measured energy distribution of the scattered neutrons consists of a part due to the spectrometer, the instrumental resolution which determines the observation time, and a part contributed by the sample: more motion in the sample results in a stronger broadening. This broadening can be extracted either by extracting the full width at half maximum (FWHM) or by fitting a model to the data.

It is useful to distinguish a coherent and an incoherent part in the scattered intensity. The intensity of the coherent part depends strongly on the momentum transfer $\hbar Q$ and gives information about the structure of the sample. Peaks at a certain Q can be roughly assigned to typical distances of $r = 2\pi/Q$ in the sample. Incoherent scattering has the same intensity at all values of Q – with a Q-dependent energy distribution – and is governed by the autocorrelation function of the nuclei.[45–47]

Due to their very large incoherent scattering cross section,[48] the hydrogen nuclei dominate the scattered signal by far. This gives the possibility to strongly diminish the contributions of specific substances by deuteration. In the measurements presented in this study, the samples are chosen such that the phospholipid molecules scatter mainly incoherently which makes the evaluation of their dynamics possible. Additionally, there is a small contribution of the coherent scattering signal which contains information about the structure of the phospholipid molecules. This part of the scattering signal is not clear enough to evaluate the structure in detail because of the choice of samples which were optimized to measure the dynamics rather than the structure of the phospholipid molecules.

All neutron measurements were performed at the neutron time-of-flight spectrometer TOFTOF at the Forschungs-Neutronenquelle Heinz Maier-Leibnitz (FRM II), Munich, Germany.[49,50] The incident wavelength was chosen as 6 Å, the chopper rotation speed 12000 rpm, and the frame overlap ratio was 4. The resulting instrumental resolution of about 60 μeV, determined by measuring a containerless vanadium standard, corresponds to an observation time of about 60 ps.[51]

The samples were filled into hollow cylindrical sample containers[52,53] with wall thicknesses of 0.2 mm if not noted otherwise. This yields transmissions in the order of 90%. Using a temperature-controlled sample environment, most measurements were performed at 20 °C, only the multibilayers were measured every 5 °C from 30 to 80 °C.

The measurement times varied from 4 h for measurements of multibilayers up to 18 h in the case of the emulsions, *i.e.* monolayers. The long measurement times diminish the relative statistical error of the data. However, the samples consist of as little as 1% of DMPC, *cf.* Table 1. This means that a big part of the measured signal must be subtracted (the contributions of D_2O and dHD) which necessitates that the resulting line shape of the vesicle and emulsion samples can not be determined with the same accuracy as the one of the multibilayer.

2.3 Data reduction and analysis

To obtain diffraction patterns, the double differential cross section was integrated over all energies. The scattering angle was converted to Q using the Bragg equation for elastically scattered neutrons. The spectrometer TOFTOF is not dedicated to structure determination by the measurement of the diffraction patterns which are only a natural by-product of the measurements. Keeping in mind that the instrumental broadening due to the divergence of the neutron beam is about 0.1 $Å^{-1}$, some information can be extracted especially from the comparison between diffraction patterns of different samples under the same experimental conditions. Dedicated diffraction measurements are however needed to obtain a clearer picture of the structure.

The data were also converted to scattering functions $S(Q, \omega)$ depending on the transfer of momentum $\hbar Q$ and energy $\Delta E = \hbar\omega$ between the neutron and the sample using the program FRIDA1.[54] The data were binned into Q steps of 0.1 $Å^{-1}$ from 0.3 to 1.8 $Å^{-1}$ and in ΔE steps of 0.01 meV from −1.00 to 1.00 meV.

The spectra of an empty can at 20 °C were subtracted from all measurements except the one of vanadium which was measured without a container. The measurements of D_2O were subtracted pro-rata from the ones of the multibilayers. For the samples with a small amount of DMPC, the amount of D_2O and, where applicable, dHD background contributions was determined by fitting a linear combination of the diffraction patterns to the diffraction pattern of fully hydrated DMPC multibilayers at the same temperature of which a D_2O measurement was pro-rata subtracted. The diffraction patterns of pure D_2O and dHD as well as the ones of the samples after background subtraction are shown in Fig. 2. Typical spectra after subtraction of the background contributions of D_2O and dHD are shown in Fig. 3.

For all measurements, the full width at half maximum (FWHM) was extracted. The small amount of phospholipid in the formulation of vesicles and especially of emulsions impedes a more detailed analysis of the line shape with a model for the molecular motions. The long-range motional component can therefore not be specifically extracted but the *mobility* can be evaluated using the additional broadening on top of the

 This journal is © The Royal Society of Chemistry 2012

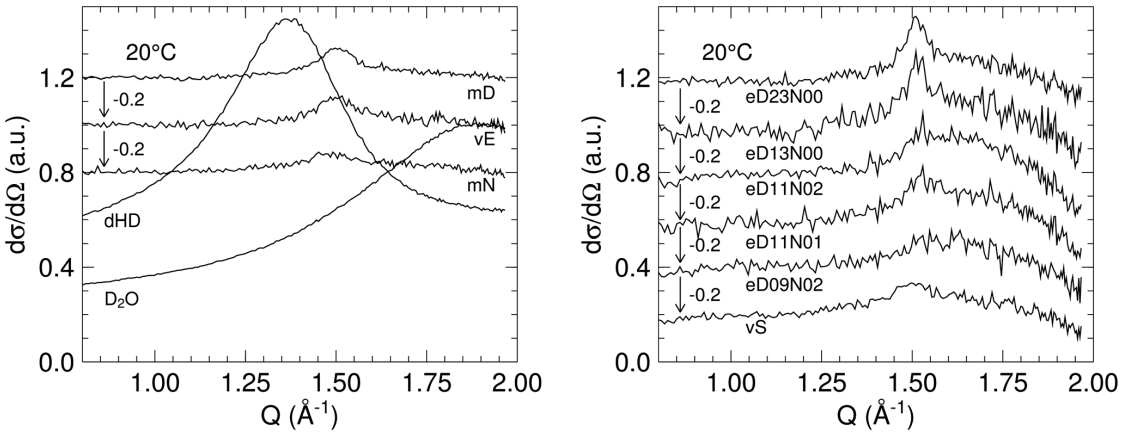

Fig. 2 Neutron diffraction patterns of the samples at a temperature of 20 °C. The samples shown on the left are bulk or extruded samples, the ones on the right are sonicated samples. The diffraction patterns were obtained as described in the text, it is indicated in the figures which patterns were subsequently shifted for better visibility. The nomenclature of the samples can be found in Table 1.

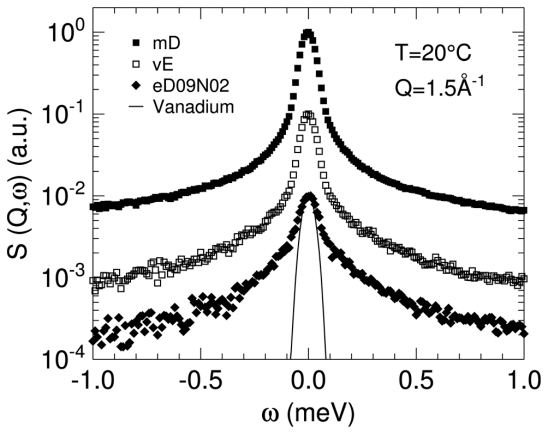

Fig. 3 Spectra of three samples after subtraction of the background contributions of D_2O and dHD together with the one of vanadium as a measure of the instrumental resolution. For better visibility, the spectra are shifted vertically so that the peak maxima are at 10^0 (multibilayer), 10^{-1} (single bilayer), and 10^{-2} (monolayer and vanadium), respectively. The nomenclature of the samples can be found in Table 1.

instrumental resolution (full width at half maximum) $\Delta(Q)$. This approach has already been employed to compare the influence of several additives on the mobility of DMPC.[22] It comprises not only the long-range motion but also local motions, for example of the hydrophobic tails. As these show a more diffusive behaviour, $\Delta(Q)$ is expected[22] to be roughly proportional to Q^2.

By dividing the $\Delta(Q)$ by the values of pure DMPC and averaging over all Q, a measure for the dynamics as compared to the one of pure DMPC was obtained which is called *relative mobility* in the following. It is interpreted as a function of an *area per molecule* (in arbitrary units) which is proportional† to the one calculated assuming a monodisperse sample with the z-average diameter Ø,

$$\text{area per molecule} \propto \frac{[\text{dHD}]}{[\text{DMPC}]\cdot\varnothing} \quad , \tag{1}$$

where the concentrations and diameter Ø are given in Table 1. With an increasing polydispersity of the sample, this quantity increasingly underestimates the true area per molecule as the big particles essentially determine the z-average[43] but the small particles provide additional surface for the phospholipid molecules.

In the case of the multibilayer samples, the high data quality allowed a more detailed data evaluation, using a model for the molecular motions. A previously introduced fit function[21] was used to extract the long-range motional component of the phospholipid molecules in multibilayers.† The theoretical fit function was numerically convolved with the instrumental resolution function as determined by the measurement of a vanadium standard.

In short, this model assumes that the spectra are caused by three independent motions: (i) the localized motions of the head group, (ii) the localized motions of the tails, and (iii) the long-range motion of the whole molecule. The localized motions were described with a so-called Brownian oscillator.[55–58] This is a very generic model for localized motions, the data do not allow a more elaborate evaluation which has been performed in other studies.[15,59]

For the long-range motion, two common models are compared: flow and diffusion.[21] Assuming flow-like motions with a Maxwell-Boltzmann velocity distribution, the fit function contains a Gaussian with a standard deviation $\sigma(Q) = v \cdot Q$ where v is the most probable flow velocity. Assuming diffusion, the fit function contains a Lorentzian with a half width at half maximum $\Gamma(Q) = D \cdot Q^2$ where D is the diffusion coefficient.

3 Results and discussion

3.1 Molecular structure

This study was primarily aimed at the *dynamics* of the phospholipid molecules in different environments and not at their

structure. Therefore, samples were chosen which scatter much more incoherently than coherently, resulting in a poor signal-to-background ratio of the coherent features. In the following, a very short summary of the coherent contributions to the data is given with the remark that dedicated measurements are needed to draw clear conclusions about the structure and position of the molecules.[60]

The diffraction patterns of the extruded vesicles are very similar to the ones of the pure DMPC multibilayer as can be seen in Fig. 2. The acyl chain correlation peak at 1.5 $Å^{-1}$ is caused by the nearest neighbour distance of the acyl chains.[61] It is a little bit less pronounced in the vesicles, indicating a less well-defined distance which could be due to the curvature of the membrane in the vesicle.

Adding NaGC to the multibilayer seems to decrease the intensity of this peak further, indicating more disorder in the tail region. A shift of the peak position in Q can not be determined reliably. However, the acyl chain correlation peak is not very sensitive to a change of the area per molecule because the acyl chains are not distributed on a homogeneous hexagonal lattice.[62] Therefore a possible extending effect of NaGC on the tail region of the DMPC molecules cannot be determined from this peak.

All samples that were produced by sonication exhibit a drop of intensity at high values of Q. By varying the amounts of subtracted D_2O and dHD, it could be excluded that this is an effect due to wrong subtraction. This is corroborated by the fact that the highest slope of the drop is at high values of Q where the diffraction patterns of both D_2O and dHD are flat, as can readily be seen in Fig. 2.

The acyl chain correlation peak of the sonicated vesicles is at the same position as the one of the extruded vesicles. The chains therefore have similar distances in the two samples. The peak is very clear and pronounced in the two emulsion samples which were stabilized with only DMPC, *i. e.* a monolayer of DMPC on dHD – even more than in the multibilayer sample. This effect has been observed before with X-ray scattering and was attributed to the removal of the chain tilt by interdigitation of the alkanes between the acyl chains.[63]

3.2 Evolution of the dynamics of DMPC without NaGC from multibi- to monolayer

The extruded vesicles show essentially the same mobility as the multibilayers, as can be seen in Fig. 4. Also, the de Gennes narrowing[64] at 1.5 $Å^{-1}$ is clearly visible for both samples, in agreement with the structure factor maximum at this position in the diffraction patterns (*cf.* Fig. 2). The sonicated vesicles exhibit systematically faster dynamics but do also show a clearly visible de Gennes narrowing.

The Q-average of the ratio of the $\Delta(Q)$ of the vesicles over the ones of the pure multibilayer, the relative mobility, summarizes the speed-up of the molecules in the vesicles as it can be extracted from the data and is shown in Fig. 5. The increase of the mobility in the sonicated vesicles is about twice as high as the one in the extruded vesicles. Three possible reasons for this speed-up were considered: a degradation of the molecules during sonication, an increase of hydration, or the strong curvature of these vesicles.

Degradation is not expected at the relatively low sound frequency of 20 kHz. However, as the hydrolysis would result in a free fatty acid and lyso-phosphatidylcholine, thin layer chromatography† was used to ascertain that less than 5% of hydrolization products were contained in the samples after sonication. Additionally, it has been shown before that on the 60 ps time scale even large amounts of additives evoke only very minor changes in mobility.[22] In the case of myristic acid, the most probable product of the lysis, the dynamics would even be expected to decrease.[22] It can be concluded that degradation is not expected, not observed, and would not explain this effect.

The mobility is known to increase with increasing hydration.[14,17] The observed increase of the mobility could therefore also be explained with an increase in hydration – a process that has been observed in many studies that compared vesicles with stacks of multibilayers. It was however found that this increase in hydration was an artifact, caused by gradients of the relative humidity in the sample cells.[65,66] The multibilayer samples presented in the present study were prepared with excess D_2O in order to exclude the possibility that such an effect played a role. As a consequence, it is assumed that the hydration is the same for all the samples. If this is not the case, the increase in hydration from multibilayers to vesicles would be a likely cause for the increase in mobility from multibilayers to vesicles.

The sonicated vesicles are much smaller than the extruded ones. Hints on faster diffusion in smaller vesicles have previously been found by NMR[67] although this was shown to be only a minor effect.[68] Also, the main phase transition was affected, smeared out and shifted to lower temperatures with smaller cooperative units.[69] While the mobility on the 60 ps time scale is hardly affected by the phase transition,[21,23] the curvature could induce geometrical packing frustration. Although the data at hand do not allow a quantification, packing frustration increases the area per phospholipid molecule which in turn would be expected to benefit the mobility.

The dynamics in the monolayers of the emulsion samples are even faster, *cf.* Fig. 4. The de Gennes narrowing is very pronounced in the two samples of pure DMPC as stabilizing layer, in agreement with the strong structure factor seen in the diffraction patterns in Fig. 2.

The mobility of phospholipid molecules in monolayers was found to be positively correlated with the area per molecule in molecular dynamics (MD) simulations[70] and fluorescence recovery after photobleaching (FRAP) studies.[71] Because of the polydispersity, it is not possible to calculate the area per molecule precisely. Regarding the sample as monodisperse with the z-average diameter, the amount of phospholipid in the sample suffices for more than a monolayer around the emulsion droplets. The rest of the phospholipid would then be present as vesicles or multibilayers in the stabilizer layer. However, the small droplets in the sample, indicated by the relatively high polydispersity index, adsorb much the superfluous phospholipid.

It is known that the mobility of phospholipid molecules on an oil–water interface follows the Stokes–Einstein prediction up to a viscosity of the oil phase of 10^5 mPa s.[72] In a subsequent experiment, this was confirmed for oils with viscosities below approximately 10^3 mPa s. At higher oil viscosities, the diffusion of the phospholipid molecules did not decrease as much as expected.[71] This was tentatively explained by a hopping mechanism where the molecules detach from the interface from time to time and diffuse in the water. In the present case with viscosities

 This journal is © The Royal Society of Chemistry 2012

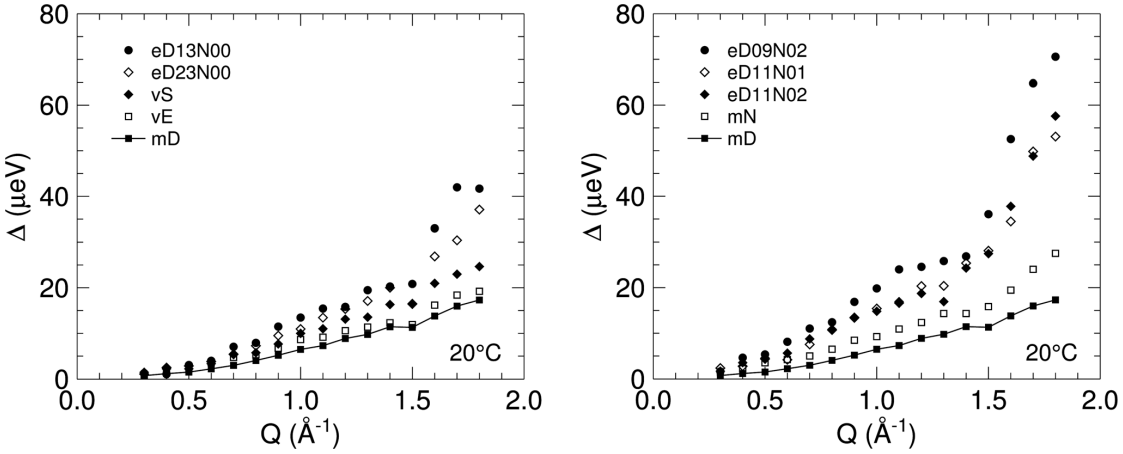

Fig. 4 The measured experimental broadenings (full width at half maximum) as a function of the momentum transfer Q measured at 20 °C. Shown in both graphs is the reference of a pure DMPC multibilayer where the points have been connected with lines to enhance the visibility. Samples without NaGC are shown on the left and samples with NaGC are shown on the right. The nomenclature of the samples can be found in Table 1.

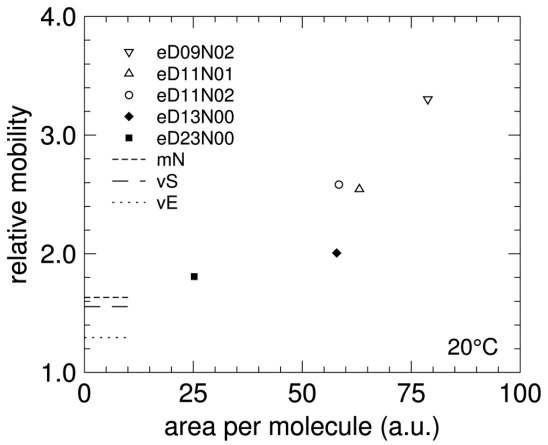

Fig. 5 The mobility of the samples relative to the pure DMPC multibilayer at 20 °C as a function of the area per molecule, calculated according to eqn (1). The samples represented with dashes are bilayers where the area per molecule is at its equilibrium value. The ones shown as points are monolayers where the area per molecule can also be influenced by the available surface of the droplets. Filled points correspond to samples without NaGC, open points to the ones with NaGC. The nomenclature of the samples can be found in Table 1.

of water between about 0.5 and 1 mPa s,[73] and hexadecane between about 2 and 4 mPa s,[74] a hopping diffusion mechanism has no significant influence.

The phospholipid molecules are therefore located at the interface between water and oil and feel the drag of both. It is generally accepted that hydrophobic molecules like alkanes mix with the hydrocarbon chains of the phospholipids – the measurements of the solubility vary[63,75–80] – and the water molecules penetrate between the head groups.[81] The mobility of the phospholipid molecules is therefore influenced by the surrounding (oil and water) as well as the neighbouring phospholipid molecules.[82]

Comparing the two emulsion samples containing 1.3% and 2.3% of DMPC, respectively, shows very little difference in the molecular mobility. The 2.3% emulsion sample contained excess phospholipid. This resulted in smaller particles, which can be seen from the high polydispersity in Table 1. The surface occupancy of the emulsion droplets in the two samples is therefore very similar. This is not reflected in the *area per molecule* used in Fig. 5 which assumes a monodisperse sample and therefore underestimates the area per molecule in the case of the polydisperse 2.3% sample significantly.

The main phase transition of phospholipid monolayers was observed to shift to lower temperatures when increasing the area per molecule[83] but in the present case of DMPC at 20 °C, it was shown that there is no phase transition when increasing the area per molecule.[84] In combination with the fact that the 60 ps dynamics are not heavily influenced by phase transitions,[21,23] it can be concluded that the big gain in relative mobility is not triggered by an unintentional phase transition but is a generic difference between bi- and monolayer.

In summary, the mobility of the phospholipid molecules is higher in single bilayers than in multibilayers and increases with increasing curvature. The mobility in monolayers is even larger, reaching about twice the mobility of the multibilayers.

3.3 Evolution of the dynamics of DMPC mixed with NaGC from multibi- to monolayer

The de Gennes narrowing in the multibilayer sample containing NaGC is at smaller Q than the one of pure DMPC, namely at 1.4 Å^{-1} (*cf.* Fig. 4). The dynamics are enhanced compared to the one of the pure multibilayer sample, as can be seen in Figs 4 and 5. This effect was observed in a previous study,[22] where changes in the mobility were explained by changes in the packing density of the phospholipid head groups.

The emulsions containing NaGC exhibit de Gennes narrowing at an even lower Q value of about 1.3 $Å^{-1}$. The proximity of this value to the position of the structure factor maximum of dHD could have been a sign of an incorrect subtraction of the dHD signal if the diffraction patterns in Fig. 2 would not clearly show that there is no coherent scattering peak at this position. Interdigitation of the hexadecane molecules between the alkyl chains of the phospholipids would probably cause an effect at this Q but this effect should then also be visible in the samples without NaGC.

Adding NaGC to the emulsions results in a jump of the mobility at constant area per molecule, as can be seen in Fig. 5 (eD13N00 *vs.* eD11N02). The size of this jump is about the same as the one that the NaGC induced in multibilayers and is discussed in detail elsewhere.[22] It can be excluded that this is a trivial result of seeing simply an additive mixture of DMPC dynamics and (faster) NaGC dynamics by taking a look at the other NaGC/DMPC compositions: an increase of the NaGC concentration at constant DMPC concentration and constant area per molecule (eD11N01 *vs.* eD11N02) does not translate directly in an increase of the mobility. In contrast, the mobility is increased when the area per molecule is increased at a constant NaGC concentration (eD09N02 *vs.* eD11N02).

At low concentrations, NaGC increases the mobility but the effect is not proportional to the amount of NaGC at higher concentrations. A similar effect has been observed before[85] where co-surfactants like NaGC were incorporated into the phospholipid layer which became saturated and further co-surfactant was not taken up. This incorporation increased the lateral pressure in the monolayer.

It is known that NaGC enhances the ability of the phospholipid to stabilize emulsions. This effect is particularly visible in samples where the dispersed oil phase crystallizes when the temperature is decreased. These samples are only stable against coagulation if NaGC is added to the DMPC. During the crystallization, the shape of the particles changes suddenly from a droplet to platelets. It seems clear that this should be connected to the speed of the stabilizer to cover the newly created surfaces.[9] In the present contribution, it could be shown that the addition of NaGC increases the mobility on a 60 ps time scale by a factor of about 1.5 compared to monolayers without NaGC. This increase of mobility is beneficial but is hardly enough for the observed drastic change of stabilizing potential. Other mechanisms can therefore be expected to contribute as well: collective motions and the adsorption from the aqueous phase, discussed below.

The presented measurements probed only the autocorrelation of the molecules under steady state conditions. Therefore, collective effects are not visible. One formation of those could be caused by the impurity sites induced by the sodium glycocholate molecules in the phospholipid lattice, inducing a calving process. Big chunks of stabilizer would separate from the covered area, swimming out onto the naked particle and cover it. Another possibility is the fast expansion of a homogeneous stabilizer layer that is driven by the big lateral pressure induced by the NaGC.[85] The corresponding collective diffusion coefficient is independent from the self diffusion coefficient measured here.

Another contribution will arise from the NaGC that is not incorporated in the monolayer and may even have solubilized a part of the phospholipid molecules into the aqueous phase.[8] This reservoir of stabilizer molecules can attach to the newly created surface directly from the solution, making the distance to be covered by diffusion much shorter.[9]

Summing up, the addition of NaGC initially enhances the mobility but this effect saturates. Having added NaGC, it is possible to reduce the amount of DMPC which in turn increases the mobility. The increase in mobility on the 60 ps time scale seems to play a secondary role in the enhancement of the stabilizing properties.

3.4 The dynamics of DMPC in multibilayers at high temperatures

Depending on the method, different measures of the width can be extracted from the same data. As done with the previous samples, the model-free determination of the full width at half maximum is plotted in Fig. 6. Because of the high quality of the spectra due to the large amount of sample, a model-based evaluation can additionally be performed which allows the specific extraction of the long-range motional component. Assuming flow-like motions, $\sigma(Q)$ is obtained; assuming diffusion $\Gamma(Q)$. Both are shown in Fig. 7.

The mobility $\Delta(Q)$, obtained from the model-free approach, is shown in Fig. 6. As expected, it increases with temperature – it is not expected to follow any particular Q dependence. A quadratic function in Q was used in Fig. 6 without a theoretical justification. The fact that it fits the data better at low temperatures than at high temperatures is therefore not meaningful. The strong rise with Q is given by the localized motions which contribute especially at high Q.

Turning to the model-bound evaluations of the long-range motional component in Fig. 7, it is clear that the extracted $\sigma(Q)$ follow the required linear dependence on Q at low temperatures while the $\Gamma(Q)$ show a good agreement with the required quadratic Q dependence at high temperatures. This shows that

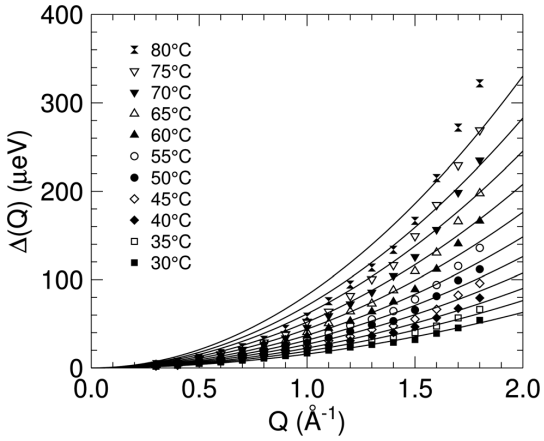

Fig. 6 The full width at half maximum of the sample spectra minus the full width at half maximum of the vanadium spectra which indicate the instrumental resolution shown as a function of Q for different temperatures. The lines are fits of quadratic functions in Q.

This journal is © The Royal Society of Chemistry 2012

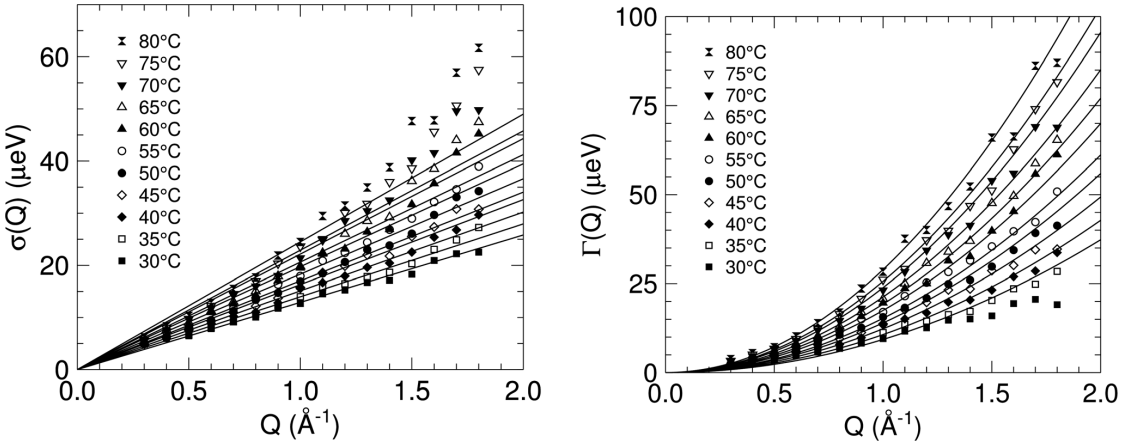

Fig. 7 Left: standard deviation σ of the narrow Gaussian component in a multicomponent fit shown as a function of Q for different temperatures. The lines are fits of linear functions in Q. Right: half width at half maximum Γ of the narrow Lorentzian component in a multicomponent fit shown as a function of Q for different temperatures. The lines are fits of quadratic functions in Q.

the observed dynamics in the 60 ps regime can be described better by the model of flow-like, cooperative rearrangements of dynamically assembled patches of molecules at low temperatures while the model of diffusive motions is the better one at high temperatures.

Concentrating on $\sigma(Q)$, the increasing deviation from a proportional dependence on Q to a more quadratic behaviour with increasing temperature was also observed in other systems. Some glass-forming liquids show a transition from flow-like displacements at temperatures shortly above the glass transition temperature to a normal diffusive behaviour at high temperatures.[86] The fact that the deviation from a linear dependence on Q is first visible at high Q has also been observed before and was discussed in connection with dynamical heterogeneities.[87]

This transition from flow-like to diffusive is also observed when changing the observation time in studies of colloidal motions:[88,89]At short times, flow-like motions are seen which constitute the steps of a random walk – the diffusion at long times. In the present case, the observation time is not changed but rather the rising temperature shifts the transition time from flow-like to diffusive towards shorter times and through the constant window of the observation time.

In order to qualify the temperature evolution of the total mobility, $\Delta(Q)$ was fitted with a quadratic function in Q as shown in Fig. 6. The temperature evolution of the long-range motion was followed by fitting $\sigma(Q)$ with a linear function in Q, *cf.* Fig. 7. We note again that these functions show systematic deviations from the data and can therefore not be seen as a consistent model. However, although the limits of validity of the models are passed, it is still possible to extract the temperature dependence of the long-range motion and total mobility qualitatively.

This approach gives access to v with the dimension of a velocity for the long-range motion and to D with the dimension of a diffusion coefficient for the total mobility. These quantities are shown in Fig. 8 in an Arrhenius plot as a function of inverse temperature. Their behaviours follow an Arrhenius temperature dependence, another indication that the dynamics at temperatures far above the main melting transition (which is at 24.3 °C†) do not show any peculiarities, as expected.

An Arrhenius behaviour of the motions of phospholipid molecules is found not only on the here-presented time scale of about 60 ps but also at about 100 ns,[90] 100 ms,[12] and 100 s.[11] It was observed that colloids with a hard-disk-like interaction potential exhibit a stronger temperature dependence, termed *super-Arrhenius*, which becomes Arrhenius-like with softer interaction potentials.[91] As the head group rotation exhibits an Arrhenius temperature dependence in the fully hydrated state

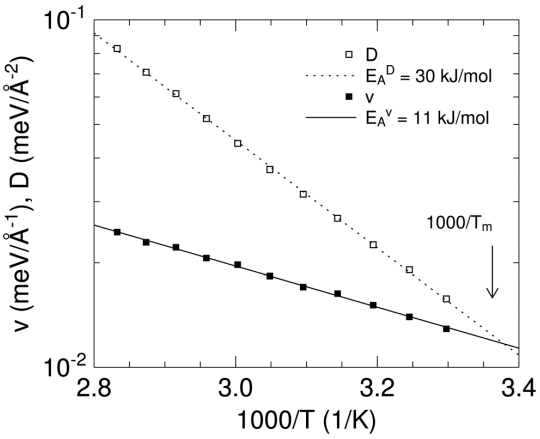

Fig. 8 An Arrhenius plot of the mobility in DMPC multibilayers for temperatures from 30 to 80 °C in steps of 5 °C. Shown are v, the best-fit values to $\sigma(Q) = v \cdot Q$, and D, the best-fit values to $\Delta(Q) = D \cdot Q^2$, together with fits of Arrhenius equations to them. The arrow denotes the temperature of the main phase transition of DMPC, determined by DSC as 24.3 °C.†

which becomes super-Arrhenius when decreasing the hydration,[92] one can speculate that the water molecules which penetrate between the head groups[81] act as a plasticiser.

Collective motions of several molecules are often connected to a super-Arrhenius temperature which was not observed here. However, this does not contradict the assumption of dynamic heterogeneities in the membrane at temperatures shortly above the main phase transition on a pico- to nanosecond time scale.[22] These have also been observed in glass formers obeying an Arrhenius behaviour[93] and even above the melting point of colloidal liquids that exhibit a first order freezing phase transition, *i. e.* that are not in the glassy regime.[30]

The fits of Arrhenius equations with a logarithmic weight yield apparent activation energies for the long-range motion $E_A^{\prime} = 11$ kJ mol^{-1} and for the mobility $E_A^{D} = 30$ kJ mol^{-1}, respectively. As discussed previously,[70] these activation energies have to be interpreted with care – especially when comparing different time scales on which they are known to depend even for simpler molecules.[94] The thermal expansion of the membrane can be expected to be the main driving force behind the speed-up of the motions, linking the dynamics to the area per molecule just as in the case of the monolayers in emulsions discussed earlier in this contribution.

The activation energies which are extracted in procedures comparable to our method[12,90] yielded about 30 kJ mol^{-1} for the long-range motion – about three times the value of 11 kJ mol^{-1} extracted in the present study. This is in agreement with our previous observation that the flow velocity of the phospholipid molecules decreases with increasing observation time[21] which means that the molecules did not experience all barriers in the picosecond time range. The agreement of the here determined apparent activation energy of the mobility with the activation energy of the long-time diffusion observed by other techniques seems to be purely coincidental.

The diffusion of probe molecules in polystyrene[95] has shown that the long-range translational and localized rotational relaxations show different temperature dependences and – exactly as in our case – the long-range component has a significantly weaker temperature dependence.

To summarize, flow-like motions are supported by the data in the observed 60 ps time scale close to the main phase transition. As the temperature is increased, the correlations between the molecules decay faster and normal diffusive behaviour is observed.

4 Conclusions

The dynamics of the phospholipid DMPC were studied with quasielastic neutron scattering on a timescale of 60 ps in multibi-, single bi- and monolayers at full hydration. Samples with low amounts of DMPC were evaluated in a model-free approach that gives access to the overall mobility of the molecules. This procedure was complemented with a model-bound data analysis for the samples with a large amount of DMPC and correspondingly good statistics.

The mobility of pure DMPC was found to increase in the following order: multibilayer (reference) < single bilayer (factor of 1.3) < monolayer (factor of 2). Within the single bilayers, the mobility increased with decreasing diameter of the vesicles (up to a factor of 1.5); in the case of the monolayers, it increased with increasing area per molecule.

The addition of sodium glycocholate (NaGC) was found to increase the mobility as well. Adding 10 weight% of NaGC (in relation to the amount of DMPC) increased the mobility similarly in the multibilayers and in the monolayers (a factor of 1.5 compared to the same systems without the addition of NaGC). Further addition of NaGC to the monolayers did not show an effect. However, having added NaGC, it was possible to further increase the area per DMPC molecule, reaching a highly increased mobility compared to the multibilayers (more than a factor of 3). It can be concluded that the packing density of the phospholipid molecules is correlated with their mobility.

The data of the unsupported multibilayers in the temperature range between 30 and 80 °C was additionally evaluated with a model-bound data evaluation. While a model of flow-like motions in the membrane fits well at low temperatures, a model of diffusive motions fits better at high temperatures. As the observation time is fixed at 60 ps, this corresponds to a decrease of the correlation times of the flow-like motions through this range when the temperature is increased.

Acknowledgements

We would like to thank Prof. W. Petry for his continuous support, T. Gutberlet for useful discussions, and the reviewers for their helpful suggestions. This work was partly supported by the Spanish Ministry of Science and Technology (FIS2008-00837) and by the Catalonia government (2009SGR-1251).

References

1 D. Axelrod, *J. Membr. Biol.*, 1983, **75**, 1.
2 G. Pabst, N. Kučerka, M.-P. Nieh, M. C. Rheinstädter and J. Katsaras, *Chem. Phys. Lipids*, 2010, **163**, 460–479.
3 S. Martins, B. Sarmento, D. C. Ferreira and E. B. Souto, *Int. J. Nanomed.*, 2007, **2**, 595–607.
4 L. Sagalowicz and M. E. Leser, *Curr. Opin. Colloid Interface Sci.*, 2010, **15**, 61.
5 D. J. McClements and Y. Li, *Adv. Colloid Interface Sci.*, 2010, **159**, 213–228.
6 R. Shukat and P. Relkin, *Colloids Surf., B*, 2011, **86**, 119–124.
7 M. Wickham, *Biochim. Biophys. Acta, Mol. Cell Biol. Lipids*, 2002, **1580**, 110.
8 P. J. Wilde and B. S. Chu, *Adv. Colloid Interface Sci.*, 2011, **165**, 14–22.
9 K. Westesen and B. Siekmann, *Int. J. Pharm.*, 1997, **151**, 35.
10 J. L. Rubenstein, B. A. Smith and H. M. McConnell, *Proc. Natl. Acad. Sci. U. S. A.*, 1979, **76**, 15–8.
11 P. F. F. Almeida, W. L. C. Vaz and T. E. Thompson, *Biochemistry*, 1992, **31**, 6739.
12 A. Filippov, G. Orädd and G. Lindblom, *Biophys. J.*, 2003, **84**, 3079.
13 J. Korlach, P. Schwille, W. W. Webb and G. W. Feigenson, *Proc. Natl. Acad. Sci. U. S. A.*, 1999, **96**, 8461–6.
14 S. König, W. Pfeiffer, T. M. Bayerl, D. Richter and E. Sackmann, *J. Phys. II*, 1992, **2**, 1589.
15 S. König, T. M. Bayerl, G. Coddens, D. Richter and E. Sackmann, *Biophys. J.*, 1995, **68**, 1871.
16 S. König and E. Sackmann, *Curr. Opin. Colloid Interface Sci.*, 1996, **1**, 78–82.
17 M. Trapp, T. Gutberlet, F. Jurányi, T. Unruh, B. Demé, M. Tehei and J. Peters, *J. Chem. Phys.*, 2010, **133**, 164505.
18 D. Berti, G. Caminati and P. Baglioni, *Phys. Chem. Chem. Phys.*, 2011, **13**, 8769–82.
19 R. Merkel, E. Sackmann and E. Evans, *J. Phys.*, 1989, **50**, 1535–1555.
20 C. Xing and R. Faller, *J. Phys. Chem. B*, 2008, **112**, 7086–94.

 This journal is © The Royal Society of Chemistry 2012

21 S. Busch, C. Smuda, L. C. Pardo and T. Unruh, *J. Am. Chem. Soc.*, 2010, **132**, 3232.
22 S. Busch and T. Unruh, *Biochim. Biophys. Acta, Biomembr.*, 2011, **1808**, 199–208.
23 S. Busch and T. Unruh, *J. Phys.: Condens. Matter*, 2011, **23**, 254205.
24 E. Falck, T. Róg, M. Karttunen and I. Vattulainen, *J. Am. Chem. Soc.*, 2008, **130**, 44–5.
25 W. L. C. Vaz and P. F. F. Almeida, *Biophys. J.*, 1991, **60**, 1553–1554.
26 J. M. Vanegas, M. L. Longo and R. Faller, *J. Am. Chem. Soc.*, 2011, **133**, 3720–3723.
27 M. Hurley and P. Harrowell, *Phys. Rev. E: Stat. Phys., Plasmas, Fluids, Relat. Interdiscip. Top.*, 1995, **52**, 1694.
28 W. Kob, C. Donati, S. Plimpton, P. Poole and S. C. Glotzer, *Phys. Rev. Lett.*, 1997, **79**, 2827.
29 W. K. Kegel and A. van Blaaderen, *Science*, 2000, **287**, 290.
30 B. Cui, B. Lin and S. A. Rice, *J. Chem. Phys.*, 2001, **114**, 9142.
31 T. Kawasaki and H. Tanaka, *J. Phys.: Condens. Matter*, 2011, **23**, 194121.
32 H. P. Zhang, A. Be'er, E.-L. Florin and H. L. Swinney, *Proc. Natl. Acad. Sci. U. S. A.*, 2010, **107**, 13626–13630.
33 J. P. Garrahan, *Proc. Natl. Acad. Sci. U. S. A.*, 2011, **108**, 4701–4702.
34 T. E. Angelini, E. Hannezo, X. Trepat, M. Marquez, J. J. Fredberg and D. A. Weitz, *Proc. Natl. Acad. Sci. U. S. A.*, 2011, **108**, 4714–4719.
35 C. B. Babayco, S. Turgut, A. M. Smith, B. Sanii, D. Land and A. N. Parikh, *Soft Matter*, 2010, **6**, 5877–5881.
36 T. Adalsteinsson and H. Yu, *Langmuir*, 2000, **16**, 9410.
37 G. Henneré, P. Prognon, F. Brion and I. Nicolis, *Chem. Phys. Lipids*, 2009, **157**, 86–93.
38 C. L. Armstrong, M. D. Kaye, M. Zamponi, E. Mamontov, M. Tyagi, T. Jenkins and M. C. Rheinstädter, *Soft Matter*, 2010, **6**, 5864–5867.
39 T. Gutberlet, D. Posselt and T. Unruh, *Influence of short chain alcohols on local dynamics of DMPC*, Forschungsneutronenquelle Heinz Maier-Leibnitz (FRM II), Technische Universität München, Germany Experimental Report 935, 2008.
40 T. Unruh, C. Smuda, G. Gemmecker and H. Bunjes, *Quasi-Elastic Neutron Scattering Conference 2006 (QENS2006)*, Warrendale, PA, 2007, pp. 137–145.
41 R. C. MacDonald, R. I. MacDonald, B. P. M. Menco, K. Takeshita, N. K. Subbarao and L.-R. Hu, *Biochim. Biophys. Acta, Biomembr.*, 1991, **1061**, 297.
42 T. G. Mason, J. N. Wilking, K. Meleson, C. B. Chang and S. M. Graves, *J. Phys.: Condens. Matter*, 2006, **18**, R635–R666.
43 B. J. Berne and R. Pecora, *Dynamic Light Scattering: With Applications to Chemistry, Biology, and Physics*, Dover Publications, 2000.
44 G. Maulucci, M. De Spirito, G. Arcovito, F. Boffi, A. C. Castellano and G. Briganti, *Biophys. J.*, 2005, **88**, 3545–50.
45 M. Bée, *Quasielastic Neutron Scattering*, Taylor & Francis, 1988.
46 G. L. Squires, *Introduction to the Theory of Thermal Neutron Scattering*, Dover Publications, 1996.
47 A. Furrer, J. Mesot and T. Strässle, *Neutron Scattering in Condensed Matter Physics (Neutron Techniques and Applications) (Series on Neutron Techniques and Applications)*, World Scientific Publishing Company, 1st edn, 2009.
48 V. F. Sears, *Neutron News*, 1992, **3**, 26.
49 T. Unruh, J. Neuhaus and W. Petry, *Nucl. Instrum. Methods Phys. Res., Sect. A*, 2007, **580**, 1414–1422.
50 T. Unruh, J. Neuhaus and W. Petry, *Nucl. Instrum. Methods Phys. Res., Sect. A*, 2008, **585**, 201.
51 T. Unruh, C. Smuda, S. Busch, J. Neuhaus and W. Petry, *J. Chem. Phys.*, 2008, **129**, 121106.
52 J. Wuttke, *Phys. B*, 1999, **266**, 112.
53 J. Wuttke, *Phys. B*, 2000, **292**, 194.
54 J. Wuttke, *Frida1: Fast Reliable Interactive Data Analysis*, 1990, http://sourceforge.net/projects/frida/, Software.
55 F. Parak, E. W. Knapp and D. Kucheida, *J. Mol. Biol.*, 1982, **161**, 177.
56 E. W. Knapp, S. F. Fischer and F. Parak, *J. Phys. Chem.*, 1982, **86**, 5042.
57 E. W. Knapp, S. F. Fischer and F. Parak, *J. Chem. Phys.*, 1983, **78**, 4701.
58 K. Achterhold, A. Ostermann, M. Moulin, M. Haertlein, T. Unruh and F. Parak, *Phys. Rev. E: Stat., Nonlinear, Soft Matter Phys.*, 2011, **84**, 041930.
59 M. Doxastakis, V. García Sakai, S. Ohtake, J. K. Maranas and J. J. de Pablo, *Biophys. J.*, 2007, **92**, 147–61.
60 T. Unruh, *J. Appl. Crystallogr.*, 2007, **40**, 1008.
61 C. Münster, J. Lu, S. Schinzel, B. Bechinger and T. Salditt, *Eur. Biophys. J.*, 2000, **28**, 683.
62 J. S. Hub, T. Salditt, M. C. Rheinstädter and B. L. de Groot, *Biophys. J.*, 2007, **93**, 3156–68.
63 T. McIntosh, S. Simon and R. MacDonald, *Biochim. Biophys. Acta, Biomembr.*, 1980, **597**, 445.
64 P. de Gennes, *Physica*, 1959, **25**, 825.
65 J. F. Nagle and S. Tristram-Nagle, *Biochim. Biophys. Acta, Rev. Biomembr.*, 2000, **1469**, 159.
66 J. Katsaras, N. Kučerka and M.-P. Nieh, *Biointerphases*, 2008, **3**, FB55.
67 D. Marsh, A. Watts and P. Knowles, *Biochim. Biophys. Acta, Biomembr.*, 1977, **465**, 500.
68 L. Lepore, J. Ellena and D. Cafiso, *Biophys. J.*, 1992, **61**, 767.
69 K. Michiko, M. Takahiro and T. Yasuhiro, *Biochim. Biophys. Acta, Lipids Lipid Metab.*, 1993, **1169**, 90.
70 M. Javanainen, L. Monticelli, J. B. de la Serna and I. Vattulainen, *Langmuir*, 2010, **26**, 15436–44.
71 R. B. Walder, A. Honciuc and D. K. Schwartz, *J. Phys. Chem. B*, 2010, **114**, 11484–11488.
72 M. Negishi, H. Seto, M. Hase and K. Yoshikawa, *Langmuir*, 2008, **24**, 8431–4.
73 G. Beggerow, in *Organic compounds – water*, ed. K. Schäfer, 1980, vol. 4, p. 239.
74 C. Wohlfarth and B. Wohlfahrt, in *C16*, ed. M. D. Lechner, 2002, vol. 18B, p. 724.
75 G. Hunt and L. Tipping, *Biochim. Biophys. Acta, Biomembr.*, 1978, **507**, 242.
76 E. Lea, *Int. J. Biol. Macromol.*, 1979, **1**, 185.
77 J. M. Pope and D. W. Dubro, *Biochim. Biophys. Acta, Biomembr.*, 1986, **858**, 243.
78 B. G. Dzikovskii and V. A. Livshits, *Russ. Chem. Bull.*, 1998, **47**, 402.
79 K. Tajima, Y. Imai, A. Nakamura and M. Koshinuma, *Colloids Surf., A*, 1999, **155**, 311.
80 A. G. Richter, S. A. Dergunov, B. Ganus, Z. Thomas, S. V. Pingali, V. Urban, Y. Liu, L. Porcar and E. Pinkhassik, *Langmuir*, 2011, **27**, 3792–3797.
81 G. Ma and H. C. Allen, *Langmuir*, 2006, **22**, 5341–9.
82 W. L. C. Vaz, R. M. Clegg and D. Hallmann, *Biochemistry*, 1985, **24**, 781.
83 D. Steppich, J. Griesbauer, T. Frommelt, W. Appelt, A. Wixforth and M. F. Schneider, *Thermo-mechanic-electrical coupling in phospholipid monolayers near the critical point*, 2010, http://arxiv.org/abs/1005.4860.
84 J. Mingins, J. A. G. Taylor, B. A. Pethica, C. M. Jackson and B. Y. T. Yue, *J. Chem. Soc., Faraday Trans. 1*, 1982, **78**, 323.
85 B.-S. Chu, A. P. Gunning, G. T. Rich, M. J. Ridout, R. M. Faulks, M. S. J. Wickham, V. J. Morris and P. J. Wilde, *Langmuir*, 2010, **26**, 9782–93.
86 S. Schramm, T. Blochowicz, E. Gouirand, R. Wipf, B. Stühn and Y. Chushkin, *J. Chem. Phys.*, 2010, **132**, 224505.
87 H. Guo, G. Bourret, M. Corbierre, S. Rucareanu, R. Lennox, K. Laaziri, L. Piche, M. Sutton, J. Harden and R. L. Leheny, *Phys. Rev. Lett.*, 2009, **102**, 075702.
88 R. Huang, I. Chavez, K. M. Taute, B. Lukić, S. Jeney, M. G. Raizen and E.-L. Florin, *Nat. Phys.*, 2011, **7**, 576–580.
89 P. N. Pusey, *Science*, 2011, **332**, 802.
90 H.-J. Galla, W. Hartmann, U. Theilen and E. Sackmann, *J. Membr. Biol.*, 1979, **48**, 215.
91 J. Mattsson, H. M. Wyss, A. Fernandez-Nieves, K. Miyazaki, Z. Hu, D. R. Reichman and D. A. Weitz, *Nature*, 2009, **462**, 83–6.
92 P. Berntsen, C. Svanberg and J. Swenson, *J. Phys. Chem. B*, 2011, **115**, 1825–1832.
93 V. Teboul, A. Monteil, L. C. Fai, A. Kerrache and S. Maabou, *Eur. Phys. J. B*, 2004, **40**, 49.
94 C. Smuda, S. Busch, G. Gemmecker and T. Unruh, *J. Chem. Phys.*, 2008, **129**, 014513.
95 M. T. Cicerone, F. R. Blackburn and M. D. Ediger, *Macromolecules*, 1995, **28**, 8224.

CREATED USING THE RSC LaTeX PCCP ARTICLE TEMPLATE – SEE www.rsc.org/electronicfiles FOR DETAILS

ARTICLE TYPE www. rsc.org/xxxxxx | XXXXXXXX

Supplementary Information: The Picosecond Dynamics of the Phospholipid Dimyristoylphosphatidylcholine in Mono- and Bilayers

Sebastian Busch,*[a] Luis Carlos Pardo,[b] Christoph Smuda,[c] and Tobias Unruh*[a,d]

Received Xth XXXXXXXXXX 20XX, Accepted Xth XXXXXXXXX 20XX
First published on the web Xth XXXXXXXXXX 20XX
DOI: 10.1039/b000000x

1 Thin Layer Chromatography

Thin layer chromatography (TLC) was performed on aluminium sheets covered with HPTLC Silica gel 60 F_{254} (Merck KGA, Darmstadt, Germany). Two measurements with different eluents were performed:

1. cyclohexane/isopropanol/water 30/40/6 (V/V), the procedure described in application #400710 of Macherey-Nagel, and in the literature [1].

2. chloroform/methanol/water 65/25/4 (V/V), described by Avanti Polar Lipids, Al, USA.

An UV lamp was used to make the substances visible.

2 Differential Scanning Calorimetry

Differential scanning calorimetry (DSC) was performed on a Setaram microDSC. 0.1 ml of sample (DMPC multibilayers in H_2O and DMPC multibilayers in D_2O) were measured against 0.1 ml of H_2O or D_2O, respectively, with a cooling/heating rate of 0.1 K/min. The shifts of the phase transition temperatures induced by the H_2O/D_2O exchange is only minor as can be seen in figure 1.

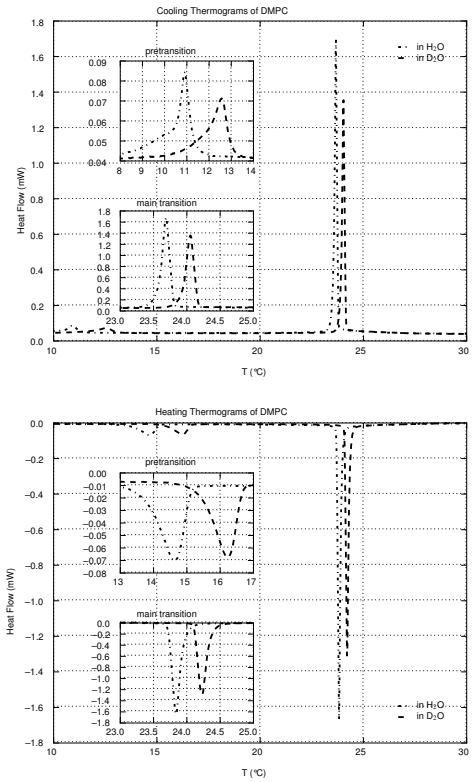

Fig. 1 Differential scanning calorimetry (DSC) measurements of DMPC in H_2O (dash-dotted lines) and D_2O (dashed lines). Shown are the cooling scan (top) and heating scan (bottom). The insets show enlarged versions of the pretransition and main transition peaks.

[a] Technische Universität München, Physik Department E13 and Forschungs-Neutronenquelle Heinz Maier-Leibnitz (FRM II), Lichtenbergstr. 1, 85748 Garching bei München, Germany. Fax: +49-89-289-14911; Tel: +49-89-289-14922; E-mail: sbusch@ph.tum.de
[b] Universitat Politècnica de Catalunya, Grup de Caracterizació de Materials, Departament de Física i Enginyeria Nuclear, ETSEIB, Diagonal 647, 08028 Barcelona, Catalonia, Spain.
[c] Eidgenössische Technische Hochschule Zürich, Animal Imaging Center – PET, Center for Radiopharmaceutical Sciences of ETH, PSI and USZ, Wolfgang-Pauli-Str. 10, 8093 Zürich, Switzerland.
[d] Friedrich-Alexander-Universität Erlangen-Nürnberg, Lehrstuhl für Kristallographie und Strukturphysik, Staudtstr. 3, 91058 Erlangen, Germany. Fax: +49-9131-85-25182; Tel.: +49-9131-85-25189 ; E-mail: Tobias.Unruh@krist.uni-erlangen.de

3 Calculation of the area per molecule

Spherical droplets with radius r and diameter $2r = \varnothing$ have a volume of $V = 4/3\pi r^3$, a surface of $S = 4\pi r^2$, and correspondingly $S/V = 3/r = 6/\varnothing \propto 1/\varnothing$. Approximating the density of all components with 1, the volume of spherical droplets in a unit sample volume is given by the concentration of perdeuterated hexadecane, [dHD]. Therefore, the surface area of the emulsion droplets in the same volume is

$$\text{area} \propto \frac{[\text{dHD}]}{\varnothing} \quad . \tag{1}$$

As the number of DMPC molecules in the same volume is proportional to the concentration of DMPC in the sample, [DMPC], one finally arrives at

$$\text{area per molecule} \propto \frac{[\text{dHD}]}{[\text{DMPC}] \cdot \varnothing} \quad . \tag{2}$$

This number is only a relatively rough measure for the true value because it assumes that the emulsion droplets are monodisperse and all DMPC molecules are adsorbed to the interface. The formula neglects the surface area occupied by NaGC molecules because the NaGC molecules are water soluble and the amount of NaGC is much lower than the one of DMPC.

4 Fit functions

The fit function used for the determination of the long-range motional component has been discussed in detail before[2]. It is

$$\begin{aligned} S(Q,\omega) = a \cdot X(Q,\omega) \otimes \\ [A_1(Q) \cdot \delta(\omega) + (1 - A_1(Q)) \cdot L_1(Q,\omega)] \otimes \\ [A_2(Q) \cdot \delta(\omega) + (1 - A_2(Q)) \cdot L_2(Q,\omega)] \end{aligned} \tag{3}$$

where X is discussed in the following, δ is the delta function, and L_1 and L_2 denote Lorentzians. The first term is caused by long-range motions, the two latter ones by localized motions.

4.1 Flow motions

Assuming flow-like motions with a Maxwell-Boltzmann distribution of the flow velocities, X is a Gaussian in ω with a standard deviation $\sigma(Q) = v \cdot Q$ where v is the most probable flow velocity.

4.2 Diffusion

Assuming diffusion, X is a Lorentzian in ω with a half width at half maximum $\Gamma(Q) = D \cdot Q^2$ where D is the diffusion coefficient.

References

1 F. M. Helmy and M. H. Hack, *Journal of Chromatography B: Biomedical Sciences and Applications*, 1986, **374**, 61.

2 S. Busch, C. Smuda, L. C. Pardo and T. Unruh, *Journal of the American Chemical Society*, 2010, **132**, 3232.

This journal is © The Royal Society of Chemistry [year]

Appendix G.

FABADA: a Fitting Algorithm for Bayesian Analysis of DAta

Luis Carlos Pardo, Muriel Rovira-Esteva, **Sebastian Busch**,
María Dolores Ruiz-Martín, and Josep Lluis Tamarit
Journal of Physics: Conference Series, 325(1):012006, 2011.
http://dx.doi.org/10.1088/1742-6596/325/1/012006

In this publication, the author actively participated in the development of the program. He incorporated cross-platform capability and replaced the central component of the software, the random number generator, with a free and open version that was publicly available. He contributed to the writing of the manuscript.

The program FABADA presented here is a Monte Carlo fit program that was used for the model-based evaluation of the data of pure DMPC [B]. One of its advantages compared to normal Levenberg-Marquardt algorithm used e. g. in [C, D] is that correlations between parameters are naturally taken into account, giving their «true» error bars.

This publication describes the general features of Bayesian fitting methods and demonstrates the versatility of the technique at several examples. The presented program features also a special optimization procedure of the parameter jump values that distinguishes it from other Bayesian fitting software [H].

Copyright 2011 by the Institute of Physics (IOP).

IOPscience iopscience.iop.org

Home Search Collections Journals About Contact us My IOPscience

FABADA: a Fitting Algorithm for Bayesian Analysis of DAta

This article has been downloaded from IOPscience. Please scroll down to see the full text article.

2011 J. Phys.: Conf. Ser. 325 012006

(http://iopscience.iop.org/1742-6596/325/1/012006)

View the table of contents for this issue, or go to the journal homepage for more

Download details:
IP Address: 129.187.254.46
The article was downloaded on 24/10/2011 at 15:18

Please note that terms and conditions apply.

FABADA: a Fitting Algorithm for Bayesian Analysis of DAta

L. C. Pardo[1], M. Rovira-Esteva[1], S. Busch[2], M. D. Ruiz-Martin[1], J. Ll. Tamarit[1]

[1]Grup de Caracterització de Materials, Departament de Física i Enginyieria Nuclear, ETSEIB, Universitat Politècnica de Catalunya, Diagonal 647, 08028 Barcelona, Catalonia, Spain
[2]Physik Department E13 and Forschungs-Neutronenquelle Heinz Maier-Leibnitz (FRM II), Technische Universität München, Lichtenbergstr. 1, 85748 Garching, Germany

Abstract. The fit of data using a mathematical model is the standard way to know if the model describes data correctly and to obtain parameters that describe the physical processes hidden behind the experimental results. This is usually done by means of a χ^2 minimization procedure. Although this procedure is fast and quite reliable for simple models, it has many drawbacks when dealing with complicated problems such as models with many or correlated parameters. We present here a Bayesian method to explore the parameter space guided only by the probability laws underlying the χ^2 figure of merit. The presented method does not get stuck in local minima of the χ^2 landscape as it usually happens with classical minimization procedures. Moreover correlations between parameters are taken into account in a natural way. Finally, parameters are obtained as probability distribution functions so that all the complexity of the parameter space is shown.

1. Introduction

Science is based on the success of an hypothesis to describe experimental results, i. e., is based on the amount of "truth" and "falsity" of an hypothesis when contrasted with experimental results [1]. In order to find a quantitative method to determine this "amount of truth", hypotheses in science should at the end be reduced to a mathematical expression depending on a set of parameters with some physical meaning. The "amount of truth" is then determined by fitting the mathematical model to some experimental data. To quantify that, a figure of merit χ^2 can be defined as

$$\chi^2 = \sum_{k=1}^{n} \frac{(H_k\{P_i\} - D_k)^2}{\sigma_k^2} \tag{1}$$

where n is the number of experimental points, D_k $(k = 1, \ldots, n)$ are the experimental data, $H_k\{P_i\}$ $(k = 1, \ldots, n)$ are the values obtained from our hypothesis (the mathematical model) using the $\{P_i\}$ $(i = 1, \ldots, m)$ set of parameters contained in the model, m is the number of parameters, and σ_k $(k = 1, \ldots, n)$ are the experimental errors associated with the respective measured points D_k.

Data fitting is usually done by minimizing χ^2 (equation 1) using the Levenberg-Marquardt algorithm, which aims to find the minimum of the $\chi^2\{P_i\}$ hypersurface. This fit procedure has a twofold goal: first, to find the set of parameters $\{P_i\}$ which best describes the experimental data within their errors, and second, using this set of parameters, to define a figure of merit

Published under licence by IOP Publishing Ltd

5th Meeting of the Spanish Neutron Scattering Association IOP Publishing
Journal of Physics: Conference Series **325** (2011) 012006 doi:10.1088/1742-6596/325/1/012006

which quantifies the "amount of truth" of the proposed hypothesis, taking into account how well it describes the data. In order to be able to compare different hypotheses with different numbers of parameters, it is reasonable to define a figure of merit which penalizes the addition of parameters such as the *reduced* χ^2 defined as $\chi^2_\nu = \frac{\chi^2}{n-m}$. In this equation, n is the number of experimental points and m is the number of parameters, so $n - m$ is the number of degrees of freedom.

This way to quantify how well experimental data are described by a hypothesis is based on what is called a frequentist approximation of the problem [2], and has many drawbacks associated with both the fit procedure (it usually gets stuck in local minima of the χ^2 hypersurface when the model is complex) and the way to quantify the correctness of the hypothesis describing experimental data. The final result using this method is characterized by a set of parameters with an associated error $(P_k \pm \varepsilon_k)$ and the figure of merit χ^2_ν. This way of quantifying the best fit to the data is based on the supposition that there is only one minimum in the $\chi^2\{P_i\}$ hypersurface within the data error, and that the functional dependence of $\chi^2\{P_i\}$ is quadratic on each parameter i (i. e., one can stop at the second term of a Taylor expansion of the obtained minimum), and thus allowing only symmetric errors. Moreover, errors are usually calculated disregarding possible correlations between parameters and are thus generally underestimated.

The main difference of Bayesian inference from the previously exposed frequentist method is the absence of *any* supposition on the $\chi^2\{P_i\}$ landscape which will rather be explicitly explored taking into account experimental data. The method results in a different way to express fitted parameters and the figure of merit showing all the complexity of the final solution: they become Probability Distribution Functions (PDFs) obtained directly from exploring the $\chi^2\{P_i\}$ hypersurface.

Although Bayesian methods are widely used in astronomy or biology [3], they are scarcely used in condensed matter and usually for very specific tasks such as in the analysis of QENS data [4], and the analysis of diffraction data [5, 6]. We present in this work a general method to perform fittings and to analyze results based exclusively on probability by using Bayesian inference.

Although the presented Bayesian method is general, it is specially useful in three situations. Firstly, when the classical fitting procedure gets stuck in a local minimum of the chi squared hypersurface, i.e. when the present parameter set does not correspond to the best obtainable fit but any small parameter value change even decreases the fit quality. This may happen for example when fitting the intramolecular structure to diffraction data [7] but is a well known problem in basically every fit normally surpassed by a careful choice of the initial parameter values. Secondly when an intricate model selection shall be performed, such as in the case of models that describe molecular motions using QENS [8] or dielectric data [9]. Finally when the model is ill defined and more than one combination of parameters is able to describe data, or when data only allows to limit the range of parameters but not to obtain a best fitting value [10].

2. Data analysis using the Bayesian method

2.1. What is behind the ubiquitous χ^2?

The objective of the so called *Bayesian methods* [4, 14] is to find the probability that a hypothesis is true given some experimental evidence. This is done by taking into account both our prior state of knowledge concerning the hypothesis, and the likelihood that the data is described by the proposed hypothesis. Using probability notation, and considering the case that the experiment consists of a series of data D_k and that the hypothesis is represented by H_k, we can relate the aforementioned probabilities using the Bayes theorem [13, 14]:

$$P(H_k \,|\, D_k) = \frac{P(D_k \,|\, H_k) P(H_k)}{P(D_k)} \tag{2}$$

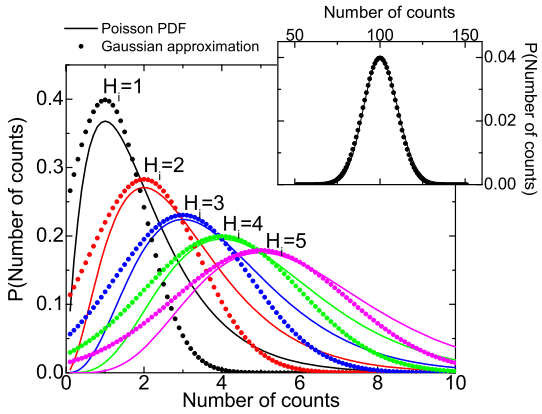

Figure 1. Poisson statistics followed by data in a counting experiment such as a scattering one (lines), and its usual Gaussian approximation (points) for an increasing number of expected counts. For an increasing number of counts, the Poisson distribution (line) can be approximated by a Gaussian function (points) with $\sigma = \sqrt{n}$, being the number of counts n. The inset shows that for a number of counts as great as 100 the approximation works quite well.

where $P(H_k\,|\,D_k)$ is called the *posterior*, the probability that the hypothesis is in fact describing the data. $P(D_k \mid H_k)$ is the likelihood, the probability that our data is well described by our hypothesis. $P(H_k)$ is called the prior, the PDF summarizing the knowledge we have beforehand about the hypothesis, and $P(D_k)$ is a normalization factor to assure that the integrated posterior probability is unity. In the following, we will assume no prior knowledge (maximum ignorance prior [14]), and in this special case Bayes theorem takes the simple form $P(H_k\,|\,D_k) \propto P(D_k\,|\,H_k) \equiv L$, where L is a short notation for likelihood.

In order to quantify the Bayes theorem, we need first to find the likelihood that one data point D_k is described by the mathematically modeled hypothesis H_k. In a counting experiment, this probability follows a Poisson distribution. It can be well approximated by a Gaussian distribution with $\sigma = \sqrt{D_k}$ (see also [14]) if the number of counts is high enough as it is shown in figure 1. Therefore for *one* experimental point ($k = i$, $i = 1, \ldots, n$):

$$P(D_{k=i}\,|\,H_{k=i}) = \frac{{H_k}^{D_k}\, e^{-H_k}}{D_k!} \approx \frac{1}{\sigma\sqrt{2\pi}} \exp\left[-\frac{1}{2}\left(\frac{H_k - D_k}{\sigma_k}\right)^2\right] \tag{3}$$

Where on the right hand side of the expression it is not explicitly written that the equation is related to a single experimental point $i = k$ for simplicity. The likelihood that the set of data points D_k is correctly described by the hypothesis H_k can be therefore written as

$$P(D_k\,|\,H_k) \propto \prod_{k=1}^{n} \exp\left[-\frac{1}{2}\left(\frac{H_k - D_k}{\sigma_k}\right)^2\right] = \exp\left[-\frac{1}{2}\sum_{k=1}^{n}\left(\frac{H_k - D_k}{\sigma_k}\right)^2\right] = \exp\left(-\frac{\chi 2}{2}\right) \;. \tag{4}$$

The figure of merit χ^2 is therefore related to the likelihood that the data is well described by the hypothesis H_k. The probability theory behind χ^2 also allows to deal with the case of experiments with only few counts where the Gaussian approximation, for which $\chi^2 = -2\ln L$, is not valid anymore and the Poisson distribution must be employed, simply by redefining χ^2 [14] as

$$\chi^2 = -2 \cdot \sum_{k=1}^{n} \ln\left[\frac{{H_k}^{D_k} e^{-H_k}}{D_k!}\right] \tag{5}$$

5th Meeting of the Spanish Neutron Scattering Association IOP Publishing
Journal of Physics: Conference Series **325** (2011) 012006 doi:10.1088/1742-6596/325/1/012006

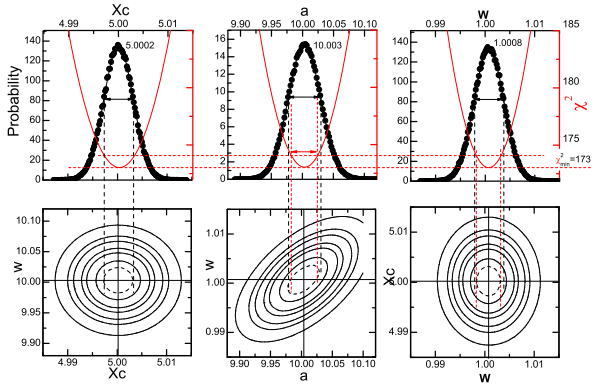

Figure 2. Upper row: PDFs associated with the center x_c, amplitude a and width w of a Gaussian function (solid circles) together with the $\chi^2(P_i)$ around its minimum value, fixing all parameters except P_i (lines). Bottom row: $\chi^2(P_i, P_j)$ plots showing the correlation between parameters, the contour lines have a distance of $\Delta\chi^2 = 1$.

2.2. The Bayesian method

The probabilistic understanding of χ^2 makes it possible to define a unique method, first to fit the experimental data, and then to analyze the obtained results, using a Markov Chain Monte Carlo (MCMC) technique where a set of parameters P_i^{new} is generated from an old set P_i^{old} by randomly changing one of the parameters, i. e., $P_i^{\text{new}} = P_i^{\text{old}} + (\text{RND} - 0.5) \cdot 2\Delta P_i^{\max}$. In the last equation $\Delta P_i^{\max}$ is the maximum change allowed for the parameter and will be called parameter jump for short, and RND is a random number between 0 and 1. The probability to accept the new set of parameters is given by

$$\frac{P(H(P_i^{\text{new}})\,|\,D_k)}{P(H(P_i^{\text{old}})\,|\,D_k)} = \exp\left(-\frac{\chi^2_{\text{new}} - \chi^2_{\text{old}}}{2}\right) \tag{6}$$

where χ^2_{new} and χ^2_{old} correspond to the χ^2 (as defined in equation 1) for the new and old set of parameters. Both fitting and analysis consist therefore in the successive generation of parameter sets $\{P_i\}$ (Markov Chains) with the successive acceptations ruled by equation 6.

3. Two academic examples

3.1. Fitting a Gaussian

In order to test the fit algorithm, a standard function such as a Gaussian

$$y(x) = a/\sqrt{2\pi w}\,\exp\left[-(x - x_c)^2/(2w^2)\right] + b \tag{7}$$

was generated with the parameter set $\{a, w, x_c\} = \{10.0, 1.0, 5.0\}$ and being b fixed to zero. The data were generated with a Normal distributed error associated with each point of 0.05 and subsequently fitted by the presented algorithm using the same formula (with $b = 0$).

The calculated PDFs associated with each parameter P_i are shown in the top row of figure 2 together with the χ^2 dependence on this parameter, calculated by varying only the parameter P_i and leaving the others fixed, i. e., making a cut of the hypersurface $\chi^2\{a, w, x_c\}$. As one may expect, the minimum of χ^2 coincides with the maximum probability of each parameter PDF.

The most probable parameter *values* – the ones where the PDF is maximal – coincide very nicely with the original values as can be seen in the top row of figure 2. In the following, the discussion will focus on the determination of the parameter *errors*. There are two ways to determine the parameter errors: (i) the commonly used definition of the error as the value of the parameter that increases χ^2 by one unit ($\Delta P = |P(\chi^2_{\min}) - P(\chi^2_{\min} + 1)|$) and (ii) the width of the Gaussian associated with the PDF (the width of the Gaussian at $y = e^{-0.5} \cdot y^{\max}$).

The obtained PDFs can be well described by a Gaussian function in the present examples (solid line in the PDFs shown in figure 2). This proves that in this simple case the minimum of $\chi^2\{P_i\}$ is quadratic in each parameter, and therefore the frequentist definitions of errors can be used – the two measures of the parameter errors should coincide. The error is the defined in such a way that P_i has a 68% probability to be within $P_i - \sigma_{P_i}$ and $P_i + \sigma_{P_i}$ (see [15]).

In figure 2 it can be seen that errors calculated from the PDFs are equal (for x_c) or larger (for a and w) than those calculated using the method of incrementing χ^2. This discrepancy can be explained by parameter correlations seen in the contour plots of the two-dimensional cuts through the $\chi^2(P_i, P_j)$ hypersurface shown in the bottom row of figure 2: from the symmetry of the contours involving x_c it can be concluded that x_c is independent from both, a and w, whereas these two parameters are correlated, causing the main axis of the contour ellipsoids to be not parallel to the parameter axes. For the parameters a and w, the error calculated from the PDF coincides with the limits of the contour $\chi^2 = \chi^2_{\min} + 1$. The error calculated from χ^2 coincides with the intersection of the contour with the x axis, thus underestimating its value.

Although this fact is well known in the frequentist approximation [15], to take correlations between parameters into account would involve diagonalizing the covariant matrix. That is scarcely done and in any case is useful only in simple cases as the one presented when errors are symmetric, i. e., when $\chi^2\{P_i\}$ is quadratic in P_i. The Bayesian approach takes in a natural way any correlation between parameters into account, and can also treat non-Gaussian PDFs being much more powerful than the frequentist approximation.

3.2. Fitting with Poisson statistics

The standard way of fitting data using the minimization of χ^2 (as defined in equation 4) is no longer valid when the number of counts is low. However, as we have seen, simply by redefining χ^2 using equation 5, we can perform the fits when the number of counts is arbitrarily low.

To test our algorithm we have generated a series of random numbers D_K following a Poisson distribution around different fixed values H_K. We have then fitted these series of randomly generated points using the usual definition of χ^2, equation 4, therefore wrongly assuming that the numbers were generated following a Gaussian PDF (see Fig. 1) and with the definition given in equation 5, that is, correctly assuming that D_K follows a Poisson PDF around H_K.

In figure 3 we show the relative discrepancy between the fitted value and the value H_K used to generate the series of points using both methods as a function of the value H_K on a logarithmic scale. As expected, for H_K greater than about 10^3 both methods yield the same result. On the contrary for smaller values the discrepancy increases, reaching 30% for $H_K = 1$.

It is therefore important to take into account that in the limit of low counts the usual approximation between Poisson and Gaussian statistics should not be used. In figure 3 it is displayed the fit of a Gaussian function (equation 7) with parameters $\{a, w, x_c, b\} = \{20, 5, 1, 2\}$ each point D_K being generated following a Poisson distribution. The fit using Poisson statistics is closer to the generated function, i. e., unaffected by the error, as it can be seen in the figure proving that the proposed algorithm is also useful to fit in the case of low count rates.

4. Conclusions

We have proposed a general Bayesian method to fit data and analyze results from the fit [12]. The classical frequentist approach makes some assumptions concerning the χ^2 landscape: there is only a minimum of $\chi^2\{P_i\}$ able to describe data within its error, this minimum has a quadratic dependence on the parameters, and the parameters are not correlated. The here proposed method avoids such problems, sampling the parameter space only with the guide of probability rules. This method has already been successfully used to analyze experiments coming from diffraction experiments [16], quasielastic neutron scattering [17, 10, 8] and dielectric spectroscopy [9]. We finally summarize the main advantages of the proposed method:

5th Meeting of the Spanish Neutron Scattering Association IOP Publishing
Journal of Physics: Conference Series **325** (2011) 012006 doi:10.1088/1742-6596/325/1/012006

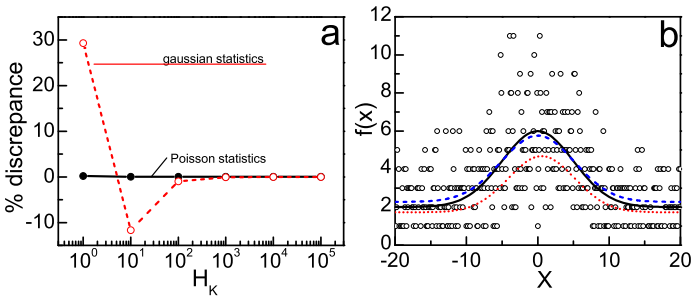

Figure 3. (a) Discrepancy between the fits to a constant value H_K set to 10^i, $i = 0, 1, \ldots, 5$ using a Gaussian (empty circles) and a Poisson statistic (full circles), being D_K values generated using a Poisson statistics. (b) Gaussian function generated assuming a low-count experiment (circles), i. e., assuming a Poisson statistics for each point. The solid line is the generated function unaffected by the error, and the dashed line the fitted function. Dotted line is the fit assuming a normal distribution of errors.

The Bayesian method will not get stuck in local minima of the χ^2 hypersurface during the fit procedure if its barrier is smaller than the error associated with the experimental data set [16].

Parameters are obtained as PDFs and, because the whole parameter space is sampled, correlations between parameters are taken into account. Moreover, a natural way to define errors based on the PDF of parameters is obtained within this method [17, 10, 9].

The likelihood (which as we have seen is directly related to χ^2) obtained by this method is also a PDF hence revealing the whole complexity of the parameter landscape. Model selection is then performed taking into account all parameter combinations compatible with the experiment [8].

This work was supported by the Spanish *Ministerio de Ciencia e Innovación* (FIS2008-00837) and by the Catalonia government (2009SGR-1251). We would also like to thank helpful comments on the manuscript made from K. Kretschmer, T. Unruh and I. Pereyra.

References

[1] Popper K R 2002 *Conjectures and Refutations: The Growth of Scientific Knowledge* ed. Routledge Classics
[2] The frequentist description defines probability of a certain event A ($P(A)$) as the limiting frequency with which the event A is observed when a great number of events A is taken into account.
[3] Trotta R 2008 *Contemp. Phys.* **49(2)** 71; Huelsenbeck J P, Ronquist F, Nielsen R and Bollback J P 2001 *Science* **294** 5550; McVean G A T, Myers S R, Hunt S, Deloukas P, Bentley D R and Donnelly P 2004 *Science* **304** 5670; Diehl R et al. 2006 *A&A* **449** 1025
[4] Sivia D, Carlile C J and Howells W S 1992 *Physica B* 182 **4** 341
[5] Bermejo F J, Santoro J, Mompean F J and Dore J C 1988 *Nucl. Instrum. Meth. Phys. Res. B*, **34** 505; Bacallado S, Chodera J D and Pande V 2009 *J. Chem. Phys.* **131(4)** 45106
[6] O Gereben, P Jóvári, L Temleitner, L Pusztai 2007 J. *Optoelectron. Adv. Mater.* 9 **10** 3021; Sz Pothoczki, L Temleitner, P Jóvári, S Kohara and L Pusztai 2009 *J. Chem. Phys.* 130 064503
[7] Adyaa A K and Bianchi L 2000 *J. Chem. Phys.* 112**9** 4231; Leclercq F, Damay P, Foukani M, Chieux P, Bellisent-Funel M C, Rassat A, Fabre C 1993 *Phys. Rev. B* 48**4** 2748
[8] Busch S, Smuda C, Pardo L C and Unruh T 2010 *J. Am. Chem. Soc.* **132(10)** 3232

[9] Martinez-Garcia J C, Tamarit J Ll, Pardo L C, Barrio M, Rzoska S J and Droz-Rzoska A 2010 *J. Phys. Chem. B* **114** 6099
[10] Pardo L C, Rovira-Esteva M, Busch S, Ruiz-Martin M D, Tamarit J Ll and Unruh T 2009 Bayesian Analysis of QENS data: From parameter determination to model selection *Preprint* arXiv:0907.3711
[11] Hastings W K 1970 *Biometrika* **57(1)** 97
[12] FABADA program (Fit Algortihm for Bayesian Analysis of DAta) can be found in http://gcm.upc.edu/members/luis-carlos/bayesiano
[13] Bayes T 1764 *Phil. trans. Roy. Soc.* **53** 370
[14] Sivia D 2006 *Data Analysis: A bayesian tutorial* Oxford University Press
[15] Press W H, Teukolsky S A, Vetterling W T and Flannery B P 1992 *Numerical Recipes in Fortran 77: the art of scientific computing* Ed. Cambridge University Press, 2nd edition
[16] Rovira-Esteva M et al. Interplay of intramolecular and intramolecular structure: a Bayesian analysis *To be published*
[17] Rovira-Esteva M et al. 2010 *Phys. Rev. B* **81(9)** 092202

Appendix H.

Fitting in a Complex χ^2 Landscape Using an Optimized Hypersurface Sampling

Luis Carlos Pardo, Muriel Rovira-Esteva, **Sebastian Busch**, Jean-François Moulin, and Josep Lluis Tamarit
Physical Review E, 84(4):046711, 2011.
http://dx.doi.org/10.1103/PhysRevE.84.046711

In this publication, the author actively participated in the development of the program. He tested the program and implemented several corrections and enhancements. He took part in the interpretation of the results and contributed to the writing of the manuscript.

In order to explore the χ^2 landscape efficiently, the program FABADA [G] was provided with the here presented optimised parameter jump sizes adaptation. A good choice of the parameter jump lengths is of utmost importance for Monte Carlo fits – if not adjusted to the right value, for example a model selection as used for the DMPC multibilayers [B], will yield erroneous results because the χ^2 hypersurface is not uniformly scanned.

Luis Carlos Pardo, Muriel Rovira-Esteva, Sebastian Busch, Jean-François Moulin, and Josep Lluis Tamarit, Physical Review E, 84(4):046711, 2011.
"Copyright 2011 by the American Physical Society."

PHYSICAL REVIEW E **84**, 046711 (2011)

Fitting in a complex χ^2 landscape using an optimized hypersurface sampling

L. C. Pardo,[1] M. Rovira-Esteva,[1] S. Busch,[2] J. -F. Moulin,[3] and J. Ll. Tamarit[1]

[1]*Grup de Caracterització de Materials, Departament de Física i Enginyieria Nuclear, ETSEIB, Universitat Politècnica de Catalunya, Diagonal 647, 08028 Barcelona, Catalonia, Spain*

[2]*Physik Department E13 and Forschungs-Neutronenquelle Heinz Maier-Leibnitz (FRM II), Technische Universität München, Lichtenbergstr. 1, 85748 Garching, Germany*

[3]*Helmholtz-Zentrum Geesthacht, Institut für Werkstoffforschung, Abteilung WPN, Instrument REFSANS, Forschungs-Neutronenquelle Heinz Maier-Leibnitz (FRM II), Lichtenbergstr. 1, 85748 Garching, Germany*

(Received 25 March 2011; revised manuscript received 12 September 2011; published 25 October 2011)

Fitting a data set with a parametrized model can be seen geometrically as finding the global minimum of the χ^2 hypersurface, depending on a set of parameters $\{P_i\}$. This is usually done using the Levenberg-Marquardt algorithm. The main drawback of this algorithm is that despite its fast convergence, it can get stuck if the parameters are not initialized close to the final solution. We propose a modification of the Metropolis algorithm introducing a parameter step tuning that optimizes the sampling of parameter space. The ability of the parameter tuning algorithm together with simulated annealing to find the global χ^2 hypersurface minimum, jumping across $\chi^2\{P_i\}$ barriers when necessary, is demonstrated with synthetic functions and with real data.

DOI: 10.1103/PhysRevE.84.046711 PACS number(s): 02.60.Pn, 02.50.Cw, 02.50.Ng, 02.50.Tt

I. INTRODUCTION

Fitting a parametrized model to experimental results is the most usual way to obtain the physics hidden behind data. However, as nicely reported by Transtrum *et al.* [1], this can be quite challenging, and it usually takes "weeks of human guidance to find a good starting point." Geometrically, the problem of finding a best fit corresponds to finding the global minimum of the χ^2 hypersurface. As this hypersurface is often full of fissures, local minima prohibit an efficient search. The human guidance consists usually of a set of tricks (depending on every particular problem) that allow us to choose the starting point in this landscape such that the first minimum found is indeed the global minimum.

This problem is usually due to the mechanism that is behind classical fit algorithms such as Levenberg-Marquardt (LM) [2]: A set of parameters $\{P_i\}$ is optimized by varying the parameters and accepting the modified parameter set as a starting point for the next iteration only if this new set reduces the value of a cost or merit function such as χ^2. From a geometrical point of view, those algorithms allow only downhill movements in the $\chi^2\{P_i\}$ hypersurface. Therefore they can get stuck in local minima or get lost in flat regions of the χ^2 landscape [1]. This means that they are able to find an optimal solution only if they are initialized around the absolute minimum of the χ^2 hypersurface.

The challenge of finding the global minimum can be alternatively tackled by Bayesian methods [3,4] as demonstrated in different fields such as astronomy or biology [5], solid-state physics [6], quasielastic neutron-scattering data analysis [7], and reverse Monte Carlo methods [8]. We follow a Bayesian approach to the fit problem in this contribution. This method is based on another mechanism to wander around in parameter space: Instead of allowing only downhill movements, parameter changes that increase χ^2 can also be accepted if the change in χ^2 is compatible with the data errors.

To do that, a Markov chain Monte Carlo (MCMC) method is used, where the Markov chains are generated by the Metropolis algorithm [9]. However, while in the case of the LM algorithm the initialization of parameters is critical to the convergence of the algorithm, it is here that the tuning of the maximum parameter change allowed at each step (called parameter jumps hereafter) is what will decide the success of the algorithm to find the global $\chi^2\{P_i\}$ minimum in an efficient way.

If the parameter jumps are chosen too small, the algorithm will always accept any parameter change, getting lost in irrelevant details of the $\chi^2\{P_i\}$ landscape. If chosen too large, the parameters will hardly be accepted, and the algorithm will get stuck every now and then. Moreover, in the case of models defined by more than one parameter, when parameter jumps are not properly chosen, the parameter space can be overexplored in the direction of those parameters with too small jump lengths; in other words, the model would be insensitive to the proposed change of these parameters. On the other hand, some other parameters can be associated to a jump so big that changes are hardly ever accepted.

Different schemes have been proposed in order to change parameter jumps to explore the target distribution efficiently using Markov chains under the generic name of adaptive MCMC [10]. Using the framework of stochastic approximation [11] we present in this work an algorithm belonging to the group of "controlled Markov chains" [12,13] where the calculation of new parameter jumps takes the history of the Markov chain and previous parameter jumps into account.

Two main approaches are known that take the Markov chain history into account: adaptive Metropolis (AM) algorithms [14] (implemented, for example, in PyMC [15]) and algorithms that use rules following the Robbins-Monro update [13,16,17]. In the first case, parameter jumps are tuned using the covariance matrix at every step, so that once the adaptation is finished the algorithm should be wandering with a parameter jump close to the "error" of the parameter (defined as the variance of the posterior parameter probability density function [PDF]). In some cases, this kind of algorithm [10] can get stuck if the acceptance ratio of a parameter is too

 ©2011 American Physical Society

high or too low. In this case the Markov chain stops learning from the past history, and thus the optimization is stopped with suboptimal parameter jumps. This problem is overcome by Robbins-Monro update rules that change parameter jumps so that they are accepted with an optimal ratio.

The main danger of optimized Metropolis algorithms is that adaptation might cause the Markov chain to not converge to the target distribution anymore. In other words, the Markov chain might lose its ergodicity. For example in the case of AM algorithms, the generated chain is not Markovian since it depends on the history of the chain. However, as demonstrated by Haario *et al.* [14], the chain is able to reproduce the target distribution, i.e., is ergodic. In the second type of algorithms, the Robbins-Monro type, ergodicity properties must be ensured by updating only at regeneration times [16]. In any case, as pointed out by Andrieu *et al.* [10], the convergence to the target distribution is ensured if optimization vanishes. In other words, if parameter jumps oscillate around a fixed value, the ergodic property of the Markov chain is ensured.

The presented algorithm is based on the stochastic approach of Robbins-Monro with an updating rule inspired by the one of Gilks *et al.* [16]. Optimization of parameter jumps is therefore performed with two goals in mind:

(1) To calculate them in such a way that all parameters are accepted with the same ratio. Adjusting parameter jumps so that all parameter changes will have the same acceptance ratio is important to explore the $\chi^2\{P_i\}$ landscape with the same efficiency in all parameter directions.

(2) To adjust parameter jumps to a value tailored to the stage of the fit. This will turn out to be important when exploring the $\chi^2\{P_i\}$ hypersurface using the simulated annealing technique [18], since this allows the parameter jumps to be optimized to explore $\chi^2\{P_i\}$ (see subsection fitting in a complex χ^2 landscape): At the beginning of the fit process the algorithm will set parameter jumps to a large value to explore large portions of the χ^2 landscape, and at the final stages these parameter jumps will be set to small values by the same algorithm in order to find its absolute minimum.

Geometrically, we can interpret the algorithm as setting the parameter step sizes to a value related to the hypersurface landscape. First, it modifies the parameter jump to take into account the shape of the hypersurface along a parameter direction. If $\chi^2\{P_k\}$ (the cut along a parameter k) is flat (the parameter direction is "sloppy" following Sethna's nomenclature [19]), the parameter step size is set to a larger value, and parameters will move faster in this sloppy direction. On the contrary, in the directions where the $\chi^2\{P_k\}$ has a larger slope (the "stiff" direction following Sethna's nomenclature), parameter steps will be set to a smaller value so that they are accepted with the same as the previous ones. Second, it modifies the parameter jumps to take the shape of the global χ^2 landscape into account when the simulated annealing is used. At the beginning of the fit parameter jumps will be set to a large value so that details of $\chi^2\{P_k\}$, i.e., local minima, will be smeared out, making it easier to find the global minimum. However, during the last steps of the fitting process, parameter steps will be set to a small value by the algorithm so that the system will be allowed to relax inside the minimum.

The present work gives a detailed description on how the algorithm works and is organized as follows: We first recall briefly on the Metropolis method applied to generate Markov chains. In the next section, the proposed algorithm to optimize the parameter step size is introduced. Then we check its robustness to find optimized parameter jumps using a simple test function; and finally we test the ability of the regenerative algorithm combined with the simulated annealing technique to find the global minimum of χ^2, even with poor initialization values, using a simple function with a complex $\chi^2\{P_i\}$ landscape. The algorithm presented in this work has been implemented in the program FABADA (Fit Algorithm for Bayesian Analysis of DAta) [20].

II. THE FIT METHOD

A. Fitting with the Bayesian ansatz

Fitting data using the Metropolis algorithm is based on an iterative process where successively proposed parameter sets are accepted according to the probability that these parameters describe the actual data, given all available evidence. Hence this method makes use of our knowledge of the error bars of the data.

We now briefly recall how this can be done using a Metropolis algorithm, to proceed in the next section with the algorithm to adjust parameter jumps.

We should first start with the probabilistic bases behind the χ^2 definition. The probability $\mathbb{P}(H|D)$ that an hypothesis H is correctly describing an experimental result D is related to the likelihood $\mathbb{P}(D|H)$ that experimental data D_k $(k = 1,\ldots,n)$ are correctly described by a model or hypothesis H_k $(k = 1,\ldots,n)$; using Bayes' theorem [3,4],

$$\mathbb{P}(H_k|D_k) = \frac{\mathbb{P}(D_k|H_k)\mathbb{P}(H_k)}{\mathbb{P}(D_k)}, \tag{1}$$

where $\mathbb{P}(H_k|D_k)$ is called the *posterior*, the probability that the hypothesis is in fact describing the data. $\mathbb{P}(D_k|H_k)$ is the *likelihood*, the probability that the description of the data by the hypothesis is good. $\mathbb{P}(H_k)$ is called the *prior*, the PDF summarizing the knowledge we have about the hypothesis before looking at the data. $\mathbb{P}(D_k)$ is a normalization factor to ensure that the integrated posterior probability is unity.

In the following we will assume no prior knowledge (maximum ignorance prior [4]), and in this special case Bayes' theorem takes the simple form

$$\mathbb{P}(H_k|D_k) \propto \mathbb{P}(D_k|H_k) \equiv L, \tag{2}$$

where L is a short notation for likelihood.

Although this is by no means a prerequisite, we will assume in the following that the likelihood that every single data point D_k described by the model or hypothesis H_k follows a Gaussian distribution. The case of a Poisson distribution was discussed previously [21]. For data with a Gaussian distributed uncertainty with width σ, the likelihood for each individual data point takes the form

$$\mathbb{P}(D_k|H_k) = \frac{1}{\sigma\sqrt{2\pi}} \exp\left[-\frac{1}{2}\left(\frac{H_k - D_k}{\sigma_k}\right)^2\right], \tag{3}$$

and correspondingly, the likelihood that *the whole* data set is described by this hypothesis is

$$\mathbb{P}(D_k|H_k) \propto \prod_{k=1}^{n} \exp\left[-\frac{1}{2}\left(\frac{H_k - D_k}{\sigma_k}\right)^2\right] = \exp\left[-\frac{1}{2}\sum_{k=1}^{n}\left(\frac{H_k - D_k}{\sigma_k}\right)^2\right] = \exp\left(-\frac{\chi^2}{2}\right). \quad (4)$$

The Metropolis algorithm will in this special case consist of the proposition of successive sets of parameters $\{P_i\}$. A new set of parameters is generated changing one parameter at a time using the rule

$$P_i^{\text{new}} = P_i^{\text{old}} + r\Delta P_i^{\max}, \quad (5)$$

where $\Delta P_i^{\max}$ is the maximum change allowed to the parameter or parameter jump and r is a random number between -1.0 and 1.0. The new set of parameters will always be accepted if it lowers the value of χ^2, or, if the opposite happens, it will be accepted with a probability

$$\frac{\mathbb{P}\left(H\{P_i^{l+1}\}|D_k\right)}{\mathbb{P}\left(H\{P_i^{l}\}|D_k\right)} = \exp\left(-\frac{\chi_{l+1}^2 - \chi_l^2}{2}\right), \quad (6)$$

where χ_{l+1}^2 and χ_l^2 correspond to the χ^2 for the proposed new set of parameters and the old one, respectively. Otherwise, this new parameter value will be rejected, and the fit function does not change during this step.

The Metropolis algorithm described here is very similar to the one used in statistical physics to find the possible molecular configurations (microstates) at a given temperature. In that case the algorithm minimizes the energy of the system while allowing changes in molecular positions that yield an increase of the energy if it is compatible with the temperature.

Inspired by the similarities between fitting data using a Bayesian approach and molecular modeling using Monte Carlo methods, a simulated annealing procedure proposed by Kirkpatrick [18] might optionally be used (see, for example, Refs. [22,23]). Following the idea of that work, the χ^2 landscape might be compared with an energy landscape used to describe glassy phenomena [24]. What we do is to start at high temperatures, i.e., in the liquid phase, where details of the energy landscape are not so important. By lowering the temperature fast enough the system might fall into a local minima, i.e., in the glassy phase. In that case the system is quenched as is normally done by standard fitting methods. The presented algorithm aims to avoid being trapped in local minima using an "annealing schedule" as suggested by Kirkpatrick. This is done by artificially increasing the errors of the data to be fitted and letting the errors slowly relax until they reach their true values. Because this is very similar to what is performed in molecular modeling, the parameter favoring the uphill movements in Eq. (7) is usually called *temperature*, yielding the acceptance rule

$$\frac{\mathbb{P}\left(H(P_i^{l+1})|D_k\right)}{\mathbb{P}\left(H(P_i^{l})|D_k\right)} = \exp\left(-\frac{\chi_{l+1}^2 - \chi_l^2}{2T}\right). \quad (7)$$

As happens with Monte Carlo simulations, increasing the temperature will increase the acceptance of parameter sets that increase χ^2, thus making the jump over χ^2 barriers between minima easier.

B. Adjusting the parameter step size

The objective of tuning the parameter step size is to choose a proper value for $\Delta P_i^{\max}$ in Eq. (5) to optimize the parameter space exploration.

Given the total number of algorithm steps N and the number of steps that yield a change in χ^2, i.e., the number of successful attempts, K, the ratio R of steps yielding a χ^2 change is $R = K/N$. R_{desired} is defined as the ratio with which *some parameter* should be accepted in a step. As we want every parameter to be changed with the same ratio, $R_{i,\text{desired}} = R_{\text{desired}}/m$ where m is the number of parameters.

The algorithm is initialized with a first guess for the parameter step sizes. This first guess, as will be seen shortly, is not important due to the fast convergence of the algorithm to the optimized values. The calculation of a new $\Delta P_i^{\max}$, i.e., the regeneration of the Markov chain, is done after N steps, i.e., at regeneration times, through the equation

$$\Delta P_i^{\max,\text{new}} = \Delta P_i^{\max,\text{old}} \frac{R_i}{R_{i,\text{desired}}}, \quad (8)$$

where R_i is the actual acceptance ratio of parameter i. Following the previous equation, if the calculated ratio $R_i/R_{i,\text{desired}}$ is equal to one, i.e., if all parameters are changing with the same predefined ratio, $\Delta P_i^{\max}$ will not be changed.

If during the fit process a change of parameter P_i is too often accepted, the parameter space is being overexplored with regard to parameter i. The algorithm will then make $\Delta P_i^{\max}$ larger in order to reduce its acceptance. The contrary happens if the acceptance is too low for a parameter: The algorithm makes $\Delta P_i^{\max}$ smaller to increase its acceptance ratio. This will set different step sizes for each parameter, making the exploration of all of them equally efficient.

III. DEMONSTRATIONS OF FITTING FUNCTIONS

A. Fitting in a well-behaved χ^2 landscape

The optimization of the parameter step size is shown using the Gaussian function

$$y(x) = \frac{A}{W\sqrt{2\pi}} \exp\left[-\frac{(x-C)^2}{2W^2}\right], \quad (9)$$

where A is the amplitude, W is the width, and C is the center of the Gaussian. A function has been generated with the parameter set $\{A,W,C\} = \{10,1,5\}$, and a normally distributed error with $\sigma = 0.1$ was added. A series of tests with different initial values for parameter jumps and different desired acceptance ratios have been carried out (see below for details). The initial parameters for the fit were $\{A,W,C\} = \{2,2,2\}$. In all cases the algorithm was able to fit the data as can be seen in Fig. 1.

The parameter step size was adjusted every 1000 steps. Three cases are shown in Fig. 2: an initial $\Delta P_i^{\max}$ of 10 (a very large jump compared to the parameter values, nearly always resulting in a rejection of the new parameters) and an R_{desired}

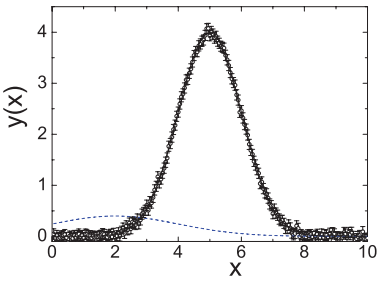

FIG. 1. (Color online) Circles: Generated Gaussian function to test the algorithm with the parameters $\{A,W,C\} = \{10,1,5\}$. Dashed line: Starting point for all performed tests ($\{A,W,C\} = \{2,2,2\}$). Solid line: Best fit, i.e., minimum χ^2 fit, of the Gaussian function.

of 66%, the same $\Delta P_i^{\max}$ with an R_{desired} of 9% and finally a $\Delta P_i^{\max}$ of 10^{-4} (a very small jump compared to the parameter values, resulting in a slow exploration of the parameter space) and an R_{desired} of 9%. It can be seen that the algorithm manages in all these extreme cases to adapt the jump size quickly and reliably in order to make R equal to R_{desired}.

In Fig. 3 we show the three individual acceptance ratios R_i for the different parameters as a function of the fit steps for different initialization values of the parameter jumps ΔP_i, for different values of R_{desired}, and setting the number of steps to recalculate parameter jumps N to 1000. When the total acceptance ratio is set to $R_{\text{desired}} = 66\%$ (solid line), the algorithm is able to change all parameter jumps [see Fig. 3(b)], making the acceptance ratio R_i of every parameter equal to $R_{\text{desired}}/m = 22\%$ and thus the total acceptance ratio R to 66%. The same happens if the acceptance is set to 9%: The algorithm finds the parameter step sizes [see dashed line in Fig. 3(b)], which yield a total acceptance ratio of 9% within the first 5000 steps, no matter how the parameter step sizes were initialized.

To explicitly show how this is linked with the geometrical features of the χ^2 landscape, the inset of Fig. 3(b) shows a cut of the χ^2 hypersurface along parameters A and C, leaving parameter W fixed to its best fit value W_{BF}. As can readily be seen, the $\chi^2\{A,C,W = W_{\text{BF}}\}$ hypersurface is sloppy in the

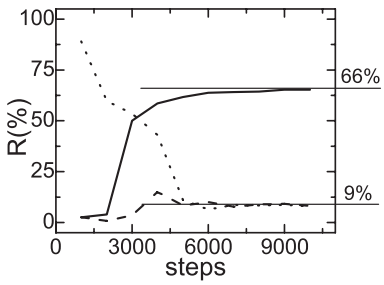

FIG. 2. Total acceptance ratio R as a function of the number of steps when R_{desired} is set to 66% and 9% (solid and dashed or dotted lines). In the second case ($R_{\text{desired}} = 9\%$), dashed and dotted lines represent the values of R as a function of algorithm step for two different parameter step size initializations ($\Delta P_i^{\max} = 10$ and $\Delta P_i^{\max} = 10^{-4}$, respectively).

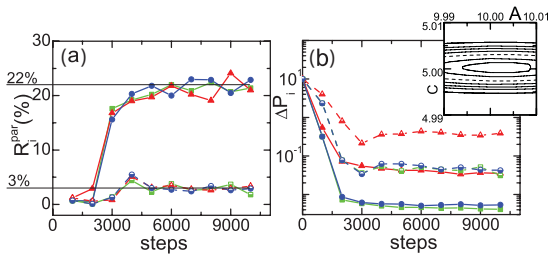

FIG. 3. (Color online) (a) Acceptance ratio R_i for parameters A, W, C involved in the fit of the Gaussian following Eq. (9) (red triangles, green squares, and blue circles, respectively) when R_{desired} is set to 66% and 9% (solid and dashed lines). (b) Parameter step size as a function of the number of steps (line and symbols code as in panel a). The inset shows a cut through the χ^2 hypersurface along A and C directions fixing W to the best-fit value.

direction of parameter A and stiff in the direction of parameter C. The algorithm has thus correctly calculated a parameter step size that is larger for A than for C, along whose direction the χ^2 well is narrower. This fact makes the final parameter step sizes proportional to the errors of each parameter—if the global minimum is not multimodal and is quadratic in all parameters, and those are not correlated.

In order to show the robustness of the algorithm, we have also made disparate initial guesses for parameter step sizes $\Delta P_i^{\max}$ about three decades below the correct acceptance ratio, setting $R_{\text{desired}} = 9\%$. As displayed in Fig. 3, after about 5000 steps the acceptance ratio R (N is again 1000 steps) has already reached the desired value. It can be seen in Fig. 4(a) that the acceptance ratio for each parameter reaches again the value $R_{\text{desired}}/m = 3\%$ and parameter step sizes are virtually equal to those obtained previously as shown in Fig. 4(b).

To stress the relevance of the aforementioned algorithm to explore the parameter space correctly, thus ensuring its convergence, we have calculated the normalized $\Delta\chi^2$PDF in all tested cases. As can be seen in Fig. 5, the $\Delta\chi^2$ PDF after 10^5 steps matches the χ^2 distribution

$$\mathbb{P}(\Delta\chi^2) \propto (\Delta\chi^2)^{\left(\frac{m}{2}-1\right)} \exp\left(-\frac{\Delta\chi^2}{2}\right), \tag{10}$$

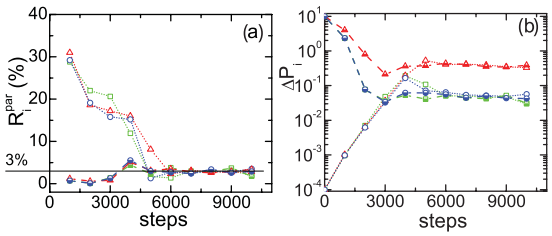

FIG. 4. (Color online) (a) Acceptance ratio R_i for parameters A (triangles), W (squares), C (circles) involved in the fit of the Gaussian following Eq. (9) when initial parameter step sizes are set to $\Delta P_i = 10$ (dashed line) and $\Delta P_i = 10^{-4}$ (dotted line). (b) Parameter step size as a function of the number of steps (lines and symbols as in panel a).

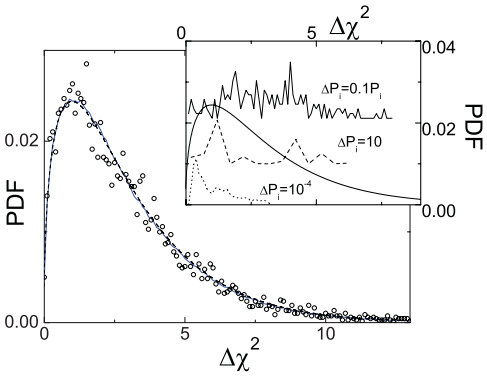

FIG. 5. (Color online) The dashed line represents a χ^2 distribution for three parameters, i.e., $m = 3$ (see text for details). Solid line is the obtained PDF associated to $\Delta\chi^2$ when calculated for 10^5 steps. Circles represent the same distribution when calculated using only 10^4 steps. The inset shows the χ^2 PDFs when calculated with parameters allowed to change with $\Delta P_i = 10^{-4}$, $\Delta P_i = 10$, $\Delta P = 0.1P_i$. Successive PDFs are displaced on the ordinate axis for clarity of the figure.

with $m = 3$ as expected [2]. In Fig. 5 we show the $\Delta\chi^2$ PDF obtained after 10^4 steps for different cases: first, setting $\Delta P_i^{\max}$ equal to the value calculated by the algorithm and, second, setting $\Delta P_i^{\max}$ equal to the initial guess, and finally to a value, calculated *a posteriori,* which is proportional to the best-fit parameters $\Delta P_i^{\max} = 0.1P_i$ (inset of Fig. 5)

As can be seen in Fig. 5, when $\Delta P_i^{\max}$ is set much higher than the optimal step sizes, the Metropolis algorithm scans the whole parameter space $\{P_i\}$, but jumping between disparate regions with very different values of χ^2, therefore with a low acceptance rate of new parameter sets (dashed line in Fig. 5). This causes a poor exploration of parameter space. In contrast, a small value overexplores only a restricted portion of $\{P_i\}$, falling very often in local minima of the parameter space (dotted line in the same figure). Also choosing parameter jumps proportional to the final parameters leads to a poor exploration of parameter space (solid line in the same figure). Finally, after the same number of steps, when using the optimized parameter step sizes obtained by the algorithm the χ^2 PDF follows the theoretical expectation, meaning that the parameter space is correctly sampled.

B. Fitting in a complex χ^2 landscape

As pointed out before, one of the main problems when dealing with data fitting using the LM algorithm is to find a proper set of initial parameters close enough to the global minimum of the $\chi^2\{P_i\}$ hypersurface. As an example we show in Fig. 6 the function $\sin(x/W)$ for $W = 5$ affected by a normal distributed error with $\sigma = 0.1$. In Fig. 7(a) we show the $\chi^2\{W\}$ landscape associated to the generated function. As can be seen, the $\chi^2\{W\}$ landscape for this function has a great number of local minima and a global minimum at $W = 5$. We have fitted the function using the LM algorithm and initializing the parameter at $W_i = 2$ and $W_i = 15$ (see Fig. 6). As expected, both fits were not able to find the global minimum that fits

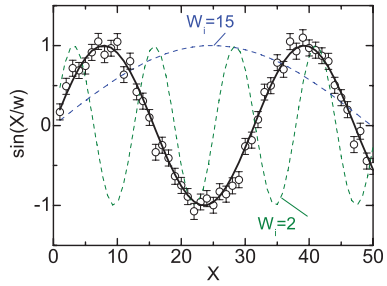

FIG. 6. (Color online) Synthetic $\sin(x/5)$ function (circles) together with the best fit using parameter step sizes tuning together with simulated annealing (line). Dashed lines are the fits using the LM algorithm with starting parameters $W_i = 2$ and $W_i = 15$.

the function. In fact, only if the LM algorithm is initialized between $W = 3.6$ and $W = 9.0$ is it able to succeed in fitting the data.

We now test the ability of our algorithm to jump across χ^2 barriers delimiting successive local minima to find the global one. For this task we have used the simulated annealing method, decreasing the temperature one decade every 3000 steps from $T = 1000$ to 1. The parameter jump calculation has been performed every $N = 1000$ steps. While the initial temperature allows to explore wide regions of the parameter space, the last temperature will let the acceptance be determined only by the real errors of the data.

In Fig. 7(b) we show the parameter W as a function of algorithm step for the two aforementioned initializations together with the χ^2 landscape (a). Parameter step sizes were initialized after a first run of optimization of 2000 steps. As can be seen in this figure, after 3000 steps both runs have already reached the absolute χ^2 minimum. Successive steps just relax the system to the final temperature $T = 1$.

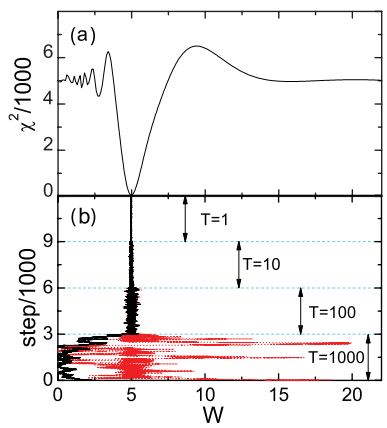

FIG. 7. (Color online) (a) $\chi^2\{W\}$ landscape obtained for the function $\sin(x/W)$ with a normal error associated of $\sigma = 0.1$ (see Fig. 6). (b) Algorithm steps for two different initializations, black solid line for $W_i = 2$ and red dashed line for $W_i = 15$, as a function of parameter W.

As it can be seen in Fig. 7, the way the minimum is reached depends on the parameter initialization. Parameter step sizes are larger for the run started with $W_i = 15$ with a flat local minimum. The contrary happens with the run initialized at $W_i = 2$, parameter step sizes are set small due to the narrow wells of the χ^2 landscape in this region. However, both runs are able to avoid getting stuck in local minima, jumping over rather high χ^2 barriers and successfully reaching the best fit.

IV. CONCLUSION

Classical fit schemes are known to fail when the parameters are not initialized close enough to the final solution. We have proposed in this work to use an Adaptive Markov Chain Monte Carlo Through Regeneration scheme, adapted from that of Gilks *et al.* [16], combined with a simulated annealing procedure to avoid this problem.

The proposed algorithm tunes the parameter step size in order to assure that all of them are accepted in the same proportion. Geometrically the parameter step size is set large when a cut of $\chi^2\{P_i\}$ along this parameter is flat, i.e., when the change of the $\chi^2\{P_i\}$ hypersurface along this parameter is sloppy. Similarly the parameter step size is set small if $\chi^2\{P_i\}$ wells are narrow.

Moreover, the step sizes can be modulated by a temperature added to the acceptance equation that makes jumps across χ^2 barriers easier, i.e., using a simulated annealing method [18]. From a geometric point of view, a high temperature makes the $\chi^2\{P_i\}$ wells artificially broader, smearing out details of local minima. This is important at the first stages of a fit process. At final stages of the fitting, temperature is decreased, making parameter jumps smaller, and thus allowing the system to relax, once it is inside the global minimum.

By fitting simulated data including statistical errors we verified that our algorithm actually fulfills the requirements of ergodicity (it converges to the target distribution), robustness (the ability to reach the χ^2 minimum independent of the choice of starting parameters), and ability to escape local minima and to explore efficiently the χ^2 landscape and guarantees that it will self-tune to converge to the global minimum avoiding an infinite search with large steps.

More complex problems have already successfully been studied with this algorithm such as model selection using quasielastic neutron-scattering data [25], nonfunctional fits in the case of dielectric spectroscopy [26], or finding the molecular structure from diffraction data with a model defined by as many as 27 parameters [27]. In the last case, the proper initialization of parameters to use a LM algorithm would have been a difficult task, made easy by the use of the presented algorithm.

ACKNOWLEDGMENTS

This work was supported by the Spanish Ministry of Science and Technology (FIS2008-00837) and by the Catalonia government (2009SGR-1251). We would also like to thank helpful comments and discussions on the manuscript made from K. Kretschmer, Anand Patil, Christopher Fonnesbeck, and A. Font.

[1] M. K. Transtrum, B. B. Machta, and J. P. Sethna, Phys. Rev. Lett. **104**, 060201 (2010).

[2] W. H. Press, S. A. Teukolsky, W. T. Vetterling, and B. P. Flannery, *Numerical Recipes in Fortran 77: The Art of Scientific Computing*, 2nd ed. (Cambridge University Press, Cambridge UK, 1992).

[3] T. Bayes, Philos. Trans. R. Soc. Lond. **53**, 370 (1764).

[4] D. Sivia, *Data Analysis—A Bayesian Tutorial* (Oxford University Press, Oxford, 2006).

[5] R. Trotta, Contemp. Phys. **49**, 71 (2008); J. P. Huelsenbeck, F. Ronquist, R. Nielsen, and J. P. Bollback, Science **294**, 2310 (2001); G. A. T. McVean, S. R. Myers, S. Hunt, P. Deloukas, D. R. Bentley, and P. Donnelly, *ibid.* **304**, 581 (2004); R. Diehl *et al.*, Astron. Astrophys. **449**, 1025 (2006); A. N. Naganathan, R. Perez-Jimenez, V. Muñoz, and J. M. Sanchez-Ruiz, Phys. Chem. Chem. Phys. **13**, 17064 (2011).

[6] J. J. Mortensen, K. Kaasbjerg, S. L. Frederiksen, J. K. Norskov, J. P. Sethna, and K. W. Jacobsen, Phys. Rev. Lett. **95**, 216401 (2005); F. J. Bermejo, J. Santoro, F. J. Mompean, and J. C. Dore, Nucl. Instrum. Meth. Phys. Res. B **34**, 505 (1988); S. Bacallado, J. D. Chodera, and V. Pande, J. Chem. Phys. **131**, 045106 (2009).

[7] D. Sivia, C. J. Carlile, and W. S. Howells, Physica B **182**, 341 (1992).

[8] R. L. McGreevy and L. Pusztai, Molec. Simul. **1**, 359 (1988); L. Pusztai, J. Non-Cryst. Sol. **227–230**, 88 (1998); R. L. McGreevy, J. Phys. Condens. Matter **13**, R877 (2001); G. Evrard and L. Pusztai, *ibid.* **17**, S1 (2005); O. Gereben, P. Jóvári, L. Temleitner, and L. Pusztai, J. Optoelectron Adv. M **9**, 3021 (2007).

[9] N. Metropolis, A. Rosenbluth, M. Rosenbluth, A. Teller, and E. Teller, J. Chem. Phys. **21**, 1087 (1953); W. K. Hastings, Biometrika **57**, 97 (1970).

[10] C. Andrieu and J. Thoms, Stat. Comput. **18**, 343 (2008).

[11] A. Benveniste, M. Métivier, and P. Priouret, *Adaptive Algorithms and Stochastic Approximations* (Springer, Berlin, 1990).

[12] V. S. Borkar, *Topics in Controlled Markov Chains* (Longman, Harlow, 1990).

[13] C. Andrieu, and C. P. Robert, Tech. Rep. 0125, Cahiers de Mathématiques du Ceremade, Université Paris-Dauphine (2001).

[14] H. Haario, E. Saksman, and J. Tammien, Bernouilli **7**, 223 (2001).

[15] A. Patil, D. Huard, and J. F. Christopher, J. Stat. Soft. **35**, 1 (2010).

[16] W. R. Gilks, G. O. Roberts, and S. K. Sahu, J. Am. Stat. Assoc. **93**, 1045 (1998).

[17] H. Robbins and S. Monro, Math. Stat. **22**, 400 (1951).

[18] S. Kirkpatrick, J. Stat. Phys. **34**, 347 (1984).

[19] J. J. Waterfall, F. P. Casey, R. N. Gutenkunst, K. S. Brown, C. R. Myers, P. W. Brouwer, V. Elser, and J. P. Sethna, Phys. Rev. Lett. **97**, 150601 (2006).

[20] FABADA program (Fit Algorithm for Bayesian Analysis of DAta) can be found at http//fisicaetseib.upc.es/gcm/members/lcpardo/software.

[21] L. C. Pardo, M. Rovira-Esteva, S. Busch, M. D. Ruiz-Martín, and J. Ll. Tamarit, in J. Phys.: Conf. Ser., Conference Proceeding of the Spanish Neutron Scattering Society Meeting 2010; L. C. Pardo, M. Rovira-Esteva, S. Busch, M. D. Ruiz-Martín, J. Ll. Tamarit, and T. Unruh, e-print arXiv:0907.3711.

[22] J. J. Mortensen, K. Kaasbjerg, S. L. Frederiksen, J. K. Nørskov, J. P. Sethna, and K. W. Jacobsen, Phys. Rev. Lett. **95**, 216401 (2005).

[23] J. S. Schulte, Phys. Rev. E **53**, R1348 (1996).

[24] P. G. Debenedetti and F. H. Stillinger, Nature (London) **410**, 259 (2001).

[25] M. Rovira-Esteva *et al.*, Phys. Rev. B **81**, 092202 (2010); S. Busch, C. Smuda, L. C. Pardo, and T. Unruh, J. Am. Chem. Soc. **132**, 3232 (2010).

[26] J. C. Martinez-Garcia, J. Ll. Tamarit, L. C. Pardo, M. Barrio, S. J. Rzoska, and A. Droz-Rzoska, J. Phys. Chem. B **114**, 6099 (2010).

[27] M. Rovira-Esteva, N. A. Murugan, L. C. Pardo, S. Busch, J. Ll. Tamarit, Sz. Pothoczki, G. J. Cuello, and F. J. Bermejo, Phys. Rev. B **84**, 064202 (2011).

Part III.

Additional Information

Appendix I.

Details of the Data Reduction

This chapter lists several programs that can be used for the data reduction. The one used in this thesis, Frida 1, will be introduced in more detail and all the errors in the program that were found during the course of this thesis are listed. A new data reduction program that was developed by the author of this thesis is advertised and the algorithm which is used for the reduction of quasielastic time-of-flight neutron scattering data is described. The chapter finishes with a presentation of the concept of an effective scattering cross section that can be used in conjunction with existing programs to make a zeroth-order correction of multiple scattering until a dedicated program for that purpose is available.

I.1. Data Reduction Software

Overview over Existing Programs. The standard data reduction and evaluation tool used at TOFTOF is the program Frida 1 [269]. It was started in 1990 by Wuttke, is written in Fortran and uses a proprietary library and compiler. These facts make it harder and harder to maintain and distribute it. Despite its age, it is however still used at several neutron sources and user groups around the world. It was even very recently ported to work with the Intel Fortran compiler.[1]

Although in use for over 20 years, there are still many errors in the algorithms. Most of them become visible only due to the high accuracy and versatility of today's instrumentation. As Frida 1 will probably stay the standard data reduction software on TOFTOF in the near future, a detailed list of bugs which were found during the course of this thesis is given below.

Most of the problems encountered during the data evaluation for this thesis could be solved within the existing program. However, taken together with the dated programming language, compiler, and libraries, it became clear that a completely other alternative must be found. In order to facilitate experiments on single crystals with TOFTOF, the software should also have additional capabilities, for example reading only the detectors in the horizontal scattering plane.

There are a few alternative programs which are potentially capable of reducing the time-of-flight data, the most important ones being

[1] Triggered by Gerald Schneider, Jülich Center for Neutron Science, 2011

- TOFSYS (Jülich) which has similar age-related problems as Frida 1. It has an interface to DISCUS, a multiple scattering simulation program.
- DATREAT (Jülich) is still in use, also at the JCNS, but suffers from similar problems than Frida 1 and TOFSYS.
- DAVE (NIST) has no read-in routine for TOFTOF data. Its features, especially regarding the data analysis, are limited so that it seems questionable if the implementation of a better interoperability is desirable.
- LAMP (ILL) can be used with TOFTOF data only since 2009.

In conclusion, none of the existing programs could fulfil the requirements at TOFTOF at the beginning of this thesis, LAMP should now be critically evaluated. This situation is common with many other neutron scattering instruments in the moment which triggered the start of development of two data reduction and analysis frameworks which are both in relatively early stages of development but aim both to become universal tools across institutes:

- The Mantid Project (initiated by ISIS, recently joined by the SNS and HFIR).
- slaw (JCNS, Joachim Wuttke) for data reduction, can be combined with e. g. Frida 2 (JCNS, Joachim Wuttke) for the data evaluation.

Although both of these projects are promising to offer a modern way of data reduction and analysis and one of them or both will probably become standard at TOFTOF at some point in the future, they are both not ready yet. As LAMP was not capable of working with TOFTOF data when this thesis was started, the data reduction procedures were implemented in a new program which can serve as a replacement for Frida 1 until a new standard is agreed on.

Errors in Frida 1. The following is a list of errors that were found during the course of this thesis. There is no central, updated version of the program but many different copies in different institutes which grew apart over time. It is therefore not possible to correct these mistakes in the copies at different institutes, every user of the program is urged to check if these errors are corrected in his or her version.

- The normalization to the incident beam monitor does not account for its wavelength-dependent sensitivity.
- The detector sensitivities are calibrated by the elastic scattering of a vanadium standard. For this purpose, the area under the elastic peak of the vanadium spectrum is integrated and stored in a variable that contained the maximum of the peak before. This value was used to detect bad detectors where the peak value or position deviates from the mean. If such a deviation is found, the detector is deleted and the procedure is restarted with an updated mean value. However, the variable that contained the peak maximum now contains the area.

- When reading the data from TOFTOF, the routine offers to subtract a background measurement right away. If the background signal happens to be stronger than the one of the sample, e. g. due to absorption, the data error bars are calculated too small by a factor 2.[2]

- The conversion of the time of flight of the neutrons to energy transfer necessarily assumes that the neutrons arrive during the same frame at which they started at the sample. If this is not the case, i. e. if the repetition rate is set so high that new neutrons start before the ones of the previous pulse arrive at the detectors, this conversion gives completely wrong results.

- For the determination of the position of the time channel of the arrival of the elastically scattered neutrons, the program searches the maximum of the arriving neutrons. If this maximum happens to be an inelastic feature (very hot samples), this point is assumed to correspond to zero energy transfer.[3]

- Even if inelastic features play no significant role, this mode of peak determination can be faulty. The conversion from time of flight to energy transfer involves multiplying the data with a factor t^{-3}, cf. section 4.1. If the peak is δ shaped, that does not shift its position. However, a broadened peak will not have the same maximum position for counts (time of flight), double differential cross section (energy transfer), or scattering function (energy transfer). It is therefore necessary to determine the time-of-flight of elastically scattered neutrons such that the maximum of the scattering function (taking the detailed balance into account) is at zero energy transfer.

- Adding spectra of detectors can cause uncontrollable shifts of the elastic peak position. If $S(Q, \omega)$ is produced, this error can be circumvented by not adding the spectra of different detectors before the conversion to Q and rebinning into slices of constant momentum transfer.

- If several detectors are at the same scattering angle (as it is the case at TOFTOF), it is not possible to normalize them by hand because the program tries to identify the detectors by their angle and does not rely on their order.

- That this cautionary measure has actually a justification becomes clear when trying to perform calculations involving one file loaded from TOFTOF and another one read in from the hard disk: Due to internal re-structuring of the data during the save and read process, this operation fails.

- The self absorption correction routine asks for the sum of coherent and incoherent scattering cross section. This is misleading as not the sum of the tabulated values of the scattering cross sections have to be used but the «effective scattering cross section» as described in detail in appendix I.3.

[2] This was not discovered by the author but by Jonas Okkels Birk, Niels Bohr Institute, Copenhagen.
[3] This was not discovered by the author.

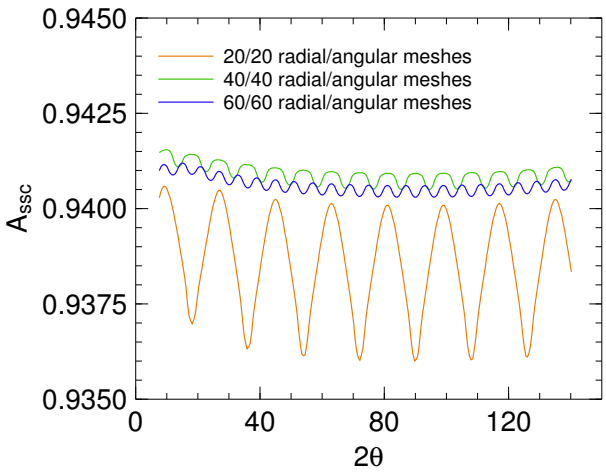

Figure I.1.: The factor calculated for the self absorption correction depends on the parameters chosen for the numerical calculation. The standard values 20/20 for the radial and angular meshes, respectively, show very big oscillations which gets smaller with an increasing number of meshes. Also the average value changes when changing the settings but in contrast to the oscillations it does not shift monotonously.

- The self absorption correction routine returns a result that has two problems which are a function of the choice supposedly only internal variables (number of radial and angular meshes). The first issue is the oscillation of the calculated value which decreases with increasing mesh numbers, the second the discontinuous shift of the absolute value by the choice of the meshes as demonstrated in figure I.1.

  Additionally to that, this routine regards all neutrons which are multiply scattered as not counted. However, these neutrons are counted, although not at the expected energy and momentum transfer. As the scattering cross sections of all the regarded samples are larger than the absorption cross sections, this effect is actually the more important one to correct but is not accounted for. The self absorption correction should therefore be replaced by a comprehensive treatment of absorption and multiple scattering.

- The transformation of the data from the recorded spectra at constant scattering angle to spectra at constant modulus of the scattering vector yields data error bars which are too large by approximately one order of magnitude.[4] This is already obvious when looking at the data because the statistical noise is much less than the error bar and prohibits any extractable information from the reduced χ^2.

- The Voigt function, the convolution of a Gaussian and a Lorentzian, is implemented using a tabulated function [270] but called wrongly, yielding wrong line width and area under the curve. Using the definitions

$$G(x) = \frac{1}{\sqrt{2\pi}\sigma} \cdot \exp\left[-\frac{1}{2}\left(\frac{x-c}{\sigma}\right)^2\right] \tag{I.1}$$

  and

$$L(x) = \frac{1}{\pi} \cdot \frac{\Gamma}{(x-c)^2 + \Gamma^2} \ , \tag{I.2}$$

[4]This was not discovered by the author but by Björn Fåk, CEA INAC SPSMS, Grenoble

their convolution is approximated using the tabulated function $K(a, b)$ [270]:

$$(G \otimes L)(x) = \frac{1}{\sqrt{2\pi} \cdot \sigma} \cdot K(a, b) \tag{I.3}$$

where a and b have to be

$$a = \frac{x - c}{\sqrt{2}\sigma} \qquad \text{and} \qquad b = \frac{\Gamma}{\sqrt{2}\sigma} \ . \tag{I.4}$$

The resulting function fulfills the checks to have (i) an area of 1 (within 1%) and (ii) a full width at half maximum of 3.6 with the following combinations of (σ, Γ): $(0, 1.8)$, $(0.01, 1.8)$, $(1.0, 1.0)$, $(1.3, 0.5)$, $(1.53, 0.01)$, $(1.53, 0)$.

- Plotting functions that are convolved online with a vanadium measurement as resolution function have sometimes wild oscillations which is obviously wrong. However, also when looking reasonable, they are often wrong, in all observed cases being plotted too low. This does not occur when the convolution is performed explicitly.

- The error bars of the fitted parameters can be corrected for correlations between the parameters by diagonalizing the covariance matrix. This is attempted but the output of the corresponding routine is processed wrongly, multiplying with the double of the reduced χ^2 which the routine does already. As the reduced χ^2 is too small due to the wrong data error bars (see above), the parameter error bars are calculated too small.

- When calculating the average value of N values y_i with error bars Δy_i, the average value $\bar{y}$ is calculated correctly as

$$\bar{y} = \sum_{i=1}^{N} \frac{y_i}{N} \tag{I.5}$$

but the error bar of the averaged value $\Delta\bar{y}$ is calculated as[5]

$$\Delta\bar{y} = \sqrt{\sum_{i=1}^{N} \frac{\Delta y_i^2}{N}} \tag{I.6}$$

instead of

$$\Delta\bar{y} = \frac{\sqrt{\sum_{i=1}^{N} \Delta y_i^2}}{N} \ . \tag{I.7}$$

[5]This was discovered in collaboration with Humphrey Morhenn, FRM II, Technische Universität München, Munich

The new neutron time-of-flight scattering data reduction library *sihl*. An object-oriented library for the data reduction of time-of-flight neutron scattering data, named *sihl* [271], has been implemented in *Python 2.5* based on the packages *scipy* [272], the also self-written *chaste* [273], and optionally *matplotlib* [274]. Whereas the scipy and matplotlib are standard Python libraries, *chaste* is a self-written collection of tools to handle data with error bars, it makes for example sure that the error bars are correctly propagated during addition etc.

chaste introduces a general class for variables, `Var`, that is the parent for the five types of variables that can be found in a typical experiment: `AddVar` is normally the dependent variable of a measurement that must be e. g. be added when adding different measurements, propagating the error bar. `EquVar` is normally the independent variable of the measurement – in order to add two measurements, these values must be equal. Apart from these, there are values like the temperature that must be averaged when two measurements are added, `AvgVar`, values that can exist only once like the name or starting time, `WinVar`, and a history of data manipulations in a `LogVar`.

Most experiments are performed in a series of varying x and measuring the corresponding y values. Such a series can have a further independent variable, called z. It is represented in the `Dataset` class which in turn can be combined with other `Datasets` into measurements of y as a function of x and z in the class `Data`.

sihl is the specialization of these concepts for neutron scattering measurements. While a `Detector` inherits from `Dataset` as it contains for example counts as a function of time-of-flight, the result of many `Detectors` is combined in a `Measurement` which correspondingly inherits from `Data`.

A `Measurement` contains algorithms needed at all spectrometers, for example normalization to the monitor counts. This is then further specialized in `TofMeasurement` which inherits from `Measurement` and adds time-of-flight specific capabilities, for example the conversion from time-of-flight to energy transfer. `ToftofMeasurement` inherits from `TofMeasurement`, adding `TOFTOF` specifics, for example reading the `TOFTOF` data file format.

These packages are now ready for active use and are already employed for data treatment in the soft matter group at `TOFTOF`. However, the measurements presented in this thesis were still reduced with the old Frida 1.

I.2. Data Reduction Procedure

In any data reduction program, a certain procedure is followed which varies only slightly between the different programs. In the following, the procedure implemented in sihl is described in detail.

Basic operations on all TOFTOF measurements.

- One measurement is often distributed over several files. Read all TOFTOF data files that contain the measurement. Take the sum of the counts of the different files – as if a single long measurement would have been performed.
- Delete the signal of detectors which are not installed.
- For powder samples: take the absolute value of the scattering angle.
- Sort the detectors by increasing scattering angle.
- Set error bars for all detectors and the monitor to the square root of the number of counts in the respective detector – if no neutron was counted, set the error bar to 1. It should be noted that the use of Gaussian statistics is in this case is not justified [G]. Luckily, the signals that are evaluated in practice are much stronger because using Poisson statistics would not only complicate the error propagation very much but would also require different approaches to fitting the data [G].
- Divide the counts in the detectors by the one in the monitor, propagating the error bar and respecting the wavelength-dependence of the monitor efficiency.
- Delete all channels in the frame which are empty, as described in section 3.2.
- Multiply the last channel which was only partially filled to get a measure for the number of neutrons it would have seen if the instrument had filled it the same time as the others. This procedure has the advantage over deleting this channel when channels are moved from one end of the frame to the other that there is no gap between two channels.
- If the time-of-flight of the elastically scattered neutrons is longer than the total length of the frame, add the total number of channels in the frame to each frame number until the elastic peak is within the frame.
- Convert the channel numbers to time-of-flight by multiplying the channel number with the length of one channel (which is given by the instrument in units of 50 ns).
- It is practical to avoid that the first channel has a time-of-flight of zero because this translates into an infinitely large energy. Therefore, the first couple of channels are moved to the end of the frame.
- Convert the time-of-flight tof to energy transfer dE. Using the length of the secondary spectrometer $l = 4\,\mathrm{m}$, the tof-axis is changed according to

$$\mathrm{d}E = E_f - E_i = \frac{1}{2} m_n \frac{l^2}{\mathrm{tof}^2} - \frac{1}{2} m_n \frac{l^2}{\mathrm{tof(elastic)}^2} \quad . \tag{I.8}$$

Because the scattering function is a density in energy (as discussed in section 2.1, this can be seen on the unit which is energy^{-1}), the intensity axis has to be changed with

$$\frac{\mathrm{d}^2\sigma}{\mathrm{d}\Omega\,\mathrm{d}E} = \frac{\mathrm{d}^2\sigma}{\mathrm{d}\Omega\,\mathrm{dtof}} \cdot \frac{\mathrm{dtof}}{\mathrm{d}E} \tag{I.9}$$

and

$$\frac{\mathrm{d}E}{\mathrm{dtof}} = \frac{m_n l^2}{\mathrm{tof}^3} \quad . \tag{I.10}$$

- Sort the channels by increasing energy transfer.
- Correct the energy-dependence of the detector efficiency using the formula and TOFTOF-specific parameters [211].
- Optional: Apply the detailed balance correction.
- Optional: Subtract the scattering of the container.

At this point, the double differential cross section $\mathrm{d}^2\sigma/\mathrm{d}(2\theta)\,\mathrm{d}E$ would be obtained if the detectors were calibrated on an absolute scale. They are not, making the normalisation to an isotropic scatterer, often vanadium, necessary.

Correcting the detector sensitivities.

- Read the vanadium data and treat as described above.
- Integrate the elastic line, correct this number with the Q-dependent Debye-Waller factor and save it per detector. Alternatively, it is possible to integrate the intensity scattered at the same Q over all E. However, in this case the intensity that is scattered into the theoretically accessible but practically uncovered dynamical range (cf. figure 3.9) is lost.
- Normalize the detector sensitivity by dividing the spectrum of every detector by this number.

The result is the double differential cross section $\mathrm{d}^2\sigma/\mathrm{d}(2\theta)\,\mathrm{d}E$ up to a scaling factor due to the normalization to the vanadium standard.

Option 1: Calculating the diffraction pattern.

- Integrate the double differential cross section over all energies, resulting in the differential cross section $\mathrm{d}\sigma/\mathrm{d}\Omega(2\theta)$ up to the aforementioned scaling factor.

This diffraction pattern is very similar to the differential cross section $\mathrm{d}\sigma/\mathrm{d}\Omega$ that is measured at dedicated diffractometers which do not analyze the energy of the neutrons after the scattering event. When measured at a diffractometer, *Plazcek corrections* can be used to account for the energy-dependent sensitivity of the detectors [160] – this effect is already corrected in the TOFTOF data as described above.

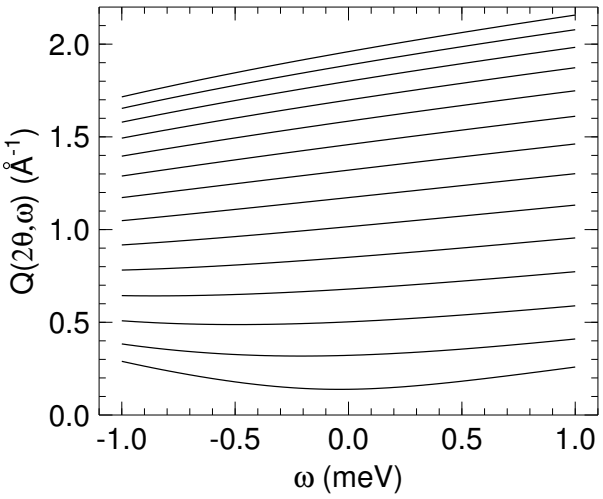

Figure I.2.: The trajectory of detectors at TOFTOF in Q-ω-space, using an incident wavelength of 6 Å. Shown are representative detectors with an equidistant spacing of 10° starting at the first detector which has a scattering angle of 7.6°. The energy transfer is shown in the quasi-elastic region of ±1 meV. The compression at large values of Q brings about that the angular range between 140° and 180° corresponds only to a relatively small area in Q-ω-space. This is also visible in figure 3.9 which gives a bigger overview of the dynamical range.

What is not corrected is the Lorentz factor – because it is different for coherent and incoherent scattering. The corresponding signals would need to be separated before this correction. The reason is that incoherent scattering results in equal intensity in equal $\mathrm{d}\Omega$. Because all detectors have the same size and are at the same distance $l = 4\,\mathrm{m}$ from the sample, no correction factor is needed. Coherent scattering of powder samples is distributed on Debye-Scherrer cones and therefore on different lengths U depending on the scattering angle 2θ:

$$U = 2\pi r = 2\pi l \sin(2\theta) \ . \tag{I.11}$$

The coherent scattering signal would need to be divided by this number. As the intensities of the Bragg peaks are not evaluated, this correction was not performed.

It can be seen in figure I.2 that this integration of intensities at a fixed scattering angle 2θ does not integrate intensities at a fixed Q. The transformation from the obtained $\mathrm{d}\sigma/\mathrm{d}\Omega(2\theta)$ via the Bragg equation

$$Q = \frac{4\pi}{\lambda} \sin\left(\frac{2\theta}{2}\right) \tag{I.12}$$

to an $\mathrm{d}\sigma/\mathrm{d}\Omega(Q)$ is therefore not correct. This was nevertheless done in this thesis because the resulting errors are expected to be very small and the scattering angle is not a physically meaningful axis.

Alternatively, one could perform a proper transformation of the double differential cross section from scattering angle to Q as shown below and integrate then. This procedure has however the drawback that intensity is lost which is scattered into regions of the dynamical range which are accessible theoretically but not experimentally, cf. figure 3.9.

Option 2: Calculating the scattering function.

- Convert the double differential cross section to the scattering function by multiplying the double differential cross section with k_i/k_f. This conversion is correct up to an overall scaling factor which contains the scattering cross sections of the vanadium and the sample.

- Convert the scattering angle 2θ to the modulus of the scattering vector Q using

$$Q = \sqrt{\frac{2m_n}{\hbar^2}\left(E_i - 2\sqrt{E_i E_f}\cdot\cos(2\theta) + E_f\right)} \quad . \tag{I.13}$$

  The corresponding trajectories of the detectors at constant 2θ after the transformation to Q are shown in figure I.2. A rescaling of the intensity axis is in this case not necessary because the scattering function is not a density in Q but a normal function. This is expressed in the unit, $[S(Q,\omega)] = \text{energy}^{-1}$: It is a density in the energy transfer but not in the momentum transfer, cf. section 2.1.

- In order to facilitate the comparison between theory and data, rebin into slices of constant Q. Stop at energy transfers when not the whole Q range is covered by the dynamical range any more. As can be seen in figure I.2, this happens at small Q (negative and positive energy transfer) as well as at large Q (negative energy transfer).

I.3. Effective Scattering Cross Section

The algorithm of Paalman and Pings [221] to correct the absorption or multiple scattering of neutrons on their way through the sample requires the scattering cross sections of the sample. It will be recalled in the following that this scattering cross section is not necessarily one of the tabulated values [189]. While a thorough correction of these effects requires the full scattering function of the sample as input, a simple way will be demonstrated that can be used to get an approximation of the *effective scattering cross section*. This value is introduced as the integrated differential cross section, i. e. as the probability that a neutron is scattered in the sample.

The need for an effective scattering cross section can be easily seen at the example of aluminium which has $\sigma_{\text{coh}} = 1.495$ barn, $\sigma_{\text{inc}} = 0.0082$ barn, and $\sigma_{\text{abs}} = 0.231$ barn. The coherent cross section dominates by far and yields a substantial scattering power. However, given the crystal structure of aluminium (fcc) with a lattice spacing of $a = 4.05$ Å [275], the coherent cross section has to be taken into account *only* if the wavelength is equal or shorter than necessary to reach $Q = 3.10$ Å^{-1}, $\lambda = 4\pi/Q \leqslant 4.05$ Å. Similarly holds for vanadium (bcc, $a = 3.02$ Å) with the cross sections $\sigma_{\text{coh}} = 0.0184$ barn, $\sigma_{\text{inc}} = 5.08$ barn, and $\sigma_{\text{abs}} = 5.08$ barn that there is no coherent scattering before $Q = 2.94$ Å^{-1}.

In fact, even when there is no coherent scattering, the effective scattering cross section cannot be simply calculated as the sum of the tabulated scattering cross sections if the sample contains several isotopes or elements due to the mixing of the nuclei. It would be possible to calculate the contributions of coherent and incoherent scattering using the scattering lengths of the nuclei and taking the structure of the molecules into account.

However, there is also a simpler approach that approximates the effective scattering cross section, assuming that not much intensity is lost into regions of Q-ω-space that are kinematically accessible but not covered by the spectrometer's detectors (cf. figure 3.9). The vanadium standard is better known than the samples, it scatters incoherently with

5.08 barn. The level of this incoherent scattering in the differential cross section can therefore be used to get the reference of 5.08 barn, provided that self absorption and multiple scattering are corrected. This knowledge can be used to calibrate the differential cross sections of the measured samples in absolute units and to obtain their effective scattering cross section by integrating over all scattering angles.

This simple approximation allows to determine the probability that a neutron is scattered in the sample without any knowledge of its composition or fractions of coherent or incoherent scattering. It can be used for a basic correction of the data of the samples for absorption and multiple scattering effects. This correction is based on the assumption that also the neutrons which are scattered again are effectively absorbed and do not reach a detector. Therefore, as stated above, a full treatment of multiple scattering effects based on a physical model of the scattering function would be preferable. Such a treatment will be available soon.[6]

[6] Joachim Wuttke, JCNS

Bibliography

[1] Sebastian Busch, Christoph Smuda, Luis Carlos Pardo, and Tobias Unruh. Molecular mechanism of long-range diffusion in phospholipid membranes studied by quasielastic neutron scattering. *Journal of the American Chemical Society*, 132 (10):3232, 2010. doi: 10.1021/ja907581s. Included as appendix in this thesis.

[2] Wolfgang Doster, Sebastian Busch, Ana M. Gaspar, Marie-Sousai Appavou, Joachim Wuttke, and Hugo Scheer. Dynamical transition of protein-hydration water. *Physical Review Letters*, 104(9):098101, 2010. doi: 10.1103/PhysRevLett.104.098101. URL `http://arxiv.org/abs/0911.5033`. Included as appendix in this thesis.

[3] Sebastian Busch and Tobias Unruh. The slow short-time motions of phospholipid molecules with a focus on the influence of multiple scattering and fitting artifacts. *Journal of Physics: Condensed Matter*, 23(25):254205, 2011. doi: 10.1088/0953-8984/23/25/254205. URL `http://arxiv.org/abs/1103.4336`. Included as appendix in this thesis.

[4] Sebastian Busch and Tobias Unruh. The influence of additives on the nanoscopic dynamics of the phospholipid dimyristoylphosphatidylcholine. *Biochimica et Biophysica Acta (BBA) – Biomembranes*, 1808(1):199–208, 2011. doi: 10.1016/j.bbamem.2010.10.012. URL `http://mediatum.ub.tum.de/node?id=1006911`. Included as appendix in this thesis.

[5] Sebastian Busch, Luis Carlos Pardo, Christoph Smuda, and Tobias Unruh. The picosecond dynamics of the phospholipid dimyristoylphosphatidylcholine in mono- and bilayers. *Soft Matter*, 8:3576, 2012. doi: 10.1039/c2sm07380c. Included as appendix in this thesis.

[6] Luis Carlos Pardo, Muriel Rovira-Esteva, Sebastian Busch, María Dolores Ruiz-Martín, and Josep Lluis Tamarit. FABADA: a Fitting Algorithm for Bayesian Analysis of DAta. *Journal of Physics: Conference Series*, 325(1):012006, 2011. doi: 10.1088/1742-6596/325/1/012006. Included as appendix in this thesis.

[7] Luis Carlos Pardo, Muriel Rovira-Esteva, Sebastian Busch, Jean-François Moulin, and Josep Lluis Tamarit. Fitting in a complex χ^2 landscape using an optimized hypersurface sampling. *Physical Review E*, 84(4):046711, 2011. doi: 10.1103/PhysRevE.84.046711. Included as appendix in this thesis.

[8] W. Hoppe, W. Lohmann, H. Markl, and H. Ziegler, editors. *Biophysik (German Edition)*. Springer, 2 edition, 1982. ISBN 9783540113355. Cited on pages 4, 29, and 30.

[9] Gregor Cevc, editor. *Phospholipids Handbook*. CRC, 1 edition, 1993. ISBN 9780824790509. Cited on pages 4, 13, 30, and 68.

[10] Erich Sackmann and Rudolf Merkel. *Lehrbuch der Biophysik (German Edition)*. Wiley-VCH, 2010. ISBN 9783527405350. Cited on pages 4, 5, and 78.

[11] Juan M. Vanegas, Marjorie L. Longo, and Roland Faller. Crystalline, ordered and disordered lipid membranes: Convergence of stress profiles due to ergosterol. *Journal of the American Chemical Society*, 133(11):3720–3723, 2011. doi: 10.1021/ja110327r. Cited on pages 5, 12, and 67.

[12] Jean-François Tocanne, Laurence Dupou-Cézanne, and André Lopez. Lateral diffusion of lipids in model and natural membranes. *Progress in Lipid Research*, 33(3):203, 1994. doi: 10.1016/0163-7827(94)90027-2. Cited on page 5.

[13] E Gorter and F Grendel. On bimolecular layers of lipoids on the chromocytes of the blood. *Journal of Experimental Medicine*, 41(4):439, 1925. doi: 10.1084/jem.41.4.439. Cited on page 5.

[14] Robert A Freitas, Jr. *Nanomedicine, Vol. I: Basic Capabilities*. Landes Bioscience, 1 edition, 1999. ISBN 9781570596803. Cited on page 5.

[15] Bruce Alberts, Alexander Johnson, Julian Lewis, Martin Raff, Keith Roberts, and Peter Walter. *Molecular Biology of the Cell*. Taylor & Francis Group, fifth edition, 2007. ISBN 978-0-8153-4105-5. Cited on page 5.

[16] S. J. Singer and G. L. Nicolson. The fluid mosaic model of the structure of cell membranes. *Science*, 175(4023):720, 1972. doi: 10.1126/science.175.4023.720. Cited on page 6.

[17] Donald M Engelman. Membranes are more mosaic than fluid. *Nature*, 438(7068): 578–80, 2005. doi: 10.1038/nature04394. Cited on page 6.

[18] S Ramadurai, A Holt, V Krasnikov, G van den Bogaart, JA Killian, and B Poolman. Lateral diffusion of membrane proteins. *J. Am. Chem. Soc.*, 131(35):12650–6, 2009. doi: 10.1021/ja902853g. Cited on page 6.

[19] Daniel Axelrod. Lateral motion of membrane proteins and biological function. *The Journal of Membrane Biology*, 75(1):1, 1983. doi: 10.1007/bf01870794. Cited on page 6.

[20] Perttu S Niemelä, Markus S. Miettinen, Luca Monticelli, Henrik Hammaren, Pär Bjelkmar, Teemu Murtola, Erik Lindahl, and Ilpo Vattulainen. Membrane proteins diffuse as dynamic complexes with lipids. *Journal of the American Chemical Society*, 132(22):7574–5, 2010. doi: 10.1021/ja101481b. Cited on page 6.

[21] Gerardo Aquino and Robert Endres. Increased accuracy of ligand sensing by receptor diffusion on cell surface. *Physical Review E*, 82(4):041902, 2010. doi: 10.1103/physreve.82.041902. Cited on page 6.

[22] Emma Leah. Cholesterol. *Lipidomics Gateway*, 2009. doi: 10.1038/lipidmaps.2009.3. Cited on page 6.

[23] K Simons and E Ikonen. Functional rafts in cell membranes. *Nature*, 387(6633): 569–72, 1997. doi: 10.1038/42408. Cited on page 6.

[24] Rodrigo F M de Almeida, Luís M S Loura, Alexander Fedorov, and Manuel Prieto. Lipid rafts have different sizes depending on membrane composition: a time-resolved fluorescence resonance energy transfer study. *J. Mol. Biol.*, 346(4): 1109–20, 2005. doi: 10.1016/j.jmb.2004.12.026. Cited on page 6.

[25] Akihiro Kusumi and Yasushi Sako. Cell surface organization by the membrane skeleton. *Current Opinion in Cell Biology*, 8(4):566, 1996. doi: 10.1016/s0955-0674(96)80036-6. Cited on page 6.

[26] T Betz, M Lenz, JF Joanny, and C Sykes. ATP-dependent mechanics of red blood cells. *Proc. Natl. Acad. Sci. U.S.A.*, 2009. doi: 10.1073/pnas.0904614106. Cited on page 6.

[27] Michael Schneider. Phospholipids for functional food. *European Journal of Lipid Science and Technology*, 103(2):98, 2001. doi: 10.1002/1438-9312(200102)103:2<98::aid-ejlt98>3.0.co;2-g. Cited on page 6.

[28] Laurent Sagalowicz and Martin E. Leser. Delivery systems for liquid food products. *Current Opinion in Colloid & Interface Science*, 15(1-2):61, 2010. doi: 10.1016/j.cocis.2009.12.003. Cited on page 6.

[29] Fude Cui, Kai Shi, Liqiang Zhang, Anjin Tao, and Yoshiaki Kawashima. Biodegradable nanoparticles loaded with insulin-phospholipid complex for oral delivery: Preparation, in vitro characterization and in vivo evaluation. *Journal of Controlled Release*, 114(2):242–250, 2006. doi: 10.1016/j.jconrel.2006.05.013. Cited on page 6.

[30] David Julian McClements and Yan Li. Structured emulsion-based delivery systems: Controlling the digestion and release of lipophilic food components. *Advances in Colloid and Interface Science*, 159(2):213–228, 2010. doi: 10.1016/j.cis.2010.06.010. Cited on page 6.

[31] Gert Fricker, Torsten Kromp, Armin Wendel, Alfred Blume, Jürgen Zirkel, Herbert Rebmann, Constanze Setzer, Ralf-Olaf Quinkert, Frank Martin, and Christel Müller-Goymann. Phospholipids and lipid-based formulations in oral drug delivery. *Pharm. Res.*, 27(8):1469–86, 2010. doi: 10.1007/s11095-010-0130-x. Cited on page 6.

[32] Renata Negrini and Raffaele Mezzenga. pH-responsive lyotropic liquid crystals for controlled drug delivery. *Langmuir : the ACS journal of surfaces and colloids*, 2011. doi: 10.1021/la200591u. Cited on page 6.

[33] Amit K Jain, Nitin K Swarnakar, Manasmita Das, Chandraiah Godugu, Raman Preet Singh, Poduri Rama Rao, and Sanyog Jain. Augmented anticancer efficacy of doxorubicin-loaded polymeric nanoparticles after oral administration in a breast cancer induced animal model. *Molecular pharmaceutics*, 2011. doi: 10.1021/mp200011f. Cited on page 6.

[34] Mei-Chin Chen, Kiran Sonaje, Ko-Jie Chen, and Hsing-Wen Sung. A review of the prospects for polymeric nanoparticle platforms in oral insulin delivery. *Biomaterials*, 2011. doi: 10.1016/j.biomaterials.2011.08.087. Cited on page 6.

[35] Shahid Rameez and Andre F Palmer. Simple method for preparing poly(ethylene glycol)-surface-conjugated liposome-encapsulated hemoglobins: Physicochemical properties, long-term storage stability, and their reactions with O_2, CO, and NO. *Langmuir : the ACS journal of surfaces and colloids*, 2011. doi: 10.1021/la201246m. Cited on page 7.

[36] Jolanda M van den Hoven, Sophie R van Tomme, Josbert M Metselaar, Bastiaan Nuijen, Jos H Beijnen, and Gert Storm. Liposomal drug formulations in the treatment of rheumatoid arthritis. *Molecular pharmaceutics*, 2011. doi: 10.1021/mp2000742. Cited on page 7.

[37] Elina Mamasheva, Christi O'Donnell, Amey Bandekar, and Stavroula Sofou. Heterogeneous liposome membranes with ph-triggered permeability enhance the in vitro antitumor activity of folate-receptor targeted liposomal doxorubicin. *Molecular pharmaceutics*, 2011. doi: 10.1021/mp200079y. Cited on page 7.

[38] Mangesh Kulkarni, Udo Greiser, Timothy O'Brien, and Abhay Pandit. A temporal gene delivery system based on fibrin microspheres. *Molecular pharmaceutics*, 2010. doi: 10.1021/mp100295z. Cited on page 7.

[39] J. M. Gutiérrez, C González, A Maestro, I Solè, C M Pey, and J Nolla. Nanoemulsions: New applications and optimization of their preparation. *Current Opinion in Colloid & Interface Science*, 13(4):245, 2008. doi: 10.1016/j.cocis.2008.01.005. Cited on page 7.

[40] Heike Bunjes. Structural properties of solid lipid based colloidal drug delivery systems. *Current Opinion in Colloid & Interface Science*, 2011. doi: 10.1016/j.cocis.2011.06.007. Cited on page 7.

[41] Susana Martins, Bruno Sarmento, Domingos C Ferreira, and Eliana B Souto. Lipid-based colloidal carriers for peptide and protein delivery–liposomes versus lipid nanoparticles. *International Journal of Nanomedicine*, 2(4):595–607, 2007. Cited on page 7.

[42] Markus Thommes, David Richard Ely, Maria Teresa Carvajal, and Rodolfo Pinal. Improvement of the dissolution rate of poorly soluble drugs by solid crystal suspensions. *Molecular pharmaceutics*, 2011. doi: 10.1021/mp1003493. Cited on page 7.

[43] Rohan V. Tikekar and N. Nitin. Effect of physical state (solid vs. liquid) of lipid core on the rate of transport of oxygen and free radicals in solid lipid nanoparticles and emulsion. *Soft Matter*, 7(18):8149, 2011. doi: 10.1039/c1sm05031a. Cited on page 7.

[44] Roberto Solaro, Federica Chiellini, and Antonella Battisti. Targeted delivery of protein drugs by nanocarriers. *Materials*, 3(3):1928, 2010. doi: 10.3390/ma3031928. Cited on pages 7 and 32.

[45] Guolin Li, Jinyao Liu, Yan Pang, Ruibin Wang, Limin Mao, Deyue Yan, Xinyuan Zhu, and Jian Sun. Polymeric micelles with water-insoluble drug as hydrophobic moiety for drug delivery. *Biomacromolecules*, 2011. doi: 10.1021/bm200372s. Cited on page 7.

[46] Jinyao Liu, Yan Pang, Wei Huang, Xiaohua Huang, Lili Meng, Xinyuan Zhu, Yongfeng Zhou, and Deyue Yan. Bioreducible micelles self-assembled from amphiphilic hyperbranched multiarm copolymer for glutathione-mediated intracellular drug delivery. *Biomacromolecules*, 2011. doi: 10.1021/bm200275j. Cited on page 7.

[47] Maheshika Kuruppuarachchi, Huguette Savoie, Ann Lowry, Cristina Alonso, and Ross W Boyle. Polyacrylamide nanoparticles as a delivery system in photodynamic therapy. *Molecular pharmaceutics*, 2011. doi: 10.1021/mp200023y. Cited on page 7.

[48] Valentina Cauda, Hanna Engelke, Anna Sauer, Delphine Arcizet, Christoph Bräuchle, Joachim O Rädler, and Thomas Bein. Colchicine-loaded lipid bilayer-coated 50 nm mesoporous nanoparticles efficiently induce microtubule depolymerization upon cell uptake. *Nano Lett.*, 10(7):2484–92, 2010. doi: 10.1021/nl100991w. Cited on page 7.

[49] Axel Schlossbauer, Simon Warncke, Philipp M E Gramlich, Johann Kecht, Antonio Manetto, Thomas Carell, and Thomas Bein. A programmable DNA-based molecular valve for colloidal mesoporous silica. *Angewandte Chemie (International ed. in English)*, 49(28):4734–4737, 2010. doi: 10.1002/anie.201000827. Cited on page 7.

[50] Rizwan Shukat and Perla Relkin. Lipid nanoparticles as vitamin matrix carriers in liquid food systems: on the role of high-pressure homogenisation, droplet size and adsorbed materials. *Colloids and Surfaces B: Biointerfaces*, 86(1):119–124, 2011. doi: 10.1016/j.colsurfb.2011.03.028. Cited on page 8.

[51] Amelia Torcello-Gómez, Julia Maldonado-Valderrama, Antonio Martín-Rodríguez, and David Julian McClements. Physicochemical properties and digestibility of emulsified lipids in simulated intestinal fluids: influence of interfacial characteristics. *Soft Matter*, 2011. doi: 10.1039/c1sm05322a. Cited on page 8.

[52] Che-Ming J Hu, Li Zhang, Santosh Aryal, Connie Cheung, Ronnie H Fang, and Liangfang Zhang. Erythrocyte membrane-camouflaged polymeric nanoparticles as a biomimetic delivery platform. *Proceedings of the National Academy of Sciences of the United States of America*, 2011. doi: 10.1073/pnas.1106634108. Cited on page 8.

[53] P. Pattekari, Z. Zheng, X. Zhang, T. Levchenko, V. Torchilin, and Y. Lvov. Top-down and bottom-up approaches in production of aqueous nanocolloids of low solubility drug paclitaxel. *Physical Chemistry Chemical Physics*, 2011. doi: 10.1039/c0cp02549f. Cited on page 8.

[54] M Wickham. A physicochemical investigation of two phosphatidylcholine/bile salt interfaces: implications for lipase activation. *Biochimica et Biophysica Acta (BBA) - Molecular and Cell Biology of Lipids*, 1580(2-3):110, 2002. doi: 10.1016/s1388-1981(01)00196-2. Cited on page 8.

[55] Kirsten Westesen and Britta Siekmann. Biodegradable colloidal drug carrier systems based on solid lipids. In Simon Benita, editor, *Microencapsulation (Drugs and the Pharmaceutical Sciences)*. Informa Healthcare, 1 edition, 1996. ISBN 9780824797034. Cited on pages 8, 15, and 72.

[56] Kirsten Westesen and Britta Siekmann. Investigation of the gel formation of phospholipid-stabilized solid lipid nanoparticles. *International Journal of Pharmaceutics*, 151(1):35, 1997. doi: 10.1016/s0378-5173(97)04890-4. Cited on pages 8, 15, and 72.

[57] Carlee E. Ashley, Eric C. Carnes, Genevieve K. Phillips, David Padilla, Paul N. Durfee, Page A. Brown, Tracey N. Hanna, Juewen Liu, Brandy Phillips, Mark B. Carter, Nick J. Carroll, Xingmao Jiang, Darren R. Dunphy, Cheryl L. Willman, Dimiter N. Petsev, Deborah G. Evans, Atul N. Parikh, Bryce Chackerian, Walker Wharton, David S. Peabody, and C. Jeffrey Brinker. The targeted delivery of multicomponent cargos to cancer cells by nanoporous particle-supported lipid bilayers. *Nature Materials*, 2011. doi: 10.1038/nmat2992. Cited on page 8.

[58] Darrell J. Irvine. Drug delivery: One nanoparticle, one kill. *Nature Materials*, 2011. doi: 10.1038/nmat3014. Cited on page 8.

[59] Himanish Basu, Aditya K. Dharmadhikari, Jayashree A. Dharmadhikari, Shobhona Sharma, and Deepak Mathur. Tank treading of optically trapped red blood cells in shear flow. *Biophysical Journal*, 101(7):1604–1612, 2011. doi: 10.1016/j.bpj.2011.08.043. Cited on page 8.

[60] P G Debenedetti and F H Stillinger. Supercooled liquids and the glass transition. *Nature*, 410(6825):259–67, 2001. doi: 10.1038/35065704. Cited on pages 8 and 11.

[61] Luca Cipelletti and Laurence Ramos. Slow dynamics in glassy soft matter. *Journal of Physics: Condensed Matter*, 17(6):R253, 2005. doi: 10.1088/0953-8984/17/6/r01. Cited on page 8.

[62] Christine Semmrich, Tobias Storz, Jens Glaser, Rudolf Merkel, Andreas R. Bausch, and Klaus Kroy. Glass transition and rheological redundancy in f-actin solutions. *Proc. Natl. Acad. Sci. U.S.A.*, 104(51):20199–203, 2007. doi: 10.1073/pnas.0705513104. Cited on page 8.

[63] Elijah Flenner, Jhuma Das, Maikel C Rheinstädter, and Ioan Kosztin. Subdiffusion and lateral diffusion coefficient of lipid atoms and molecules in phospholipid bilayers. *Physical Review E*, 79(1):011907, 2009. doi: 10.1103/physreve.79.011907. URL `http://arxiv.org/abs/0809.2986`. Cited on pages 8, 9, and 67.

[64] Joachim Wuttke. Fast relaxation in viscous liquids. In Bernhard Kramer, editor, *Advances in Solid State Physics 40*, volume 40 of *Advances in Solid State Physics*, page 481. Springer Berlin / Heidelberg, 2000. doi: 10.1007/bfb0108374. Cited on page 8.

[65] Wolfgang Götze. *Complex Dynamics of Glass-Forming Liquids: A Mode-Coupling Theory (International Series of Monographs on Physics)*. Oxford University Press, USA, 2009. ISBN 9780199235346. Cited on page 9.

[66] Ludovic Berthier and G. Tarjus. Testing "microscopic" theories of glass-forming liquids. *The European Physical Journal E*, 34(9):66004, 2011. doi: 10.1140/epje/i2011-11096-5. Cited on page 9.

[67] G. Biroli and J.-P. Bouchaud. The random first-order transition theory of glasses: a critical assessment, 2009. URL `http://www.arxiv.org/abs/0912.2542`. Cited on page 9.

[68] G. Biroli and J.-P. Bouchaud. Diverging length scale and upper critical dimension in the mode-coupling theory of the glass transition. *Europhysics Letters (EPL)*, 67 (1):21–27, 2004. doi: 10.1209/epl/i2004-10044-6. Cited on page 9.

[69] Giulio Biroli, Jean-Philippe Bouchaud, Kunimasa Miyazaki, and David R Reichman. Inhomogeneous mode-coupling theory and growing dynamic length in supercooled liquids. *Physical Review Letters*, 97(19):195701, 2006. doi: 10.1103/physrevlett.97.195701. Cited on page 9.

[70] A. Meyer, S. Stüber, D. Holland-Moritz, O. Heinen, and Tobias Unruh. Determination of self-diffusion coefficients by quasielastic neutron scattering measurements of levitated ni droplets. *Physical Review B*, 77(9), 2008. doi: 10.1103/physrevb.77.092201. Cited on page 9.

[71] Michio Tokuyama. Single master curve for self-diffusion coefficients in distinctly different glass-forming liquids. *Physical Review E*, 82(4), 2010. doi: 10.1103/physreve.82.041501. Cited on page 9.

[72] Rongxin Huang, Isaac Chavez, Katja M. Taute, Branimir Lukić, Sylvia Jeney, Mark G. Raizen, and Ernst-Ludwig Florin. Direct observation of the full transition from ballistic to diffusive brownian motion in a liquid. *Nature Physics*, 2011. doi: 10.1038/nphys1953. Cited on page 9.

[73] Henry Eyring. Viscosity, plasticity, and diffusion as examples of absolute reaction rates. *The Journal of Chemical Physics*, 4(4):283, 1936. doi: 10.1063/1.1749836. Cited on page 10.

[74] B Nijboer and A Rahman. Time expansion of correlation functions and the theory of slow neutron scattering. *Physica*, 32(2):415, 1966. doi: 10.1016/0031-8914(66)90068-1. Cited on page 10.

[75] Jean Pierre Boon and Sidney Yip. *Molecular Hydrodynamics*. McGraw-Hill Inc., US, 1980. ISBN 9780070065604. Cited on pages 10, 17, and 21.

[76] Morrel H Cohen and David Turnbull. Molecular transport in liquids and glasses. *The Journal of Chemical Physics*, 31(5):1164, 1959. doi: 10.1063/1.1730566. Cited on pages 10 and 13.

[77] David Turnbull and Morrel H Cohen. Free-volume model of the amorphous phase: Glass transition. *The Journal of Chemical Physics*, 34(1):120, 1961. doi: 10.1063/1.1731549. Cited on page 10.

[78] David Turnbull and Morrel H Cohen. On the free-volume model of the liquid-glass transition. *The Journal of Chemical Physics*, 52(6):3038, 1970. doi: 10.1063/1.1673434. Cited on page 10.

[79] Martin Goldstein. Viscous liquids and the glass transition: A potential energy barrier picture. *The Journal of Chemical Physics*, 51(9):3728, 1969. doi: 10.1063/1.1672587. Cited on page 10.

[80] R. Richert and C. A. Angell. Dynamics of glass-forming liquids. V. on the link between molecular dynamics and configurational entropy. *The Journal of Chemical Physics*, 108(21):9016, 1998. doi: 10.1063/1.476348. Cited on page 10.

[81] M D Ediger. Spatially heterogeneous dynamics in supercooled liquids. *Annu Rev Phys Chem*, 51:99–128, 2000. doi: 10.1146/annurev.physchem.51.1.99. Cited on page 10.

[82] Gerold Adam and Julian H. Gibbs. On the temperature dependence of cooperative relaxation properties in glass-forming liquids. *The Journal of Chemical Physics*, 43(1):139, 1965. doi: 10.1063/1.1696442. Cited on page 10.

[83] Jeppe C. Dyre, Tina Hechsher, and Kristine Niss. A brief critique of the Adam-Gibbs entropy model. *Journal of Non-Crystalline Solids*, 355(10-12):624, 2009. doi: 10.1016/j.jnoncrysol.2009.01.039. Cited on page 10.

[84] M. Hurley and Peter Harrowell. Kinetic structure of a two-dimensional liquid. *Physical Review E*, 52(2):1694, 1995. doi: 10.1103/physreve.52.1694. Cited on pages 10 and 67.

[85] Willem K. Kegel and Alfons van Blaaderen. Direct observation of dynamical heterogeneities in colloidal hard-sphere suspensions. *Science*, 287(5451):290, 2000. doi: 10.1126/science.287.5451.290. Cited on page 10.

[86] Bente M. I. Flier, Moritz Baier, Johannes Huber, Klaus Müllen, Stefan Mecking, Andreas Zumbusch, and Dominik Wöll. Single molecule fluorescence microscopy investigations on heterogeneity of translational diffusion in thin polymer films. *Physical Chemistry Chemical Physics*, 2011. doi: 10.1039/c0cp01801e. Cited on page 10.

[87] Zexin Zhang, Peter Yunker, Piotr Habdas, and A. Yodh. Cooperative rearrangement regions and dynamical heterogeneities in colloidal glasses with attractive versus repulsive interactions. *Physical Review Letters*, 107(20):208303, 2011. doi: 10.1103/PhysRevLett.107.208303. Cited on page 10.

[88] H. P. Zhang, Avraham Be'er, E.-L. Florin, and Harry L. Swinney. Collective motion and density fluctuations in bacterial colonies. *Proceedings of the National Academy of Sciences of the United States of America*, 107(31):13626–13630, 2010. doi: 10.1073/pnas.1001651107. Cited on page 10.

[89] T. E. Angelini, E. Hannezo, X. Trepat, M. Marquez, J. J. Fredberg, and D A Weitz. Glass-like dynamics of collective cell migration. *Proceedings of the National Academy of Sciences*, 108(12):4714–4719, 2011. doi: 10.1073/pnas.1010059108. Cited on page 10.

[90] Juan P Garrahan. Dynamic heterogeneity comes to life. *Proceedings of the National Academy of Sciences of the United States of America*, 108(12):4701–4702, 2011. doi: 10.1073/pnas.1101436108. Cited on page 10.

[91] Luis Cisneros, John Kessler, Sujoy Ganguly, and Raymond Goldstein. Dynamics of swimming bacteria: Transition to directional order at high concentration. *Physical Review E*, 83(6), 2011. doi: 10.1103/physreve.83.061907. Cited on page 10.

[92] Sharon C. Glotzer. Spatially heterogeneous dynamics in liquids: insights from simulation. *Journal of Non-Crystalline Solids*, 274(1-3):342, 2000. doi: 10.1016/s0022-3093(00)00225-8. Cited on page 10.

[93] X. Han and H. Schober. Transport properties and Stokes-Einstein relation in a computer-simulated glass-forming $Cu_{33.3}Zr_{66.7}$ melt. *Physical Review B*, 83(22), 2011. doi: 10.1103/physrevb.83.224201. Cited on pages 10 and 67.

[94] Bianxiao Cui, Binhua Lin, and Stuart A Rice. Dynamical heterogeneity in a dense quasi-two-dimensional colloidal liquid. *The Journal of Chemical Physics*, 114(20): 9142, 2001. doi: 10.1063/1.1369129. Cited on pages 10 and 67.

[95] Ronen Zangi and Stuart A Rice. Cooperative dynamics in two dimensions. *Physical Review Letters*, 92(3):035502, 2004. doi: 10.1103/physrevlett.92.035502. Cited on pages 10 and 12.

[96] Andrew Marcus, Jeremy Schofield, and Stuart A Rice. Experimental observations of non-Gaussian behavior and stringlike cooperative dynamics in concentrated quasi-two-dimensional colloidal liquids. *Physical Review E*, 60(5):5725, 1999. doi: 10.1103/physreve.60.5725. Cited on pages 10 and 12.

[97] Hideyuki Mizuno and Ryoichi Yamamoto. Computational studies on dynamical heterogeneity in a highly supercooled liquid, 2010. URL `http://arxiv.org/abs/1009.1733`. Cited on page 11.

[98] Nicolas Giovambattista, Sergey Buldyrev, Francis Starr, and H. Stanley. Connection between Adam-Gibbs theory and spatially heterogeneous dynamics. *Physical Review Letters*, 90(8):085506, 2003. doi: 10.1103/physrevlett.90.085506. Cited on page 11.

[99] Takeshi Kawasaki, Takeaki Araki, and Hajime Tanaka. Correlation between dynamic heterogeneity and medium-range order in two-dimensional glass-forming liquids. *Physical Review Letters*, 99(21):215701, 2007. doi: 10.1103/physrevlett.99.215701. Cited on pages 11, 71, and 79.

[100] Takeshi Kawasaki and Hajime Tanaka. Structural origin of dynamic heterogeneity in three-dimensional colloidal glass formers and its link to crystal nucleation. *Journal of Physics: Condensed Matter*, 22(23):232102, 2010. doi: 10.1088/0953-8984/22/23/232102. Cited on page 11.

[101] Takeshi Kawasaki and Hajime Tanaka. Structural signature of slow dynamics and dynamic heterogeneity in two-dimensional colloidal liquids: glassy structural order. *Journal of Physics. Condensed Matter*, 23(19):194121, 2011. doi: 10.1088/0953-8984/23/19/194121. Cited on page 11.

[102] Hajime Tanaka, Takeshi Kawasaki, Hiroshi Shintani, and Keiji Watanabe. Critical-like behaviour of glass-forming liquids. *Nature Materials*, 9(4):324–31, 2010. doi: 10.1038/nmat2634. Cited on page 11.

[103] Hajime Tanaka. Roles of bond orientational ordering in glass transition and crystallization. *Journal of Physics: Condensed Matter*, 23(28):284115, 2011. doi: 10.1088/0953-8984/23/28/284115. Cited on pages 11 and 68.

[104] Johan Mattsson, Hans M Wyss, Alberto Fernandez-Nieves, Kunimasa Miyazaki, Zhibing Hu, David R Reichman, and David A Weitz. Soft colloids make strong

glasses. *Nature*, 462(7269):83–6, 2009. doi: 10.1038/nature08457. Cited on pages 11 and 15.

[105] Sow-Hsin Chen, L Liu, E Fratini, P Baglioni, A Faraone, and E. Mamontov. Observation of fragile-to-strong dynamic crossover in protein hydration water. *Proc. Natl. Acad. Sci. U.S.A.*, 103(24):9012–6, 2006. doi: 10.1073/pnas.0602474103. Cited on pages 11, 29, 56, 75, and 117.

[106] Yael Sarah Elmatad, David Chandler, and Juan P Garrahan. Corresponding states of structural glass formers. ii. *J Phys Chem B*, 114(51):17113–9, 2010. doi: 10.1021/jp1076438. Cited on page 11.

[107] S Khodadadi, J H Roh, A Kisliuk, E. Mamontov, M. Tyagi, S A Woodson, R M Briber, and AP Sokolov. Dynamics of biological macromolecules: not a simple slaving by hydration water. *Biophys. J.*, 98(7):1321–6, 2010. doi: 10.1016/j.bpj.2009.12.4284. Cited on page 11.

[108] S A Lusceac and M Vogel. ^{2}H NMR study of the water dynamics in hydrated myoglobin. *J Phys Chem B*, 114(31):10209–16, 2010. doi: 10.1021/jp103663t. Cited on page 11.

[109] S. Capaccioli, K. L. Ngai, S. Ancherbak, P. A. Rolla, and N. Shinyashiki. The role of primitive relaxation in the dynamics of aqueous mixtures, nano-confined water and hydrated proteins. *Journal of Non-Crystalline Solids*, 357(2):641, 2011. doi: 10.1016/j.jnoncrysol.2010.07.054. Cited on page 11.

[110] S Capponi, A. Arbe, S Cerveny, R Busselez, B Frick, J P Embs, and J Colmenero. Quasielastic neutron scattering study of hydrogen motions in an aqueous poly(vinyl methyl ether) solution. *J Chem Phys*, 134(20):204906, 2011. doi: 10.1063/1.3592560. Cited on page 11.

[111] Yael Sarah Elmatad. Fragile-to-strong crossover in supercooled liquids remains elusive. *Proceedings of the National Academy of Sciences of the United States of America*, 2011. doi: 10.1073/pnas.1103757108. URL `http://arxiv.org/abs/1103.6063`. Cited on page 11.

[112] F. Mallamace, C. Corsaro, Sow-Hsin Chen, and H. E. Stanley. Reply to Elmatad: Supercooled viscous liquids display a fragile-to-strong dynamic crossover. *Proceedings of the National Academy of Sciences*, 2011. doi: 10.1073/pnas.1106373108. Cited on page 11.

[113] Salvatore Magazù, Federica Migliardo, and Antonio Benedetto. Puzzle of protein dynamical transition. *The journal of physical chemistry. B*, 2011. doi: 10.1021/jp111421m. Cited on page 11.

[114] A. Chumakov, I. Sergueev, U. van Bürck, W. Schirmacher, T. Asthalter, R. Rüffer, O. Leupold, and W. Petry. Collective nature of the boson peak and universal

transboson dynamics of glasses. *Physical Review Letters*, 92(24):245508, 2004. doi: 10.1103/PhysRevLett.92.245508. Cited on page 11.

[115] Antina Ghosh, Vijayakumar Chikkadi, Peter Schall, Jorge Kurchan, and Daniel Bonn. Density of states of colloidal glasses. *Physical Review Letters*, 104(24): 248305, 2010. doi: 10.1103/physrevlett.104.248305. Cited on page 11.

[116] Antina Ghosh, Romain Mari, Vijayakumar Chikkadi, Peter Schall, Jorge Kurchan, and Daniel Bonn. Density of states of colloidal glasses and supercooled liquids. *Soft Matter*, 6(13):3082, 2010. doi: 10.1039/c0sm00265h. Cited on pages 11, 12, and 69.

[117] Walter Schirmacher, Gregor Diezemann, and Carl Ganter. Harmonic vibrational excitations in disordered solids and the "boson peak". *Physical Review Letters*, 81 (1):136–139, 1998. doi: 10.1103/PhysRevLett.81.136. Cited on page 12.

[118] D Kaya, N L Green, C E Maloney, and M F Islam. Normal modes and density of states of disordered colloidal solids. *Science*, 329(5992):656–8, 2010. doi: 10.1126/science.1187988. Cited on pages 12 and 69.

[119] Asaph Widmer-Cooper, Heidi Perry, Peter Harrowell, and David R Reichman. Irreversible reorganization in a supercooled liquid originates from localized soft modes. *Nature Physics*, 4(9):711, 2008. doi: 10.1038/nphys1025. Cited on page 12.

[120] Asaph Widmer-Cooper and Peter Harrowell. Free volume cannot explain the spatial heterogeneity of Debye-Waller factors in a glass-forming binary alloy. *Journal of Non-Crystalline Solids*, 352(42-49):5098, 2006. doi: 10.1016/j.jnoncrysol.2006.01.136. Cited on pages 12 and 68.

[121] Asaph Widmer-Cooper and Peter Harrowell. Predicting the long-time dynamic heterogeneity in a supercooled liquid on the basis of short-time heterogeneities. *Physical Review Letters*, 96(18):185701, 2006. doi: 10.1103/physrevlett.96.185701. Cited on page 12.

[122] Ke Chen, Wouter Ellenbroek, Zexin Zhang, Daniel Chen, Peter Yunker, Silke Henkes, Carolina Brito, Olivier Dauchot, Wim van Saarloos, Andrea Liu, and A. Yodh. Low-frequency vibrations of soft colloidal glasses. *Physical Review Letters*, 105(2):025501, 2010. doi: 10.1103/physrevlett.105.025501. Cited on page 12.

[123] Claudio Donati, Jack Douglas, Walter Kob, Steven Plimpton, Peter Poole, and Sharon C. Glotzer. Stringlike cooperative motion in a supercooled liquid. *Physical Review Letters*, 80(11):2338, 1998. doi: 10.1103/physrevlett.80.2338. Cited on page 12.

[124] B Rossi, G Viliani, E Duval, L Angelani, and W Garber. Temperature-dependent vibrational heterogeneities in harmonic glasses. *Europhysics Letters (EPL)*, 71(2): 256, 2007. doi: 10.1209/epl/i2004-10535-4. Cited on page 12.

[125] K. Vollmayr-Lee, W. Kob, K. Binder, and A. Zippelius. Dynamical heterogeneities below the glass transition. *The Journal of Chemical Physics*, 116(12):5158, 2002. doi: 10.1063/1.1453962. Cited on page 12.

[126] D J Ashton and J P Garrahan. Relationship between vibrations and dynamical heterogeneity in a model glass former: extended soft modes but local relaxation. *Eur Phys J E Soft Matter*, 30(3):303–7, 2009. doi: 10.1140/epje/i2009-10531-6. Cited on page 12.

[127] H. von Grünberg, P. Keim, K Zahn, and G Maret. Elastic behavior of a two-dimensional crystal near melting. *Physical Review Letters*, 93(25), 2004. doi: 10.1103/physrevlett.93.255703. Cited on page 12.

[128] F. Saija, S. Prestipino, and P. V. Giaquinta. Entropy, correlations, and ordering in two dimensions. *The Journal of Chemical Physics*, 113(7):2806, 2000. doi: 10.1063/1.1305887. Cited on page 12.

[129] Hans-Joachim Galla, W Hartmann, U Theilen, and Erich Sackmann. On two-dimensional passive random walk in lipid bilayers and fluid pathways in biomembranes. *The Journal of Membrane Biology*, 48(3):215, 1979. doi: 10.1007/bf01872892. Cited on pages 12, 13, and 66.

[130] J L Rubenstein, B A Smith, and Harden M McConnell. Lateral diffusion in binary mixtures of cholesterol and phosphatidylcholines. *Proc. Natl. Acad. Sci. U.S.A.*, 76(1):15–8, 1979. Cited on page 13.

[131] Paulo F F Almeida, Winchil L C Vaz, and T E Thompson. Lateral diffusion in the liquid phases of dimyristoylphosphatidylcholine/cholesterol lipid bilayers: a free volume analysis. *Biochemistry*, 31(29):6739, 1992. doi: 10.1021/bi00144a013. Cited on pages 13, 32, 66, 68, and 71.

[132] Andrey Filippov, Greger Orädd, and Göran Lindblom. The effect of cholesterol on the lateral diffusion of phospholipids in oriented bilayers. *Biophysical Journal*, 84 (5):3079, 2003. doi: 10.1016/s0006-3495(03)70033-2. Cited on pages 13, 66, 70, and 71.

[133] Michael J. Skaug, Roland Faller, and Marjorie L. Longo. Correlating anomalous diffusion with lipid bilayer membrane structure using single molecule tracking and atomic force microscopy. *The Journal of Chemical Physics*, 134(21):215101, 2011. doi: 10.1063/1.3596377. Cited on page 13.

[134] J Korlach, P Schwille, W W Webb, and G W Feigenson. Characterization of lipid bilayer phases by confocal microscopy and fluorescence correlation spectroscopy. *Proc. Natl. Acad. Sci. U.S.A.*, 96(15):8461–6, 1999. Cited on page 13.

[135] V. Mueller, C. Ringemann, A. Honigmann, G. Schwarzmann, R. Medda, M. Leutenegger, S. Polyakova, V. N. Belov, S. W. Hell, and C. Eggeling. Sted

nanoscopy reveals molecular details of cholesterol- and cytoskeleton-modulated lipid interactions in living cells. *Biophysical Journal*, 101(7):1651–1660, 2011. doi: 10.1016/j.bpj.2011.09.006. Cited on page 13.

[136] Sabine König, W Pfeiffer, Thomas M Bayerl, D Richter, and Erich Sackmann. Molecular dynamics of lipid bilayers studied by incoherent quasi-elastic neutron scattering. *Journal de Physique II France*, 2(8):1589, 1992. doi: 10.1051/jp2:1992100. Cited on pages 13, 66, and 67.

[137] Maikel C Rheinstädter, Jhuma Das, Elijah Flenner, Beate Brüning, Tilo Seydel, and Ioan Kosztin. Motional coherence in fluid phospholipid membranes. *Physical Review Letters*, 101(24):248106, 2008. doi: 10.1103/physrevlett.101.248106. Cited on pages 13, 14, 31, 67, and 78.

[138] Winchil L C Vaz and Dieter Hallmann. Experimental evidence against the applicability of the Saffman-Delbrück model to the translational diffusion of lipids in phosphatidylcholine bilayer membranes. *FEBS Letters*, 152(2):287, 1983. doi: 10.1016/0014-5793(83)80397-4. Cited on page 13.

[139] Winchil L C Vaz, Robert M Clegg, and Dieter Hallmann. Translational diffusion of lipids in liquid crystalline phase phosphatidylcholine multibilayers. a comparison of experiment with theory. *Biochemistry*, 24(3):781, 1985. doi: 10.1021/bi00324a037. Cited on page 13.

[140] J Tabony and B Perly. Quasielastic neutron scattering measurements of fast local translational diffusion of lipid molecules in phospholipid bilayers. *Biochimica et Biophysica Acta (BBA) - Biomembranes*, 1063(1):67, 1991. doi: 10.1016/0005-2736(91)90354-b. Cited on pages 13, 64, and 67.

[141] Winchil L C Vaz and Paulo F F Almeida. Microscopic versus macroscopic diffusion in one-component fluid phase lipid bilayer-membranes. *Biophys. J.*, 60(6):1553–1554, 1991. doi: 10.1016/S0006-3495(91)82190-7. Cited on page 13.

[142] Emma Falck, Michael Patra, Mikko Karttunen, Marja T Hyvönen, and Ilpo Vattulainen. Lessons of slicing membranes: interplay of packing, free area, and lateral diffusion in phospholipid/cholesterol bilayers. *Biophys. J.*, 87(2):1076–91, 2004. doi: 10.1529/biophysj.104.041368. Cited on pages 13, 66, 68, 71, and 79.

[143] Paulo F F Almeida, Winchil L C Vaz, and T E Thompson. Lipid diffusion, free area, and molecular dynamics simulations. *Biophys. J.*, 88(6):4434–8, 2005. doi: 10.1529/biophysj.105.059766. Cited on pages 13, 66, 68, and 71.

[144] Emma Falck, Michael Patra, Mikko Karttunen, Marja T Hyvönen, and Ilpo Vattulainen. Response to comment by almeida et al.: free area theories for lipid bilayers–predictive or not? *Biophys. J.*, 89(1):745–52, 2005. doi: 10.1529/biophysj.105.065714. Cited on pages 13, 66, 68, and 71.

[145] Matti Javanainen, Luca Monticelli, Jorge Bernardino de la Serna, and Ilpo Vattulainen. Free volume theory applied to lateral diffusion in langmuir monolayers: atomistic simulations for a protein-free model of lung surfactant. *Langmuir*, 26 (19):15436–44, 2010. doi: 10.1021/la102454m. Cited on pages 14, 66, and 68.

[146] Gary S Ayton and Gregory A Voth. Mesoscopic lateral diffusion in lipid bilayers. *Biophys. J.*, 87(5):3299–311, 2004. doi: 10.1529/biophysj.104.047811. Cited on pages 14 and 15.

[147] Teemu Murtola, Tomasz Róg, Emma Falck, Mikko Karttunen, and Ilpo Vattulainen. Transient ordered domains in single-component phospholipid bilayers. *Physical Review Letters*, 97(23):238102, 2006. doi: 10.1103/physrevlett.97.238102. Cited on page 14.

[148] Matthew Roark and Scott E Feller. Molecular dynamics simulation study of correlated motions in phospholipid bilayer membranes. *The journal of physical chemistry. B*, 113(40):13229–34, 2009. doi: 10.1021/jp902186f. Cited on pages 14 and 67.

[149] Y Gambin, R Lopez-Esparza, M Reffay, E Sierecki, N S Gov, M Genest, R S Hodges, and W Urbach. Lateral mobility of proteins in liquid membranes revisited. *Proc. Natl. Acad. Sci. U.S.A.*, 103(7):2098–102, 2006. doi: 10.1073/pnas.0511026103. Cited on page 14.

[150] Emma Falck, Tomasz Róg, Mikko Karttunen, and Ilpo Vattulainen. Lateral diffusion in lipid membranes through collective flows. *Journal of the American Chemical Society*, 130(1):44–5, 2008. doi: 10.1021/ja7103558. Cited on pages 14, 64, 66, 67, 68, and 95.

[151] Jakob Wohlert and Olle Edholm. Dynamics in atomistic simulations of phospholipid membranes: Nuclear magnetic resonance relaxation rates and lateral diffusion. *The Journal of Chem. Phys.*, 125(20):204703, 2006. doi: 10.1063/1.2393240. Cited on pages 14 and 67.

[152] Sabine König, Thomas M Bayerl, G Coddens, D Richter, and Erich Sackmann. Hydration dependence of chain dynamics and local diffusion in L-α-dipalmitoylphosphtidylcholine multilayers studied by incoherent quasi-elastic neutron scattering. *Biophysical Journal*, 68(5):1871, 1995. doi: 10.1016/s0006-3495(95)80364-4. Cited on pages 15 and 64.

[153] Marcus Trapp, Thomas Gutberlet, Fanni Jurányi, Tobias Unruh, Bruno Demé, Moeava Tehei, and Judith Peters. Hydration dependent studies of highly aligned multilayer lipid membranes by neutron scattering. *The Journal of Chemical Physics*, 133(16):164505, 2010. doi: 10.1063/1.3495973. Cited on pages 15, 30, and 31.

[154] Manolis Doxastakis, Victoria García Sakai, S Ohtake, J K Maranas, and Juan J de Pablo. A molecular view of melting in anhydrous phospholipidic membranes.

Biophys. J., 92(1):147–61, 2007. doi: 10.1529/biophysj.106.089631. Cited on pages 15 and 58.

[155] P Berntsen, C Svanberg, and Jan Swenson. Interplay between hydration water and headgroup dynamics in lipid bilayers. *The Journal of Physical Chemistry. B*, 115(8):1825–1832, 2011. doi: 10.1021/jp110899j. Cited on pages 15 and 29.

[156] Beate Brüning, Maikel C Rheinstädter, A Hiess, B Weinhausen, T Reusch, S Aeffner, and Tim Salditt. Influence of cholesterol on the collective dynamics of the phospholipid acyl chains in model membranes. *The European physical journal. E, Soft matter*, 31(4):419–28, 2010. doi: 10.1140/epje/i2010-10574-6. Cited on pages 15, 31, and 32.

[157] Christopher B. Babayco, Sennur Turgut, Andreia Michelle Smith, Babak Sanii, Donald Land, and Atul N. Parikh. A comparison of lateral diffusion in supported lipid monolayers and bilayers. *Soft Matter*, 6:5877–5881, 2010. doi: 10.1039/c0sm00643b. Cited on page 15.

[158] Robert B Walder, Andrei Honciuc, and Daniel K Schwartz. Phospholipid diffusion at the oil-water interface. *The Journal of Physical Chemistry. B*, 114(35):11484–11488, 2010. doi: 10.1021/jp1053869. Cited on page 15.

[159] Marc Bée. *Quasielastic Neutron Scattering*. Taylor & Francis, 1988. ISBN 9780852743713. Cited on pages 17, 19, and 20.

[160] Gordon Leslie Squires. *Introduction to the Theory of Thermal Neutron Scattering*. Dover Publications, 1996. ISBN 048669447X. Cited on pages 17, 19, 26, and 190.

[161] Sebastian Busch. Protein diffusion in concentrated solutions. Master's thesis, Technische Universität München, 2007. URL `http://users.physik.tu-muenchen.de/sbusch/diplomarbeit.pdf`. Cited on page 17.

[162] Sow-Hsin Chen and Michael Kotlarchyk. *Interaction of Photons and Neutrons With Matter: An Introduction*. World Scientific Publishing Company, 2 edition, 2007. ISBN 9789810242145. Cited on page 17.

[163] Albert Furrer, Joël Mesot, and Thierry Strässle. *Neutron Scattering in Condensed Matter Physics (Neutron Techniques and Applications) (Series on Neutron Techniques and Applications)*. World Scientific Publishing Company, 1 edition, 2009. ISBN 9789810248314. Cited on pages 17 and 19.

[164] Christoph Smuda, Sebastian Busch, Humphrey Morhenn, and Tobias Unruh. QuasiElastic Neutron Scattering at the time-of-flight spectrometer TOFTOF at the FRM II, 2010. URL `http://www.ph.tum.de/studium/praktika/fopra/versuche/61/Anleitung_TOFTOF.pdf`. Cited on page 17.

[165] Léon van Hove. Correlations in space and time and born approximation scattering in systems of interacting particles. *Physical Review*, 95(1):249, 1954. doi: 10.1103/physrev.95.249. Cited on page 17.

[166] Joachim Wuttke, M. Kiebel, E. Bartsch, Franz Fujara, Winfried Petry, and H. Sillescu. Relaxation and phonons in viscous and glassy orthoterphenyl by neutron scattering. *Zeitschrift für Physik B Condensed Matter*, 91(3):357, 1993. doi: 10.1007/bf01344065. Cited on page 19.

[167] Javier Perez, Jean-Marc Zanotti, and Dominique Durand. Evolution of the internal dynamics of two globular proteins from dry powder to solution. *Biophysical Journal*, 77(1):454, 1999. doi: 10.1016/s0006-3495(99)76903-1. Cited on page 19.

[168] Marc Bée. A physical insight into the elastic incoherent structure factor. *Physica B Condensed Matter*, 182(4):323, 1992. doi: 10.1016/0921-4526(92)90034-p. Cited on pages 19 and 20.

[169] G. E. Uhlenbeck and L S Ornstein. On the theory of the Brownian motion. *Physical Review*, 36(5):823, 1930. doi: 10.1103/physrev.36.823. Cited on page 20.

[170] E W Knapp, S F Fischer, and F Parak. Protein dynamics from Mössbauer spectra. the temperature dependence. *The Journal of Physical Chemistry*, 86(26):5042, 1982. doi: 10.1021/j100223a002. Cited on page 20.

[171] F Parak, E W Knapp, and D Kucheida. Protein dynamics: Mössbauer spectroscopy on deoxymyoglobin crystals. *Journal of Molecular Biology*, 161(1):177, 1982. doi: 10.1016/0022-2836(82)90285-6. Cited on page 20.

[172] E W Knapp, S F Fischer, and F Parak. The influence of protein dynamics on Mössbauer spectra. *The Journal of Chemical Physics*, 78(7):4701, 1983. doi: 10.1063/1.445316. Cited on page 20.

[173] Wolfgang Doster and Marcus Settles. Protein-water displacement distributions. *Biochim. Biophys. Acta*, 1749(2):173–86, 2005. doi: 10.1016/j.bbapap.2005.03.010. Cited on page 20.

[174] E. M. Purcell. Life at low reynolds number. *American Journal of Physics*, 45(1):3, 1977. doi: 10.1119/1.10903. Cited on page 21.

[175] Robert Brown. Xxvii. a brief account of microscopical observations made in the months of june, july and august 1827, on the particles contained in the pollen of plants; and on the general existence of active molecules in organic and inorganic bodies. *Philosophical Magazine Series 2*, 4(21):161–173, 1828. doi: 10.1080/14786442808674769. Cited on page 21.

[176] Albert Einstein. Über die von der molekularkinetischen theorie der wärme geforderte bewegung von in ruhenden flüssigkeiten suspendierten teilchen. *Annalen der Physik*, 322(8):549–560, 1905. doi: 10.1002/andp.19053220806. Cited on page 21.

[177] P de Gennes. Liquid dynamics and inelastic scattering of neutrons. *Physica*, 25 (7-12):825, 1959. doi: 10.1016/0031-8914(59)90006-0. Cited on page 21.

[178] Kurt Sköld. Small energy transfer scattering of cold neutrons from liquid argon. *Physical Review Letters*, 19(18):1023, 1967. doi: 10.1103/physrevlett.19.1023. Cited on page 21.

[179] Reiner Zorn. Neutron spectroscopy for confinement studies. *The European Physical Journal Special Topics*, 189(1):65, 2010. doi: 10.1140/epjst/e2010-01310-4. Cited on page 22.

[180] K S Singwi and Alf Sjölander. Diffusive motions in water and cold neutron scattering. *Physical Review*, 119(3):863, 1960. doi: 10.1103/physrev.119.863. Cited on page 22.

[181] Wolfgang Nolting. *Grundkurs Theoretische Physik 6: Statistische Physik (Springer-Lehrbuch)*. Springer, Berlin, 6 edition, 2007. ISBN 9783540688709. Cited on page 22.

[182] E. van Putten, D. Akbulut, J. Bertolotti, W. Vos, A. Lagendijk, and A. Mosk. Scattering lens resolves sub-100 nm structures with visible light. *Physical Review Letters*, 106(19), 2011. doi: 10.1103/physrevlett.106.193905. Cited on page 24.

[183] Carlo Manzo, Thomas S van Zanten, and Maria F Garcia-Parajo. Nanoscale fluorescence correlation spectroscopy on intact living cell membranes with NSOM probes. *Biophys. J.*, 100(2):L8–L10, 2011. doi: 10.1016/j.bpj.2010.12.3690. Cited on page 24.

[184] Konstantin Ulrich, Monica Sanders, Farida Grinberg, Petrik Galvosas, and Sergey Vasenkov. Application of pulsed field gradient NMR with high gradient strength for studies of self-diffusion in lipid membranes on the nanoscale. *Langmuir : the ACS journal of surfaces and colloids*, 24(14):7365–70, 2008. doi: 10.1021/la8002355. Cited on page 24.

[185] G Pabst, N Kučerka, M-P Nieh, Maikel C Rheinstädter, and J Katsaras. Applications of neutron and x-ray scattering to the study of biologically relevant model membranes. *Chemistry and Physics of Lipids*, 163(6):460–479, 2010. doi: 10.1016/j.chemphyslip.2010.03.010. Cited on page 24.

[186] F Sette. Dynamics of glasses and glass-forming liquids studied by inelastic x-ray scattering. *Science*, 280(5369):1550, 1998. doi: 10.1126/science.280.5369.1550. Cited on page 24.

[187] Sow-Hsin Chen, C Y Liao, H W Huang, T M Weiss, Marie-Claire Bellissent-Funel, and F Sette. Collective dynamics in fully hydrated phospholipid bilayers studied by inelastic x-ray scattering. *Physical Review Letters*, 86(4):740, 2001. doi: 10.1103/physrevlett.86.740. Cited on page 24.

[188] Sebastian Busch, Torben H. Jensen, Yuriy Chushkin, and Andrei Fluerasu. Dynamics in shear flow studied by x-ray photon correlation spectroscopy. *European Physical Journal E*, 26:55–62, 2008. doi: 10.1140/epje/i2007-10305-2. URL http://arxiv.org/abs/0803.2843. Cited on page 24.

[189] Varley F Sears. Neutron scattering lengths and cross sections. *Neutron News*, 3(3): 26, 1992. doi: 10.1080/10448639208218770. URL http://www.ncnr.nist.gov/resources/n-lengths/. Cited on pages 25 and 192.

[190] M. Hishida and K. Tanaka. Long-range hydration effect of lipid membrane studied by terahertz time-domain spectroscopy. *Physical Review Letters*, 106(15), 2011. doi: 10.1103/physrevlett.106.158102. Cited on pages 29 and 31.

[191] Norbert Kučerka, Yufeng Liu, Nanjun Chu, Horia I Petrache, Stephanie Tristram-Nagle, and John F Nagle. Structure of fully hydrated fluid phase DMPC and DLPC lipid bilayers using x-ray scattering from oriented multilamellar arrays and from unilamellar vesicles. *Biophys. J.*, 88(4):2626–37, 2005. doi: 10.1529/biophysj.104.056606. Cited on page 30.

[192] Jan Swenson, Florian Kargl, P Berntsen, and C Svanberg. Solvent and lipid dynamics of hydrated lipid bilayers by incoherent quasielastic neutron scattering. *The Journal of chemical physics*, 129(4):045101, 2008. doi: 10.1063/1.2955753. Cited on page 30.

[193] Victor V Volkov, D Jason Palmer, and Roberto Righini. Heterogeneity of water at the phospholipid membrane interface. *The journal of physical chemistry. B*, 111(6): 1377–83, 2007. doi: 10.1021/jp065886t. Cited on page 31.

[194] K J Tielrooij, D Paparo, L Piatkowski, H J Bakker, and M Bonn. Dielectric relaxation dynamics of water in model membranes probed by terahertz spectroscopy. *Biophys. J.*, 97(9):2484–92, 2009. doi: 10.1016/j.bpj.2009.08.024. Cited on page 31.

[195] Maikel C Rheinstädter, C Ollinger, G Fragneto, Franz Demmel, and Tim Salditt. Collective dynamics of lipid membranes studied by inelastic neutron scattering. *Physical Review Letters*, 93(10):108107, 2004. doi: 10.1103/physrevlett.93.108107. Cited on pages 31 and 68.

[196] Maikel C Rheinstädter, Tilo Seydel, Franz Demmel, and Tim Salditt. Molecular motions in lipid bilayers studied by the neutron backscattering technique. *Physical Review E*, 71(6):061908, 2005. doi: 10.1103/physreve.71.061908. Cited on page 31.

[197] Maikel C Rheinstädter, Wolfgang Häußler, and Tim Salditt. Dispersion relation of lipid membrane shape fluctuations by neutron spin-echo spectrometry. *Physical Review Letters*, 97(4):048103, 2006. doi: 10.1103/physrevlett.97.048103. Cited on page 31.

[198] Maikel C Rheinstädter, Tilo Seydel, and Tim Salditt. Nanosecond molecular relaxations in lipid bilayers studied by high energy-resolution neutron scattering and in situ diffraction. *Physical Review E*, 75(1):011907, 2007. doi: 10.1103/physreve.75.011907. Cited on page 31.

[199] Maikel C Rheinstädter, Karin Schmalzl, Kathleen Wood, and Dieter Strauch. Protein-protein interaction in purple membrane. *Physical Review Letters*, 103(12): 128104, 2009. doi: 10.1103/physrevlett.103.128104. Cited on page 31.

[200] Martin Kaye, Karin Schmalzl, Valeria Nibali, Mounir Tarek, and Maikel C Rheinstädter. Ethanol enhances collective dynamics of lipid membranes. *Physical Review E*, 83(5), 2011. doi: 10.1103/physreve.83.050907. Cited on page 31.

[201] Hanna P Wacklin. Composition and asymmetry in supported membranes formed by vesicle fusion. *Langmuir : the ACS journal of surfaces and colloids*, 2011. doi: 10.1021/la200683e. Cited on page 31.

[202] Debora Berti, Gabriella Caminati, and Piero Baglioni. Functional liposomes and supported lipid bilayers: towards the complexity of biological archetypes. *Phys Chem Chem Phys*, 13(19):8769–82, 2011. doi: 10.1039/c0cp02400g. Cited on page 31.

[203] Clare L. Armstrong, Martin D. Kaye, Michaela Zamponi, Eugene Mamontov, Madhusudan Tyagi, Timothy Jenkins, and Maikel C Rheinstädter. Diffusion in single supported lipid bilayers studied by quasi-elastic neutron scattering. *Soft Matter*, 6:5864–5867, 2010. doi: 10.1039/c0sm00637h. Cited on pages 31 and 67.

[204] Ulrike Lauf. *DMPC-Nanotubes – Untersuchungen einer neuartigen Vesikelstruktur in Dispersionen aus 1,2-Dimyristoyl-sn-glycero-3-phosphatidylcholin*. PhD thesis, Friedrich-Schiller-Universität Jena, 2003. Cited on page 31.

[205] Ulrike Lauf, Alfred Fahr, Kirsten Westesen, and Anne S Ulrich. Novel lipid nanotubes in dispersions of dmpc. *Chemphyschem : a European journal of chemical physics and physical chemistry*, 5(8):1246–9, 2004. doi: 10.1002/cphc.200400235. Cited on page 31.

[206] Jochen S Hub, Tim Salditt, Maikel C Rheinstädter, and Bert L de Groot. Short-range order and collective dynamics of dmpc bilayers: a comparison between molecular dynamics simulations, x-ray, and neutron scattering experiments. *Biophys. J.*, 93(9):3156–68, 2007. doi: 10.1529/biophysj.107.104885. Cited on pages 32 and 78.

[207] M J Hope, M B Bally, G Webb, and P R Cullis. Production of large unilamellar vesicles by a rapid extrusion procedure. characterization of size distribution, trapped volume and ability to maintain a membrane potential. *Biochimica et Biophysica Acta (BBA) - Biomembranes*, 812(1):55, 1985. doi: 10.1016/0005-2736(85)90521-8. Cited on page 33.

[208] S. Torquato, T. Truskett, and P G Debenedetti. Is random close packing of spheres well defined? *Physical Review Letters*, 84(10):2064–2067, 2000. doi: 10.1103/physrevlett.84.2064. Cited on page 33.

[209] Bruce J. Berne and Robert Pecora. *Dynamic Light Scattering: With Applications to Chemistry, Biology, and Physics*. Dover Publications, 2000. ISBN 9780486411552. Cited on page 34.

[210] Robert C MacDonald, Ruby I MacDonald, Bert Ph M Menco, Keizo Takeshita, Nanda K Subbarao, and Lan-rong Hu. Small-volume extrusion apparatus for preparation of large, unilamellar vesicles. *Biochimica et Biophysica Acta (BBA) - Biomembranes*, 1061(2):297, 1991. doi: 10.1016/0005-2736(91)90295-j. Cited on page 33.

[211] Tobias Unruh, Jürgen Neuhaus, and Winfried Petry. The high-resolution time-of-flight spectrometer TOFTOF. *Nucl. Instrum. Methods Phys. Res., Sect. A*, 580 (3):1414–1422, 2007. doi: 10.1016/j.nima.2007.07.015. Cited on pages 35, 36, 37, and 190.

[212] Tobias Unruh, Jürgen Neuhaus, and Winfried Petry. The high-resolution time-of-flight spectrometer TOFTOF (vol 580, pg 1414, 2007). *Nucl. Instrum. Methods Phys. Res., Sect. A*, 585(3):201, 2008. doi: 10.1016/j.nima.2007.11.019. Cited on pages 35, 36, and 37.

[213] Stephan V Roth. *Konzeption und neutronenoptische Optimierung des kalten Flugzeitspektrometers am FRM-II*. PhD thesis, Technische Universität München, 2001. Cited on pages 36 and 37.

[214] Ana M. Gaspar. Methods for analytically estimating the resolution and intensity of neutron time-of-flight spectrometers. the case of the TOFTOF spectrometer, 2007. URL `http://arxiv.org/abs/0710.5319`. Cited on page 36.

[215] Joseph Cerny, Claude Détraz, and Richard Pehl. Li^4 and the excited levels of He^4. *Physical Review Letters*, 15(7):300, 1965. doi: 10.1103/physrevlett.15.300. Cited on page 38.

[216] L. Passell and R. Schermer. Measurement of the spin dependence of the He^3(n,p)T reaction and of the nuclear susceptibility of adsorbed He^3. *Physical Review*, 150(1): 146, 1966. doi: 10.1103/physrev.150.146. Cited on page 38.

[217] Richard B Firestone. *Table of Isotopes CD-ROM*. Wiley-Interscience, 8 cdr edition, 1996. ISBN 9780471164050. Cited on page 38.

[218] Tobias Unruh, Christoph Smuda, Sebastian Busch, Jürgen Neuhaus, and Winfried Petry. Diffusive motions in liquid medium-chain *n*-alkanes as seen by quasielastic time-of-flight neutron spectroscopy. *The Journal of Chemical Physics*, 129:121106, 2008. doi: 10.1063/1.2990026. Cited on page 40.

[219] Joachim Wuttke. Improved sample holder for multidetector neutron spectrometers. *Physica B Condensed Matter*, 266(1-2):112, 1999. doi: 10.1016/s0921-4526(98)01503-8. Cited on page 43.

[220] Joachim Wuttke. Self-absorption coefficient for tubular samples – Erratum and Addendum to Physica B 266 (1999) 112. *Physica B Condensed Matter*, 292(3-4): 194, 2000. doi: 10.1016/s0921-4526(00)00479-8. Cited on page 43.

[221] H H Paalman and C J Pings. Numerical evaluation of x-ray absorption factors for cylindrical samples and annular sample cells. *Journal of Applied Physics*, 33(8): 2635, 1962. doi: 10.1063/1.1729034. Cited on pages 48 and 192.

[222] Ana M. Gaspar, Marie-Sousai Appavou, Sebastian Busch, Tobias Unruh, and Wolfgang Doster. Dynamics of well-folded and natively disordered proteins in solution: a time-of-flight neutron scattering study. *European Biophysics Journal with Biophysics Letters*, 37:573–582, 2008. doi: 10.1007/s00249-008-0266-3. Cited on page 49.

[223] Thomas Weise. *Global Optimization Algorithms - Theory and Application*. Self-Published, second edition, 2009. URL `http://www.it-weise.de/`. Online available at http://www.it-weise.de/. Cited on pages 51 and 76.

[224] M. Clutton-Brock. Likelihood distributions for estimating functions when both variables are subject to error. *Technometrics*, 9(2):261–269, 1967. URL `http://www.jstor.org/stable/1266422`. Cited on pages 51 and 52.

[225] Jay Orear. Least squares when both variables have uncertainties. *American Journal of Physics*, 50(10):912, 1982. doi: 10.1119/1.12972. Cited on page 52.

[226] Matthew Lybanon. Comment on "least squares when both variables have uncertainties". *American Journal of Physics*, 52(3):276, 1984. doi: 10.1119/1.13713. Cited on page 52.

[227] Jay Orear. Erratum for "least squares when both variables have uncertainties" [am. j. phys. 50, 912 (1982)]. *American Journal of Physics*, 52(3):278, 1984. doi: 10.1119/1.13941. Cited on page 52.

[228] Matthew Lybanon. A better least-squares method when both variables have uncertainties. *American Journal of Physics*, 52(1):22, 1984. doi: 10.1119/1.13822. Cited on page 52.

[229] George E. P. Box. Science and statistics. *Journal of the Am. Stat. Assoc.*, 71(356): 791–799, 1976. URL `http://www.jstor.org/stable/2286841`. Cited on page 54.

[230] Andreas Maximilian Stadler, Lambert van Eijck, Franz Demmel, and Gerhard M Artmann. Macromolecular dynamics in red blood cells investigated using neutron spectroscopy. *J R Soc Interface*, 8(57):590–600, 2011. doi: 10.1098/rsif.2010.0306. URL `http://arxiv.org/abs/1104.1551`. Cited on page 54.

[231] F Fujara and W Petry. Fast local motion around t_g in a molecular glass as observed by incoherent neutron scattering. *Europhysics Letters (EPL)*, 4(8):921–927, 1987. doi: 10.1209/0295-5075/4/8/011. Cited on page 57.

[232] B. Frick, D. Richter, W. Petry, and U. Buchenau. Study of the glass transition order parameter in amorphous polybutadiene by incoherent neutron scattering. *Zeitschrift für Physik B Condensed Matter*, 70(1):73–79, 1988. doi: 10.1007/BF01320541. Cited on page 57.

[233] Wolfgang Doster, Stephen Cusack, and Winfried Petry. Dynamical transition of myoglobin revealed by inelastic neutron scattering. *Nature*, 337(6209):754–6, 1989. doi: 10.1038/337754a0. Cited on pages 57 and 77.

[234] Wolfgang Doster, M Diehl, R Gebhardt, Ruep E Lechner, and J Pieper. Tof-elastic resolution spectroscopy: time domain analysis of weakly scattering (biological) samples. *Chemical Physics*, 292(2-3):487, 2003. doi: 10.1016/s0301-0104(03)00156-3. Cited on pages 57 and 58.

[235] Salvatore Magazù, Giacomo Maisano, Federica Migliardo, Giovanni Galli, Antonio Benedetto, Denis Morineau, F Affouard, and M Descamps. Characterization of molecular motions in biomolecular systems by elastic incoherent neutron scattering. *The Journal of chemical physics*, 129(15):155103, 2008. doi: 10.1063/1.2989804. Cited on page 58.

[236] Salvatore Magazù, Giacomo Maisano, Federica Migliardo, and Antonio Benedetto. Biomolecular motion characterization by a self-distribution-function procedure in elastic incoherent neutron scattering. *Physical Review E*, 79(4):041915, 2009. doi: 10.1103/physreve.79.041915. Cited on page 58.

[237] Andreas Roncat, Gunther Bergauer, and Norbert Pfeifer. B-spline deconvolution for differential target cross-section determination in full-waveform laser scanning data. *ISPRS Journal of Photogrammetry and Remote Sensing*, 66(4):418, 2011. doi: 10.1016/j.isprsjprs.2011.02.002. Cited on page 59.

[238] José Teixeira, Marie-Claire Bellissent-Funel, Sow-Hsin Chen, and Albert-José Dianoux. Experimental determination of the nature of diffusive motions of water molecules at low temperatures. *Physical Review A*, 31(3):1913, 1985. doi: 10.1103/physreva.31.1913. Cited on page 63.

[239] Christoph Smuda, Sebastian Busch, Gerd Gemmecker, and Tobias Unruh. Self-diffusion in molecular liquids: Medium-chain n-alkanes and coenzyme Q_{10} studied by quasielastic neutron scattering. *The Journal of Chemical Physics*, 129:014513, 2008. doi: 10.1063/1.2943673. Selected for the Virtual Journal of Biological Physics Research 16(2), 2008. Cited on pages 65 and 66.

[240] Andreas Meyer, Joachim Wuttke, Winfried Petry, Oliver G Randl, and Helmut R Schober. Slow motion in a metallic liquid. *Physical Review Letters*, 80(20):4454, 1998. doi: 10.1103/physrevlett.80.4454. Cited on page 66.

[241] Rainer A Böckmann, Agnieszka Hac, Thomas Heimburg, and Helmut Grubmüller. Effect of sodium chloride on a lipid bilayer. *Biophysical Journal*, 85(3):1647, 2003. doi: 10.1016/s0006-3495(03)74594-9. Cited on page 66.

[242] Christopher Hofsäß, Erik Lindahl, and Olle Edholm. Molecular dynamics simulations of phospholipid bilayers with cholesterol. *Biophysical Journal*, 84(4):2192, 2003. doi: 10.1016/s0006-3495(03)75025-5. Cited on page 67.

[243] K Zahn and G Maret. Dynamic criteria for melting in two dimensions. *Physical Review Letters*, 85(17):3656, 2000. doi: 10.1103/physrevlett.85.3656. Cited on pages 67, 68, and 69.

[244] H König, R Hund, K Zahn, and G Maret. Experimental realization of a model glass former in 2d. *Eur Phys J E Soft Matter*, 18(3):287–93, 2005. doi: 10.1140/epje/e2005-00034-9. Cited on pages 67 and 79.

[245] W. C. Duer, J. R. Greenstein, G. B. Oglesby, and F. J. Millero. Qualitative observations concerning packing densities for liquids, solutions, and random assemblies of spheres. *Journal of Chemical Education*, 54(3):139, 1977. doi: 10.1021/ed054p139. Cited on page 68.

[246] Ludovic Berthier and Giulio Biroli. Theoretical perspective on the glass transition and amorphous materials. *Reviews of Modern Physics*, 83(2):587, 2011. doi: 10.1103/revmodphys.83.587. Cited on page 68.

[247] Ludovic Berthier. Dynamic heterogeneity in amorphous materials. *Physics*, 4:42, 2011. doi: 10.1103/physics.4.42. Cited on page 68.

[248] Etienne Bernard and Werner Krauth. Two-step melting in two dimensions: First-order liquid-hexatic transition. *Physical Review Letters*, 107(15):155704, 2011. doi: 10.1103/physrevlett.107.155704. Cited on page 68.

[249] Siewert J Marrink, Jelger Risselada, and Alan E. Mark. Simulation of gel phase formation and melting in lipid bilayers using a coarse grained model. *Chem. Phys. Lipids*, 135(2):223–44, 2005. doi: 10.1016/j.chemphyslip.2005.03.001. Cited on page 68.

[250] Nadezhda Gribova, Axel Arnold, Tanja Schilling, and Christian Holm. How close to two dimensions does a lennard-jones system need to be to produce a hexatic phase? *J Chem Phys*, 135(5):054514, 2011. doi: 10.1063/1.3623783. Cited on page 68.

[251] Subhadip Ghosh, Aniruddha Adhikari, Supratik Sen Mojumdar, and Kankan Bhattacharyya. A fluorescence correlation spectroscopy study of the diffusion of an organic dye in the gel phase and fluid phase of a single lipid vesicle. *The journal of physical chemistry. B*, 114(17):5736–41, 2010. doi: 10.1021/jp911971p. Cited on page 69.

[252] Megumi Shintani, Ken Yoshida, Shun Sakuraba, Masaru Nakahara, and Nobuyuki Matubayasi. NMR-NOE and MD simulation study on phospholipid membranes: Dependence on membrane diameter and multiple time scale dynamics. *The Journal of Physical Chemistry B*, page 110705093840002, 2011. doi: 10.1021/jp204051f. Cited on page 71.

[253] Cameron Neylon, Carol Tenopir, Suzie Allard, Kimberly Douglass, Arsev Umur Aydinoglu, Lei Wu, Eleanor Read, Maribeth Manoff, and Mike Frame. Data sharing by scientists: Practices and perceptions. *PLoS ONE*, 6(6):e21101, 2011. doi: 10.1371/journal.pone.0021101. Cited on page 75.

[254] Alexander Szalay and Jim Gray. The world-wide telescope. *Science*, 293(5537): 2037–2040, 2001. doi: 10.1126/science.293.5537.2037. Cited on page 75.

[255] E. Birney, T. J. Hudson, E. D. Green, C. Gunter, S. Eddy, J. Rogers, J. R. Harris, S. D. Ehrlich, R. Apweiler, C. P. Austin, et al. Prepublication data sharing. *Nature*, 461(7261):168–170, 2009. doi: 10.1038/461168a. Cited on page 75.

[256] Paul N. Schofield, Tania Bubela, Thomas Weaver, Lili Portilla, Stephen D. Brown, John M. Hancock, David Einhorn, Glauco Tocchini-Valentini, Martin Hrabe de Angelis, and Nadia Rosenthal. Post-publication sharing of data and tools. *Nature*, 461(7261):171–173, 2009. doi: 10.1038/461171a. Cited on page 75.

[257] Eric O Lebigot. uncertainties. `http://packages.python.org/uncertainties/`, 2010. URL `http://packages.python.org/uncertainties/`. Software. Cited on page 75.

[258] Anand Patil, David Huard, and Christopher J. Fonnesbeck. Pymc: Bayesian stochastic modelling in python. *Journal of Statistical Software*, 35(4):1–81, 2010. ISSN 1548-7660. URL `http://www.jstatsoft.org/v35/i04`. Cited on page 76.

[259] Walter R. Gilks, Gareth O. Roberts, and Sujit K. Sahu. Adaptive markov chain monte carlo through regeneration. *Journal of the American Statistical Association*, 93(443):1045, 1998. doi: 10.2307/2669848. Cited on page 76.

[260] Emma Falck, Michael Patra, Mikko Karttunen, Marja T Hyvönen, and Ilpo Vattulainen. Impact of cholesterol on voids in phospholipid membranes. *The Journal of chemical physics*, 121(24):12676–89, 2004. doi: 10.1063/1.1824033. Cited on page 79.

[261] Manolis Doxastakis, Amadeu K Sum, and Juan J de Pablo. Modulating membrane properties: the effect of trehalose and cholesterol on a phospholipid bilayer. *The*

journal of physical chemistry. B, 109(50):24173–81, 2005. doi: 10.1021/jp054843u. Cited on page 79.

[262] Tomasz Róg, Marta Pasenkiewicz-Gierula, Ilpo Vattulainen, and Mikko Karttunen. Ordering effects of cholesterol and its analogues. *Biochim. Biophys. Acta*, 1788(1): 97–121, 2009. doi: 10.1016/j.bbamem.2008.08.022. Cited on page 79.

[263] Donna N. Perera and Peter Harrowell. Relaxation dynamics and their spatial distribution in a two-dimensional glass-forming mixture. *The Journal of Chemical Physics*, 111(12):5441, 1999. doi: 10.1063/1.479804. Cited on page 79.

[264] Takayuki Narumi, Scott V. Franklin, Kenneth W. Desmond, Michio Tokuyama, and Eric R. Weeks. Spatial and temporal dynamical heterogeneities approaching the binary colloidal glass transition. *Soft Matter*, 2011. doi: 10.1039/c0sm00756k. Cited on page 79.

[265] Todd P W McMullen, Ruthven N. A. H. Lewis, and Ronald N McElhaney. Differential scanning calorimetric study of the effect of cholesterol on the thermotropic phase behavior of a homologous series of linear saturated phosphatidylcholines. *Biochemistry*, 32(2):516–522, 1993. doi: 10.1021/bi00053a016. Cited on page 79.

[266] François Sausset and Gilles Tarjus. Comment on "correlation between dynamic heterogeneity and medium-range order in two-dimensional glass-forming liquids". *Physical Review Letters*, 100(9):099601, 2008. doi: 10.1103/physrevlett.100.099601. Cited on page 79.

[267] Takeshi Kawasaki, Takeaki Araki, and Hajime Tanaka. Reply to comment on "correlation between dynamic heterogeneity and medium-range order in two-dimensional glass-forming liquids". *Physical Review Letters*, 100(9):099602, 2008. doi: 10.1103/physrevlett.100.099602. Cited on page 79.

[268] Luca Cipelletti, Laurence Ramos, S Manley, E. Pitard, D A Weitz, Eugene E. Pashkovski, and Marie Johansson. Universal non-diffusive slow dynamics in aging soft matter. *Faraday Discussions*, 123:237, 2002. doi: 10.1039/b204495a. Cited on page 95.

[269] Joachim Wuttke. Frida1: Fast reliable interactive data analysis, 1990–. URL `http://sourceforge.net/projects/frida/`. Software. Cited on page 183.

[270] D G Rancourt. Accurate site populations from Mössbauer spectroscopy. *Nuclear Instruments and Methods in Physics Research Section B Beam Interactions with Materials and Atoms*, 44(2):199, 1989. doi: 10.1016/0168-583x(89)90428-x. Cited on pages 186 and 187.

[271] Sebastian Busch. sihl: Scattered intensity handling library. `http://www.thamnos.de/repos/sihl/`, 2009–. URL `http://www.thamnos.de/repos/sihl/`. Software. Cited on page 188.

[272] Eric Jones, Travis Oliphant, Pearu Peterson, et al. SciPy: Open source scientific tools for Python, 2001–. URL `http://www.scipy.org/`. Cited on page 188.

[273] Sebastian Busch. chaste: Collection of tools for handling data with standard errors. `http://www.thamnos.de/repos/chaste/`, 2008–. URL `http://www.thamnos.de/repos/chaste/`. Software. Cited on page 188.

[274] John D. Hunter. Matplotlib: A 2D graphics environment. *Computing In Science & Engineering*, 9(3):90–95, 2007. Cited on page 188.

[275] Neil W. Ashcroft and David N. Mermin. *Solid State Physics*. Thomson Press (India) Ltd, 2003. ISBN 9788131500521. Cited on page 192.

Acknowledgements

It is my pleasure and concern to thank the many people without whom this thesis could not have been carried out. Representatively for them all, I would like to mention

Prof. Winfried Petry for supervising this thesis, his steady interest in the progress, and – representatively for many – for the outstanding conditions at the Forschungs-Neutronenquelle Heinz Maier-Leibnitz (FRM II).

Prof. Martin Zacharias and Prof. Andreas Bausch who accepted to chair and to correct this dissertation, respectively. Further, I would like to thank Prof. Bausch to spark my interest in biophysics during my studies.

Prof. Tobias Unruh for countless hours of discussion in his office in Munich and for counterbalancing my urge to reanalyze vanadium for the $(n+1)^{\text{th}}$ time.

Luis Carlos Pardo who explained glass physics and Bayesian concepts to me. And again. And again...

Jean-François Moulin for abducting me now and then into the beautiful south of Munich and nearly daily into interesting science and python topics.

Joachim Wuttke to whom I could come with any new idea I had – only to find out that he had had this very idea already many years ago.

Muriel Rovira-Esteva for introducing me to the subtleties of the structure of liquids, allowing me to profit from her work, and letting me know about interesting job offers.

Kathrin Buchner for everything – help, food, chocolate, mountains, walks, runs, and movies to name just a few.

Humphrey Morhenn, Martin Schmiele, and Christoph Smuda for the good times we had in the office; Christoph for his start-off aid and Humphrey for a helping hand on TOFTOF.

Marie-Sousai Appavou, Wolfgang Doster, and Ana Gaspar for keeping me involved in their research and for several cultural and culinary getaways.

Sarah Kurmulis for her help with the dynamic light scattering setup and for helping out with sample changes at TOFTOF.

Johannes Brunner for taking the neutron radiography of our sample can at ANTARES.

Prof. Erich Sackmann for his encouragement.

Thomasz Róg for his hospitality in Helsinki.

Jakob Mayer for making the FRM II very quickly my new home.

The whole chair E13 at the physics department – my second home.

My family, parents, brothers and sisters as well as Jennifer for making this work possible – and especially for letting me know that their love is completely independent from it.

I further thank Ana, Humphrey, Jean-François, Luis Carlos, and Tobias for reading the manuscript critically and their numerous comments; and last but not least the reader who actually made his or her way through to the last page.

Thank you.